Graefes Arch Clin Exp Ophthalmol (2015) 253:295–305
DOI 10.1007/s00417-014-2868-z

GENETICS

# Histopathological comparison of eyes from patients with autosomal recessive retinitis pigmentosa caused by novel *EYS* mutations

**Vera L. Bonilha · Mary E. Rayborn · Brent A. Bell · Meghan J. Marino · Gayle J. Pauer · Craig D. Beight · John Chiang · Elias I. Traboulsi · Joe G. Hollyfield · Stephanie A. Hagstrom**

Received: 25 July 2014 / Revised: 12 November 2014 / Accepted: 14 November 2014 /

**Abstract** To evaluate the retinal histopathology in donor eyes from patients with autosomal recessive retinitis pigmentosa (arRP) caused by *EYS* mutations. Eyes from a 72-year-old female (donor 1, family 1), a 91-year-old female (donor 2, family 2), and her 97-year-old sister (donor 3, family 2) were evaluated with macroscopic, scanning laser ophthalmoscopy (SLO) and optical coherence tomography (OCT) imaging. Age-similar normal eyes and an eye donated by donor 1's asymptomatic mother (donor 4, family 1) were used as controls. The perifovea and peripheral retina were processed for microscopy and immunocytochemistry with markers for cone and rod photoreceptor cells. DNA analysis revealed *EYS* mutations c.2259+1G>A and c.2620C>T (p.Q874X) in family 1, and c.4350_4356del (p.I1451Pfs*3) and c.2739-?_3244+?del in family 2. Imaging studies revealed the presence of bone spicule pigment in arRP donor retinas. Histology of all three affected donor eyes showed very thin retinas with little evidence of stratified nuclear layers in the periphery. In contrast, the perifovea displayed a prominent inner nuclear layer. Immunocytochemistry analysis demonstrated advanced retinal degenerative changes in all eyes, with near-total absence of rod photoreceptors. In addition, we found that the perifoveal cones were more preserved in retinas from the donor with the midsize genomic rearrangement (c.4350_4356del (p.I1451Pfs*3) and c.2739-?_3244+?del) than in retinas from the donors with the truncating (c.2259+1G>A and c.2620C>T (p.Q874X) mutations. Advanced retinal degenerative changes with near-total absence of rods and preservation of some perifoveal cones are observed in arRP donor retinas with *EYS* mutations.

**Keywords** Recessive retinitis pigmentosa · *EYS* mutations · Histopathology · Immunohistochemistry

## Introduction

The inherited retinal diseases referred to as retinitis pigmentosa (RP) exhibit a wide variety of genetic heterogeneity, variable expressivity, allelic heterogeneity, and phenotypic variability. RP is the most common form of inherited retinal degeneration, affecting 1 in 3,500 people, with more than 1 million patients worldwide [1, 2]. It is characterized by progressive rod and cone photoreceptor cell dysfunction, and results in the clinical appearance of optic nerve pallor, retinal vascular attenuation, and peripheral pigmentary and atrophic changes. Visual deficits in affected individuals initially include night blindness, due to rod photoreceptor loss, followed by progressive loss of peripheral vision. Ultimately, nearly all patients lose central vision between the ages of 50 and 80 years [3].

Families with RP demonstrate all known patterns of Mendelian inheritance, including autosomal dominant, autosomal recessive, and X-linked. Non-Mendelian inheritance patterns such as digenic and maternal inheritance have also been reported. Sixty percent of all RP cases are autosomal recessive (arRP) [4]. Currently, mutations have been identified in 35 different genes in arRP patients (http://www.sph.uth.tmc.edu/Retnet/). Together, mutations in these genes account for approximately 50 % of cases. The genes that are associated

V. L. Bonilha (✉) · M. E. Rayborn · B. A. Bell · M. J. Marino · G. J. Pauer · C. D. Beight · E. I. Traboulsi · J. G. Hollyfield · S. A. Hagstrom
Ophthalmic Research - i31, Cleveland Clinic, Cole Eye Institute,
9500 Euclid Avenue, Cleveland, OH 44195, USA
e-mail: bonilhav@ccf.org

V. L. Bonilha · E. I. Traboulsi · J. G. Hollyfield · S. A. Hagstrom
Department of Ophthalmology, Cleveland Clinic Lerner College of Medicine of Case Western Reserve University, Cleveland,
OH 44195, USA

J. Chiang
Casey Eye Institute, Portland, OR 97239, USA

with arRP encode proteins that exert their function in different pathways within the retina, including the phototransduction cascade (*CNGA1*, *CNGB1*, *PDE6A*, *PDE6B*, *RGR*, *RHO*, *SAG*), vitamin A metabolism (*ABCA4*, *LRAT*, *RLBP1*, *RPE65*), structural or signaling functions (*CRB1*, *RP1*, *TULP1*, *USH2A*), transcriptional regulation (*NR2E3*, *NRL*), and retinal pigment epithelium (RPE) phagocytosis (*MERTK*), or have unknown functions (*CERKL*, *PRCD*, *PROM1*) [5].

Approximately 5–16 % of arRP cases [6] result from mutations in the *eyes shut homolog* (*EYS*) gene, identified at the RP25 locus [5, 7]. Spanning over 2,000 bp (6p12.1-6q15), *EYS* is one of the largest genes expressed in the human eye to date [7]. The longest isoform of *EYS* encodes a protein of 3,165 amino acids whose function remains to be elucidated. The only characterized EYS homologue, Drosophila's spacemaker or SPAM, is involved in the assembly of the light-sensitive rhabdomere, the insect equivalent of vertebrate photoreceptor outer segments [8]. Indeed, the human EYS protein is localized to the photoreceptor outer segments [7]. Considering the evolutionary data and the known function of the Drosophila ortholog, *EYS* is likely to play a role in the modeling and integrity of retinal architecture [8].

Mutations in more than 60 genes are known to cause RP. Early histopathologic studies of human RP retinas were performed in tissue from donors with unknown genetic mutations and involved only descriptive studies [9–18]. The next group of manuscripts utilized immunocytochemistry assays to analyze the effects of the disease on photoreceptors and the other retinal cells [19–24]. A few recent studies reported histopathologic findings from RP patients with different known gene mutations, including rhodopsin (*RHO*) [21, 25–29], pre-mRNA processing factor 8 (*PRPC8*) [30], retinitis pigmentosa GTPase regulator (*RPGR*) [31, 32], ATP-binding cassette, sub-family A, member 4 (*ABCA4*) [33]. Such types of studies are crucial to understand how these genetic mutations lead to dysfunction and photoreceptor cell death in RP patients.

Here we report the ocular histopathology in eyes from three arRP donors with mutations in *EYS*. We focus on retinal pathology changes and the effect of the disease on the distribution of photoreceptors and other retinal cells. Eye donor 1 carries two heterozygous novel truncating *EYS* gene mutations, and the related eye donors 2 and 3 have two heterozygous *EYS* deletion mutations. Given the limited molecular characterization of affected individuals whose eyes have been made available for postmortem examination, the opportunity to combine genetic and phenotypic findings is unprecedented.

## Methods

*Tissue acquisition and fixation* Donor eyes were obtained through the Foundation Fighting Blindness (FFB) Eye Donor Program (Columbia, MD, USA). Immunocytochemical analysis was performed with the approval of the Cleveland Clinic Institutional Review Board (IRB #14-057). The research adhered to the tenets of the Declaration of Helsinki. The analyzed tissue included FFB donations #228, 649, 696, 789, 870, 923 and 937. Eyes were obtained from a 72-year-old female (donor 1, family 1, II-4, FFB #923), a 97-year-old female (donor 2, family 2, II-1, FFB #937), and her 91-year-old sister (donor 3, family 2, II-2, FFB #870) (Fig. 1a and b). The asymptomatic carrier mother (donor 4, family 1, I-2, FFB #228) of donor 1 was also evaluated (Fig. 1a and b). Eyes were enucleated 6 h postmortem and fixed in 4 % paraformaldehyde (PF) and 0.5 % glutaraldehyde in phosphate buffer. The globes were stored in 2 % paraformaldehyde in PBS. Postmortem eyes from 61-, 65-, and 88-year-old donors without a history of retinal disease were used as controls.

*Genetic analysis* Approximately 10 ml of peripheral blood was collected from donor 1 (family member II-4) and family members II-5, II-6, II-7, II-8 from family 1. Blood was also collected from donor 2 (II-1) of family 2. DNA was extracted and purified from leukocytes by means of the Gentra Systems PUREGENE DNA Purification Kit (Qiagen). DNA for donors 3 (II-2, family 2) and 4 (I-2, family 1) was extracted from fixed or frozen retinal tissue samples using the Gentra Systems PUREGENE DNA Purification Kit (Qiagen).

In family 1, direct testing for mutations in 13 arRP genes (*VMD2*, *CNGA1*, *CNGB1*, *CRB1*, *EYS*, *LRAT*, *NR2E3*, *NRL*, *PDE6A*, *PDE6B*, *RHO*, *RPE65*, *USH2A*) was performed on patient II-5 by PCR amplification and DNA sequencing in two directions of all coding exons and exon/intron boundaries, including at least 50 nucleotides into the intron. Two novel heterozygous mutations were identified in *EYS* (GenBank RefSeq NM_001142800.1), c.2259+1G>A and c.2620C>T (p.Q874X). Segregation analysis was performed using sequence analysis in all available family members.

In family 2, DNA from patient II-1 (donor 2) was evaluated by Asper Ophthalmics using an APEX (arrayed primer extension)-based test. Seven hundred and ten mutations in 28 arRP genes (*CERKL*, *CNGA1*, *CNGB1*, *MERTK*, *PDE6A*, *PDE6B*, *PNR*, *RDH12*, *RGR*, *RLBP1*, *SAG*, *TULP1*, *CRB*, *RPE65*, *USH2A*, *USH3A*, *LRAT*, *PROML1*, *PBP3*, *EYS*, *ABCA4*, *AIPL1*, *CNGA3*, *CNGB3*, *GRK1*, *IMPG2*, *RHO*, and *RP1*) were evaluated. One heterozygous mutation in *EYS* was identified, a 7 base pair deletion notated as c.4350_4356del (p.I1451Pfs*3). In an attempt to identify the second pathogenic mutation, PCR products corresponding to the complete *EYS* coding sequence were amplified from genomic DNA and evaluated by sequence analysis. No mutation was identified. To further search for the second pathogenic variation, the DNA was analyzed using a comparative genomic hybridization array (Oxford Gene Technology; Eye gene array v2). Array data was analyzed by using CytoSure software. A heterozygous midsize genomic rearrangement, c.2739-?_3244+?del, was identified.

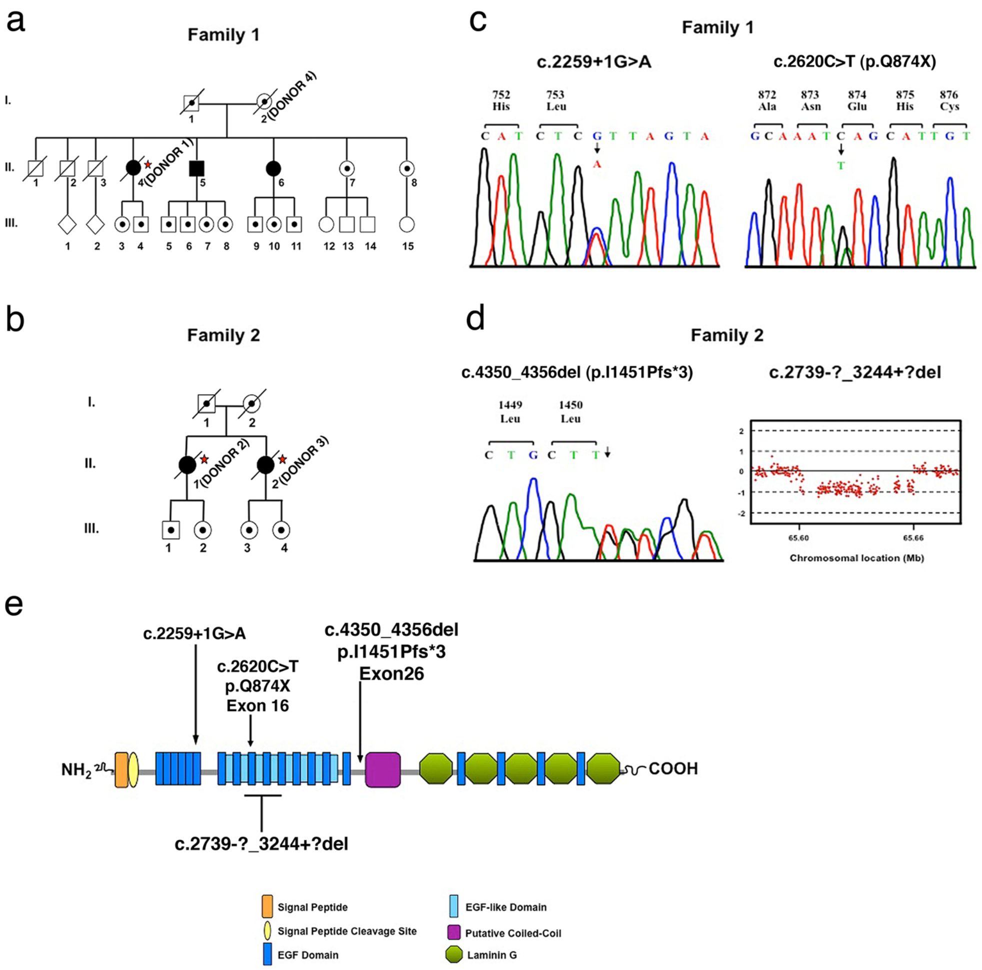

**Fig. 1** Mutational analysis of individuals with arRP due to *EYS* mutations **a** Pedigree of family 1. *Slashed symbols* reflect deceased family members. Affected family members are shown with *filled symbols*, unaffected family members are shown with *unfilled symbols*, and unaffected carrier family members are shown with *unfilled symbols with a black dot* inside. Postmortem analysis was done on affected member II-4, referred to as donor 1 (*), and in their unaffected mother (I-2), referred to as donor 4 (*). **b** Pedigree of family 2. Postmortem analysis was done on affected members II-1 and II-2, referred to as donors 2 (*) and 3 (*) respectively. **c** Sequence analysis of family 1 identified two heterozygous *EYS* mutations, c.2259+1G>A and p.Q874X. DNA analysis was performed on all three affected members (II-4, II-5 and II-6), their two unaffected living sisters (II-7 and II-8), and their mother (I-2). **d** Sequence analysis of family 2 identified a heterozygous 7 base pair deletion in *EYS*, p.I1451Pfs*3. Comparative genomic hybridization identified a heterozygous deletion of exons 15–18, c.2739-?_3244+?del. DNA analysis was performed in two affected family members, II-1 and II-2. **e** Predicted domain structure and distribution of the four *EYS* mutations identified in this study

To further search for the second pathogenic variation, the DNA was analyzed using a comparative genomic hybridization array (Oxford Gene Technology; Eye gene array v2). Array data was analyzed by using CytoSure software. A heterozygous midsize genomic rearrangement, c.2739-?_3244+?del, was identified. The four-exon deletion was confirmed by qPCR analysis using primers Hs06795327 and Hs06137405 (Life Technologies).

*Fundus imaging* Macroscopic fundus images were collected using a Zeiss AxioCam MRC5 camera equipped with a macro zoom lens (Zoom 700 Navitar TV Lens, Navitar, Inc, Rochester, NY, USA) and AxioVision AC Software (Carl Zeiss MicroImaging, Inc.). Prior to imaging, the anterior segment of each eye was removed using a custom-made eye globe holder and microtome blade (AccuEdge 4685, Sakura Finetek USA, Inc., Torrence, CA, USA). The remaining posterior segment was transferred to a custom-made plexiglass chamber, which permitted containment of both the sample and PBS immersion fluids required for imaging. Within the plexiglass chamber, the sample was placed with the posterior pole oriented downward and the opened anterior segment directed upward. The plexiglass chamber was then filled with PBS to the level of the anterior segment opening. In order to eliminate specular reflections from vitreous interface, several drops of PBS were dispensed into the open eye cup using a pipette. Angled illumination from a bifurcated fiber optic light source (Fostec EJA, Schott North America, Inc., Elmsford, NY, USA) was used to illuminate the sample for image acquisition.

*Scanning laser ophthalmoscope (SLO)* SLO images were collected using a model HRA2 confocal scanning laser ophthalmoscope (Heidelberg Engineering, Inc.) in the same manner as the macroscopic fundus images. The HRA2 was rotated 90° so that the scan direction was perpendicular to the table surface. The system was operated in high-resolution mode, which provides an image pixel format of 1536 × 1536 when used with a 55° wide-field objective lens. SLO images of the posterior pole were collected using infrared reflectance (SLO-IR), infrared dark field (SLO-IRDF), autofluorescence (SLO-AF), and red-free dark field (SLO-RFDF) imaging modes at field of view (FOV) settings of 55°, 35°, and 25°. Online algorithms within the HRA2 system software enabled automatic real-time averaging and tracking of sequentially collected images. This parameter was preset for averaging 25 image frames, which further enhanced signal-to-noise ratio and image contrast, especially for autofluorescence (SLO-AF) mode.

*Spectral domain optical coherence tomography (SD-OCT)* SD-OCT images were collected using an SD-OCT system (Model SDOIS, Bioptigen, Inc.) in a manner similar to the aforementioned macroscopic and SLO imaging modalities. A single telecentric objective lens was employed to collect 5× 5 mm and 10×10 mm FOV of the posterior pole. The SDOIS system has a center operating wavelength of ~840 nm, spectral bandwidth of 65 nm, and axial, in-depth resolution of ~6–7 μm (in air). A 1-mm ruby sphere was placed on the optic nerve head to provide a reference scale. SD-OCT imaging was performed using the following scan parameters: (1) 5-mm linear scan of the horizontal meridian through the optic nerve and fovea @ 1000 A-scans/B-scan, (2) 10-mm linear scan of the horizontal meridian through the optic nerve and fovea @ 1000 A-scans/B-scan, (3) 5-mm$^2$ volume scan of the posterior pole @ 500 B-scans/volume × 250 A-scans/B-scan, and (4) 10-mm$^2$ volume scan of the posterior pole @ 500 B-scans/volume×250 A-scans/B-scan. Post-acquisition images were averaged with a line and frame filter settings of 3 and 3 respectively via the Bioptigen InVivoVue SDOIS Software version 1.7.

*Semi-thin epon sections and morphological analysis* A small area of the retina/RPE/choroid complex from both the perifoveal and peripheral regions of the arRP donors, asymptomatic mother, and controls were fixed in 2.5 % glutaraldehyde in 0.1 M cacodylate buffer, sequentially dehydrated in ethanol, and embedded in Epon. Plastic sections (1 μm) of all samples were stained with toluidine blue and photographed by light microscopy with a Zeiss Imager Z.1 microcroscope equipped with a Zeiss AxioCam MRC5 camera.

*Immunohistochemistry* Small areas from the perifovea and peripheral eye wall were cut and infused with 10 and 20 % sucrose in PBS, and embedded in Tissue-Tek “4583” (Miles Inc., Elkhart, IN, USA). 10 μm cryosections were cut on a HM 505E cryostat (Microm, Walldorf, Germany) equipped with a CryoJane Tape-Transfer system (Instrumedics, Inc., Hackensack, NJ, USA). Prior to labeling, embedding medium was removed through two consecutive PBS incubations for 20 min. The tissue was then processed for immunofluorescence labeling. Sections were blocked in PBS supplemented with 1 % BSA for 30 min and incubated with monoclonal antibodies 1D4 to rhodopsin (ab5417, 1:1000, from Abcam), 7G6 to cone arrestin (1:100, from Dr. P. MacLeish, Morehouse School of Medicine, Atlanta, GA, USA), and polyclonal antibodies to red/green cone opsin (AB5405, 1:1200, Chemicon) in PBS/BSA overnight at 4 °C. Cell nuclei were labeled with TO-PRO®-3 iodide (blue, 1 mg/ml, Molecular Probes, Eugene, OR, USA). Sections were then labeled with secondary antibodies goat anti-mouse IgG Alexa Fluor 488 (1:1000; Molecular Probes), goat anti-rabbit IgG Alexa Fluor 594 (1:1000; Molecular Probes), and goat anti-rabbit IgG Alexa Fluor 488 (1:1000; Molecular Probes) for 1 h at room temperature. Sections were analyzed using a Leica laser scanning confocal microscope (TCS-SP2, Leica, Exton, PA, USA). A series of 1 μm *xy* (en face) sections were collected. Each individual *xy* image of the retinas stained represents a three-dimensional projection of the entire cryosection (sum of all images in the stack). Microscopic panels were composed using AdobePhotoshop CS3 (Adobe, San Jose, CA, USA). Two different commercially available EYS antibodies were tested but failed to react with our tissue, probably due to the presence of glutaraldehyde in the fixative buffer.

## Results

### Clinical findings

Two unrelated families were evaluated. Family 1 reported Irish and French ancestry, whereas family 2 is Scandinavian. Donor 1 (family 1, II-4) was most recently examined at age 70, 2 years before her death (Fig. 1a, star). At that time, her visual acuity was hand motion OD and 20/400 OS. Dilated fundus examination of both eyes showed a pale optic nerve head, attenuated vessels, and bone spicule pigment in the periphery with pavingstone degeneration inferiorly. She also had some mottled RPE pigmentation in her left eye. No other clinical or imaging information was available. Donor 2 (family 2, II-1) was last examined at age 96, 1 year before her death (Fig. 1b). At that time, her visual acuity was 20/400 OU. Dilated fundus exam showed optic disc atrophy, choroidal atrophy, vascular attenuation, and chorioretinal degeneration. Donor 3 (family 2, II-2) was last examined at age 88, 3 years prior to her death (Fig. 1b). She had light perception vision in both eyes. Her previous fundus examinations showed the typical triad of characteristics indicative of RP — optic nerve head pallor, attenuated retinal vessels, and bone spicule pigmentation in the periphery. Clinical records were not available for donor 4 (family 1, I-2) (Fig. 1a).

### Molecular genetic analysis

In family 1, genetic analysis was performed on the affected donor 1 (II-4), her unaffected mother (donor 4, I-2), two affected siblings (II-5 and II-6), and two unaffected siblings (II-7 and II-8) (Fig. 1a). DNA sequence analysis in comparison to GenBank entry NM_001142800 revealed two novel heterozygous mutations in *EYS*, c.2259+1G>A and c.2620C>T (p.Q874X), in patient II-5 (Fig. 1c). Segregation analysis revealed that both affected sisters, II-4 (donor 1) and II-6, carried both mutations; while the two unaffected sisters were both heterozygous for the c.2259+1G>A mutation.

In family 2, genetic analysis was performed on affected donor 2 (II-1) (Fig. 1b). DNA analysis revealed a heterozygous 7 bp deletion in *EYS*, c.4350_4356del (p.I1451Pfs*3), and comparative genomic hybridization revealed an additional deletion of exons 15–18, c.2739-?_3244+?del (Fig. 1d). Targeted sequence analysis in patient II-2 (donor 3) revealed that she was also heterozygous for p.I1451Pfs*3 (Fig. 1b). Insufficient DNA from donor 3 prevented the performance of midsize deletion analysis. The locations of these identified mutations relative to the predicted EYS protein domain structure are shown in Fig. 1e.

### Ex-vivo imaging of donor eyes

The combination of fundus, confocal scanning laser ophthalmoscopy (SLO) and spectral-domain optical coherence tomography (SD-OCT) imaging systems can provide comprehensive characterization of retinal lesions prior to histopathology [34]. Therefore, these imaging techniques were performed on all arRP and control eye donors, and qualitatively compared (Figs. 2 and 3). Anatomical landmarks, such as the optic nerve and fovea, were clearly identified in each donor eye using all three imaging modalities.

Visible light fundus imaging showed inherent differences between the control and arRP eyes, which included the presence or absence of peripheral bone spicule pigment and inherent differences in the overall color hue of the fundus. Bone spicule pigment density was more pronounced in donor 3 (Fig. 2d) than in donors 1 and 2 (Fig. 2b and c). The fundi of arRP donor eyes had hues that were similar in appearance, but were more “whitish” in color (Fig. 2b to d) than the control eye (Fig. 2a). Optic disc pallor, attenuated retinal vessels, and profound atrophy of the RPE and choriocapillaris were only observed in arRP eyes.

Examination by SLO revealed areas of detached retina in the control eye (Fig. 2e and i, asterisks) and in the majority (2/3) of arRP eyes (Fig. 2f, h, j and l, asterisks); the retinal detachments were attributed to post-mortem enucleation and removal of anterior segments in preparation for imaging. In arRP eyes, both SLO infrared (SLO-IR) and autofluorescence (SLO-AF) showed bone spicule pigment in agreement with fundus macroscopic imaging. SLO-IR imaging revealed loss of RPE in the posterior pole including the macula, perimacula, and areas surrounding the optic nerve in the eyes of donors 2 and 3 (Fig. 2g and h) as compared to control (Fig. 2e). SLO-AF imaging identified hypofluorescence in one contiguous region involving the macula and area surrounding the optic disk of donor 3 (Fig. 2l), as opposed to the focal loss of RPE in demarcated regions in eyes from donors 1 and 2 (Fig. 2j and k), and an absence of both abnormal findings in the control retina (Fig. 2i). These data suggest that different *EYS* mutations in arRP donors lead to retinal changes that can be observed using multiple imaging modalities.

SD-OCT imaging was performed on each of the arRP and control eyes (Fig. 3). In-depth B-scans from the control eye (Fig. 3a and e) revealed a normal-appearing retina with clearly defined fovea, some evidence of laminar architecture, and no appreciable evidence of retinal thinning and/or degeneration. Images from arRP donors revealed retinas of appreciable thickness but with less organized architecture and integrity in the macular region (Fig. 3b-d and f-h, bracket). In contrast, the peripheral regions showed a retina that was thinner than control eyes, suggesting loss of cells and axons (data not shown). Eyes from donors 2 and 3 had macular detachments between the optic nerve and fovea (Fig. 3g and h, asterisk) that were not previously identified by either fundus macroscopic imaging or SLO techniques. Donor 2’s eye also showed what appeared to be a choroidal detachment adjacent to the optic nerve and below the region of retinal detachment (Fig. 3g, arrow). These data suggest that arRP *EYS* mutations lead to the atrophy of the retinas, in addition to causing substantial disorganization of the cellular layers in the macular and perifoveal regions.

### Histopathology of donor retinas

To evaluate the effect of *EYS* mutations on retinal structure, toluidine blue-stained plastic sections of arRP and control donor eyes were examined. A schematic drawing depicts the regions harvested and processed for observation in both the morphological and immunohistological assays (Fig. 4a). These include: the periphery (Fig. 4a, region 1) and perifovea (Fig. 4a, region 2). Histology of control retinas in the periphery (Fig. 4b) and perifovea (Fig. 4f) showed normal lamination patterns. In all three arRP donors, a highly degenerated retina with disorganization of the retinal laminae and gliosis was evident in all peripheral areas analyzed (Fig. 4c–e). Moreover, photoreceptor outer segments were also absent in all areas analyzed. Intraretinal bone spicule pigment was

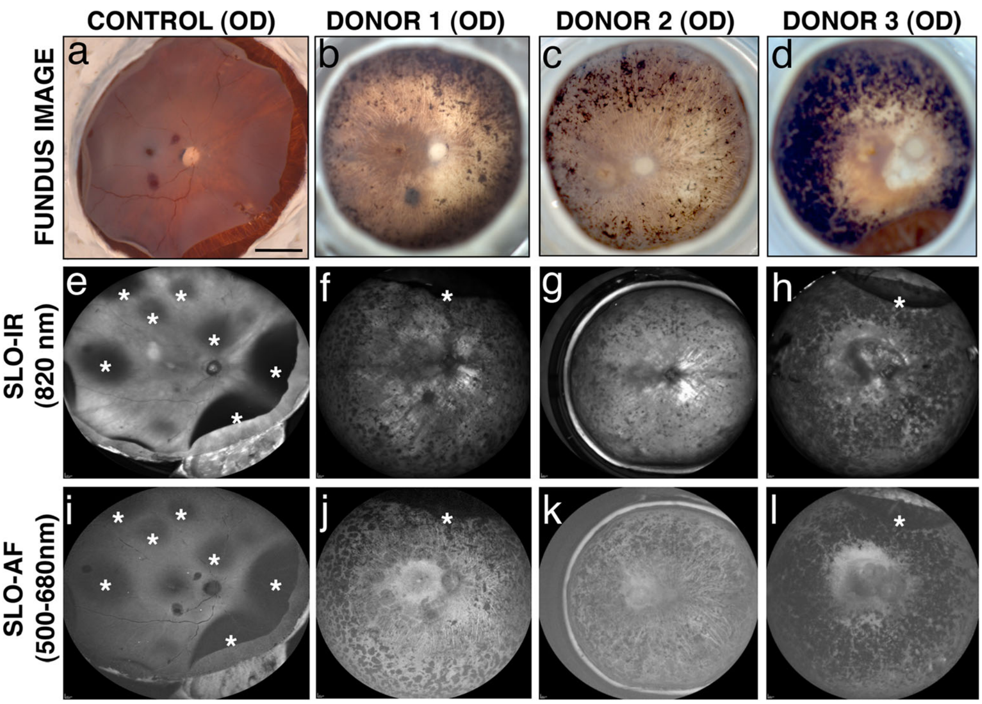

**Fig. 2** Ex-vivo imaging of arRP donor eyes with *EYS* mutations. Fundus images (**a-d**) and SLO images (**e-l**) were collected from donors 1, 2, and 3 and an age-similar control. In the control eye, detached retinas are apparent with all imaging modalities (**a**, **e**, **i**, *). In all three arRP eyes, fundus images reveal bone spicule pigment in mid-peripheral and peripheral areas to varying degrees (**b**–**d**). SLO-IR imaging identified degeneration in the entire posterior pole region including the macula, perimacula, and areas surrounding the optic nerve, due to focal loss of RPE in donors 2 (**g**) and 3 (**h**) as compared to an age-similar control eye (**e**). SLO-AF imaging identified hypofluorescence in one contiguous region involving the macula and area surrounding the optic disk of donor 3 (**l**), as opposed to the individually demarcated and isolated regions seen with both donors 1 (**j**) and 2 (**k**) and the control eye (**i**). *Scale bars* in fundus image=0.5 cm

visible in the retinas of donors 2 (Fig. 4d, arrow) and 3 (Fig. 4e, arrow). The perifovea displayed a prominent inner nuclear layer. Eyes from donors 2 (Fig. 4h) and 3 (Fig. 4i) displayed localized areas of RPE atrophy in the perifovea, whereas the RPE was uniformly thin in the perifovea of donor 1 (Fig. 4g). Patchy, disorganized cones were observed subjacent to the RPE in the perifovea of donors 2 (Fig. 4h, arrowheads) and 3 (Fig. 4i, arrowheads). These data suggest that the

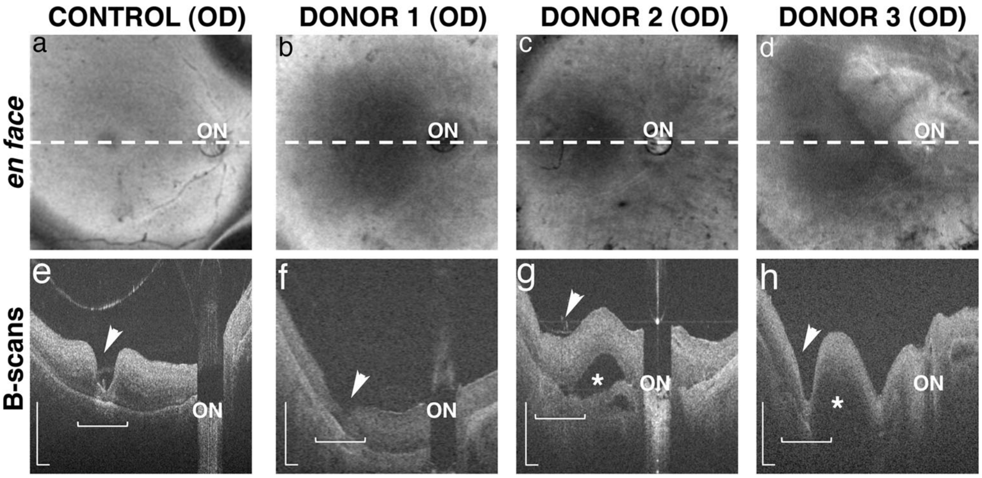

**Fig. 3** Ex-vivo OCT imaging of arRP donor eyes with *EYS* mutations. OCT images were collected from donors 1, 2, and 3 and an age-similar control. En-face images reveal the location (*dashed lines*) of the in-depth, B-scan images of control (**a**) and arRP donors 1 (**b**), 2 (**c**) and 3 (**d**). The fovea (*arrowhead*) and optic nerve (*ON*) were identified in all donor eyes. In-depth B-scans from the control eye (**e**) revealed a normal appearing retina with clearly defined fovea, some evidence of laminar architecture, and no appreciable evidence of retinal thinning or degeneration. Images from the arRP donors (**f**–**h**) revealed retinas of appreciable thickness but with less organized architecture and integrity in the macular region (*horizontal bracket*). In contrast, the perimacular regions showed some evidence of thinned retina relative to the control retina, suggesting degeneration. Donors 2 (**g**) and 3 (**h**) had macular (*) and choroidal (*arrow*) detachments, as indicated in the B-scans. B-scan scale is 0.5 mm

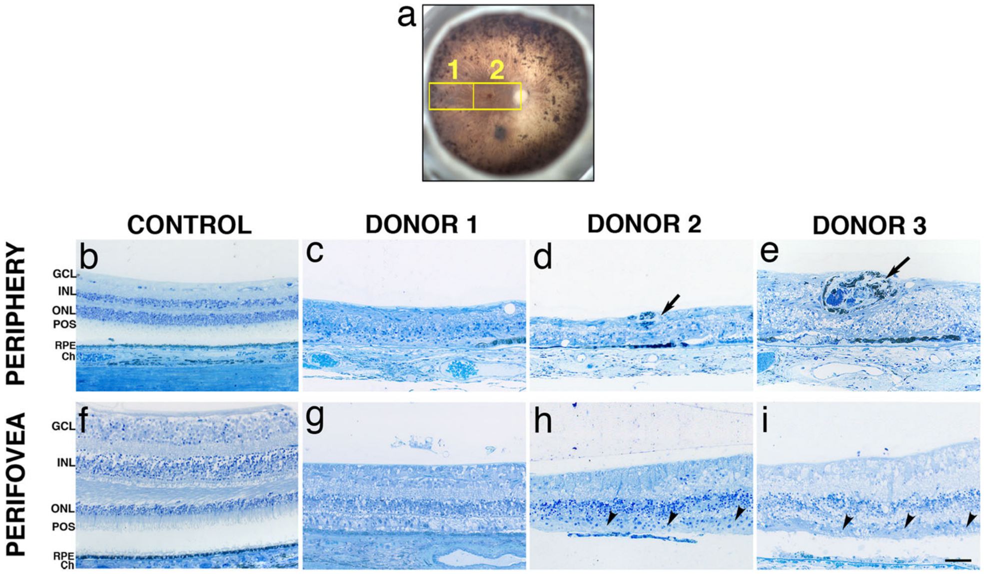

**Fig. 4** Histology of arRP donor eyes with *EYS* mutations. A fundus image of the studied eye (*OS*) with a schematic drawing of the regions cut and processed for cryosectioning and immunolabeling is shown (**a**). Toluidine blue-stained plastic sections (1 μm) of retinas from donors 1, 2, and 3 and an age-similar control. Morphology of the control retina in the periphery (**b**) and perifoveal (**f**) regions displayed typical retinal lamina. Histology of the periphery of all three donors revealed a highly degenerated retina with disorganization of the lamina and cellular layers and gliosis in all areas analyzed (**c**–**e**). Photoreceptor outer segments were also absent in all areas analyzed. Intraretinal bone spicule pigments were visible in the retinas of donors 2 (**d**, *arrow*) and 3 (**e**, *arrow*). In contrast, the perifovea of all arRP donors displayed a prominent inner nuclear layer. Donors 2 (**h**) and 3 (**i**) displayed localized areas of RPE atrophy, whereas the RPE was thin in the perifovea of donor 1 (**g**) as compared to the control donor (**f**). Patchy, disorganized cone remnants were observed on top of the RPE in the perifovea of donors 2 (**h**, *arrowhead*) and 3 (**i**, *arrowhead*). *GCL*=ganglion cell layer; *INL*=inner nuclear layer; *ONL*=outer nuclear layer; *POS*=photoreceptor outer segments; *RPE*=retinal pigment epithelium; *Ch*=Choroid. *Scale bar*=50 μm

*EYS* mutations cause profound changes in the retina, leading to the loss of several retinal cell layers and the appearance of gliosis.

## Immunohistochemistry of donor retinas

Human EYS protein is localized to the photoreceptor outer segments, and is believed to play a role in the modeling of retinal architecture [8]. In order to investigate if mutations in *EYS* affect the retinal architecture, immunofluorescent studies with antibodies to photoreceptor outer segment proteins were performed. Immunostaining of control retinas with rhodopsin antibodies revealed that rhodopsin distribution was restricted to the rod outer segments in the retinal periphery (Fig. 5a) and perifovea (Fig. 5e). Rhodopsin-labeled cells were rarely encountered in the retinal periphery of donor 1 (Fig. 5b) while some were still present in the periphery of donors 2 (Fig. 5c) and 3 (Fig. 5d). Rhodopsin-positive cells were also observed along the outer retina directly abutting the choroid in some areas where the RPE was absent (Fig. 5c and d, arrows). In addition, rhodopsin was not restricted to the outer segments in all the arRP donor retinas and rhodopsin-positive cells had lost their slim, rod-shaped morphology. In the perifovea of donors 1 (Fig. 5f) and 2 (Fig. 5g), no rhodopsin-labeled cells were found, while donor 3 (Fig. 5h) displayed several disorganized rhodopsin-labeled cells. Although the retinas had reached an advanced stage of degeneration, our data suggest that the *EYS* mutations identified in arRP donors have an effect on the subcellular localization of rhodopsin and the distribution of rhodopsin-positive cells retinas.

Next, we investigated the distribution of cone photoreceptors in retinas harboring *EYS* mutations. Immunostaining of control retinas with cone arrestin antibodies revealed that the protein was distributed along the entire conical-shaped plasma membrane, from the tip of the outer segment to the synaptic base, both in the retinal periphery (Fig. 6a, green) and in the perifovea (Fig. 6e, green). Immunostaining of control retinas with antibodies against red–green cone opsin revealed that this protein is restricted to cone outer segments, both in the periphery (Fig. 6a, red) and perifovea (Fig. 6e, red). Strikingly, cones were mostly absent from the periphery of all the arRP donor retinas (Fig. 6b-d). However, in the perifovea of all arRP donors, cone arrestin staining displayed the typical conical-shaped cellular distribution, with lack of synaptic terminals and outer segments (Fig. 6e-h). These cone arrestin-positive cells were also characterized by the redistribution of red-green opsin to the inner segments and cell bodies. In the perifovea of donor 1, red–green opsin labeling was significantly decreased and the cone arrestin distribution was mostly confined to a row of shortened cells (Fig. 6f). Interestingly, the perifovea from both donors 2 (Fig. 6g) and 3

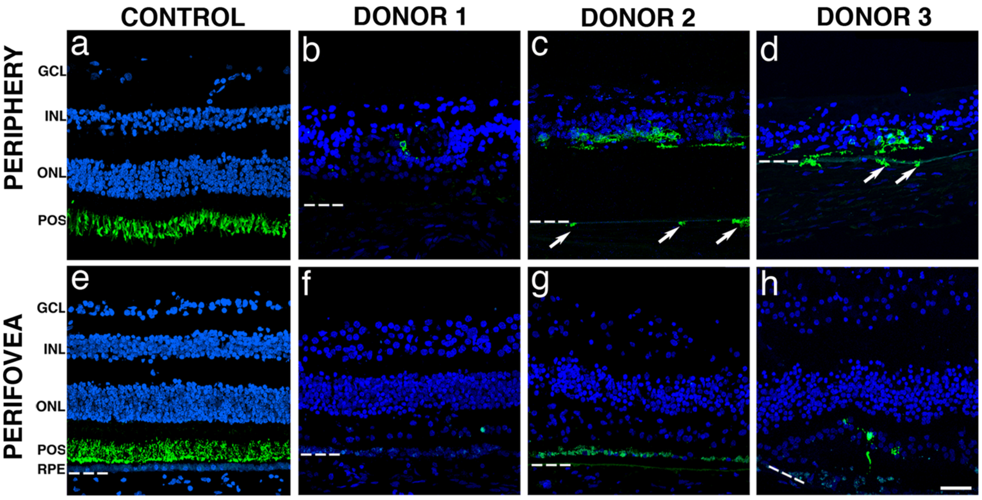

**Fig. 5** Immunocytochemistry of arRP retinal sections with *EYS* mutations stained with rhodopsin antibodies. Immunofluorescence of arRP retinal sections labeled with antibodies to rhodopsin (*green*) showed significantly decreased staining when compared to control. The control retina showed that rhodopsin was restricted to the rod outer segments in both the periphery (**a**) and perifovea (**e**). Rhodopsin-labeled cells were essentially absent from the periphery of donor 1 (**e**). However, rhodopsin-labeled cells were still present in the periphery of donors 2 (**c**) and 3 (**d**). Of interest, some rhodopsin-labeled cells were observed in the choroid of these eyes (*arrows*). In the perifovea, donors 1 (**f**) and 2 (**g**) displayed no rods, while donor 3 (**h**) displayed a few disorganized rods. Bruch's membrane is indicated by *hashed white line*. Nuclei were labeled with TO-PRO-3. *GCL*=ganglion cell layer; *INL*=inner nuclear layer; *ONL*=outer nuclear layer; *POS*=photoreceptor outer segments; *RPE*= retinal pigment epithelium. *Scale bar*=40 µm

(Fig. 6h) displayed cone arrestin-labeled cells concentrated in areas that still had some RPE cells. These cones displayed a distribution of red–green opsin through the entire cell body. These data suggest that *EYS* mutations cause a profound loss of peripheral cones, and can affect the subcellular localization of cone opsin- and cone arrestin-positive cells in the few perifoveal cones that survive.

## Histology and immunocytochemistry of the unaffected eye from the mother of donor 1

The retinal periphery of the unaffected mother of donor 1 (donor 4) revealed typical retinal lamination similar to an age-similar control; however, a significant decrease in the number of nuclei of the inner and outer nuclear layers was

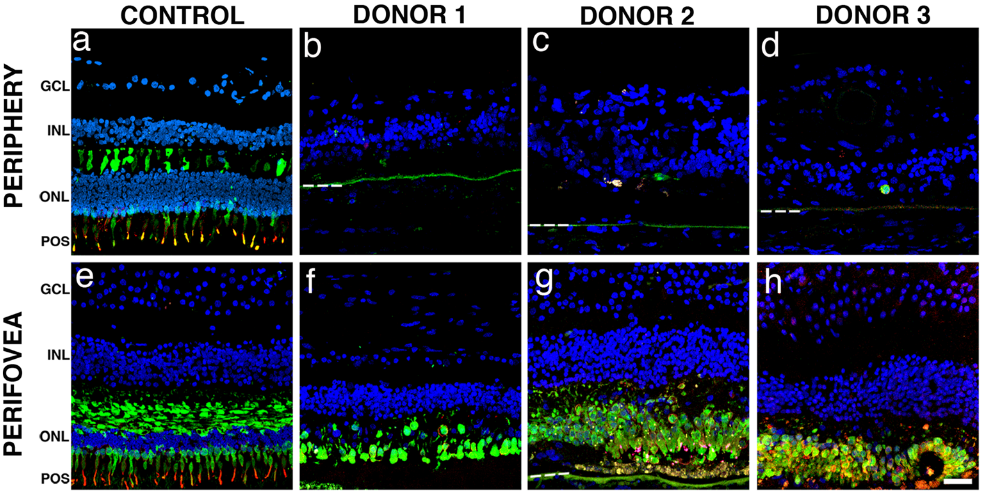

**Fig. 6** Immunocytochemistry of arRP retinal sections with *EYS* mutations stained with cone-specific antibodies. Immunofluorescence of arRP retinal sections labeled with antibodies to cone arrestin (*green*) and red/green cone opsin (*red*) showed significantly decreased staining in the periphery when compared to control. In the peripheral (**a**) and perifoveal (**e**) regions of the control retina, cone arrestin was distributed along the entire plasma membrane, from the tip of the outer segment to the synaptic base, while the red/green cone opsin was restricted to the outer segments. Cone-specific labeled cells were mostly absent from the periphery of all three arRP donor retinas (**b**–**d**). In contrast, cone-specific labeled cells were present but highly disorganized in the perifovea of donor 1 (**f**). Interestingly, the perifovea from both donor 2 (**g**) and 3 (**h**) displayed disorganized cone-specific labeled cells concentrated in the areas that still maintained RPE. Bruch's membrane is indicated by *hashed white line*. Nuclei were labeled with TO-PRO-3. *GCL*=ganglion cell layer; *INL*= inner nuclear layer; *ONL*=outer nuclear layer; *POS*=photoreceptor outer segments. *Scale bar*=40 µm

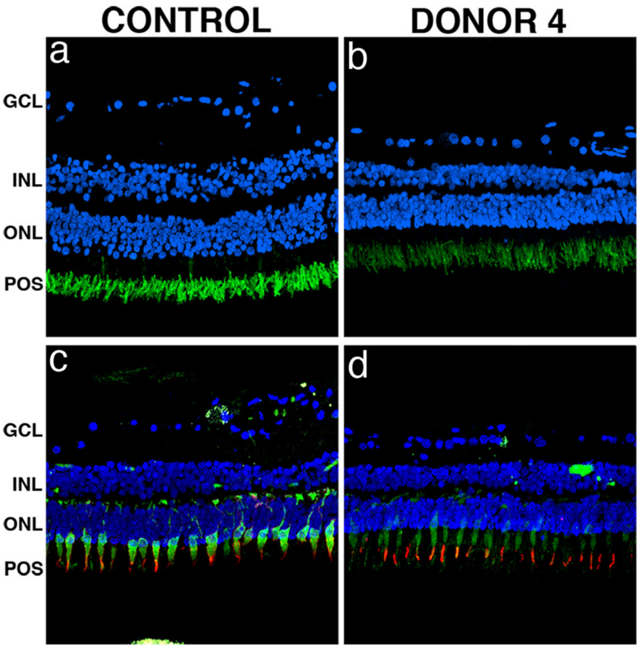

**Fig. 7** Immunocytochemistry of retinal sections of an unaffected carrier with a heterozygous *EYS* mutation. Immunofluorescence of peripheral retina sections of the unaffected mother of donor 1 (donor 4) labeled with antibodies to rhodopsin, cone arrestin, and red/green cone opsin showed no significant changes in staining of these proteins as compared to control. The unaffected carrier donor retina displayed both rhodopsin (**b**, *green*) and red/green cone opsin (**d**, *red*) restricted to the photoreceptor outer segments as observed in control retinas (**a**, **c**). Cone arrestin labeling in the unaffected carrier donor retina (**d**, *green*) displayed similar distribution when compared to the control retina (**c**). Nuclei were labeled with TO-PRO-3. *GCL*=ganglion cell layer; *INL*=inner nuclear layer; *ONL*=outer nuclear layer; *POS*=photoreceptor outer segments. *Scale bar*=40 μm

noted (Fig.7b and d). In addition, donor 4 displayed both rhodopsin (Fig. 7b, green) and red–green cone opsin (Fig. 7d, red) distribution restricted to the photoreceptor outer segments, as observed in the control retinas (Fig. 7a and c). Cone arrestin was also distributed throughout the entire cell in donor 4 (Fig. 7d, green), similarly to the control retinas (Fig. 7c). These data suggest that the unaffected mother of the arRP donor 1, carrying an obligatory heterozygous *EYS* mutation, does not display any significant changes in retinal structure, and is similar to age-similar normal controls.

## Discussion

The examination of postmortem eye tissues obtained from individuals in whom the disease-causing gene has been identified offers a unique opportunity to study the relationship between genotype and disease pathogenesis and the effects of the genetic defect on retinal structures. There continues to be a relative lack of the combination of genetic information with clinical and histopathological data from the same individual. We present for the first time the ocular histopathological changes in two arRP families with different, novel mutations in the *EYS* gene. We compare the relationship between genotype and disease phenotype in these eyes.

The gene responsible for arRP at the RP25 locus was identified several years ago as *EYS* (an ortholog of Drosophila eyes shut, eys), and encodes an ortholog of the *Drosophila* protein SPAM [7], a multi-domain protein containing 3,165 amino acids and comprised of several protein motifs commonly found in extracellular molecules (Fig. 1e). EYS consists of 21 epidermal growth factor (EGF)-like domains in its N-terminal region, followed by five C-terminal laminin G domains that are interspersed with additional EGF repeats. The protein is also predicted to contain a signal peptide for secretion into the extracellular environment. Drosophila spam is expressed in the eye of several insect species with an open rhabdom system, wherein the rhabdomeres or photoreceptor cells of each ommatidium in the compound eye are separated from each other, allowing each photoreceptor to act as an independent unit. Loss of *EYS* switches an open rhabdom system to a more primitive closed one found in insects such as ants and bees [7]. Considering the evolutionary data and the known function of the Drosophila ortholog, human EYS is likely to have a role in the integrity of photoreceptor architecture. Indeed, immunohistochemical studies confirmed the localization of this protein to the photoreceptor outer segments [7]. Interestingly, despite the reported mutations and the presumed loss of function leading to arRP, *EYS* is not present in rodent eyes, making this gene the fourth Mendelian disease–associated human gene whose orthologs are disrupted or absent from rodent genomes [7].

*EYS* is a major arRP disease-causing gene. Mutations have been identified in families of different ancestral origin, and are estimated to account for 5–16 % of arRP cases [6]. The types of mutations identified in patients include missense, nonsense, microdeletions and insertions, 5'UTR variations, and copy-number variations such as midsize genomic rearrangements. In the present study, we performed a comprehensive comparison of four eye donors (three affected and one carrier) from two unrelated families with *EYS* mutations, including clinical, genetic, and morphologic analyses. The heterozygous *EYS* mutations c.2259+1G>A and c.2620C>T were identified in family 1, whereas the heterozygous mutations p.I1451Pfs*3 and c.2739-?_3244+?del were identified in family 2. The two mutations in family 1 are novel, and have not been reported in previous studies in patients of different ethnicities [6, 35–43]. On the other hand, the deletions identified in family 2 have been previously reported [6, 35, 36, 41, 42]. All four mutations described in the present report are considered pathogenic. Two of them (c.2259+1G>A and p.Q874X) are located within EGF domains, and are predicted to have a truncating effect on the protein. p.I1451Pfs*3 is predicted to lead to a premature stop codon three amino acids downstream, and probably truncates the last half of the protein, including the coiled coil domain and all laminin G domains. c.2739-?_3244+?del is predicted to lead to a loss of four exons, which deletes a portion of the EGF domains. In family 1, it is likely that the altered mRNA transcripts would be degraded through nonsense-mediated decay. In family 2, it is possible that the mRNA from the midsize four-exon deletion is used for protein translation, and leads to an abnormal yet partially functional protein product.

Clinically, patients carrying pathogenic *EYS* mutations have night blindness as the initial symptom, as well as retinal bone spicule pigmentation and attenuated retinal vessels, followed by progressive visual field constriction. On average, visual acuity begins to decrease at around 30 years of age, and continues to deteriorate over the next few decades [6, 36, 43]. The phenotype in patients with RP due to EYS mutations has been described previously, and is relatively homogeneous [6, 38, 44, 45]. Generally, they exhibit markedly reduced scotopic and photopic responses on ERG, have retinal thinning with macular involvement on OCT, and have a fundus appearance typical for RP. Overall, patients with EYS mutations have a more severe clinical course than some of the other RP genotypes. Central vision is relatively preserved until late in the disease course.

In the present study of eyes from older individuals with *EYS* mutations, both imaging and histological examinations revealed highly degenerated retinas, with little evidence of stratified nuclear layers in the periphery. In contrast, the perifoveal region maintained a prominent inner nuclear layer. Donors 2 (age 97) and 3 (age 91) from family 2 had a few areas of preserved RPE in both the periphery and perifovea, whereas the RPE was thin in the perifovea and absent in the periphery of donor 1 (age 72). Rods were mostly absent in all arRP donors, except in the periphery, where the cells appeared morphologically abnormal. Cones were also mostly absent from the periphery of all arRP donors; however, patches of cones were observed in the perifovea of donors 2 and 3. This preservation of cones in the perifovea is probably responsible for the central vision that some patients maintain until late in the course of the disease.

It is important to note that the donor ages differed by 20–25 years, suggesting that different stages of the disease may be represented in the tissues studied. Interestingly, the disease pathology of the older aged donors from family 2 appeared to be less severe. We speculate that the retinas from donors 2 and 3 would have had better morphology than the retina from donor 1 if they would have been evaluated at a similar age. It is possible that the two different types of mutations represented in these donors may show specific differences in the rate of retinal degeneration, but this is beyond what can be inferred by the end-stage pathology of limited specimens.

The data presented here provides new insights into the pathology and disease manifestation caused by *EYS* mutations. Previous studies have shown that *EYS* mutations lead to severe defects in inter-rhabdomeral space formation in *Drosophila* eyes [8]. As a result, it has been hypothesized that the human EYS protein may be essential for the formation and integrity of the photoreceptor outer segment and overall retinal architecture. We show that combinations of four different *EYS* mutations lead to advanced retinal degeneration, with near-total loss of rods. The preservation of macular cones in arRP donor retinas with a midsize exonic deletion may indicate an ability for individuals with this type of mutation to maintain some central vision for a longer duration than individuals with truncating mutations and despite severe visual dysfunction, suggesting an opportunity for cell rescue if therapy becomes available. This observation is significant due to the estimation that midsize genomic rearrangements in *EYS* are responsible for the disease in ~4 % of arRP cases in the absence of other mutations, and constitute the second pathogenic variation in ~15 % of cases where a second mutation is detected by sequence analysis [41]. Further experimental research will be required to corroborate this possible association. The present study demonstrates that the identification of disease-causing mutations, combined with the histopathological analyses of donor eyes, provides a more comprehensive platform for the study of the natural history of retinal dystrophies, and possible predictions of the clinical course of the disease. These observations undoubtedly help genetic counseling as well as future targeted therapies.

**Acknowledgments** The authors thank Dr. Peter MacLeish (Morehouse School of Medicine, Atlanta, GA, USA) for providing us with the antibody to cone arrestin (7G6), and Xiaoping Yang for expert technical assistance. Supported by The Foundation Fighting Blindness Histopathology Grant F-OH01-1102-0231 (JGH), Research Center Grants from The Foundation Fighting Blindness (JGH), Research to Prevent Blindness Unrestricted Grant, The Llura and Gordon Gund Foundation, and National Institutes of Health grant R01EY014240-08 (JGH).

## References

1. Boughman JA, Conneally PM, Nance WE (1980) Population genetic studies of retinitis pigmentosa. Am J Hum Genet 32:223–235
2. Bunker CH, Berson EL, Bromley WC, Hayes RP, Roderick TH (1984) Prevalence of retinitis pigmentosa in Maine. Am J Ophthalmol 97:357–365
3. Dryja TP, McGee TL, Hahn LB, Cowley GS, Olsson JE, Reichel E, Sandberg MA, Berson EL (1990) Mutations within the rhodopsin gene in patients with autosomal dominant retinitis pigmentosa. N Engl J Med 323:1302–1307
4. Tsang SH, Wolpert K (2010) The genetics of retinitis pigmentosa. Retinal Physician, November
5. Collin RW, Littink KW, Klevering BJ, van den Born LI, Koenekoop RK, Zonneveld MN, Blokland EA, Strom TM, Hoyng CB, den Hollander AI, Cremers FP (2008) Identification of a 2 Mb human ortholog of Drosophila eyes shut/spacemaker that is mutated in patients with retinitis pigmentosa. Am J Hum Genet 83:594–603
6. Littink KW, van den Born LI, Koenekoop RK, Collin RW, Zonneveld MN, Blokland EA, Khan H, Theelen T, Hoyng CB, Cremers FP, den Hollander AI, Klevering BJ (2010) Mutations in the EYS gene account for approximately 5% of autosomal recessive

retinitis pigmentosa and cause a fairly homogeneous phenotype. Ophthalmology 117:2026–2033, 2033 e2021-2027

7. Abd El-Aziz MM, Barragan I, O'Driscoll CA, Goodstadt L, Prigmore E, Borrego S, Mena M, Pieras JI, El-Ashry MF, Safieh LA, Shah A, Cheetham ME, Carter NP, Chakarova C, Ponting CP, Bhattacharya SS, Antinolo G (2008) EYS, encoding an ortholog of Drosophila spacemaker, is mutated in autosomal recessive retinitis pigmentosa. Nat Genet 40:1285–1287
8. Zelhof AC, Hardy RW, Becker A, Zuker CS (2006) Transforming the architecture of compound eyes. Nature 443:696–699
9. Mizuno K, Nishida S (1967) Electron microscopic studies of human retinitis pigmentosa. I. Two cases of advanced retinitis pigmentosa. Am J Ophthalmol 63:791–803
10. Kolb H, Gouras P (1974) Electron microscopic observations of human retinitis pigmentosa, dominantly inherited. Invest Ophthalmol Vis Sci 13:487–498
11. Szamier RB, Berson EL (1977) Retinal ultrastructure in advanced retinitis pigmentosa. Invest Ophthalmol Vis Sci 16:947–962
12. Rayborn ME, Moorhead LC, Hollyfield JG (1982) A dominantly inherited chorioretinal degeneration resembling sectoral retinitis pigmentosa. Ophthalmology 89:1441–1454
13. Szamier RB, Berson EL (1982) Histopathologic study of an unusual form of retinitis pigmentosa. Invest Ophthalmol Vis Sci 22:559–570
14. Szamier RB, Berson EL (1985) Retinal histopathology of a carrier of X-chromosome-linked retinitis pigmentosa. Ophthalmology 92:271–278
15. Szamier RB, Berson EL, Klein R, Meyers S (1979) Sex-linked retinitis pigmentosa: ultrastructure of photoreceptors and pigment epithelium. Invest Ophthalmol Vis Sci 18:145–160
16. Farber DB, Flannery JG, Bird AC, Shuster T, Bok D (1987) Histopathological and biochemical studies on donor eyes affected with retinitis pigmentosa. Prog Clin Biol Res 247:53–67
17. Tucker GS, Jacobson SG (1988) Morphological findings in retinitis pigmentosa with early diffuse rod dysfunction. Retina 8:30–41
18. Santos A, Humayun MS, de Juan E Jr et al (1997) Preservation of the inner retina in retinitis pigmentosa. A morphometric analysis. Arch Ophthalmol 115:511–515
19. Li ZY, Kljavin IJ, Milam AH (1995) Rod photoreceptor neurite sprouting in retinitis pigmentosa. J Neurosci 15:5429–5438
20. Li ZY, Possin DE, Milam AH (1995) Histopathology of bone spicule pigmentation in retinitis pigmentosa. Ophthalmology 102:805–816
21. Fariss RN, Apte SS, Luthert PJ, Bird AC, Milam AH (1998) Accumulation of tissue inhibitor of metalloproteinases-3 in human eyes with Sorsby's fundus dystrophy or retinitis pigmentosa. Br J Ophthalmol 82:1329–1334
22. Milam AH, Li ZY, Fariss RN (1998) Histopathology of the human retina in retinitis pigmentosa. Prog Retin Eye Res 17:175–205
23. Tulvatana W, Adamian M, Berson EL, Dryja TP (1999) Photoreceptor rosettes in autosomal dominant retinitis pigmentosa with reduced penetrance. Arch Ophthalmol 117:399–402
24. Fariss RN, Li ZY, Milam AH (2000) Abnormalities in rod photoreceptors, amacrine cells, and horizontal cells in human retinas with retinitis pigmentosa. Am J Ophthalmol 129:215–223
25. Li ZY, Jacobson SG, Milam AH (1994) Autosomal dominant retinitis pigmentosa caused by the threonine-17-methionine rhodopsin mutation: retinal histopathology and immunocytochemistry. Exp Eye Res 58:397–408
26. Milam AH, Li ZY, Cideciyan AV, Jacobson SG (1996) Clinicopathologic effects of the Q64ter rhodopsin mutation in retinitis pigmentosa. Invest Ophthalmol Vis Sci 37:753–765
27. To K, Adamian M, Dryja TP, Berson EL (2000) Retinal histopathology of an autopsy eye with advanced retinitis pigmentosa in a family with rhodopsin Glu181Lys. Am J Ophthalmol 130:790–792
28. John SK, Smith JE, Aguirre GD, Milam AH (2000) Loss of cone molecular markers in rhodopsin-mutant human retinas with retinitis pigmentosa. Mol Vis 6:204–215
29. To K, Adamian M, Dryja TP, Berson EL (2002) Histopathologic study of variation in severity of retinitis pigmentosa due to the dominant rhodopsin mutation Pro23His. Am J Ophthalmol 134:290–293
30. To K, Adamian M, Berson EL (2004) Histologic study of retinitis pigmentosa due to a mutation in the RP13 gene (PRPC8): comparison with rhodopsin Pro23His, Cys110Arg, and Glu181Lys. Am J Ophthalmol 137:946–948
31. Aguirre GD, Yashar BM, John SK et al (2002) Retinal histopathology of an XLRP carrier with a mutation in the RPGR exon ORF15. Exp Eye Res 75:431–443
32. Jacobson SG, Buraczynska M, Milam AH et al (1997) Disease expression in X-linked retinitis pigmentosa caused by a putative null mutation in the RPGR gene. Invest Ophthalmol Vis Sci 38:1983–1997
33. Mullins RF, Kuehn MH, Radu RA et al (2012) Autosomal recessive retinitis pigmentosa due to ABCA4 mutations: clinical, pathologic, and molecular characterization. Invest Ophthalmol Vis Sci 53:1883–1894
34. Bagheri N, Bell BA, Bonilha VL, Hollyfield JG (2012) Imaging human postmortem eyes with SLO and OCT. Adv Exp Med Biol 723:479–488
35. Abd El-Aziz MM, O'Driscoll CA, Kaye RS, Barragan I, El-Ashry MF, Borrego S, Antinolo G, Pang CP, Webster AR, Bhattacharya SS (2010) Identification of novel mutations in the ortholog of Drosophila eyes shut gene (EYS) causing autosomal recessive retinitis pigmentosa. Invest Ophthalmol Vis Sci 51:4266–4272
36. Audo I, Sahel JA, Mohand-Said S, Lancelot ME, Antonio A, Moskova-Doumanova V, Nandrot EF, Doumanov J, Barragan I, Antinolo G, Bhattacharya SS, Zeitz C (2010) EYS is a major gene for rod–cone dystrophies in France. Hum Mutat 31:E1406–E1435
37. Barragan I, Borrego S, Pieras JI, Gonzalez-del Pozo M, Santoyo J, Ayuso C, Baiget M, Millan JM, Mena M, Abd El-Aziz MM, Audo I, Zeitz C, Littink KW, Dopazo J, Bhattacharya SS, Antinolo G (2010) Mutation spectrum of EYS in Spanish patients with autosomal recessive retinitis pigmentosa. Hum Mutat 31:E1772–E1800
38. Bandah-Rozenfeld D, Littink KW, Ben-Yosef T et al (2010) Novel null mutations in the EYS gene are a frequent cause of autosomal recessive retinitis pigmentosa in the Israeli population. Invest Ophthalmol Vis Sci 51:4387–4394
39. Huang Y, Zhang J, Li C, Yang G, Liu M, Wang QK, Tang Z (2010) Identification of a novel homozygous nonsense mutation in EYS in a Chinese family with autosomal recessive retinitis pigmentosa. BMC Med Genet 11:121
40. Khan MI, Collin RW, Arimadyo K et al (2010) Missense mutations at homologous positions in the fourth and fifth laminin A G-like domains of eyes shut homolog cause autosomal recessive retinitis pigmentosa. Mol Vis 16:2753–2759
41. Pieras JI, Barragan I, Borrego S et al (2011) Copy-number variations in EYS: a significant event in the appearance of arRP. Invest Ophthalmol Vis Sci 52:5625–5631
42. Hosono K, Ishigami C, Takahashi M et al (2012) Two novel mutations in the EYS gene are possible major causes of autosomal recessive retinitis pigmentosa in the Japanese population. PLoS ONE 7:e31036
43. Suto K, Hosono K, Takahashi M et al (2014) Clinical phenotype in ten unrelated Japanese patients with mutations in the EYS gene. Ophthalmic Genet 35:25–34
44. Iwanami M, Oshikawa M, Nishida T, Nakadomari S, Kato S (2012) High prevalence of mutations in the EYS gene in Japanese patients with autosomal recessive retinitis pigmentosa. Invest Ophthalmol Vis Sci 53:1033–1040
45. Katagiri S, Akahori M, Hayashi T et al (2014) Autosomal recessive cone-rod dystrophy associated with compound heterozygous mutations in the EYS gene. Doc Ophthalmol 128:211–217

*Ophthalmic Genetics*, Early Online, 1–11, 2014
© Informa Healthcare USA, Inc.
ISSN: 1381-6810 print / 1744-5094 online
DOI: 10.3109/13816810.2014.958861

RESEARCH REPORT

# Retinal Histopathology in Eyes from a Patient with Stargardt disease caused by Compound Heterozygous *ABCA4* Mutations*

Vera L. Bonilha[1], Mary E. Rayborn[1], Brent A. Bell[1], Meghan J. Marino[1], Gerald A. Fishman[2], and Joe G. Hollyfield[1]

*[1]Cole Eye Institute, Department of Ophthalmology, Cleveland Clinic Lerner College of Medicine, Cleveland, OH, USA, and [2]Chicago Lighthouse for People Who Are Blind or Visually Impaired, Chicago, IL, USA*

## ABSTRACT

*Background*: The goal of this study was to define the histopathology of the retina in donor eyes from a patient with Stargardt disease (STGD1) due to compound mutations in the *ABCA4* gene.

*Materials and Methods*: Eyes were obtained from a 66-year-old female and fixed within 18 hours postmortem. The fundi of the posterior globes were evaluated with macroscopic, SLO and OCT imaging. The perifoveal and peripheral regions were processed for electron microscopy and immunocytochemistry using cell specific antibodies. Two age-similar normal eyes were used as controls. Prior ophthalmic examinations and genetic test results were also reviewed.

*Results*: All imaging modalities showed scattered bone spicules in the peripheral retina. Atrophy of the RPE was present around the optic nerve as evidenced by the absence of SLO autofluorescence. Histology analysis showed a severely degenerated fovea with little evidence of any retinal layering or remaining RPE. The fovea was severely degenerated, with little evidence of any retinal cell layer, including the RPE. In contrast, retinal nuclear layers were present in the periphery. The perifoveal region contained few cones labeled with cone-specific antibodies; some rhodopsin-labeled cells, reactive glia labeled with GFAP; and decreased autofluorescence of the RPE. The fovea was free of cone-specific labeling, contained a few disorganized rhodopsin-labeled cells and showed substantial GFAP labeling and no autofluorescent material in the retina. The periphery displayed stubby cells labeled with cone-specific antibodies, decreased rhodopsin-labeled cells, increased GFAP staining, and autofluorescent granules in the RPE.

*Conclusions*: The histopathology of the retina in this patient with Stargardt disease displayed a highly degenerated fovea. In all retinal locations studied, cones were more severely affected than rods.

**Keywords:** *ABCA4*, histology, immunohistochemistry, photoreceptors, Stargardt disease

## INTRODUCTION

Stargardt disease (STGD1, OMIM# 248200), is an early onset form of macular degeneration with an estimated frequency between 1 in 8000 and 1 in 10,000.[1] Most cases of Stargardt disease are autosomal recessive and caused by mutations in the *ABCA4* gene located on chromosome 1p22.1. Mutations in *ABCA4* have been associated with several different clinical phenotypes – Stargardt disease/fundus flavimaculatis, autosomal recessive retinitis pigmentosa, autosomal recessive cone-rod dystrophy, bulls eye maculopathy, and age-related macular degeneration.[2] Over 700 disease-causing mutations[3] in the *ABCA4* gene have been identified, and some studies suggest genotype–phenotype correlations.[4–6]

---

Received 16 April 2014; revised 19 August 2014; accepted 23 August 2014; published online 22 September 2014

*Preliminary data from this study were presented at the 2013 annual meeting of the Association for Research in Vision and Ophthalmology.

Correspondence: Vera L. Bonilha, PhD, Cleveland Clinic Foundation, The Cole Eye Institute, 9500 Euclid Avenue, i31, Cleveland, OH 44195, USA. Tel: +1 216 445 7690. Fax: +1 216 445 3670. E-mail: bonilhav@ccf.org

STGD is characterized by progressive macular atrophy accompanied by the loss of central vision.[7,8] Excessive accumulation of lipofuscin in the RPE is an early feature of the disease.[9,10] The *ABCA4* gene encodes a transport protein located in the photoreceptor outer segment disc margin that facilitates the translocation of all-trans retinal through the disc membrane lipid bilayer.[11] *ABCA4* mutations cause a dysfunction of this transport that results in the retention of all-trans retinal within the photoreceptor disc and disrupts normal retinoid movement. Ultimately, there is an increase in retinoid accumulation in the RPE as shed tips of the outer segment containing excessive retinoid load are phagocytized. Within the RPE the all-trans retinal is converted to A2-E, a major component of lipofuscin, which is thought to be toxic to both the RPE and the photoreceptors.[12,13] It is not known whether the ultimate loss of vision in patients with STGD occurs primarily from dysfunction of the RPE, photoreceptors, or both.

Little is known about how mutations in the ABCA4 protein lead to the degeneration of the retina, RPE and eventually the choroid. In the present study, we analyzed the retina, RPE and choroid morphology and the distribution of various retinal cell markers in the donor eyes from a female with mutations in the *ABCA4* gene. To our knowledge this is the first histopathological description of STGD1 donor eyes to be reported in which specific mutations in the *ABCA4* gene causing the disease is known.

## MATERIALS AND METHODS

### Patient Information

The donor globes from a 66-year-old female with STGD1 were enucleated 18 hours postmortem and fixed in 4% paraformaldehyde (PF) and 0.5% glutaraldehyde in phosphate buffer. Postmortem eyes from a 61- and a 65-year-old donor without a history of retinal disease were used as control tissues (donation numbers #649 and 696) and were fixed within 12.5 and 14.5 hours postmortem. The STGD1 tissue was obtained 10 years subsequent to her last clinical visit. The recovery of the eye donation was coordinated through the Foundation Fighting Blindness (FFB) Rare Eye Donor Program (Columbia, MD) (donation number #863). The histopathologic and immunocytochemical analysis was performed with the approval of the Cleveland Clinic Institutional Review Board (IRB #14-057).

For full details of the methods, instruments and analyses, please see the Supplementary material online.

## RESULTS

### Clinical Findings

The Stargardt patient was initially seen clinically by one of the authors (GAF) at age 31 years for the evaluation of decreased vision that had been noted since 1st grade. Visual acuity was best corrected to 20/300 in each eye. She was diagnosed as having Stargardt disease based upon her fundus appearance.

When last seen by GAF at age 55 years, best corrected visual acuity was 20/400 in the right eye and 8/225 in the left. Goldmann visual field testing showed a large central scotoma in each eye with normal peripheral boundaries to both II4e and V4e test targets. Her corneas and lenses were clear. Ocular pressures were 13 mmHg OD and 11 mmHg OS. There were extensive atrophic-appearing changes in the RPE and choroid within the macula with hypopigmented lesions throughout the posterior pole consistent with partially resorbed fundus flecks. Previous genetic testing identified two heterozygous mutations, p.Gly1961Glu and IVS46 + 2 C > G, in the *ABCA4* gene, which were consistent with her clinical diagnosis of Stargardt disease.

### *In Vivo* Imaging Analysis

Fundus photographs of both eyes from the STGD patient showed severe degenerative changes of the retina (Figure 1). Images from the donor's last ocular exam, 11 years prior to her death, showed a normal-appearing optic disc, prominent choroidal vessels, RPE atrophy (Figure 1A and B, arrowheads), and hyperpigmented areas in the perifoveal region (Figure 1A and B, arrows).

### *Ex-Vivo* Imaging Analysis

Images of the postmortem posterior globes similarly displayed prominent choroidal vessels due to RPE atrophy (Figure 1C and D, arrowheads) as well as hyperpigmented areas in the perifovea (Figure 1C and D, arrows). Scanning laser ophthalmoscopy (SLO) and spectral-domain optical coherence tomography (SD-OCT) imaging of the donor eyes were performed to characterize the retinal lesions of the STGD eyes. The optic nerve head (Supplementary Figure 1A–D, arrows – available online only) was clearly identified in each donor eye using all imaging modalities. SLO-IR imaging of the STGD eyes identified the hypopigmented macula as seen on the fundus image (Supplementary Figure 1B, arrowheads). SLO-AF imaging of STGD

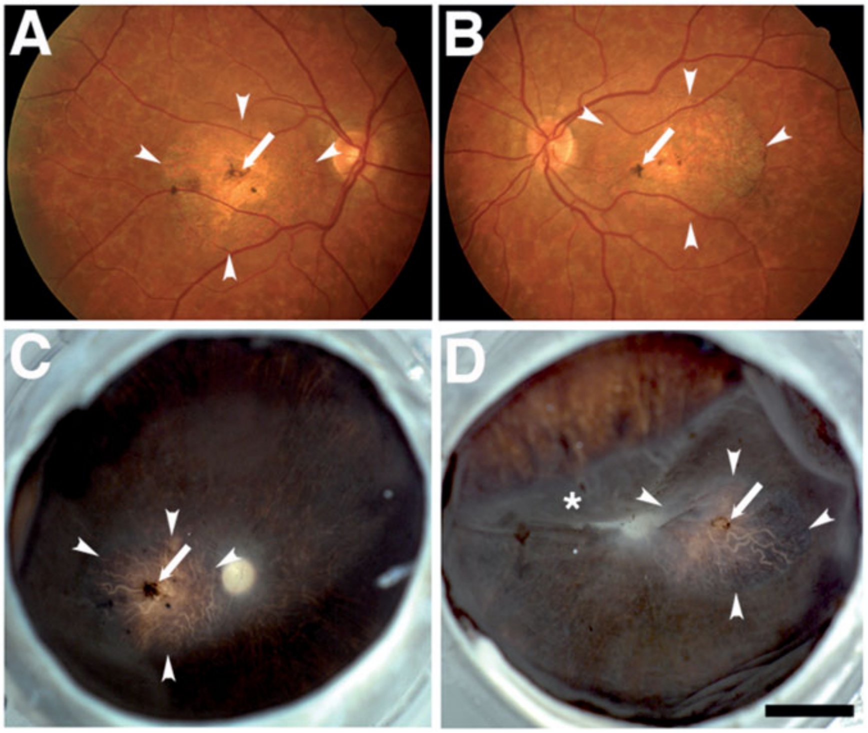

FIGURE 1. Fundus photographs of both eyes from a Stargardt (STGD) patient. Images obtained when the STGD donor had her last ocular exam, 11 years prior to her death, show a normal-appearing optic disc, retinal vessels, and a well-circumscribed region within the macula that consisted of an atrophic change involving both the RPE and the choroid (A, B, outlined by arrowheads). Focal small hyperpigmented lesions within the circumscribed macular region were also observed (A, B, arrows). Similarly, images of fixed postmortem posterior globes showed atrophic changes of the RPE and choroidal vessels (outlined by arrowheads, C, D) in addition to small hyperpigmented lesions (C, D, arrows; *indicates retinal detachment). Bar = 0.5 cm.

eyes identified that the area surrounding the optic nerve and fovea showed evidence of RPE atrophy (Supplementary Figure 1D, arrowheads) compared to the control eyes (Supplementary Figure 1C). The area surrounding the optic nerve of the STGD eye showed atrophic changes of the RPE and the choroidal vessels, the latter is usually obscured by the RPE. Only the retinal vasculature was clearly visible in the control eyes.

Both the control and STGD eyes were also evaluated with SD-OCT imaging (Supplementary Figure 2 – available online only). The fovea (Supplementary Figure 2A, arrow) and optic nerve (Supplementary Figure 2A, ON) were clearly evident with SD-OCT *en face* imaging in the control eye. Several areas near the fovea and optic nerve in the STGD eyes showed degenerative changes in the retina (Supplementary Figure 2B). SD-OCT in-depth B-scans identified retinal changes including disorganization of retinal lamina and absence of the photoreceptor layer in the STGD eyes (Supplementary Figure 2D) when compared to the control eyes (Supplementary Figure 2C).

## Histopathology

Semi-thin sections of epon-embedded tissue were analyzed and compared to age-similar controls in the perifoveal region (Figure 2A, regions 1 to 5) and periphery (Supplementary Figure 3 – available online only, region 6 in Figure 2A). A schematic drawing depicts the regions harvested and processed for observation in both the morphological and immunohistological assays (Figure 2A). These include: the distal (Figure 2A, regions 1, and 5) and proximal perifoveal regions (Figure 2A, regions 2, and 4), fovea (Figure 2A, region 3), and the periphery (Figure 2A, region 6). The fundus images from the STGD donor showed extensive macular atrophy overall. As a consequence, we focused our analysis on the fovea (Figure 2D, region 3 in Figure 2A) and the surrounding perifoveal regions (Figure 2C and E, regions 1 and 5 in Figure 2A). The retina of the control eye displayed each of the usual retinal lamina and the RPE (Figure 2B). The retina of the STGD donor showed varying degrees of retinal changes in each of the regions studied when compared to control retina (Figure 2B). In the perifoveal region of the STGD donor (Figure 2C and E, regions 1 and 5 in Figure 2A), the outer nuclear layer and photoreceptors were absent and the number of nuclei across the inner nuclear layer was substantially reduced. Although the RPE was mostly absent from these areas with retinal changes, a few isolated RPE cells remained (Figure 2C, arrow). Bruch's membrane (BM) was evident in these areas (Figure 2C and E, arrowheads).

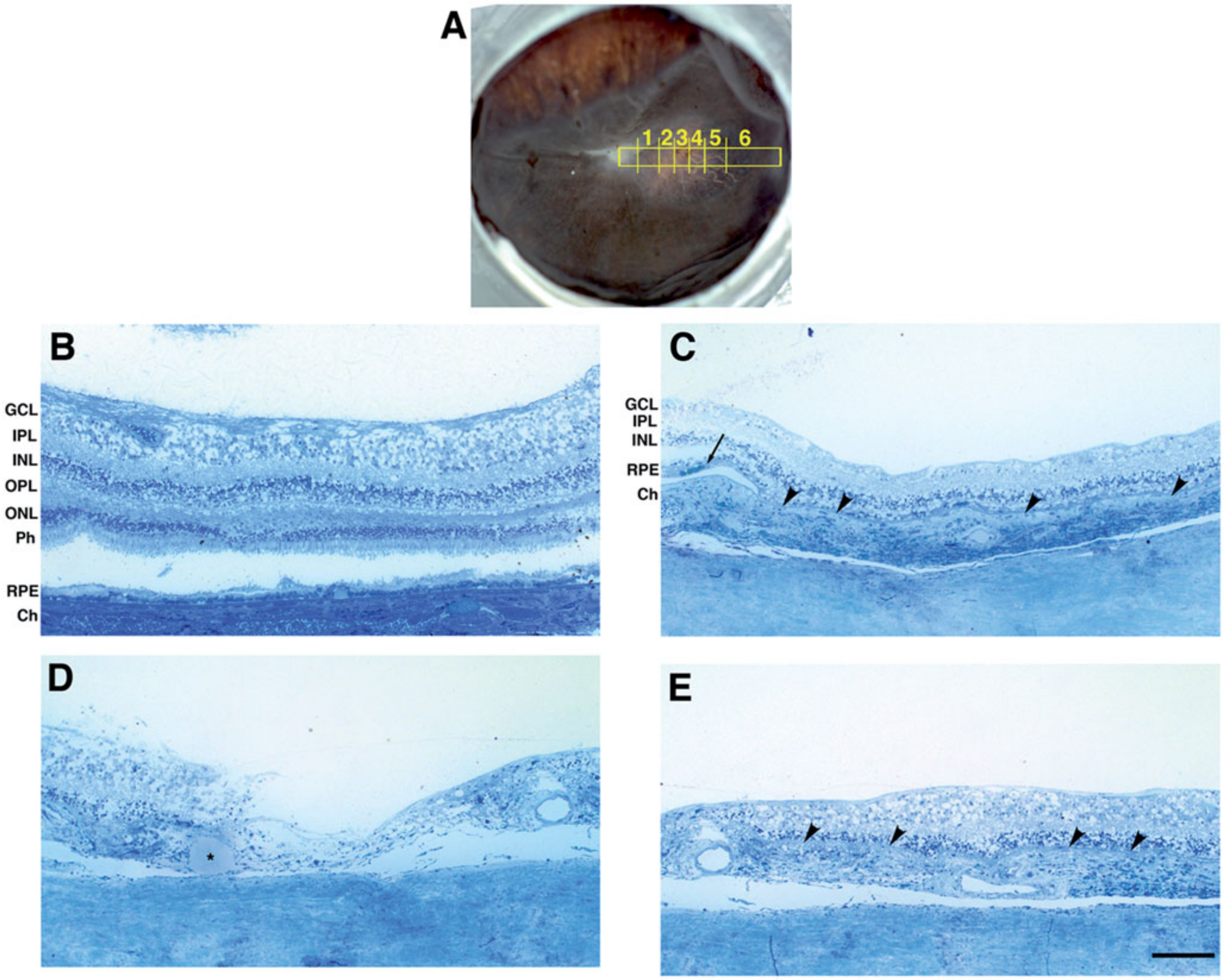

FIGURE 2. Histology of the central retina of the Stargardt disease (STGD) donor's retina. (A) A fundus image of the studied eye (OS) with a schematic drawing of the regions cut and processed for cryosectioning and immunolabeling is shown. Toluidine blue-stained plastic sections (1 μm) from the STGD donor (C, D, E) and age-similar control (B). The retina section of a control donor displays several distinct layers including the ganglion cell layer (GCL), inner (IPL) and outer plexiform (OPL) layers, inner (INL) and outer nuclear (ONL) layers, photoreceptors (Ph) and the retinal pigment epithelium (RPE) (B). The STGD retina displayed different degrees of retinal degeneration in each of the regions observed. The perifoveal region of the STGD donor (C, E) displayed absence of the ONL, and Ph and the nuclei in the INL were significantly decreased. The RPE was mostly absent from these areas but a few RPE cells were still present (C, arrow) and Bruch's membrane (BM) was still present (C, E, arrowheads). The perifoveal region of the STGD donor displayed a highly degenerate retina with little evidence of any stratified nuclear layers and the presence of a giant lipophilic drop in the choroid (D, *); BM was absent in this area. The choroid (Ch) was degenerated in both perifoveal and foveal regions. Bar = 100 μm.

The fovea (Figure 2D and region 3 in Figure 2A) was highly degenerated as evidenced by the paucity of photoreceptors and the disorganization of the surrounding retina where distinct retinal lamina are usually found. A large lipid-like droplet was also present in the choroid (Figure 2D, asterisk); BM was absent in this area.

Based on histology, the control retina was normal in morphology with distinct laminae in the periphery (Supplementary Figure 3A). In the STGD donor periphery (Supplementary Figure 3B), all the retinal layers were present, with some degenerative changes in the outer plexiform layer thickness. The RPE displayed normal thickness in the control sample (Supplementary Figure 3C) but it was reduced from normal thickness and displayed lack of pigment in the STGD donor (Supplementary Figure 3D).

## Immunohistochemistry

To evaluate molecular changes associated with the pathology in this STGD donor, tissue from the regions described above were cryosectioned and prepared for immunocytochemistry. Initially, the distribution of the cone cytoplasmic marker 7G6 was evaluated in both the STGD donor and an age-similar-control eye using samples from the perifoveal (Figure 3, regions 1 to 5 in Figure 2A) and peripheral locations (Supplementary Figure 4 – available online only, region 6 in Figure 2A). Using this cone-specific antibody, we observed substantial differences in labeling patterns between the STGD donor retina and the control sample. Control retinas labeled with cone arrestin antibody showed that arrestin was distributed along the entire conical-shaped plasma membrane, from the tip of the outer segment to the synaptic base. In contrast, red/green cone opsins were restricted to the outer segments of the cones (Figure 3A, arrows). A few cone arrestin-labeled cells were present in the distal perifoveal region of the STGD donor (Figure 3B). However, the red/green opsins were distributed throughout the entire cell body of these cells (Figure 3B, arrows). Cone-specific markers labeling was not observed in either the proximal perifoveal region (Figure 3C) or in the fovea (Figure 3D). The distal perifoveal region where the RPE was present displayed a few cone-labeled cells (Figure 3E). As seen in the plastic sections, the cryosections also showed absence of RPE, with preservation of BM (Figure 3C, arrowheads). The fovea was highly degenerated with loss of retinal lamina and absence of both the RPE and BM (Figure 3D). Arrestin-labeled cones with normal morphology were evident in the peripheral samples from the control retina (Supplementary Figure 4A and B). However, only stubby, degenerate arrestin-labeled cones were found in the periphery of the STGD donor (Supplementary Figure 4C and D). Label distribution of the red/green opsin immunoreactivity was present over the entire plasma membrane of cones labeled in the peripheral retinal sample of the STGD eyes, (Supplementary Figure 4C and D, arrows) while red/green opsin immunoreactivity was restricted to the cone outer segments in control retina (Supplementary Figure 4A and B, arrows).

Control retinas labeled with blue cone opsin antibodies displayed immunoreactivity restricted to the outer segment in perifoveal samples (Figure 3F, arrows). In contrast, blue cone opsin was present in the cell bodies (Figure 3J, arrow) of the cones of the STGD donor retina. Blue cone opsin-labeled cells were absent from the distal perifoveal region (Figure 3G), the proximal perifovea (Figure 3H), and the fovea (Figure 3I) of the STGD donor retina where the RPE was missing. However, a few atrophic blue opsin-labeled cells were still found in the distal perifoveal region of the STGD donor retina where RPE was present (Figure 3J). Müller cells were labeled to some extent with the GFAP antibody. The GFAP-labeled cytoplasmic filaments in Müller cells were not detected in the perifoveal region of the control donor retina (Figure 3F). The Müller cells were hypertrophic and were observed in the inner retina of the distal perifoveal region of the STGD donor (Figure 3G), where the RPE was absent. However, extensive GFAP immunoreactivity was present in the retinal samples from the proximal perifoveal region (Figure 3H) and in the fovea (Figure 3I) of the STGD donor retina. GFAP immunoreactivity was also observed in the distal perifoveal region where the RPE was still present (Figure 3J). While blue cone opsin is restricted to the outer segments of the cones in the control (Supplementary Figure 5A and B, arrows – available online only) it was not in the STGD donor retina in the periphery (Supplementary Figure 5C and D, arrows). In this area in the STGD donor retina, the Müller cells had undergone reactive gliosis throughout the retina and their hypertrophic processes were GFAP positive (Supplementary Figure 5C and D, arrows) but not in the control retina (Supplementary Figure 5A and B).

The rod outer segments were visualized through labeling with rhodopsin antibodies. Control retinas labeled with rhodopsin antibody displayed restricted distribution of this protein to the outer segment of rods in the perifoveal region of the control donor (Figure 3K, arrows). In the STGD donor retina, rhodopsin-labeled cells were decreased, stubby and rhodopsin distribution was not restricted to the outer segments of the cells in most of the distal perifoveal region (Figure 3L, arrows). In the proximal perifoveal region (Figure 3M, arrows) and in the fovea (Figure 3N, arrows) rhodopsin-labeled cells were almost completely absent with the presence of a few clearly disorganized and morphologically different cells. A few rhodopsin-labeled cells were still found in the distal perifoveal region of the STGD donor retina where the RPE was present (Figure 3O). Calbindin D labeling in the control retina was present in sparse neurons in the ganglion cell layer, in amacrine, bipolar and cones in the perifoveal region (Figure 3K). However, in the STGD donor, less calbindin D-positive cells were observed in the distal perifoveal region and they were observed scattered throughout the entire retina (Figure 3L and O). In the proximal perifoveal region (Figure 3M) and in the fovea (Figure 3N) calbindin D labeled cells were not present. In the periphery, both control (Supplementary Figure 6A and B – available online only) and STGD (Supplementary Figure 6C and D) retinas labeled with rhodopsin antibody displayed restricted distribution of this protein to the outer segment of rods. Interestingly, calbindin D-positive cells in the control retina (Supplementary Figure 6A and B) labeled cones, cells in the outer plexiform layer and sparse neurons in the ganglion cell layer. In the STGD donor retina (Suppl. Fig. 6C and D, arrowheads) calbindin D labeling was increased in all layers and also identified the presence of stubby cones.

Stargardt disease is characterized by excessive accumulation of the blue-shifted autofluorescence

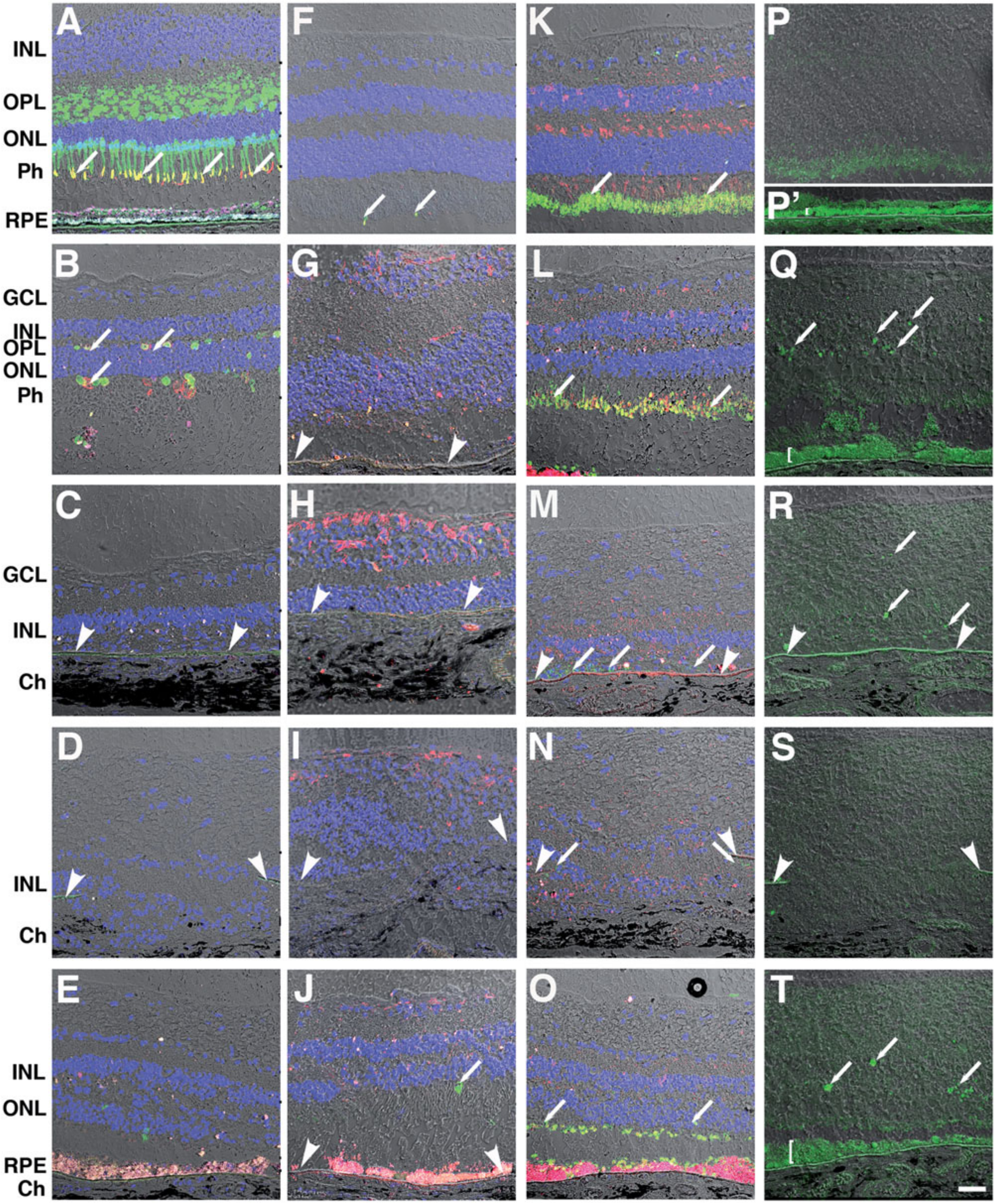

FIGURE 3. Immunolocalization of red/green and blue cone opsins, cone arrestin, rhodopsin and GFAP in the central region of the Stargardt disease (STGD) retina. Cryosections of both the STGD (B–T) and an age-similar-control (A, F, K, P, P′) retinas were labeled with antibodies specific to cone arrestin marker 7G6, blue cone opsin and rhodopsin (green) and the red/green cone opsins (red). Cell nuclei were labeled with TO-PRO-3 (blue). Control retinas (A) labeled with cone arrestin antibodies displayed distribution from the tip of the outer segment to the synaptic base. In contrast, red/green (A) and blue cone (F) opsins, and rhodopsin (K) were restricted to the outer segments of the cones (arrows); no GFAP-labeled filaments were observed (F). The distal perifoveal region of the STGD donor was characterized by the presence of a few cone arrestin-labeled cells (B, E), an almost complete absence of blue cone opsin (G, J), the decreased presence of rhodopsin-labeled cells, with the resulting cells displaying stubby and unrestricted rhodopsin distribution (L, O) and hypertrophic Müller cells labeled with GFAP (G, J). The red/green opsins

*continued*

lipofuscin granules in the RPE cytoplasm. Therefore, autofluorescent material in the RPE of the perifoveal region (Figure 3P to T) and peripheral locations (Supplementary Figure 7 – available online only) were analyzed and compared to a control. RPE from age-similar control eyes (Figure 3P′) showed the presence of autofluorescent granules in the cytoplasm. The RPE of the STGD donor was hypertrophic and displayed significantly decreased autofluorescent granules in the distal perifoveal region (Figure 3Q and T, bracket). RPE was absent in the proximal perifoveal region (Figure 3R) and in the fovea (Figure 3S) of the STGD eye. Control retinas also displayed weak cytoplasmic autofluorescence in the photoreceptor inner and outer segments that were detached from the RPE during tissue processing (Figure 3P). Interestingly, several large autofluorescent granules were observed in the STGD donor's inner retina in both the distal (Figure 3Q and T, arrows) and proximal perifoveal locations (Figure 3R, arrows). In the periphery, even though the age-similar control RPE displayed abundant autofluorescent granules (Supplementary Figure 7A and B), the RPE of the STGD donor showed an increased accumulation of autofluorescent granules (Supplementary Figure 7C and D).

## Morphological and Ultrastructural Pathology

The ultrastructure of RPE and Bruch's membrane in the perifoveal region of the control and STGD donors were analyzed by TEM. Control RPE displayed photoreceptor outer segments opposed to the RPE apical surface (Figure 4A). In the STGD donor, RPE cells were observed in direct contact with rod nuclei in some areas (Figure 4B, RN). The basal surface of the control RPE contained numerous basal infoldings (Figure 4A, BI) but in the STGD eye, the basal surface of the RPE was relatively smooth, with little evidence of basal infoldings (Figure 4B). The cytoplasm of the control RPE contained lipofuscin (Figure 4C, Lip) and a few melanin granules (Figure 4C, MG). In contrast, the cytoplasm of the STGD donor RPE was filled with lipofuscin and melanolipofuscin granules (Figure 4D). The BM of the control donor displayed typical pentalaminar structure (Figure 4E) while the STGD BM was disorganized and thicker than that of the control (Figure 4F). The RPE basal surface in the control eye showed close interaction with the BM, which is also the interacting matrix for the blood supplying choriocapillaris (Figure 4G). In contrast, the STGD donor eye displayed areas where RPE was absent but the subjacent choriocapillaris remained (Figure 4H).

## DISCUSSION

Of the two heterozygous mutations in the *ABCA4* gene observed in our patient, the p.Gly1961Glu mutation has been observed previously.[12,14–19] It is the most common mutation detected in *ABCA4* with a frequency that varies from approximately 0.2% in Europeans[20,21] to approximately 10% in East African populations.[14,22,23] In addition, this mutation has also been identified in patients with autosomal recessive cone–rod dystrophy[2,24,25] and age-related macular degeneration.[12,18,26]

A recent report classified the severity of phenotypes in individuals carrying homozygous p.Gly1961Glu mutations as mild to moderate based on clinical characteristics including: age of onset; the minimum angle of visual acuity resolution; fundus appearance; autofluorescence pattern; and ERG characteristics.[15,16] Additional reports also indicate that patients homozygous for this mutation usually have a milder form of the disease, with more severe phenotypes linked to the presence of a third or fourth *ABCA4* mutation.[3,27]

The fundus of the STGD patient analyzed here displayed significant RPE atrophy with a predilection to occur within the perifoveal region, consistent with previous reports indicating that the p.Gly1961Glu mutation is associated with anatomical and functional pathologies more notable to this location.[3,27] Previous studies reported that STGD patients carrying homozygous p.Gly1961Glu mutations had localized dysfunction confined to the macula and central fovea, accompanied by reduced retinal thickness in these regions as measured by OCT.[16] In addition, OCT scans

*Figure 3. continued*
were distributed throughout the entire cell body of the cells (B, arrows) in this area. Cone-specific markers and rhodopsin labeling was not observed in the fovea (D, I, N) and in the proximal perifoveal region (C, H); a few disorganized rhodopsin-labeled cells were present in the proximal perifoveal region (M, arrows). RPE from the STGD donor was hypertrophic and displayed significantly decreased autofluorescent granules in the distal perifoveal region (Q, T, bracket) when compared to RPE in an age-similar control eyes (P′). Control retinas also displayed weak, mostly cytoplasmic autofluorescence in the photoreceptor inner and outer segments detached from the top of the RPE (P). RPE was absent in the fovea (S) and in the proximal perifoveal region (R). Several autofluorescent granules were observed in the STGD donor inner retina in the distal (Q, T, arrows) and in the proximal perifoveal regions (R, arrows). In the proximal perifovea (C, H, M, R) and partially in the fovea (D, I, N, S, arrowheads), BM was evident. The individual images are differential interference contrast (DIC) microscopy overlaid with the immunofluorescence labeling. INL, inner nuclear layer; OPL, outer plexiform layer; ONL, outer nuclear layer; Ph, photoreceptors; RPE, retinal pigment epithelium. Bar = 40 μm.

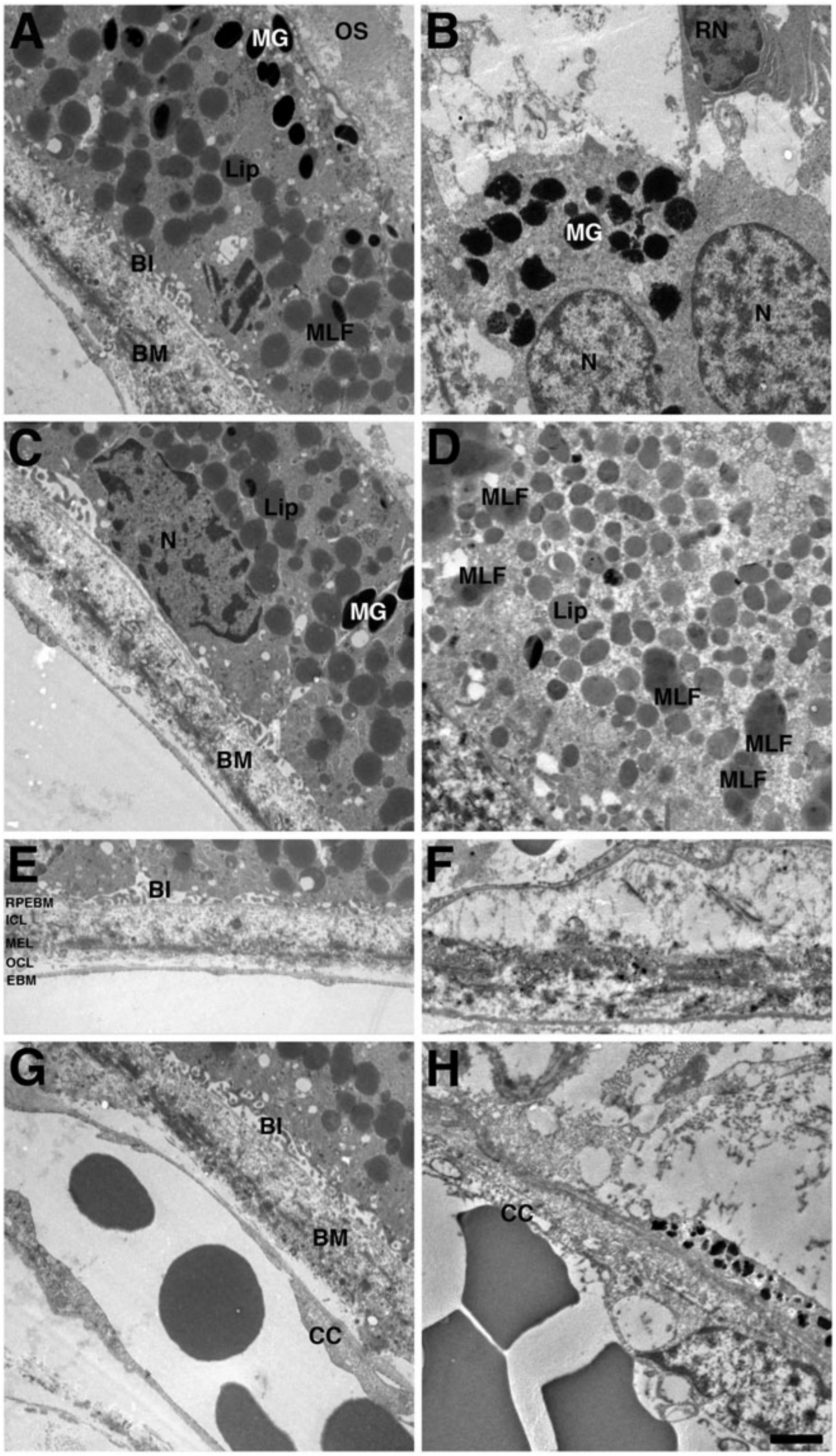

FIGURE 4. Ultrastructural analysis of RPE degeneration in the Stargardt disease (STGD) donor's retina. The control RPE eye displayed photoreceptor outer segments lying in contact with the RPE apical surface (A). In the STGD donor, RPE cells are observed in direct contact with rod nuclei in some areas (B, RN). The basal surface of the control RPE elaborated numerous basal infoldings (A, BI) but the STGD basal surface showed an absence of these structures (B). The cytoplasm of the control RPE contained lipofuscin (C, Lip) and a few melanin granules (C, MG). In contrast, the cytoplasm of the STGD donor RPE was filled with lipofuscin and melanolipofuscin granules (D, MLF). The BM of the control donor displayed typical pentalaminar structure (E) while the STGD BM was disorganized and thicker than that of the control (F). In the control eye the RPE basal surface was interacting with the BM (G). In contrast, the STGD donor eye displayed areas where RPE was absent but the subjacent choriocapillaris remained (H). N, nucleus; BI, basal infoldings; MG, melanin granules; Lip, lipofuscin; MLF, melanolipofuscin; CC, choriocapillaris; RPEBM, RPE basement membrane; ICL, inner collagenous layer; MEL, middle elastic layer; OCL, outer collagenous layer; EBM, choroidal endothelial cell basement membrane; RN, rod nuclei. Bars = 2 μm.

of STGD patients heterozygous for the p.Gly1961Glu mutation showed extensive loss of outer retinal layers in regions with subjacent RPE atrophy.[28] OCT B-scans of the STGD donor analyzed here displayed structural differences in the retina that suggested disorganization and absence of a photoreceptor layer in the fovea and surrounding perifovea.

RPE lipofuscin was measured *in vivo* with fundus autofluorescence using SLO imaging. The STGD donor analyzed here displayed central macular atrophy and decreased foveal autofluorescence on SLO imaging, indicative of RPE atrophy. Our data are consistent with previous reports of STGD patients,[28,29] including those carrying the p.Gly1961Glu mutation.[3,15,27] Longitudinal studies of SGTD patients reported progressive increases in autofluorescence followed by reduced autofluorescence in the perifoveal region.[3,28,30] The RPE in the donor eye studied here showed an abundance of lipofuscin in the areas where the RPE remained. Our analysis of cryosections revealed higher levels of autofluorescence in the RPE in the periphery of this STGD donor eye. Lower levels of autofluorescence in the fovea and perifovea were probably due to RPE atrophy in the region.

Lipofuscin granules are fluorescent, heterologous waste material that accumulates with age in a variety of postmitotic cells, but are particularly prominent in the RPE.[31–33] They contain primarily lipid soluble material with less than 1% protein.[33] Much of the lipofuscin fluorescence comes from A2E (*N*-retinylidin-*N*-retinylethanolamin), which contains two vitamin A derivatives covalently linked to ethanolamine. The relative amount of lipofuscin accumulation in the RPE is associated with at least a partially functioning, albeit dysfunctional, retinoid cycle. In this regard, it is notable that lipofuscin is significantly reduced in mice lacking the retinol isomerase (RPE65) that generates 11-cis-retinol[34] and also in animals treated with reagents that disrupt the visual cycle or that reduce serum vitamin A.[35–38]

The abundance of lipofuscin in the RPE of STGD individuals has been reported to result from the absence of a functional ABCA4, resulting in the delivery of large amounts of all-trans retinoid within the shed tips of outer segment debris that is phagocytized by the RPE. In contrast, in normal individuals, retinoids are transported within the outer segment discs by a functional ABCA4 and moved to the RPE for eventual conversion to the 11-cis-configuration. Thus, in visually normal individuals, the phagocytized shed tips contain lower retinoid levels compared to individuals with STGD. The arrival of altered retinoids associated with outer segment debris reaching the RPE by way of the phagosome appears to be the cause of the higher levels of lipofuscin present in the RPE in individuals with this disease.

It has been reported that the p.Gly1961Glu mutation is expected to cause decreased ATP binding and ATPase activity of the ABCA4 transporter found in both rods and cones.[39] However, little is known about how *ABCA4* mutations lead to degeneration of the retina and RPE. In our donor's eyes, degenerative changes were more severe in cones than in rods. Whether this reflects more sensitivity of cones to the mutation, or whether the lipofuscin debris is more deleterious to cones than to rods cannot be distinguished from these observations.

In the retina studied here, a few cone opsin-labeled cells were present in the distal perifoveal region. These cells displayed the red/green opsins distributed throughout the cell body. Previous analysis of mice models[40] and of retinas from eyes of donors with several retinal degenerations suggests that mislocalization of cone opsins are an early event and may precede cone cell death.[41–44] In addition, cone-specific labeling was not observed in the fovea or in the proximal perifoveal region, indicating that cones have been lost from these locations. Our results are in agreement with a previous study that analyzed patients with STGD with well-defined atrophic macular lesions.[29] Another study aimed to investigate the correlation between macular cone structure, fundus autofluorescence, and visual functions in patients with STGD.[28] A report by Chen and colleagues in 2011 provided "a model of progression in STGD which lipofuscin accumulation results in homogeneously increased autofluorescence with cone spacing abnormalities, followed by heterogeneously increased autofluorescence with cone loss, then reduced autofluorescence with cone and RPE cell death".[28] These conclusions are supported by the observation that the lipofuscin fluorophores, A2E and A2PE-$H_2$, are markedly elevated in the RPE of postmortem eyes from STGD patients[45] and in the abcr$-/-$ mouse model of STGD.[46] The A2E cytotoxicity in RPE cells is well documented and is assumed to occur through a series of biochemical reactions, cellular interactions and genetic activation that ultimately leads to RPE and overlying photoreceptor cell death.[47–52] Our ultrastructural observation of the STGD donor RPE showed that lipofuscin and melanolipofuscin granules were substantially increased in the RPE cytoplasm in the perifoveal region, where RPE was present but cones were significantly decreased. These data suggest that cone degeneration and death are associated with the accumulation of lipofuscin in the RPE.

OCT imaging identified disruptions in Bruch's membrane of STGD patients carrying compound heterozygous for the p.His1406Tyr and p.Gly1961Glu mutations in the *ABCA4* gene.[53] We found Bruch's membrane loss in the fovea using histology and cryosectioning methods. The ultrastructural analysis of the STGD donor identified increased thickening of Bruch's membrane, particularly in the central elastin lamina. This observation is consistent with studies of the abca4−/− mouse, which showed that they exhibit a 2-fold increase in Bruch's membrane thickness.[54]

A previous histopathologic study from donor eyes of a STGD patient (genotype unknown) showed elevated levels of lipofuscin in the peripheral RPE and in surviving photoreceptor inner segments. This same study also found loss of RPE in the macula and Muller cell hypertrophy. In addition, degenerated rods and cones with abnormal structure, but qualitatively normal immunoreactivity to rod- and cone-specific markers, were observed.[55]

In conclusion, we correlated the clinical, genetic, histopathologic and immunocytochemical findings in donor eyes from a patient with Stargardt disease due to *ABCA4* mutations. Overall, the retina was severely degenerated. A few surviving cones were present in the distal perifoveal region but were absent in the fovea. In contrast, more rods were present in the perifovea and a few disorganized rhodopsin-labeled cells were still present in the fovea. Finally, RPE was absent below the fovea but present in the distal perifoveal region. Previous reports suggest that the p.Gly1961Glu mutation leads to a less severe phenotype. It is likely that the severity of the phenotype of this SGTD donor is due to the presence of compound heterozygous mutations, in which the IVS46 + 2C > G mutation is more deleterious.

## ACKNOWLEDGEMENTS

The authors thank Dr Peter MacLeish (Morehouse School of Medicine, Atlanta, GA) for providing us with the antibody to cone cytoplasmic marker (7G6), and Dr Grazyna Adamus, (Oregon Health and Science University, Portland, OR) for providing us with the antibody to rhodopsin (B6-30N).

## DECLARATION OF INTEREST

The authors report no conflicts of interest. The authors alone are responsible for the content and writing of the paper.

The Foundation Fighting Blindness, Columbia, MD, Research to Prevent Blindness, Wolf Family Foundation, The Llura & Gordon Gund Foundation and National Eye Institute supported this work.

## REFERENCES

1. Blacharski PA. Fundus flavimaculatus. In: Newsome DA, editor. Retinal dystrophies and degenerations, 1st ed. New York: Raven Press; 1988. pp 135–159.
2. Klevering BJ, Yzer S, Rohrschneider K, et al. Microarray-based mutation analysis of the ABCA4 (ABCR) gene in autosomal recessive cone-rod dystrophy and retinitis pigmentosa. Eur J Hum Genet 2004;12:1024–1032.
3. Burke TR, Fishman GA, Zernant J, et al. Retinal phenotypes in patients homozygous for the G1961E mutation in the ABCA4 gene. Invest Ophthalmol Vis Sci 2012;53:4458–4467.
4. Lois N, Holder GE, Bunce C, et al. Phenotypic subtypes of Stargardt macular dystrophy-fundus flavimaculatus. Arch Ophthalmol 2001;119:359–369.
5. Gemenetzi M, Lotery AJ. Phenotype/genotype correlation in a case series of Stargardt's patients identifies novel mutations in the ABCA4 gene. Eye (Lond) 2013;27:1316–1319.
6. Kjellstrom U. Association between genotype and phenotype in families with mutations in the ABCA4 gene. Mol Vis 2014;20:89–104.
7. Fishman GA, Farber M, Patel BS, et al. Visual acuity loss in patients with Stargardt's macular dystrophy. Ophthalmology 1987;94:809–814.
8. Rotenstreich Y, Fishman GA, Anderson RJ. Visual acuity loss and clinical observations in a large series of patients with Stargardt disease. Ophthalmology 2003;110:1151–1158.
9. Cideciyan AV, Aleman TS, Swider M, et al. Mutations in ABCA4 result in accumulation of lipofuscin before slowing of the retinoid cycle: a reappraisal of the human disease sequence. Hum Mol Genet 2004;13:525–534.
10. Eagle Jr RC, Lucier AC, Bernardino Jr VB, Yanoff M. Retinal pigment epithelial abnormalities in fundus flavimaculatus: a light and electron microscopic study. Ophthalmology 1980;87:1189–1200.
11. Azarian SM, Travis GH. The photoreceptor rim protein is an ABC transporter encoded by the gene for recessive Stargardt's disease (ABCR). FEBS Lett 1997;409:247–252.
12. Allikmets R, Shroyer NF, Singh N, et al. Mutation of the Stargardt disease gene (ABCR) in age-related macular degeneration. Science 1997;277:1805–1807.
13. Sun H, Nathans J. ABCR, the ATP-binding cassette transporter responsible for Stargardt macular dystrophy, is an efficient target of all-trans-retinal-mediated photooxidative damage in vitro. Implications for retinal disease. J Biol Chem 2001;276:11766–11774.
14. Aguirre-Lamban J, Gonzalez-Aguilera JJ, Riveiro-Alvarez R, et al. Further associations between mutations and polymorphisms in the ABCA4 gene: clinical implication of allelic variants and their role as protector/risk factors. Invest Ophthalmol Vis Sci 2011;52:6206–6212.
15. Fishman GA, Stone EM, Grover S, et al. Variation of clinical expression in patients with Stargardt dystrophy and sequence variations in the ABCR gene. Arch Ophthalmol 1999;117:504–510.
16. Fujinami K, Sergouniotis PI, Davidson AE, et al. The clinical effect of homozygous ABCA4 alleles in 18 patients. Ophthalmology 2013;120:2324–2331.
17. Genead MA, Fishman GA, Stone EM, et al. The natural history of Stargardt disease with specific sequence mutation in the ABCA4 gene. Invest Ophthalmol Vis Sci 2009;50:5867–5871.
18. Michaelides M, Chen LL, Brantley Jr MA, et al. ABCA4 mutations and discordant ABCA4 alleles in patients and siblings with bull's-eye maculopathy. Br J Ophthalmol 2007;91:1650–1655.
19. Lewis RA, Shroyer NF, Singh N, et al. Genotype/phenotype analysis of a photoreceptor-specific ATP-binding cassette transporter gene, ABCR, in Stargardt disease. Am J Hum Genet 1999;64:422–434.

20. Webster AR, Heon E, Lotery AJ, et al. An analysis of allelic variation in the ABCA4 gene. Invest Ophthalmol Vis Sci 2001;42:1179–1189.
21. Allikmets R. Further evidence for an association of ABCR alleles with age-related macular degeneration. The International ABCR Screening Consortium. Am J Hum Genet 2000;67:487–491.
22. Guymer RH, Heon E, Lotery AJ, et al. Variation of codons 1961 and 2177 of the Stargardt disease gene is not associated with age-related macular degeneration. Arch Ophthalmol 2001;119:745–751.
23. Rivera A, White K, Stohr H, et al. A comprehensive survey of sequence variation in the ABCA4 (ABCR) gene in Stargardt disease and age-related macular degeneration. Am J Hum Genet 2000;67:800–813.
24. Ducroq D, Shalev S, Habib A, et al. Three different ABCA4 mutations in the same large family with several consanguineous loops affected with autosomal recessive cone-rod dystrophy. Eur J Hum Genet 2006;14: 1269–1273.
25. Rudolph G, Kalpadakis P, Haritoglou C, et al. Mutations in the ABCA4 gene in a family with Stargardt's disease and retinitis pigmentosa (STGD1/RP19). Klin Monbl Augenheilkd 2002;219:590–596.
26. Maugeri A, van Driel MA, van de Pol DJ, et al. The 2588G–>C mutation in the ABCR gene is a mild frequent founder mutation in the Western European population and allows the classification of ABCR mutations in patients with Stargardt disease. Am J Hum Genet 1999;64:1024–1035.
27. Cella W, Greenstein VC, Zernant-Rajang J, et al. G1961E mutant allele in the Stargardt disease gene ABCA4 causes bull's eye maculopathy. Exp Eye Res 2009;89:16–24.
28. Chen Y, Ratnam K, Sundquist SM, et al. Cone photoreceptor abnormalities correlate with vision loss in patients with Stargardt disease. Invest Ophthalmol Vis Sci 2011;52: 3281–3292.
29. Chen Y, Roorda A, Duncan JL. Advances in imaging of Stargardt disease. Adv Exp Med Biol 2010;664:333–340.
30. Lois N, Halfyard AS, Bird AC, et al. Fundus autofluorescence in Stargardt macular dystrophy-fundus flavimaculatus. Am J Ophthalmol 2004;138:55–63.
31. Sparrow JR, Boulton M. RPE lipofuscin and its role in retinal pathobiology. Exp Eye Res 2005;80:595–606.
32. Brunk UT, Terman A. Lipofuscin: mechanisms of age-related accumulation and influence on cell function. Free Radic Biol Med 2002;33:611–619.
33. Ng KP, Gugiu B, Renganathan K, et al. Retinal pigment epithelium lipofuscin proteomics. Mol Cell Proteomics 2008;7:1397–1405.
34. Katz ML, Redmond TM. Effect of Rpe65 knockout on accumulation of lipofuscin fluorophores in the retinal pigment epithelium. Invest Ophthalmol Vis Sci 2001;42: 3023–3030.
35. Sieving PA, Chaudhry P, Kondo M, et al. Inhibition of the visual cycle in vivo by 13-cis retinoic acid protects from light damage and provides a mechanism for night blindness in isotretinoin therapy. Proc Natl Acad Sci USA 2001; 98:1835–1840.
36. Radu RA, Han Y, Bui TV, et al. Reductions in serum vitamin A arrest accumulation of toxic retinal fluorophores: a potential therapy for treatment of lipofuscin-based retinal diseases. Invest Ophthalmol Vis Sci 2005;46: 4393–4401.
37. Radu RA, Mata NL, Nusinowitz S, et al. Treatment with isotretinoin inhibits lipofuscin accumulation in a mouse model of recessive Stargardt's macular degeneration. Proc Natl Acad Sci USA 2003;100:4742–4747.
38. Maiti P, Kong J, Kim SR, et al. Small molecule RPE65 antagonists limit the visual cycle and prevent lipofuscin formation. Biochemistry 2006;45:852–860.
39. Sun H, Smallwood PM, Nathans J. Biochemical defects in ABCR protein variants associated with human retinopathies. Nat Genet 2000;26:242–246.
40. Hong DH, Pawlyk BS, Shang J, et al. A retinitis pigmentosa GTPase regulator (RPGR)-deficient mouse model for X-linked retinitis pigmentosa (RP3). Proc Natl Acad Sci USA 2000;97:3649–3654.
41. Bonilha VL, Trzupek KM, Li Y, et al. Choroideremia: analysis of the retina from a female symptomatic carrier. Ophthalmic Genet 2008;29:99–110.
42. Curcio CA, Allen KA, Sloan KR, et al. Distribution and morphology of human cone photoreceptors stained with anti-blue opsin. J Comp Neurol 1991;312:610–624.
43. Milam AH, Rose L, Cideciyan AV, et al. The nuclear receptor NR2E3 plays a role in human retinal photoreceptor differentiation and degeneration. Proc Natl Acad Sci USA 2002;99:473–478.
44. To KW, Adamian M, Jakobiec FA, et al. Histopathologic and immunohistochemical study of an autopsy eye with X-linked cone degeneration. Arch Ophthalmol 1998;116: 100–103.
45. Mata NL, Weng J, Travis GH. Biosynthesis of a major lipofuscin fluorophore in mice and humans with ABCR-mediated retinal and macular degeneration. Proc Natl Acad Sci USA 2000;97:7154–7159.
46. Weng J, Mata NL, Azarian SM, et al. Insights into the function of Rim protein in photoreceptors and etiology of Stargardt's disease from the phenotype in abcr knockout mice. Cell 1999;98:13–23.
47. van der Burght BW, Hansen M, Olsen J, et al. Early changes in gene expression induced by blue light irradiation of A2E-laden retinal pigment epithelial cells. Acta Ophthalmol 2013;91:e537–545.
48. De S, Sakmar TP. Interaction of A2E with model membranes. Implications to the pathogenesis of age-related macular degeneration. J Gen Physiol 2002;120:147–157.
49. Ma W, Coon S, Zhao L, et al. A2E accumulation influences retinal microglial activation and complement regulation. Neurobiol Aging 2013;34:943–960.
50. Wielgus AR, Chignell CF, Ceger P, et al. Comparison of A2E cytotoxicity and phototoxicity with all-trans-retinal in human retinal pigment epithelial cells. Photochem Photobiol 2010;86:781–791.
51. Maeda A, Maeda T, Golczak M, et al. Involvement of all-trans-retinal in acute light-induced retinopathy of mice. J Biol Chem 2009;284:15173–15183.
52. Travis GH, Golczak M, Moise AR, et al. Diseases caused by defects in the visual cycle: retinoids as potential therapeutic agents. Annu Rev Pharmacol Toxicol 2007;47: 469–512.
53. Park SP, Chang S, Allikmets R, et al. Disruption in Bruch membrane in patients with Stargardt disease. Ophthalmic Genet 2012;33:49–52.
54. Radu RA, Hu J, Yuan Q, Welch DL, et al. Complement system dysregulation and inflammation in the retinal pigment epithelium of a mouse model for Stargardt macular degeneration. J Biol Chem 2011;286:18593–18601.
55. Birnbach CD, Jarvelainen M, Possin DE, et al. Histopathology and immunocytochemistry of the neurosensory retina in fundus flavimaculatus. Ophthalmology 1994;101:1211–1219.

# DJ-1-Dependent Regulation of Oxidative Stress in the Retinal Pigment Epithelium (RPE)

**Karen G. Shadrach, Mary E. Rayborn, Joe G. Hollyfield, Vera L. Bonilha***

Department of Ophthalmic Research, The Cole Eye Institute, Cleveland Clinic Lerner College of Medicine, Cleveland, Ohio, United States of America

## Abstract

***Background:*** DJ-1 is found in many tissues, including the brain, where it has been extensively studied due to its association with Parkinson's disease. DJ-1 functions as a redox-sensitive molecular chaperone and transcription regulator that robustly protects cells from oxidative stress.

***Methodology:*** Retinal pigment epithelial (RPE) cultures were treated with $H_2O_2$ for various times followed by biochemical and immunohistological analysis. Cells were transfected with adenoviruses carrying the full-length human DJ-1 cDNA and a mutant construct, which has the cysteine residues at amino acid 46, 53 and 106 mutated to serine (C to S) prior to stress experiments. DJ-1 localization, levels of expression and reactive oxygen species (ROS) generation were also analyzed in cells expressing exogenous DJ-1 under baseline and oxidative stress conditions. The presence of DJ-1 and oxidized DJ-1 was evaluated in human RPE total lysates. The distribution of DJ-1 was assessed in AMD and non-AMD cryosectionss and in isolated human Bruch's membrane (BM)/choroid from AMD eyes.

***Principal Findings:*** DJ-1 in RPE cells under baseline conditions, displays a diffuse cytoplasmic and nuclear staining. After oxidative challenge, more DJ-1 was associated with mitochondria. Increasing concentrations of $H_2O_2$ resulted in a dose-dependent increase in DJ-1. Overexpression of DJ-1 but not the C to S mutant prior to exposure to oxidative stress led to significant decrease in the generation of ROS. DJ-1 and oxDJ-1 intensity of immunoreactivity was significantly higher in the RPE lysates from AMD eyes. More DJ-1 was localized to RPE cells from AMD donors with geographic atrophy and DJ-1 was also present in isolated human BM/choroid from AMD eyes.

***Conclusions/Significance:*** DJ-1 regulates RPE responses to oxidative stress. Most importantly, increased DJ-1 expression prior to oxidative stress leads to decreased generation of ROS, which will be relevant for future studies of AMD since oxidative stress is a known factor affecting this disease.

**Citation:** Shadrach KG, Rayborn ME, Hollyfield JG, Bonilha VL (2013) DJ-1-Dependent Regulation of Oxidative Stress in the Retinal Pigment Epithelium (RPE). PLoS ONE 8(7): e67983. doi:10.1371/journal.pone.0067983

**Editor:** Xianglin Shi, University of Kentucky, United States of America

**Received** March 18, 2013; **Accepted** May 23, 2013; **Published** July 2, 2013

**Funding:** Supported by NIH grants EY014240, Research Center Grants from The Foundation Fighting Blindness and Research to Prevent Blindness. The funders had no role in study design, data collection and analysis, decision to publish, or preparation of the manuscript.

**Competing Interests:** The authors have declared that no competing interests exist.

* Email: bonilhav@ccf.org

## Introduction

The retinal pigment epithelium (RPE) constitutes a monolayer of cuboidal cells. Its apical surface faces a very complex extracellular matrix called the interphotoreceptor matrix (IPM) that also surrounds the photoreceptor cells projecting from the outer retina. The RPE basal surface faces the underlying Bruch's membrane (BM) [1]. The RPE exhibit a number of highly specialized functions, including phagocytosis of shed tips of photoreceptor outer segments, directional transport of nutrients into and removal of waste products from photoreceptor cells, optimization of ion concentrations in the surrounding tissues, elimination of fluid from the IPM, and visual pigment regeneration and transport which, is essential to retinal homeostasis and vision.

The RPE cells live under chronic oxidative stress because of the lifelong exposure to light, high oxygen consumption and high oxygen partial pressure from the underlying choriocapillaris. In addition, phagocytosed shed photoreceptor outer segments are enriched in polyunsaturated fatty acids such as docosahexaenoate (DHA) and retinoids, which are highly susceptible to lipid peroxidation and fracgmentation leading to lipid peroxide–derived protein modifications [2,3]. Finally, phagocytosis itself increases oxidative stress resulting in the generation of endogenous reactive oxygen species (ROS) [4,5]. This hostile oxidative environment is thought to contribute to retinal disease. Indeed, it was suggested that oxidative stress affecting the physiological function and leading to focal loss of the RPE cells is a major factor contributing to geographic atrophy, and vision loss in the elderly blinding disease age-related macular degeneration (AMD) [6,7]. However, it remains to be determined why the initial retinal degeneration occurs and how degeneration processes progress as a result of continued oxidative insults.

Deletion or homozygous mutations of DJ-1 gene (*PARK7* locus) have been shown to cause early-onset autosomal recessive Parkinson's disease (PD) [8]. The DJ-1 gene encodes a highly conserved protein with 189 amino acids and a molecular weight of ~20 kDa. DJ-1 has been implicated in diverse cellular processes, including cellular transformation and tumorigenesis [9,10,11], transcriptional regulation [12,13,14,15], androgen receptor signaling [16], chaperone [17,18], spermatogenesis [19], and oxidative stress response [20,21,22].

Oxidative stress occurs when there is an imbalance between the biological processes that produce ROS and the protective mechanisms within cells that scavenge ROS. Several studies have demonstrated that DJ-1 robustly protects cells from oxidative stress through distinct cellular pathways [20,21,23,24,25,26,27,28,29]. DJ-1 can eliminate $H_2O_2$ by becoming oxidized itself and thus functioning as a scavenger of ROS [20,21,30,31]. It was also proposed that some of the protective actions of DJ-1 might occur at the transcriptional level [32]. DJ-1 binds to PIAS proteins, a family of SUMO-1 ligases that modulate the activity of various transcription factors [16]. Wild-type DJ-1 sequesters the death protein Daxx in the nucleus, preventing it from binding and activating its effector kinase, apoptosis signal-regulating kinase 1 (Ask1) in the cytoplasm [33]. Others showed that DJ-1 is a transcriptional co-activator that interacts with the nuclear proteins p54nrb and PSF [34] again to protect against apoptosis. DJ-1 also stabilizes the antioxidant transcriptional master regulator nuclear factor erythroid-2 related factor 2 (Nrf2) [15,35] by preventing association with its inhibitor protein Keap1. Therefore, DJ-1 may act as a transcriptional co-factor that regulates the response to oxidative stress. DJ-1 has also been reported to confer protection against endoplasmic reticulum (ER) stress, proteasomal inhibition, and toxicity induced by overexpression of Pael-R [36]. Recently reported data showed that the apparently pleiotropic roles of DJ-1 seem to be related to the single function of binding multiple mRNA transcripts with a GG/CC-rich sequence [37]. More recently it was shown that DJ-1 plays a role in maintenance of mitochondria structure by counteracting the mitochondrial impairment induced by the tumour suppressor protein p53 [38]. Moreover, overexpression of the gene encoding DJ-1 protects against oxidative injury whereas knocking down the expression by RNAi enhances susceptibility to oxidative stress [21,36,39,40,41,42,43]. Thus, DJ-1 may play a crucial role both sensing and conferring protection against a range of oxidative stressors, through multiple mechanisms.

Previously, we have identified DJ-1 peptides in both young and aged RPE lysates using a proteomic approach [44]. In this study, we describe DJ-1 expression, distribution and function in RPE cells under baseline conditions and following oxidative stress. We also analyze DJ-1 and oxDJ-1 levels in human RPE lysates from non-AMD and AMD donors. Finally, we describe DJ-1 distribution in the RPE from non-AMD and AMD donors with geographic atrophy, and in isolated human BM/choroid (with drusen) from AMD eyes. Adaptation to changes in oxidative environments is critical for the survival of retina and the RPE. Therefore, knowledge of the DJ-1 function in oxidative stress in the RPE will provide insight into biochemical processes that support and maintain vision in physiological and pathological conditions.

## Results

### DJ-1 Expression and Distribution in RPE Cell Cultures

Recently, we identified DJ-1 peptides in both young and aged RPE lysates using proteomic analysis [44]. To decipher the molecular mechanism of DJ-1 function we decided to use several previously characterized RPE cell cultures. One was the newly characterized B6-RPE07 mouse RPE cell line, capable of displaying a polarized phenotype when cultured in a serum free epithelial medium and plated on collagen-coated Transwells [45]. We also used two human RPE cell lines: ARPE-19 and D407. We also used mouse primary RPE cultures, which morphologically resemble RPE cells *in vivo* due to their elaboration of apical microvilli and basal infoldings on their surfaces [46]. The initial characterization of these four cell lines analyzed the expression of DJ-1 by Western analysis (Fig. 1A and B) and immunofluorescence (Fig. 1C to F). A major band of ~25 kDa was observed in the extracts of all the RPE cell lines (Fig. 1A, lanes 1 to 3) and mouse primary RPE (Fig. 1A, lane 5) when compared to extracts from mouse brain (Fig. 1A, lane 4). Immunoblots of RPE lysates obtained from all cell cultures demonstrated heterogeneity in the levels of expression of DJ-1 when compared to the expression of the loading control protein GAPDH (Fig. 1B). DJ-1 expression in mouse primary RPE lysates displayed the highest levels of expression of DJ-1 among the RPE cells tested (Fig. 1A, lane 5). Confocal microscopy *en face* examination of paraformaldehyde-fixed monolayers grown on polycarbonate filters revealed that under baseline conditions, DJ-1 displays a diffuse cytoplasmic and, in some cells, nuclear staining (Fig. 1C to F, arrows) in all the RPE cell lines analyzed. DJ-1 analysis in polarized RPE monolayers established that although each one of the RPE cell cultures have different levels of DJ-1, they all display similar subcellular distribution of DJ-1.

### DJ-1 Expression in RPE Cells Subjected to Oxidative Stress

To evaluate the role of oxidative stress on DJ-1 expression, RPE cultures were plated, incubated with $H_2O_2$ and the expression and distribution of DJ-1 was analyzed (Fig. 2). A representative Western is shown. A dose response relating DJ-1 expression in ARPE-19 (Fig. 2A, lanes 1 to 6) and D407 (Fig. 2A, lanes 7 to 12) is observed when cells are exposed to increasing concentrations of $H_2O_2$ for 1 hr. While exposure of ARPE-19 cells to $H_2O_2$ at 400 $\mu$M was sufficient to significantly enhance DJ-1 levels, a lower concentration (100 $\mu$M) was adequate to modulate DJ-1 levels in D407 cells. Quantitation of the intensity of immunoreactivity in blots from three independent experiments showed that DJ-1 increased 5.0 and 3.6 fold in ARPE-19 incubated with 400 and 600 $\mu$M $H_2O_2$ and up to 5.7 fold in D407 cells incubated with 200 $\mu$M $H_2O_2$ when compared with control cell RPE cultures (Fig. 2C). Similarly, both ARPE-19 (Fig. 2B, lanes 13 to 18) and D407 (Fig. 2b, lanes 19 to 24) also displayed a dose response when cells were exposed to increasing concentrations of $H_2O_2$ for 18 hrs. Quantitation of these blots showed that the intensity of DJ-1 immunoreactivity was 1.4, 1.3 and 1.8 fold higher in ARPE-19 incubated with 400 to 800 $\mu$M $H_2O_2$ and up to 1.6 fold greater in D407 cells incubated with 100 to 800 mM $H_2O_2$ when compared with control cell RPE cultures (Fig. 2D). Finally, ARPE-19 and D407 monolayers exposed to oxidative stress induced by incubation with increasing concentration of 4-hydroxynonenal (4-HNE), a lipid peroxidation product, for 12 (Figure S1) and 24 hrs (data not shown) also displayed increased DJ-1 immunoreactivity.

We also analyzed the distribution of DJ-1 in several RPE cell cultures plated on Transwell inserts non-incubated or incubated with 100 $\mu$M $H_2O_2$ overnight followed by immunofluorescence (Fig. 2E to J). Confocal microscopy *en face* examination of paraformaldehyde-fixed monolayers revealed a diffuse staining for DJ-1 consistent with a cytoplasmic localization in ARPE-19 (Fig. 2E), B6-RPE07 (Fig. 2G) and in mouse primary RPE (Fig. 2I) monolayers under baseline conditions. Oxidative stress induced by $H_2O_2$ leads to a visible increase in immunocytochemical staining for DJ-1 (Fig. 2F, H, J). In addition, to this visible increase in DJ-1 staining, an induced intracellular redistribution of DJ-1 to an aggregated, perinuclear localization was also observed (Fig. 2F, H, J). Our results suggested that DJ-1 immunoreactivity is increased and redistributed within RPE cells subjected to oxidative stress.

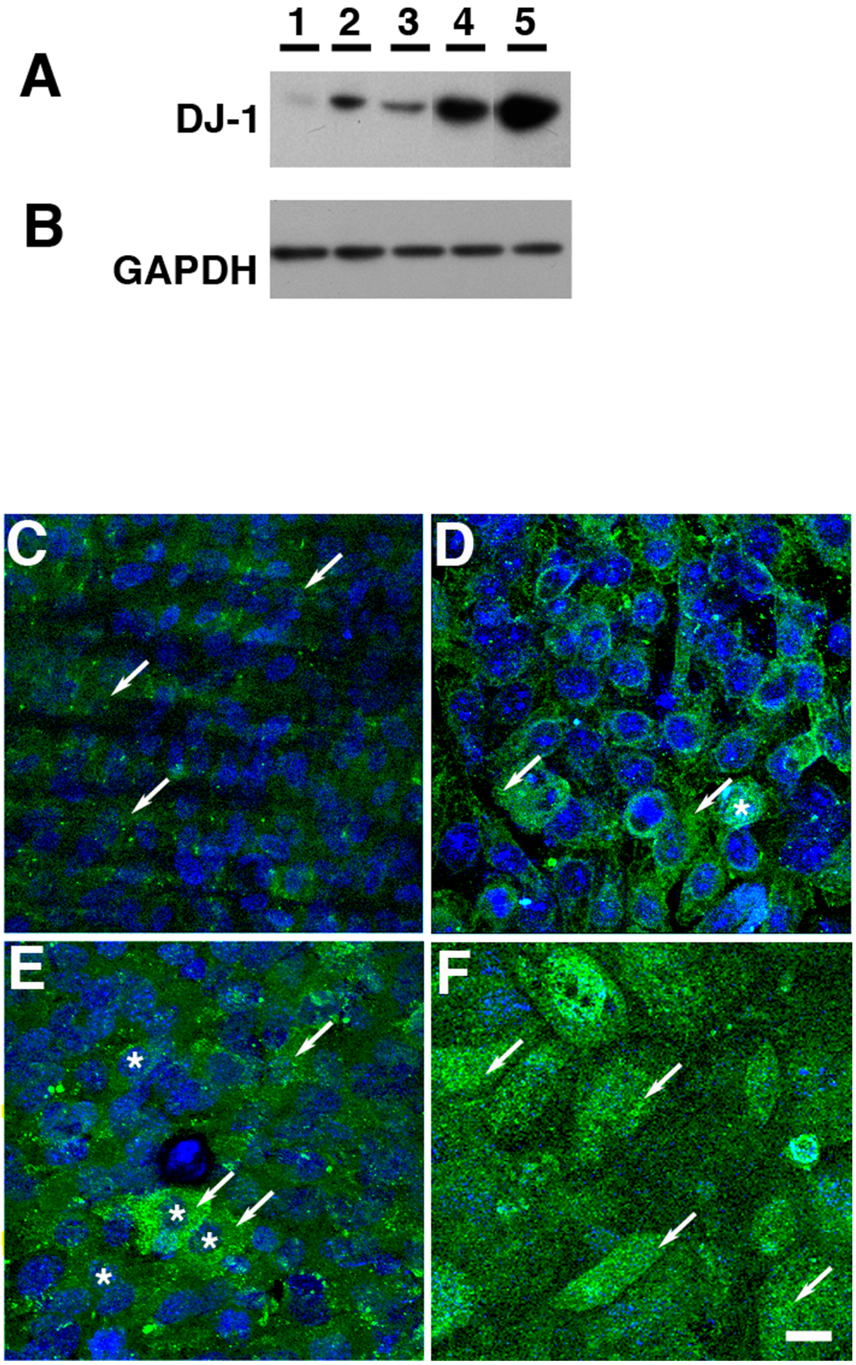

**Figure 1. DJ-1 is present in RPE cell cultures.** Lysates of the human RPE cell lines ARPE-19 (A, lane 1) and D407 (A, lane 2), the mouse RPE cell line B6-RPE07 (A, lane 3), mouse primary RPE (A, lane 4) and mouse brain lysates (A, lane 5) were harvested and analyzed by immunoblot assay with DJ-1 antibody. The DJ-1 signal varied in intensity in each RPE cell culture. Each lane contained 20 μg of protein. Protein loads were confirmed in replicate blots probed with GAPDH (B). Alternatively, monolayers of ARPE-19 (C), D407 (D), B6-RPE07 (E) and mouse primary RPE (F) were fixed with paraformaldehyde before extraction with Triton X-100 and labeling with DJ-1 antibodies. Cell nuclei were labeled with TO-PRO-3. DJ-1 labeling was diffusely distributed in the cytoplasm (arrows) and in the nuclei (*) of some of the cells (C-F, arrows). Scale bar = 20 μm.
doi:10.1371/journal.pone.0067983.g001

## DJ-1 Localization in RPE Cells Subjected to Oxidative Stress

Further experiments were carried out in several RPE cultures plated on Transwell inserts non-incubated or incubated with 100 μM $H_2O_2$ overnight followed by immunofluorescence to confirm the intracellular localization of DJ-1 upon oxidative injury (Fig. 3). Confocal microscopy *en face* examination of paraformaldehyde-fixed monolayers again revealed a diffuse staining for DJ-1 consistent with a cytoplasmic localization in mouse primary RPE (Fig. 3A) and in ARPE-19 (Fig. 2G) monolayers. Monolayers were also labeled with antibodies specific to the mitochondrial marker OxPhos Complex IV subunit I (COX IV, Fig. 3B, E, H, K). Under baseline conditions, both RPE monolayers displayed no

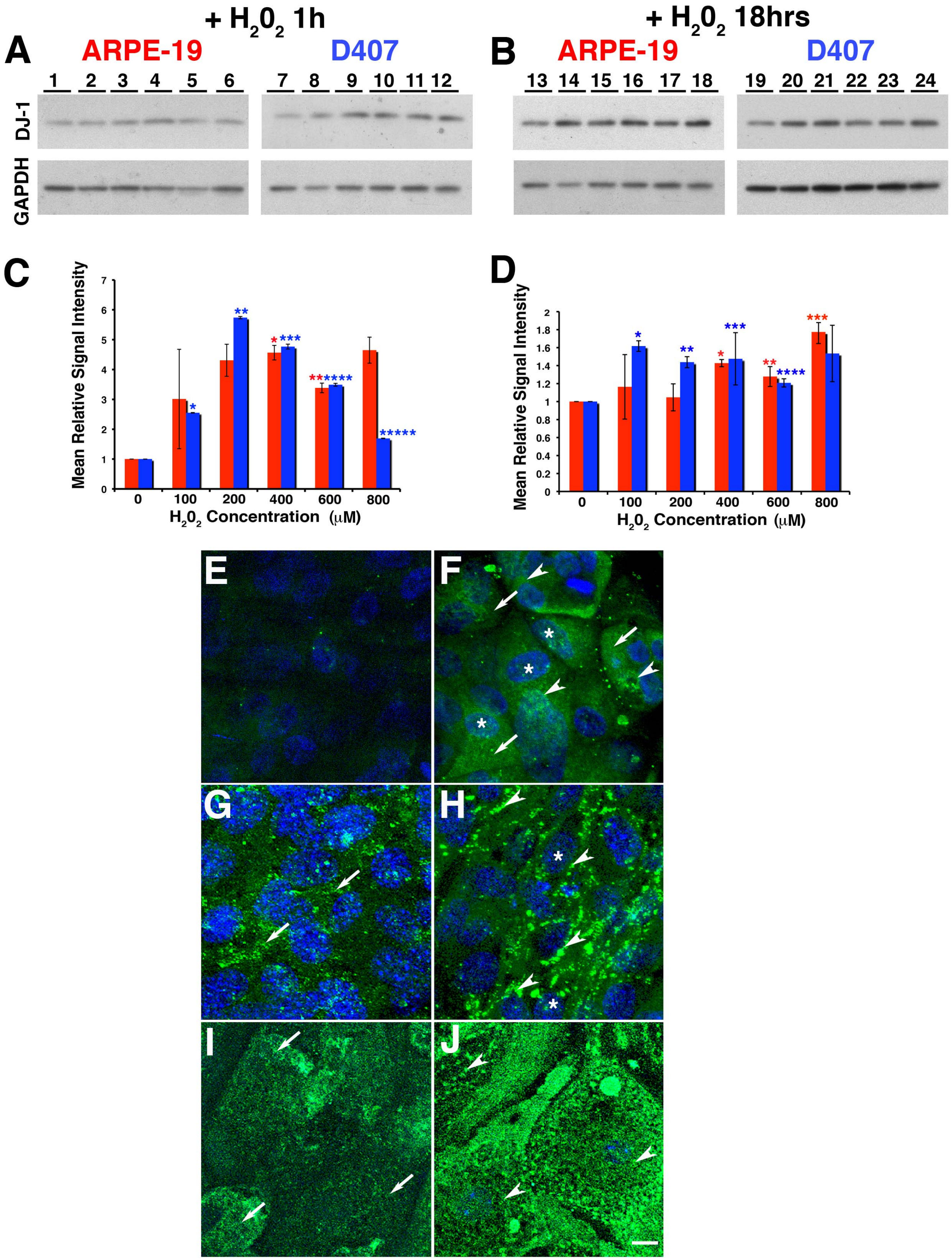
+ $H_2O_2$ 1h
A
ARPE-19
D407
1 2 3 4 5 6
7 8 9 10 11 12
DJ-1
GAPDH
+ $H_2O_2$ 18hrs
B
ARPE-19
D407
13 14 15 16 17 18
19 20 21 22 23 24
C
Mean Relative Signal Intensity
0 1 2 3 4 5 6 7
0 100 200 400 600 800
$H_2O_2$ Concentration (μM)
*
**
* ***
** ****
*****
D
Mean Relative Signal Intensity
0 0.2 0.4 0.6 0.8 1 1.2 1.4 1.6 1.8 2
0 100 200 400 600 800
$H_2O_2$ Concentration (μM)
*
**
* ***
** ****
***
E
F
G
H
I
J
*

**Figure 2. Oxidative stress induced by $H_2O_2$ increases DJ-1 levels and leads to intracellular redistribution of DJ-1 in RPE cells.** ARPE-19 and D407 monolayers were treated with increasing concentrations (0 to 800 μM) of $H_2O_2$ for 1 hr (A) and 18 hrs (B), harvested, and analyzed by immunoblot assay with DJ-1 antibody (upper panel). Each lane contained 20 μg of protein. Protein loadings were confirmed in replicate blots probed with GAPDH (lower panel). A representative Western is shown. A dose response of ARPE-19 (A, lanes 1 to 6) and D407 (A, lanes 7 to 12) is observed when cells are exposed to increasing concentrations of $H_2O_2$ for 1 hr. Quantitation of these blots showed that DJ-1 immunoreactivity was 5.0 and 3.6 fold higher in ARPE-19 incubated with 400 and 600 μM $H_2O_2$ and up to 5.7 fold higher in D407 cells incubated with 200 μM $H_2O_2$ when compared with control cell RPE cultures (C). Plotted signals represent the intensity for each band normalized to GAPDH signal and compared to the intensity of the control, untreated cells (lanes 1, 7, 13, 19). Red columns = ARPE-19; blue columns = D407 cells. Data is expressed as mean relative signal intensity ± SEM (n = 3). Asterisks denote statistical significance compared with control untreated cells (*p = 0.0160 and **p = 0.0145 in the ARPE-19 and *p<0.0001, **p<0.0001, ***p = 0.0005, ****p = 0.0004 and p***** = 0.0001 in D407 cells). Similarly, both ARPE-19 (Fig. B, lanes 13 to 18) and D407 (Fig. 2b, lanes 19 to 24) also displayed a dose response when cells were exposed to increasing concentrations of $H_2O_2$ for 18 hrs. Quantitation of these blots showed that DJ-1 immunoreactivity was 1.4, 1,3 and 1.8 fold higher in ARPE-19 incubated with 400 to 800 mM $H_2O_2$ and up to 1.6 fold higher in D407 cells incubated with 100 to 800 μM $H_2O_2$ when compared with control cell RPE cultures (D). Asterisks denote statistical significance compared with control untreated cells (*p = 0.0010, **p = 0.0146 and ***p = 0.0185 in the ARPE-19 and *p = 0.0005, **p = 0.0020, ***p = 0.0177 and ****p = 0.0103 in D407 cells). **E–J.** Confocal immunofluorescence staining of ARPE-19 (E, F), B6-RPE07 (G, H) and mouse primary RPE cultures (I, J) fixed before extraction with Triton X-100 and labeling with DJ-1 antibody. Cell nuclei were labeled with TO-PRO-3. Observations demonstrated that at baseline conditions, DJ-1 is diffused in the cytoplasm (arrows) and nuclei (*) of polarized RPE cells (E, G, I). With 18 hrs of exposure to 400 μM $H_2O_2$ (F, H, J), the diffused cytoplasmic DJ-1 staining disappears and pronounced aggregated perinucler staining (arrowheads) for DJ-1 is apparent. Scale bar = 10 μm.
doi:10.1371/journal.pone.0067983.g002

significant colocalization with the mitochondrial marker in overlaid images (Fig. 3C and I). Oxidative stress induced by $H_2O_2$ lead to a visible increase in immunocytochemical staining for DJ-1 (Fig. 3D and J). In addition, an intracellular redistribution of DJ-1 immunoreactivity leading to COX IV colocalization was also observed (Fig. 3F and L).

Additional experiments carried out in RPE cells plated on coverslips and incubated with the mitochondrial staining Mito-Tracker were also performed (Figure S2). B6-RPE07 monolayers were fixed and labeled for DJ-1 (Figure S2A and S2D) after loading with the mitochondrial staining MitoTracker (Figure S2B and S2E). Similar to results reported above with antibody labeling, DJ-1 showed little specific localization to mitochondria under baseline conditions (Figure S2A and S2C). However, treatment with $H_2O_2$ caused increased redistribution of DJ-1 to mitochondria as shown in the overlain images (Figure S2D and S2F, arrows). In addition, an increase in mitochondria labeling is also evident in the RPE cells subjected to oxidative stress. Together, our observations indicate that DJ-1 is redistributed to the mitochondria in RPE cells under oxidative stress.

## Detection of DJ-1 Oxidation at Cysteine 106 (oxDJ-1) in Cells Subjected to Oxidative Stress

DJ-1 has three cysteine (C) residues at amino acids 46, 53 and 106. C106 in DJ-1 is the first to become oxidized by the addition of cysteine sulfinic acid ($C\text{-}SO_2H$) and then C46 and C53 become oxidized upon oxidative stress, resulting in scavenging of reactive oxidative species (ROS) and enhancing DJ-1 association with mitochondria [23,47,48]. To check for alterations in DJ-1 oxidative stress, ARPE-19 cultures at baseline and under oxidative stress conditions were reacted with an antibody generated against a synthetic peptide containing $SO_3H$ at C106 of DJ-1 [49]. If RPE cells under stress generate DJ-1 oxidized at C106, it may be increased during this time. Immunoblots of lysates of ARPE-19 cells obtained from cultures subjected to oxidative stress induced by exposure to $H_2O_2$ for 1 hr (Fig. 4A) and 18 hrs (Fig. 4B) demonstrated a progressive increase in oxDJ-1 with a dose response increase in cultures under short-term oxidative tress (Fig. 4A). Interestingly, the oxDJ-1 detected mostly in cultures under oxidative stress, displayed a molecular weight ~110 kDa. We also tested ARPE-19 cultures for the expression of oxDJ-1 by immunofluorescence (Fig. 4C to E). Polarized monolayers plated on Transwells under baseline culture conditions failed to display labeling with the antibody to oxDJ-1 (Fig. 4C). However, several cells displayed staining with the antibody to oxDJ-1 when monolayers were incubated with $H_2O_2$ for 1 h (Fig. 4D) and 18 hrs (Fig. 4E). The large increase of oxDJ-1 content when RPE cultures were under oxidative stress suggests that this DJ-1 in RPE indeed undergoes oxidation under oxidative stress.

## Regulation and Distribution of DJ-1 Oxidation at C Residues in Cells Subjected to Oxidative Stress

The above data suggested that oxidation of DJ-1 C residues is correlated to the presence of oxidative stress. To further understand the function of DJ-1 oxidation RPE cultures were infected with adenoviruses carrying full-length human DJ-1 cDNA (hDJ-1 Ad) and a mutant construct, which has the C residues at amino acids 46, 53 and 106 mutated to serine (S), (C to S Ad) prior to stress experiments followed by evaluation of content and localization of DJ-1 in RPE cultures (Fig. 5). Immunoblots of lysates revealed that ARPE-19 cultures transduced with the hDJ-1 (Fig. 5A, lane 3) and with the C to S Ad constructs (Fig. 5, lane 2) displayed significant increased immunoreactivity of DJ-1 when compared to ARPE-19 control cultures (Fig. 5A, lane 1) and normalized to the levels of GAPDH (Fig. 5B) under baseline conditions. Quantification of these lysates demonstrated a 1.6 and 1.8 fold increase in the content of DJ-1 in ARPE-19 transduced with the C to S and hDJ-1 Ad, respectively (Fig. 5C), when comparing DJ-1 immunoreactivity to the one of ARPE-19 with normal levels of DJ-1. In addition, a significant increase in the immunoreactivity of DJ-1 was observed when ARPE-19 cultures were subjected to oxidative stress induced by $H_2O_2$ (Fig. 5A, $+H_2O_2$). Quantification of the immunoblots of these lysates demonstrated a 2.8, 1.4 and 4.8 fold increase in the immunoreactivity of DJ-1 in ARPE-19 cells and in ARPE-19 cells transduced with the C to S and hDJ-1 Ad, respectively (Fig. 5C), when comparing signal intensities to the one of ARPE-19 DJ-1 levels in baseline culture conditions.

To compare the distribution of endogenous and exogenous DJ-1 under baseline and oxidative stress conditions, ARPE-19 cells and ARPE-19 cells transducing exogenous DJ-1 were fixed and labeled for the distribution of DJ-1 and mitochondria (Fig. 5D to I). Double labeling cells on Transwells with antibodies to DJ-1 (green) and the mitochondria protein COX IV (red) showed little colocalization of DJ-1 with COX IV in control ARPE-19 cultures (Fig. 5D) and in ARPE-19 overexpressing full-length DJ-1 (Fig. 5E) and the C to S mutant DJ-1 (Fig. 5F) under baseline culture conditions. However, a significant colocalization of DJ-1 with COX IV could be observed in ARPE-19 cells (Fig. 5G and inset) and ARPE-19 cultures overexpressing full-length DJ-1 (Fig. 5H and inset) when incubated with $H_2O_2$. Opposing, ARPE-19 cultures overexpressing the C to S mutant DJ displayed no

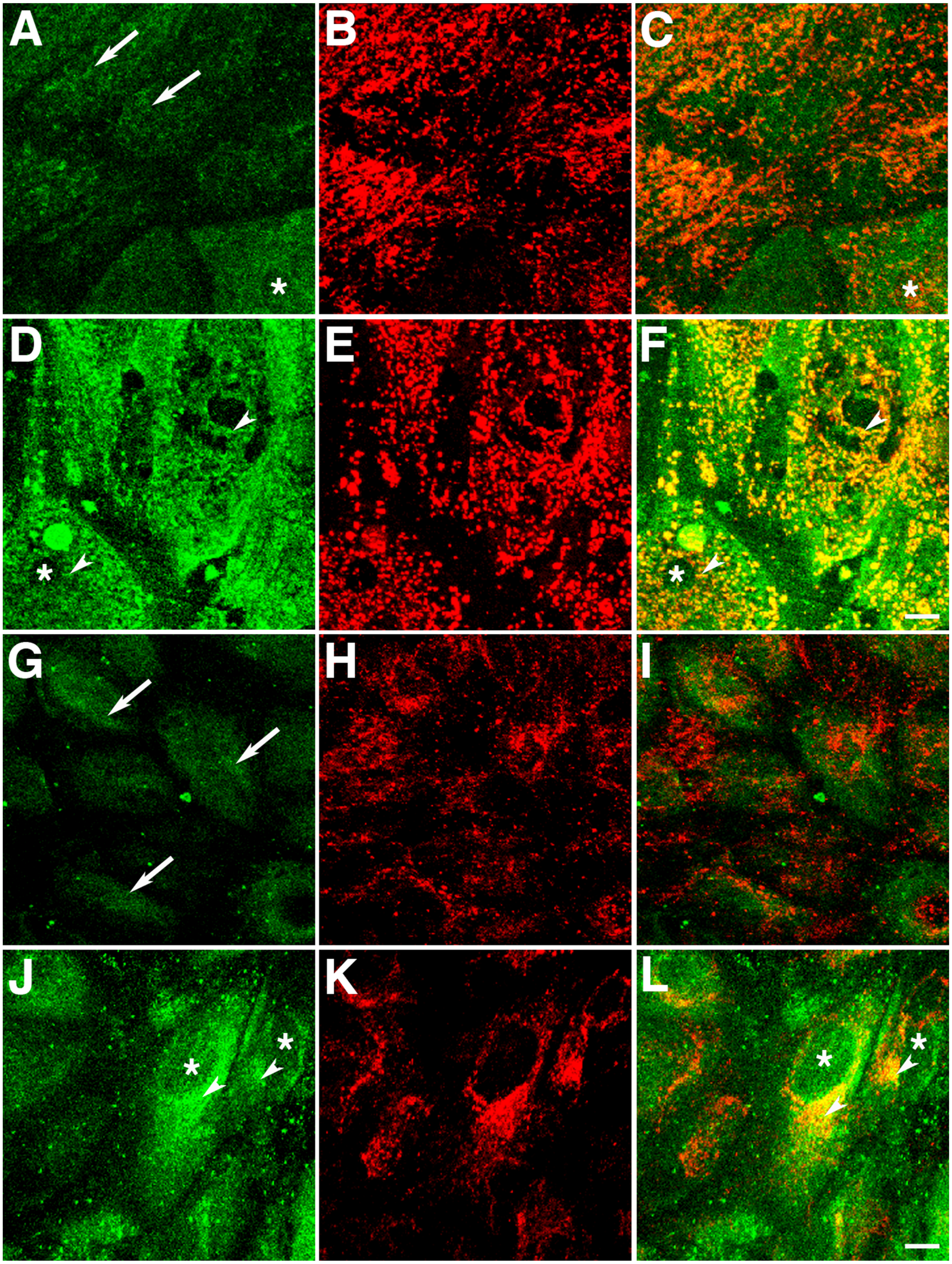

**Figure 3. Oxidative stress-dependent translocation of DJ-1 into mitochondria.** Representative confocal micrographs of mouse primary RPE (A–F) and ARPE-19 (G–L) monolayers plated on Transwells® and labeled with antibodies to DJ-1 (A, D, G, J) and COX IV (B, E, H, K). Under baseline conditions, there is very little colocalization between DJ-1 and COX IV, as observed in overlaid images (C, I) for both RPE cultures; DJ-1 is mostly distributed trough the cytoplasm (arrows) and to the nuclei (*) of some cells. Upon oxidative stress induced by incubation with 400 μM $H_2O_2$ for 1 hr, DJ-1 staining is increased both in the mouse primary (D) and ARPE-19 (J) cultures. In cultures treated with $H_2O_2$ some DJ-1 re-distributed to mitochondria (arrowheads) and displayed significant colocalization with COX IV in overlaid images (F, L). Scale bar = 10 μm.
doi:10.1371/journal.pone.0067983.g003

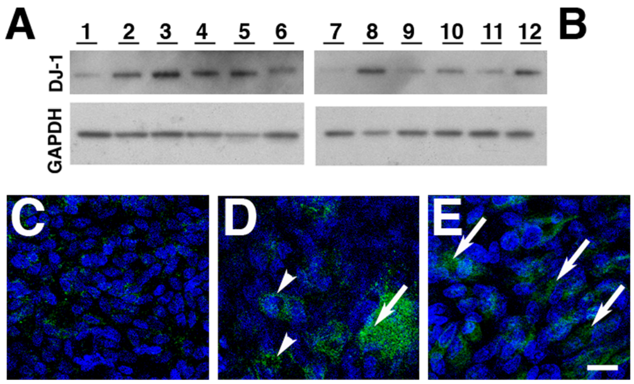

**Figure 4. Presence of oxDJ-1 in RPE cells subjected to oxidative stress.** ARPE-19 monolayers were treated with increasing concentrations (0 to 800 μM) of $H_2O_2$ for 1 hr (A) and 18 hs (B), harvested, and analyzed by immunoblot assay with oxDJ-1 antibody (upper panel). Protein loadings were confirmed in replicate blots probed with GAPDH (lower panel). Each lane contained 20 μg of protein. A dose response is observed when cells are exposed to increasing concentrations of $H_2O_2$ for 1 h (A, lanes 1 to 6) and 18 hrs (B, lanes 7 to 12). Confocal immunofluorescence staining of baseline ARPE-19 cultures (C) fixed before extraction with Triton X-100 and labeling with oxDJ-1 antibodies revealed absence of oxDJ-1. However, oxDJ-1 is observed in the cytoplasm (arrows) and perinuclear area (arrowheads) of RPE cells exposure to 400 μM $H_2O_2$ for 1 h (D) and 18 hrs (E). Cell nuclei were labeled with TO-PRO-3. Scale bar = 20 μm.
doi:10.1371/journal.pone.0067983.g004

colocalization between the distribution of DJ-1 and COX IV (Figure 5I and inset) under oxidative stress. Altogether, our results showed that DJ-1 C residues are important for their increased response and redistribution to the mitochondria in cells subjected to oxidative stress.

### Functional Role of DJ-1 C Oxidation in Cells Subjected to Oxidative Stress

To determine whether DJ-1 oxidation at its C residues could protect RPE cells against oxidative stress, we subjected ARPE-19 cells and ARPE-19 cells overexpressing full-length and C to S mutant DJ-1 to oxidative stress induced by $H_2O_2$ and labeling of ROS generation through to incubation with CM-$H_2$DCFDA (Fig. 6). No ROS were observed in ARPE-19 cells under normal culture conditions (Fig. 6A). However, significant intracellular ROS generation was observed when ARPE-19 (Fig. 6B) and ARPE-19 monolayers overexpressing the C to S mutant DJ-1 (Fig. 6C) were subjected to oxidative stress. Strikingly, no ROS was generated when ARPE-19 monolayers were overexpressing the full length DJ-1 (Fig. 6D). An inverse dose response of ARPE-19 monolayers overexpressing full length DJ-1 was observed when cells were infected with decreasing concentrations of hDJ-1 adenovirus (Fig. 6E and F), suggesting a gene-dosage effect. These results suggested that DJ-1 C oxidation is necessary for DJ-1 to protect RPE cells under oxidative stress from the intracellular generation of ROS.

### Detection of DJ-1 in Human RPE Cells Isolated from the Eyes from AMD and non-AMD Donors

To better understand the significance of our RPE culture findings, DJ-1 presence in RPE lysates isolated from human donor eyes was carried out. DJ-1 presence was also probed in RPE cells isolated from donors with AMD, a blinding disease affecting the elderly, with an established contribution of oxidative stress to the pathogenesis of the disease (Fig. 7). DJ-1 was detected and highly expressed in the RPE lysates from AMD donors (Fig. 7A, lanes 6 to 10) when compared to the RPE lysates from non-AMD donors (Fig. 7A, lanes 1 to 5). DJ-1 immunoreactivity was normalized to the GAPDH content of the samples (Fig. 7C). Quantitation of these blots showed that DJ-1 immunoreactivity was increased ~2.5 fold in RPE isolated from AMD donors when compared with RPE isolated from non-AMD donors (Fig. 7D).

Our *in vitro* data showed that DJ-1 is oxidized at C106 when the cells are exposed to oxidative stress. To check if oxDJ-1 is present in RPE cells *in vivo*, RPE lysates from AMD and non-AMD donors were probed for this modification with a specific antibody (Fig. 7B). oxDJ-1 was present in the RPE lysates from AMD donors at higher levels (Fig. 7B, lanes 6 to 10) when compared to the RPE lysates from non-AMD donors (Fig. 7B, lanes 1 to 5). DJ-1 immunoreactivity was normalized to the GAPDH content of the samples (Fig. 7C). Quantitation of these blots showed that oxDJ-1 immunoreactivity was ~6 fold higher in RPE isolated from AMD donors when compared with RPE isolated from non-AMD donors (Fig. 7D).

We next immunohistologically examined the location of DJ-1 in RPE from non-AMD and AMD donor eyes with geographic atrophy (Fig. 7E to L) and isolated BM/choroid from the perimacula of AMD donors (Fig. 7M to P). Immunostaining of DJ-1 was detected mostly in the RPE nuclei (arrowheads) but also in the cytoplasm of non-AMD donors (Fig. 7F and H, arrows). Significantly more DJ-1 was detected through out the cytoplasm of RPE cells from two different AMD donors wit geographic atrophy (Fig. 7J and L, arrows). Interestingly, DJ-1 presence in RPE cells became less intense at distances away from the region of RPE atrophy (Figure S3). In addition, in BM/choroid isolated from two different AMD donors and drusen (insoluble aggregates localized underneath the RPE embodying the hallmark lesions of the disease, asterisks), in these samples were also specifically labeled with the DJ-1 antibody (Fig. 7N and P). In contrast, no significant DJ-1 labeling was observed when sections were reacted with the DJ-1 antibody, pre-absorbed with lysates from cells overexpressing exogenous DJ-1 (Fig. 7E, 7G, 7I, 7K, 7M and 7O). Our results showed that higher levels of DJ-1 and oxDJ-1 are present in RPE cells from AMD donors. In addition, we also reported that DJ-1 is also present in the hallmark lesion of this disease.

## Discussion

Previous reports showed that DJ-1 is ubiquitously expressed in numerous tissues including the pancreas, kidney, skeletal muscle, liver, placenta, heart and brain, with high expression in astrocytes of the frontal cortex and substantia nigra [9]. We recently reported the identification of DJ-1 peptides in both young and aged RPE lysates using proteomics together with confirmation of the localization of DJ-1 in RPE cells in rat retinas using immunohistochemistry [44]. Here, we described DJ-1 increased expression and redistribution to mitochondria of RPE cells under oxidative stress. In addition, we report that overexpression of full-length DJ-1, prior to exposure to oxidative stress, led to significant decrease in the generation of ROS. Most importantly, increased DJ-1 and oxDJ-1 were detected by Western blot in human RPE lysates from AMD donors. Finally, immunohistology detected DJ-1in isolated human BM/choroid and in drusen from AMD eyes.

Results reported here in RPE cultures under baseline and oxidative stress conditions are in agreement with previous reporting of the subcellular distribution of DJ-1. At the subcellular level, under baseline conditions, DJ-1 is found mostly in the cytoplasm [32] and to a lesser extent in the mitochondria [23] and

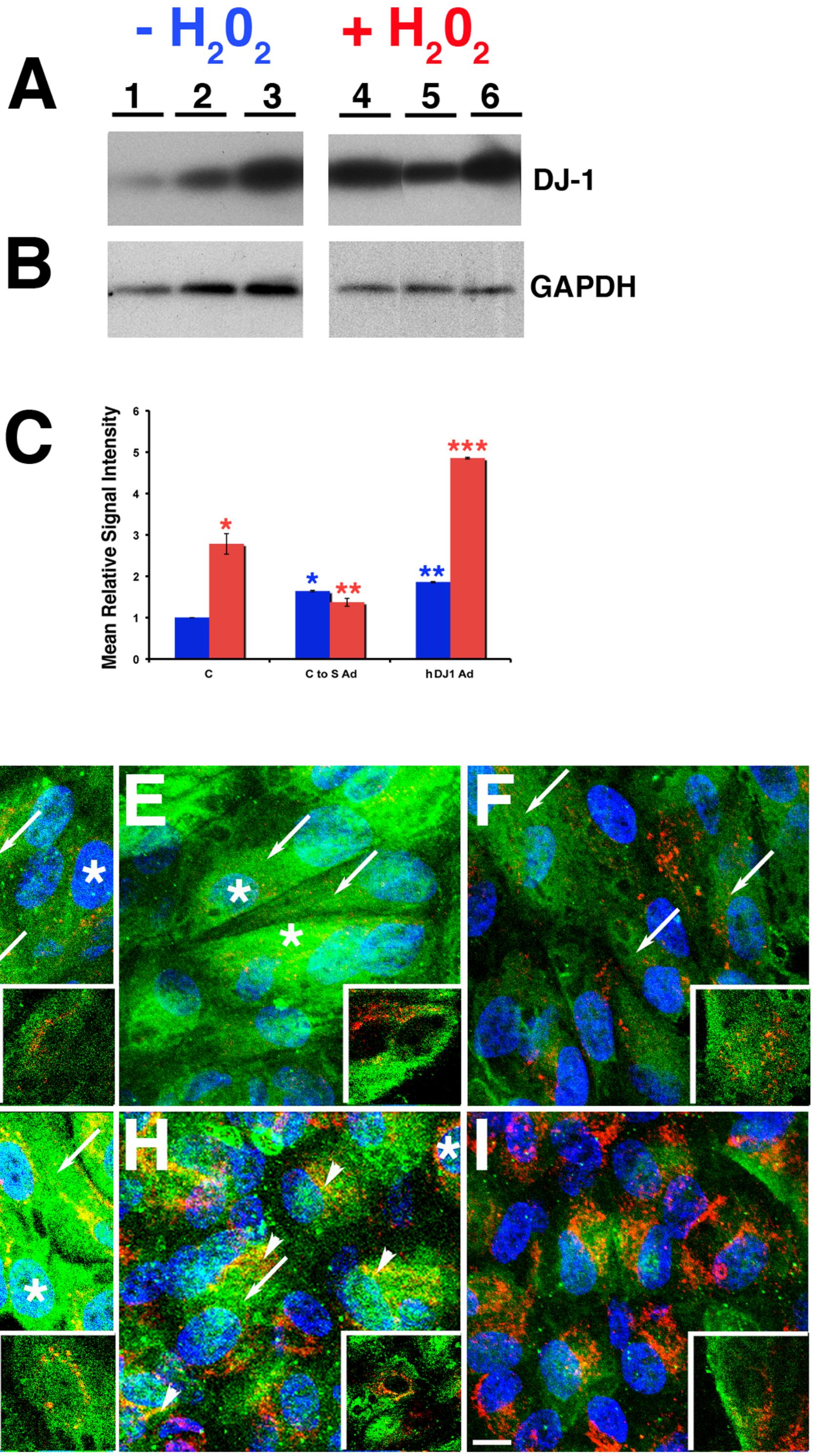

**Figure 5. Overexpression of DJ-1 full-length lead to increased levels and redistribution in RPE cells upon oxidative stress.** ARPE-19 monolayers were transduced with high titer ($5\times10^6$ pfu) adenovirus carrying full length human DJ-1 (hDJ-1 Ad) or adenovirus carrying DJ-1 C to S mutant (C to S Ad). Forty-eight hours later cultures were treated (A, lanes 4 to 6) or not (A, lanes 1 to 3) with 400 µM $H_2O_2$, harvested, and analyzed by immunoblot assay with DJ-1 antibody (A). Each lane contained 20 µg of protein. Protein loads were confirmed in replicate blots probed with GAPDH (B). Immunoblots of lysates revealed that ARPE-19 cultures transduced with the hDJ-1 (A, lane 3) and with the C to S Ad constructs (A, lane 2) displayed significant increased immunoreactivity of DJ-1 when compared to ARPE-19 control cultures (A, lane 1) under baseline conditions. Quantification of immunoblots of these cultures demonstrated a 1.6 and 1.8 fold increase in the expression levels of DJ-1 in ARPE-19 transduced with the C to S and hDJ-1 Ad, respectively (C, blue columns). Blue columns = baseline ARPE-19 cultures; Red columns = ARPE-19 incubated with 400 µM $H_2O_2$ for 1 hr. Data expressed as mean relative signal intensity ± SEM (n = 3). Asterisks denote statistical significance compared with control ARPE-19 untreated cells (*$p = 0.0007$ in ARPE-19 transduced with C to S Ad and **$p < 0.0001$ ARPE-19 transduced with hDJ-1 Ad). In addition, a significant increase in the immunoreactivity of DJ-1 was observed when ARPE-19 cultures (A, lane 4) and ARPE-19 overexpressing the hDJ-1 Ad were subjected

to oxidative stress (A, lane 6). Quantification of the immunoblots of these lysates demonstrated a 2.8, 1.4 and 4.8 fold increase in the immunoreactivity of DJ-1 in ARPE-19 cells and in ARPE-19 cells transduced with the C to S and hDJ-1 Ad, respectively (C, red columns), when comparing signal intensities to the one of ARPE-19 not overexpressing exogenous DJ-1 in baseline culture conditions. These differences were statistically significant (*p = 0.0020 in the ARPE-19, **p = 0.0177 in ARPE-19 transduced with C to S Ad and ***p<0.0001 ARPE-19 transduced with hDJ-1 Ad). **D–I:** Confocal microscopy of ARPE-19 monolayers fixed, permeabilized with a buffer containing Triton X-100, and processed for indirect immunofluorescence with DJ-1 (green) and COX IV (red) antibodies. Cell nuclei were labeled with TO-PRO-3. Under baseline conditions there is very little colocalization between DJ-1 and COX IV in control ARPE-19 (D) and in ARPE-19 transduced with hDJ-1 Ad (E) and C to S Ad (F); DJ-1 is distributed in the cytoplasm (arrows) and nuclei (*) of cells. Upon oxidative stress induced by incubation with 400 μM $H_2O_2$ for 1 h, DJ-1 staining redistributed intracellularly to mitochondria (arrowheads) and colocalized with COX IV both in ARPE-19 (G) and ARPE-19 transduced with hDJ-1 Ad (H) but not in ARPE-19 cultures transduced with the C to S Ad (I). Insets: close up images of the DJ-1 and COX IV labeling. Scale bar = 10 μm.
doi:10.1371/journal.pone.0067983.g005

nucleus [50]. Under conditions of oxidative stress, more DJ-1 redistributes to mitochondria and later to the nucleus, and this correlates with the ability of DJ-1 to confer neuroprotection [23].

Our results reporting increased levels of DJ-1 in RPE cells subjected to oxidative stress induced by incubation with $H_2O_2$ and 4-HNE suggest that DJ-1 functions as a sensor of cellular redox homeostasis, which reacts to oxidative stress by increasing DJ-1 content. Similar data was previously reported when experiments were carried out in other cell types under oxidative stress induced by several agents [30,51,52,53,54,55,56,57].

DJ-1 has three C at amino acid numbers 53, 46 and 106, which can become oxidized upon oxidative stress and oxidation of C106 (oxDJ-1) is essential for DJ-1 to exert its full activities. In the present study we report the presence of oxDJ-1 in RPE cells in response to oxidative stress using antibodies that specifically recognize DJ-1 oxidized at C106 (oxDJ-1). Similar results have also been previously reported in other cells types and PD animal models [18,47,58,59,60]. DJ-1 has four Met (M) residues, which are also susceptible to oxidation in addition to the three C residues already cited. The oxidation of the M to the sulfoxide (1 O), and C to the sulfenic acid (1 O), sulfinic acid (2 Os) or sulfonic acid (3 Os) is expected to lead to increases in the number of O atoms in the protein ranging from four, if all four M residues are oxidized, and nine if all three C residues are fully oxidized, for a potential total of 13 additional oxygen atoms [18]. Interestingly, the molecular weight of the protein detected in RPE cells incubated with $H_2O_2$ displayed a higher molecular weight than the reported DJ-1 molecular weight (~25 kDa). The meaning of this observation is not fully known but it may be related to the generation of several DJ-1 isoforms resulting from the oxidation of the M and C residues [18,54,61].

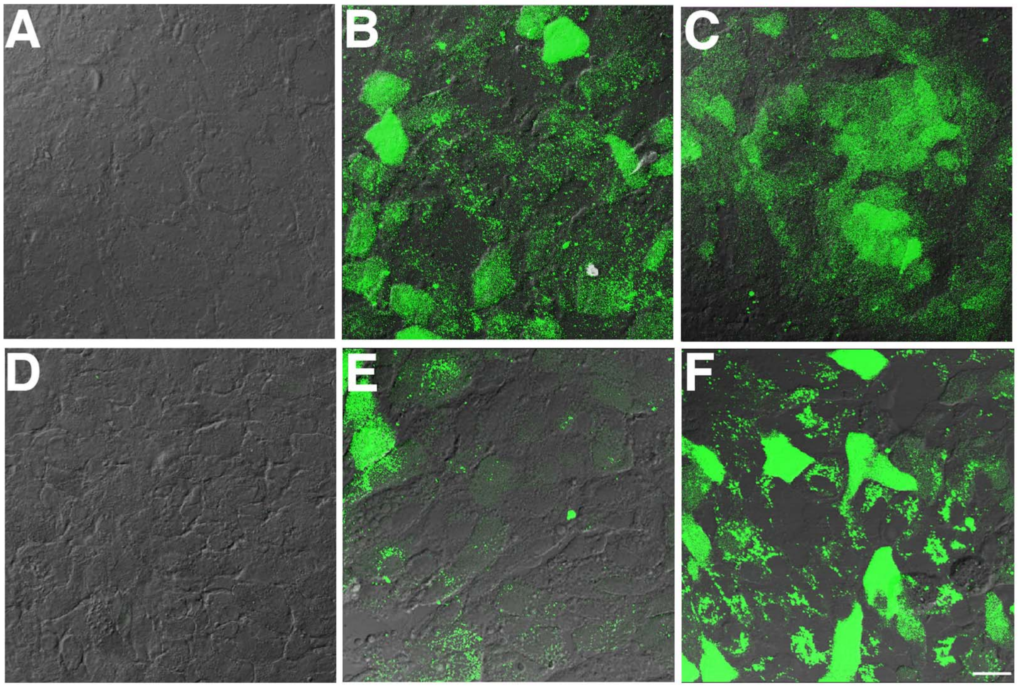

**Figure 6. Overexpression of DJ-1 full length prior to oxidative stress leads to decreased levels of $H_2O_2$-induced ROS generation by RPE cells.** ARPE-19 control cultures (A, B) and ARPE-19 transduced with adenovirus carrying full length human DJ-1 (hDJ-1 Ad) or adenovirus carrying DJ-1 C to S mutant (C to S Ad). Forty-eight hours following infection with adenovirus, cultures were treated with 800 μM $H_2O_2$ for 1 h followed by incubation with CM-$H_2$DCFDA and the fluorescence intensity of oxidized DCF (green) was then visualized by confocal microscopy. Cellular images were obtained by difference interference contrast (DIC) and overlaid on the fluorescence image of generated ROS. Images indicated that no ROS generation is observed in RPE cells at basal conditions (A) while upon oxidative stress incubation, appreciable ROS generation throughout the entire cell body of cells is observed (B). RPE cultures transduced with the high titer ($5\times10^6$ pfu) of the C to S Ad displayed appreciable ROS generation when cells were exposed to oxidative stress (C). Markedly, RPE cultures transduced with the high titer of the hDJ-1 Ad ($5\times10^6$ pfu) did not display ROS generation when exposed to oxidative stress (D). However, ROS generation was increasingly observed when RPE cultures were infected with increasing dilutions of hDJ-1 Ad, such as $4\times10^6$ pfu (E) and $3\times10^6$ pfu (F). Scale bar = 20 μm.
doi:10.1371/journal.pone.0067983.g006

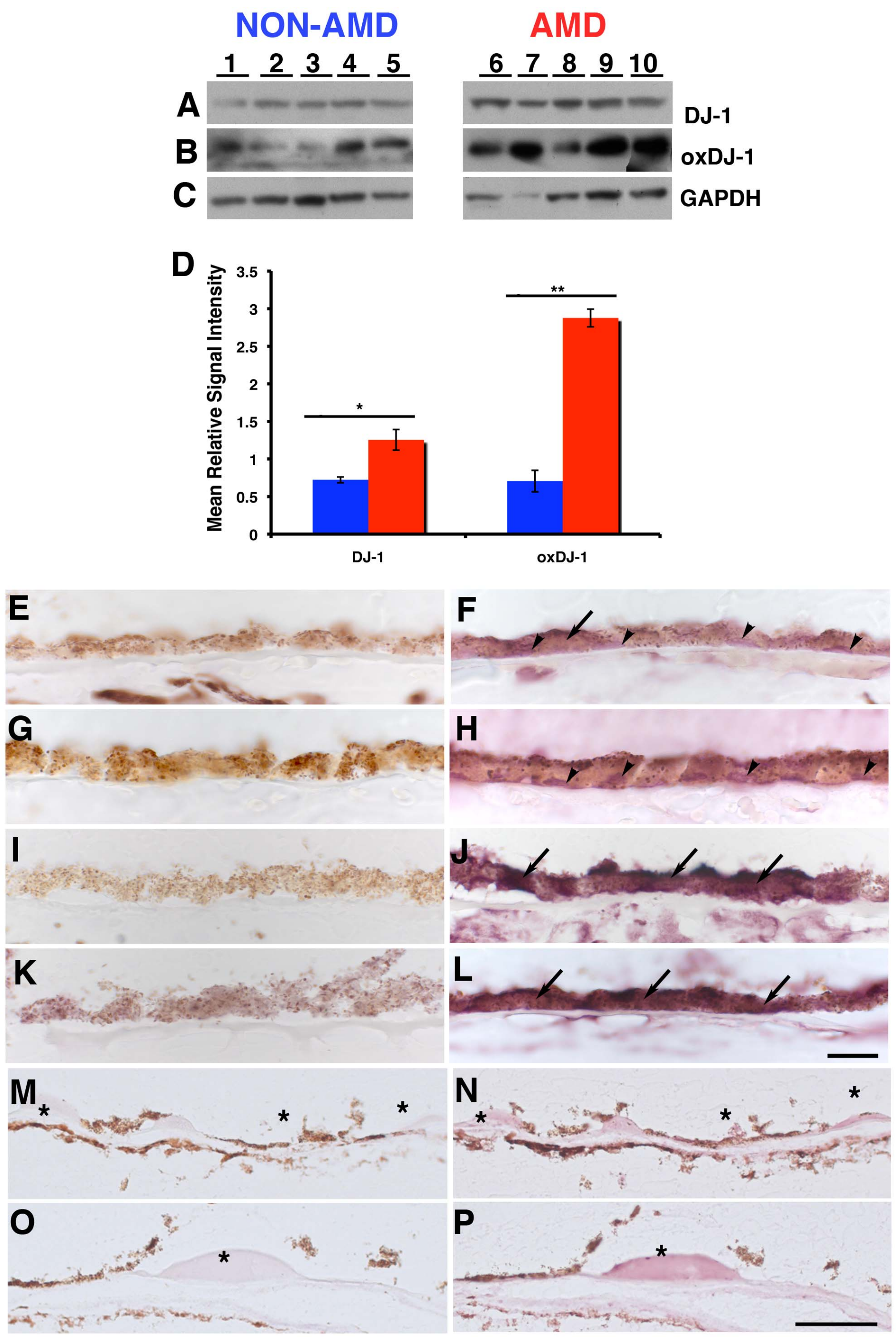

**Figure 7. Increased levels of DJ-1 and oxDJ-1 in RPE lysates and tissue from AMD donors.** Lysates of human RPE isolated from non-AMD (A to C lanes 1 to 5) and AMD donors (A to C, lanes 6 to 10) were harvested and analyzed by immunoblot assay with DJ-1 antibody (A) and oxDJ-1 antibody (B). Each lane contained 20 µg of protein. Protein loads were confirmed in replicate blots probed with GAPDH (C). Immunoblots of lysates revealed that AMD RPE displayed significant increased immunoreactivity of both DJ-1 (A) and oxDJ-1 (B) when compared to non-AMD RPE lysates. Quantification of immunoblots demonstrated a 1.7 and 4 fold increase in the expression levels of DJ-1 and oxDJ-1, respectively (D). Blue columns = non-AMD; Red columns = AMD. Data is expressed as mean relative signal intensity ± SEM (n = 8). Asterisks denote statistical significance compared with non-AMD RPE (*p = p = 0.0098 for DJ-1 and **p = 0.0058 for oxDJ-1). Alternatively, cryosections of different non-AMD (E–H) and AMD (I to L) donors with geographic atrophy, and isolated Bruch's membrane (BM) and choroid from two different AMD donors were (M to P) labeled with DJ-1 antibody. Negative control sections were reacted with DJ-1 antibody pre-absorbed with lysates of cells overexpressing DJ-1 and shoed no DJ-1 labeling (E, G, I, K, M, O). DJ-1 labeling was detected mostly in the RPE nuclei (arrowheads) but also in the cytoplasm of non-AMD donors (F and H, arrows). Significantly more DJ-1 was detected all over the cytoplasm of RPE cells from two different AMD donors (J and L, arrows), while DJ-1 was diffusely distributed in isolated BM and in drusen (E, G, asterisks). Scale bars (E to L) = 10 µm; (M to P) = 50 µm.
doi:10.1371/journal.pone.0067983.g007

The importance of DJ-1 C oxidation is also highlighted in RPE cells overexpressing C to S DJ-1 mutant that are exposed to oxidative stress, which are unable to increase DJ-1 levels and redistribute DJ-1 intracellularly to mitochondria. Our results, together with previous reports, suggests that DJ-1 C oxidation is important for protein stabilization [61,62,63,64] and mitochondria localization [23,52,65].

We demonstrated that overexpression of full-length but not the C to S mutant DJ-1 lead to significant decrease in the generation of intracellular ROS. The data suggests DJ-1 C oxidation – dependent elimination of ROS in cells under oxidative stress. Similar findings have been reported [52,57,66,67,68,69].

We demonstrate here for the first time that DJ-1 levels are increased in RPE lysates from AMD donors and that DJ-1 immunolocalization in RPE is also increased in AMD donors displaying geographic atrophy. AMD is a multi-factorial disease with known established risk factors including age, cigarette smoking, family history, gender, high blood pressure, high fat diet and race [70,71,72]. However, our understanding of the detailed molecular mechanisms of the development of AMD still remains limited, and to date, there is no proficient cure or preventive treatment. Oxidative stress affecting the physiological function and leading to the death of the RPE cells is a major factor contributing to the pathogenesis of AMD [6,7]. Therefore, limiting RPE oxidative stress may represent an effective way to slow or possibly reverse vision loss of patients due to diseases such as AMD. Indeed, several *in vitro* studies have shown that oxidative stress-related RPE cell death and dysfunction was improved when the cells were treated with antioxidants [73,74,75,76]. Furthermore, a significant reduction toward retinal degeneration was reported in clinical trials involving AMD patients ingesting antioxidants such as lutein, zeaxanthin, zinc, vitamin C, and vitamin E [77,78]. It is likely that the increased levels of DJ-1 in RPE lysates from AMD donors is related to increased oxidative stress in these RPE cells *in vivo*. Increased levels of DJ-1 were also reported in the brains of PD and Alzheimer's disease (AD) patients [27].

The increased presence of oxDJ-1 was reported in corneal buttons from Fuchs endothelial corneal dystrophy patients [56]. In addition, the presence of several oxidized DJ-1 isoforms have been found in patients with PD [79] and in patients with AD [27]. These data suggest that the DJ-1 oxidation status modulates its functions and that deregulation of DJ-1 oxidation may lead to the onset of diseases such as AMD [48]. In the present study we detected the increased presence of oxDJ-1 in RPE lysates from AMD donors using an antibody that detects oxidation at C106. Future experiments will be required to fully understand the significance of our finding.

A high number of mitochondria are present in the RPE due to its high metabolic activity [80]. During oxidative phosphorylation, the mitochondria produce the majority of the cellular energy in the form of ATP and also generate ROS as well [81,82]. A vicious circle of destruction takes place when ROS, including those produced in mitochondria by the electron transport chain, are generated leading to the preferred damage of mitochondrial genome (mtDNA). In turn, damaged mtDNA induces mitochondrial dysfunction with disturbance of oxidative phosphorylation and even higher production of ROS [2,83]. Therefore, it is not surprising that mitochondrial dysfunctions leading to increased ROS generation and mtDNA damage and specific hapogroups have been implicated in the pathophysiology of AMD [84,85,86,87,88,89,90,91,92]. We have shown here that an increased association of DJ-1 with mitochondria is observed in cells under oxidative stress. Therefore, it is likely that DJ-1 is "over-oxidized" in RPE cells from AMD patients failing to associate with the mitochondria and protect RPE cells from oxidative stress. Further experiments should concentrate on the analysis of DJ-1 intracellular distribution and oxidative isoforms in AMD and non-AMD RPE.

We reported here that DJ-1 was detected in Bruch's membrane and drusen isolated from two different AMD donors raising the question of how a cytoplasmic protein could be detected extracellularly. Previously, we [93,94] and other groups [95,96,97,98] reported that many of proteins found in drusen are normally found intracellularly in the RPE. These results suggest that RPE cells from AMD donors release intracellular proteins along their basal surface through a yet unknown mechanism where they become concentrated in drusen. DJ-1 is an intracellular protein. However, recently DJ-1 has emerged as a significant biomarker since its presence has been detected in the serum of gastric cancer [99], prostate carcinomas [100], pancreatic cancer [101], non-small cell lung cancer [102] and uveal melanoma [103] patients. Similarly, higher DJ-1 levels have been noted in nipple secretions from breast carcinoma patients [104]. Moreover, DJ-1 has been detected in cerebrospinal fluid from Parkinson's Disease patients [105,106,107] and urine from hepatocellular carcinoma [108] patients. Future studies will be needed to investigate how RPE cells release DJ-1 and to determine if it can be detected in the serum of AMD patients.

In summary, due to the evidence presented here connecting DJ-1 to protection against oxidative stress, it is conceivable that manipulation of DJ-1 function may be used to protect RPE cells from the oxidative stress implicated in AMD pathology.

## Methods

### Ethics Statement

The immunocytochemistry and Western analysis of human isolate RPE and BM/choroid is exempt of IRB approval since the human tissue was obtained and used after deceased.

All animal work was conducted in compliance with the Animal Welfare Act and Public Health Services policies, and under the oversight and approval of the Cleveland Clinic Institutional Animal Care and Use Committee (IACUC, protocol number ARC 2010-0136). All efforts were made to minimize animal suffering.

### RPE Cell Cultures

Unless specified all media components were prepared in-house at the Cleveland Clinic cell culture lab core from commercially produced powders from Invitrogen, Sigma-Aldrich, and Caisson Labs.

The established cell line D407 [109], obtained as a gift from Dr. Richard Hunt (University of South Carolina School of Medicine, SC) was cultured at the temperature of 37°C as previously described [109]. B6-RPE07 mouse cells were cultured as previously described [45]. Briefly, cells were grown in Dulbecco's modified Eagle's medium (DMEM) supplemented with 3% heat-inactivated fetal bovine serum, glutamax (Gibco), non-essential amino acids, and penicillin/streptomycin. To promote differentiation, B6-RPE and D407 cells, which have a very high rate of growth, were transferred to and cultured in serum-free epithelial medium for two passages (Quantum 286 for epithelia cells; PAA Laboratories Ltd.) before plating on laminin-(BD Biosciences, San Jose, CA) and collagen-coated Transwell inserts (Corning, Corning, NY), respectively. The human RPE cell line ARPE-19 was obtained from American Type Culture Collection (Manassas, VA, USA). The cells were maintained in DMEM/F12 1:1 containing 10% FBS and 5.5 mmol D-glucose in a humidified incubator at 37°C in 5% CO2. The medium was changed every 3–4 days. Polarized ARPE-19 cells were plated and cultured for 3 weeks on collagen-coated Transwell inserts in 1% FBS medium before using in experiments. Primary mouse retinal pigment epithelium was isolated as previously described [110]. Briefly, eyes from ~2 week-old C57BL/6J mice were treated with 0.5 mg/ml bovine hyaluronidase (Sigma Chemical, St. Louis, MO) and 0.05 mg/ml of collagenase (Sigma-Aldrich) followed by and 0.1% trypsin (Difco-BD Biosciences, Sparks, MD) in buffer for 60 min each incubation to allow the mechanical separation of the neural retina and exposure of the RPE. Patches of RPE were peeled off manually from Bruch's membrane. To further dissociate the RPE patches, purified RPE cells were incubated with 0.05% trypsin/0.53 mM EDTA for 2 min at 37°C.

## Human Eye Tissue

Donor eyes were obtained from the Cleveland Eye Bank or through the Foundation Fighting Blindness Eye (FFB) Donor Program (Columbia, MD). Tissue from 22 different donors were analyzed including 12 samples from non-AMD donors and 17 from AMD donors many of which, had previously been described [111]. The donor ages ranged between 35 and 91 years and the interval between time of death and tissue processing varied between 4 and 35.5 hours. Eye bank records accompanying the donor eyes indicated whether the donor had AMD or no known eye diseases.

## Oxidative Stress Treatment

Monolayers were rinsed with warm PBS and incubated with PBS for 5 min at 37°C. Oxidative stress was induced by incubation with culture medium supplemented with 0–800 μM $H_2O_2$ for 1 and 24 hours. Alternatively, monolayers were stressed with 0–100 μM 4-HNE for 12 and 24 hours in SFM. Following this incubation, monolayers were washed with pre-warmed PBS and either fixed with 4% paraformaldehyde made in PBS and processed for immunofluorescence labeling or scraped and pelleted down to be processed for biochemistry analysis.

## Adenovirus Infection

ARPE-19 cells were cultured as previously described. The replication-defective adenovirus vectors Ad5CMVPARK7 (for expression of human DJ-1 under control of a human cytomegalovirus [CMV] promoter) and AdCMVPARK7. C to S (for expression of human DJ-1 with the cysteine at residues 46, 53 and 106 mutated to serine) were prepared and titered by Welgen Inc. (Worcester, MA) using PARK7 human cDNA clone obtained from Origene (SC115623, Rockville, NY). To transduce cells, adenoviruses were mixed with transduction medium (20 mM Hepes-buffered DMEM containing 0.2% BSA) and incubated with cells for 2 h at a concentration of $5\times10^6$ plaque forming units (pfu)/cell unless specified in text. Cells on Transwells had viruses added to both apical and basal surface. After infection, transduction medium was replaced by normal culture medium and cells were returned to incubator. Two days after adenovirus transduction, cells were washed with pre-warmed PBS and either fixed with 4% paraformaldehyde made in PBS and processed for immunofluorescence or scraped and pelleted down to be processed for biochemistry analysis. Alternatively, cells were exposed to oxidative stress as described above and then processed for immunofluorescence or biochemistry analysis.

## Cell Loading with Fluorescent Probe to Detect Reactive Oxygen Species (ROS) Production

ARPE-19 monolayers were plated on glass coverslips and cultured as described above. Monolayers infected or not with adenoviruses as described above, were subjected to oxidative stress as described above. A 10 μM stock solution of CM-$H_2$DCFDA (Molecular Probes, C6827) was prepared in DMSO immediately before use. Monolayers were loaded by a 15-min incubation with 10 μM DCFH-DA at room temperature in the dark. Following incubation, monolayers were washed with pre-warmed PBS at room temperature and carefully mounted immediately on the microscope slide in vectashield. Labeled cells were analyzed using a Leica laser scanning confocal microscope (TCS-SP2, Leica, Exton, PA). Cellular images were obtained by difference interference contrast (DIC).

## Immunofluorescence of Cells

RPE monolayers on Transwells were fixed in 4% paraformaldehyde for 30 minutes at 4°C. Cells were blocked in PBS +1% BSA and incubated overnight at 4°C with poyclonal antibody directed against DJ-1 (NB300-270, 1:750; Novus), and DJ-1 oxidized at C106 (oxDJ-1, HCA024, 1:50; AbD serotec, Oxford, UK) and monoclonal antibody directed against OxPhos Complex IV subunit I (COX IV, 459600, 1:500; Invitrogen). Alexa Fluor488, Alexa Fluor594 and anti-Myc Tag Alexa Fluor488 secondary antibodies were added at room temperature for 1 hour (1:1000; Molecular Probes and 1:500; Millipore) and cell nuclei were labeled with TO-PRO®-3 iodide (1:5000; Molecular Probes). Monolayers were analyzed using a Leica laser scanning confocal microscope. A series of 1 μm *xy* (*en face*) sections were collected. Each individual *xy* image of the retinas stained represents a three-dimensional projection of the entire cryosection (sum of all images in the stack). Microscopic panels were composed using Adobe Photoshop CS3 (Adobe, San Jose, CA).

## Immunohistology of Human Donor Tissue

To determine the localization of DJ-1 in RPE cells from non–AMD and AMD eyes and BM/choroid isolated from AMD donors, immunohistochemical assays were performed using cryosections in the peri-macular area. Isolated BM/choroid strips were isolated from the eyecups as previously described [94]. Eye pieces of retina-RPE-choroid were cut and fixed by immersion in 4% paraformaldehyde made in PBS overnight at 4°C, quenched with 50 mM NH4Cl made in PBS for 1 h at 4°C, infused successively with 10% and 20% sucrose made in the same buffer and with Tissue-Tek "4583" (Miles Inc., Elkhart, IN) as previously described [111]. Cryosections (8 μm) were cut on a cryostat HM 505E (Microm, Walldorf, Germany) equipped with a CryoJane Tape-Transfer system (Instrumedics, Inc., Hackensack, NJ, USA). Cryosections were washed, and processed for antigen retrieval in pre-heated Trilogy (Cell Marque, Rocklin, CA) by incubation for 30 min. in a steamer followed by transfer to room temperature for 20 min. to allow cryosections to cool down. Sections were blocked with PBS +1% BSA and probed with the DJ-1 antibody (TA301239, 1:750, Origene) overnight at 4°C followed by labeling with Vectastain Elite ABC reagent (Vector Laboratories, Inc., Burlingame, CA) according to the manufacture's directions. Negative controls were pre-absorbed overnight in the rotator with 5 μg of lysates of HEK293 cells overexpressing PARK7. Labeling was detected through incubation with ImmPACT VIP peroxidase substrate (Vector Laboratories) according to the manufacturer's instructions. Slides were mounted in cytoseal (Richard-Allan-Scientific, Kalamazoo, MI). The sections were examined with a

Zeiss AxioImager.Z1 light microscope and the images were digitized using a Zeiss AxioCam MRc5 camera.

### Western Blot Analysis

RPE cells were solubilized in RIPA buffer (0.1% SDS, 1% Triton X100, 1% deoxycholate, 0.15 M NaCl, 2 mM EDTA, 25 mM Tris pH 7.4) supplemented with a cocktail of protease and phosphatase inhibitors (Sigma Chemical Co., St. Louis, MO). Total RPE lysates (20 μg protein) were resolved by SDS-PAGE on 4–20% Novex®-Tris-Glycine gel (Invitrogen Corporation, Carlsbad, CA) and electro-transferred to Immobilon PVDF membranes (Millipore, Bedford, MA). Membranes were blocked with HyBLOCKER liquid blocking reagent (Denville Scientific Inc., Metuchen, NJ) for 30 min. and incubated overnight in the same solution with antibodies to DJ-1 (NB300-270, 1:2000; Novus), DJ-1 oxidized at C106 (oxDJ-1, HCA024, 1:200; AbD serotec), GAPDH (ab9484, 1:1000; Abcam). Protein detection was performed with secondary antibodies conjugated to peroxidase and visualized using ECL Plus Western Blotting detection reagent (GE Healthcare Bio-Sciences Corp, Piscataway, NJ). PVDF membranes were exposed to film. Films were scanned and figures were composed using Adobe Photoshop CS3. Signal intensities were quantified using ImageJ 1.43u (http://rsb.info.nih.gog/ij).

## Supporting Information

**Figure S1 Oxidative stress induced by 4-HNE increases DJ-1 levels in RPE cells.** ARPE-19 and D407 monolayers were treated with increasing concentrations (0 to 100 μM) of 4-HNE for 12 hrs (A) harvested, and analyzed by immunoblot assay with DJ-1 antibody (upper panel). Each lane contained 20 μg of protein. Protein loadings were confirmed in replicate blots probed with GAPDH (lower panel). A dose response of ARPE-19 (A, lanes 1 to 6) and D407 (A, lanes 7 to 12) is observed when cells are exposed to increasing concentrations of 4-HNE for 12 hrs. Quantitation of these blots showed that DJ-1 immunoreactivity was 1.5 and 1.4 fold higher in ARPE-19 incubated with 5 and 10 μM HNE and up to 2.1 fold in D407 cells incubated with 25 μM HNE when compared with control cell RPE cultures (B). Plotted data represent the intensity values for each band normalized to GAPDH signal and compared to the intensity of the control, untreated cells (lanes 1, 7). Red columns = ARPE-19; blue columns = D407 cells. Data is expressed as mean relative signal intensity ± SEM (n = 3). Asterisks denote statistical significance compared with control untreated cells (*p = 0.0097 and **p<0.0001 in the ARPE-19 and *p = 0.0006, **p = 0.0499, ***p = 0.0020, ****p<0.0001 in D407 cells).
(TIF)

**Figure S2 Oxidative stress-dependent translocation of DJ-1 into mitochondria**. Representative confocal micrographs of B6-RPE07 monolayers plated on glass coverslips and labeled with antibodies to DJ-1 (A, D) and the mitochondrial staining MitoTracker (B, E). Cell nuclei were labeled with TO-PRO-3. Under baseline conditions, there is very little colocalization between DJ-1 and MitoTracker, as observed in overlaid images (C). Upon oxidative stress induced by incubation with 200 μM $H_2O_2$ for 18 hrs, the diffused cytoplasmic DJ-1 staining disappears. Moreover, in overlaid images a pronounced mitochondrial staining for DJ-1 is apparent when cells are exposed to oxidative stress (F, arrows). Scale bar = 20 μm.
(TIF)

**Figure S3 Increased levels of DJ-1 in region of RPE atrophy in AMD donor.** Cryosections of non-AMD (A) and AMD (B, C) donors with geographic atrophy were labeled with DJ-1 antibody. DJ-1 labeling was detected mostly in the RPE nuclei (arrowheads) but also in the cytoplasm (A, arrows) of non-AMD donors; labeling was also observed in the choriocapillaris (A, double arrowheads). Significantly more DJ-1 was detected all over the cytoplasm of RPE cells (B, arrows) and choriocapillaris (B, double arrowheads) from an AMD donor with geographic atrophy in the atrophic region; labeling was also significantly more intense in the choriocapillaris in this region. DJ-1 labeling of a druse (B, asterisks) is also observed. Interestingly, in this same AMD donor eye, at distances away from the region of RPE atrophy, DJ-1 immunoreactivity was similar to that observed in the RPE normal control eyes (C). Scale bars = 10 μm.
(TIF)

## Acknowledgments

The authors thank Xiaoping Yang for technical assistance in the preparation of this paper.

## Author Contributions

Conceived and designed the experiments: VLB. Performed the experiments: KGS MER VLB. Analyzed the data: VLB JGH. Contributed reagents/materials/analysis tools: VLB JGH. Wrote the paper: VLB.

## References

1. Bok D (1993) The retinal pigment epithelium: a versatile partner in vision. J Cell Sci Suppl 17: 189–195.
2. Liang FQ, Godley BF (2003) Oxidative stress-induced mitochondrial DNA damage in human retinal pigment epithelial cells: a possible mechanism for RPE aging and age-related macular degeneration. Exp Eye Res 76: 397–403.
3. Tanito M, Brush RS, Elliott MH, Wicker LD, Henry KR, et al. (2009) High levels of retinal membrane docosahexaenoic acid increase susceptibility to stress-induced degeneration. J Lipid Res 50: 807–819.
4. Miceli MV, Liles MR, Newsome DA (1994) Evaluation of oxidative processes in human pigment epithelial cells associated with retinal outer segment phagocytosis. Exp Cell Res 214: 242–249.
5. Tate DJ, Jr., Miceli MV, Newsome DA (1995) Phagocytosis and H2O2 induce catalase and metallothionein gene expression in human retinal pigment epithelial cells. Invest Ophthalmol Vis Sci 36: 1271–1279.
6. Beatty S, Koh H, Phil M, Henson D, Boulton M (2000) The role of oxidative stress in the pathogenesis of age-related macular degeneration. Surv Ophthalmol 45: 115–134.
7. Drobek-Slowik M, Karczewicz D, Safranow K (2007) [The potential role of oxidative stress in the pathogenesis of the age-related macular degeneration (AMD)]. Postepy Hig Med Dosw (Online) 61: 28–37.
8. Bonifati V, Rizzu P, Squitieri F, Krieger E, Vanacore N, et al. (2003) DJ-1(PARK7), a novel gene for autosomal recessive, early onset parkinsonism. Neurol Sci 24: 159–160.
9. Nagakubo D, Taira T, Kitaura H, Ikeda M, Tamai K, et al. (1997) DJ-1, a novel oncogene which transforms mouse NIH3T3 cells in cooperation with ras. Biochem Biophys Res Commun 231: 509–513.
10. Hod Y (2004) Differential control of apoptosis by DJ-1 in prostate benign and cancer cells. J Cell Biochem 92: 1221–1233.
11. Gao X, Ning Y (2011) Cancer and Parkinson's disease: the odd couple. Drugs Today (Barc) 47: 215–222.
12. Hod Y, Pentyala SN, Whyard TC, El-Maghrabi MR (1999) Identification and characterization of a novel protein that regulates RNA-protein interaction. J Cell Biochem 72: 435–444.
13. Shinbo Y, Taira T, Niki T, Iguchi-Ariga SM, Ariga H (2005) DJ-1 restores p53 transcription activity inhibited by Topors/p53BP3. Int J Oncol 26: 641–648.
14. Zhong N, Kim CY, Rizzu P, Geula C, Porter DR, et al. (2006) DJ-1 transcriptionally up-regulates the human tyrosine hydroxylase by inhibiting the sumoylation of pyrimidine tract-binding protein-associated splicing factor. J Biol Chem 281: 20940–20948.
15. Clements CM, McNally RS, Conti BJ, Mak TW, Ting JP (2006) DJ-1, a cancer- and Parkinson's disease-associated protein, stabilizes the antioxidant transcriptional master regulator Nrf2. Proc Natl Acad Sci U S A 103: 15091–15096.
16. Takahashi K, Taira T, Niki T, Seino C, Iguchi-Ariga SM, et al. (2001) DJ-1 positively regulates the androgen receptor by impairing the binding of PIASx alpha to the receptor. J Biol Chem 276: 37556–37563.

17. Shendelman S, Jonason A, Martinat C, Leete T, Abeliovich A (2004) DJ-1 is a redox-dependent molecular chaperone that inhibits alpha-synuclein aggregate formation. PLoS Biol 2: e362.
18. Zhou W, Zhu M, Wilson MA, Petsko GA, Fink AL (2006) The oxidation state of DJ-1 regulates its chaperone activity toward alpha-synuclein. J Mol Biol 356: 1036–1048.
19. Yoshida K, Sato Y, Yoshiike M, Nozawa S, Ariga H, et al. (2003) Immunocytochemical localization of DJ-1 in human male reproductive tissue. Mol Reprod Dev 66: 391–397.
20. Mitsumoto A, Nakagawa Y (2001) DJ-1 is an indicator for endogenous reactive oxygen species elicited by endotoxin. Free Radic Res 35: 885–893.
21. Taira T, Saito Y, Niki T, Iguchi-Ariga SM, Takahashi K, et al. (2004) DJ-1 has a role in antioxidative stress to prevent cell death. EMBO Rep 5: 213–218.
22. Martinat C, Shendelman S, Jonason A, Leete T, Beal MF, et al. (2004) Sensitivity to oxidative stress in DJ-1-deficient dopamine neurons: an ES-derived cell model of primary Parkinsonism. PLoS Biol 2: e327.
23. Canet-Aviles RM, Wilson MA, Miller DW, Ahmad R, McLendon C, et al. (2004) The Parkinson's disease protein DJ-1 is neuroprotective due to cysteine-sulfinic acid-driven mitochondrial localization. Proc Natl Acad Sci U S A 101: 9103–9108.
24. Takahashi-Niki K, Niki T, Taira T, Iguchi-Ariga SM, Ariga H (2004) Reduced anti-oxidative stress activities of DJ-1 mutants found in Parkinson's disease patients. Biochem Biophys Res Commun 320: 389–397.
25. Kim RH, Smith PD, Aleyasin H, Hayley S, Mount MP, et al. (2005) Hypersensitivity of DJ-1-deficient mice to 1-methyl-4-phenyl-1,2,3,6-tetrahydropyrindine (MPTP) and oxidative stress. Proc Natl Acad Sci U S A 102: 5215–5220.
26. Park J, Kim SY, Cha GH, Lee SB, Kim S, et al. (2005) Drosophila DJ-1 mutants show oxidative stress-sensitive locomotive dysfunction. Gene 361: 133–139.
27. Choi J, Sullards MC, Olzmann JA, Rees HD, Weintraub ST, et al. (2006) Oxidative damage of DJ-1 is linked to sporadic Parkinson and Alzheimer diseases. J Biol Chem 281: 10816–10824.
28. Meulener MC, Xu K, Thomson L, Ischiropoulos H, Bonini NM (2006) Mutational analysis of DJ-1 in Drosophila implicates functional inactivation by oxidative damage and aging. Proc Natl Acad Sci U S A 103: 12517–12522.
29. Kahle PJ, Waak J, Gasser T (2009) DJ-1 and prevention of oxidative stress in Parkinson's disease and other age-related disorders. Free Radic Biol Med 47: 1354–1361.
30. Mitsumoto A, Nakagawa Y, Takeuchi A, Okawa K, Iwamatsu A, et al. (2001) Oxidized forms of peroxiredoxins and DJ-1 on two-dimensional gels increased in response to sublethal levels of paraquat. Free Radic Res 35: 301–310.
31. Zhou W, Freed CR (2005) DJ-1 up-regulates glutathione synthesis during oxidative stress and inhibits A53T alpha-synuclein toxicity. J Biol Chem 280: 43150–43158.
32. Bonifati V, Rizzu P, van Baren MJ, Schaap O, Breedveld GJ, et al. (2003) Mutations in the DJ-1 gene associated with autosomal recessive early-onset parkinsonism. Science 299: 256–259.
33. Junn E, Taniguchi H, Jeong BS, Zhao X, Ichijo H, et al. (2005) Interaction of DJ-1 with Daxx inhibits apoptosis signal-regulating kinase 1 activity and cell death. Proc Natl Acad Sci U S A 102: 9691–9696.
34. Xu J, Zhong N, Wang H, Elias JE, Kim CY, et al. (2005) The Parkinson's disease-associated DJ-1 protein is a transcriptional co-activator that protects against neuronal apoptosis. Hum Mol Genet 14: 1231–1241.
35. Malhotra D, Thimmulappa R, Navas-Acien A, Sandford A, Elliott M, et al. (2008) Decline in NRF2-regulated antioxidants in chronic obstructive pulmonary disease lungs due to loss of its positive regulator, DJ-1. Am J Respir Crit Care Med 178: 592–604.
36. Yokota T, Sugawara K, Ito K, Takahashi R, Ariga H, et al. (2003) Down regulation of DJ-1 enhances cell death by oxidative stress, ER stress, and proteasome inhibition. Biochem Biophys Res Commun 312: 1342–1348.
37. van der Brug MP, Blackinton J, Chandran J, Hao LY, Lal A, et al. (2008) RNA binding activity of the recessive parkinsonism protein DJ-1 supports involvement in multiple cellular pathways. Proc Natl Acad Sci U S A 105: 10244–10249.
38. Ottolini D, Cali T, Negro A, Brini M (2013) The Parkinson disease-related protein DJ-1 counteracts mitochondrial impairment induced by the tumour suppressor protein p53 by enhancing endoplasmic reticulum-mitochondria tethering. Hum Mol Genet.
39. Larsen NJ, Ambrosi G, Mullett SJ, Berman SB, Hinkle DA (2011) DJ-1 knock-down impairs astrocyte mitochondrial function. Neuroscience 196: 251–264.
40. Mullett SJ, Hinkle DA (2011) DJ-1 deficiency in astrocytes selectively enhances mitochondrial Complex I inhibitor-induced neurotoxicity. J Neurochem 117: 375–387.
41. Gonzalez-Polo R, Niso-Santano M, Moran JM, Ortiz-Ortiz MA, Bravo-San Pedro JM, et al. (2009) Silencing DJ-1 reveals its contribution in paraquat-induced autophagy. J Neurochem 109: 889–898.
42. Yamashita S, Mori A, Kimura E, Mita S, Maeda Y, et al. (2010) DJ-1 forms complexes with mutant SOD1 and ameliorates its toxicity. J Neurochem 113: 860–870.
43. Lev N, Ickowicz D, Barhum Y, Lev S, Melamed E, et al. (2009) DJ-1 protects against dopamine toxicity. J Neural Transm 116: 151–160.
44. Gu X, Neric NJ, Crabb JS, Crabb JW, Bhattacharya SK, et al. (2012) Age-related changes in the retinal pigment epithelium (RPE). PLoS One 7: e38673.
45. Chen M, Muckersie E, Robertson M, Fraczek M, Forrester JV, et al. (2008) Characterization of a spontaneous mouse retinal pigment epithelial cell line B6-RPE07. Invest Ophthalmol Vis Sci 49: 3699–3706.
46. Bonilha VL, Finnemann SC, Rodriguez-Boulan E (1999) Ezrin promotes morphogenesis of apical microvilli and basal infoldings in retinal pigment epithelium. J Cell Biol 147: 1533–1548.
47. Kinumi T, Kimata J, Taira T, Ariga H, Niki E (2004) Cysteine-106 of DJ-1 is the most sensitive cysteine residue to hydrogen peroxide-mediated oxidation in vivo in human umbilical vein endothelial cells. Biochem Biophys Res Commun 317: 722–728.
48. Wilson MA (2011) The role of cysteine oxidation in DJ-1 function and dysfunction. Antioxid Redox Signal 15: 111–122.
49. Ooe H, Iguchi-Ariga SM, Ariga H (2006) Establishment of specific antibodies that recognize C106-oxidized DJ-1. Neurosci Lett 404: 166–169.
50. Zhang L, Shimoji M, Thomas B, Moore DJ, Yu SW, et al. (2005) Mitochondrial localization of the Parkinson's disease related protein DJ-1: implications for pathogenesis. Hum Mol Genet 14: 2063–2073.
51. Ooe H, Taira T, Iguchi-Ariga SM, Ariga H (2005) Induction of reactive oxygen species by bisphenol A and abrogation of bisphenol A-induced cell injury by DJ-1. Toxicol Sci 88: 114–126.
52. Lev N, Ickowicz D, Melamed E, Offen D (2008) Oxidative insults induce DJ-1 upregulation and redistribution: implications for neuroprotection. Neurotoxicology 29: 397–405.
53. George S, Mok SS, Nurjono M, Ayton S, Finkelstein DI, et al. (2010) alpha-Synuclein transgenic mice reveal compensatory increases in Parkinson's disease-associated proteins DJ-1 and parkin and have enhanced alpha-synuclein and PINK1 levels after rotenone treatment. J Mol Neurosci 42: 243–254.
54. Inberg A, Linial M (2010) Protection of pancreatic beta-cells from various stress conditions is mediated by DJ-1. J Biol Chem 285: 25686–25698.
55. Knobbe CB, Revett TJ, Bai Y, Chow V, Jeon AH, et al. (2011) Choice of biological source material supersedes oxidative stress in its influence on DJ-1 in vivo interactions with Hsp90. J Proteome Res 10: 4388–4404.
56. Bitar MS, Liu C, Ziaei A, Chen Y, Schmedt T, et al. (2012) Decline in DJ-1 and decreased nuclear translocation of Nrf2 in Fuchs endothelial corneal dystrophy. Invest Ophthalmol Vis Sci 53: 5806–5813.
57. Joselin AP, Hewitt SJ, Callaghan SM, Kim RH, Chung YH, et al. (2012) ROS-dependent regulation of Parkin and DJ-1 localization during oxidative stress in neurons. Hum Mol Genet 21: 4888–4903.
58. Saito Y, Hamakubo T, Yoshida Y, Ogawa Y, Hara Y, et al. (2009) Preparation and application of monoclonal antibodies against oxidized DJ-1. Significant elevation of oxidized DJ-1 in erythrocytes of early-stage Parkinson disease patients. Neurosci Lett 465: 1–5.
59. Akazawa YO, Saito Y, Hamakubo T, Masuo Y, Yoshida Y, et al. (2010) Elevation of oxidized DJ-1 in the brain and erythrocytes of Parkinson disease model animals. Neurosci Lett 483: 201–205.
60. Kitamura Y, Watanabe S, Taguchi M, Takagi K, Kawata T, et al. (2011) Neuroprotective effect of a new DJ-1-binding compound against neurodegeneration in Parkinson's disease and stroke model rats. Mol Neurodegener 6: 48.
61. Hulleman JD, Mirzaei H, Guigard E, Taylor KL, Ray SS, et al. (2007) Destabilization of DJ-1 by familial substitution and oxidative modifications: implications for Parkinson's disease. Biochemistry 46: 5776–5789.
62. Blackinton J, Ahmad R, Miller DW, van der Brug MP, Canet-Aviles RM, et al. (2005) Effects of DJ-1 mutations and polymorphisms on protein stability and subcellular localization. Brain Res Mol Brain Res 134: 76–83.
63. Gorner K, Holtorf E, Waak J, Pham TT, Vogt-Weisenhorn DM, et al. (2007) Structural determinants of the C-terminal helix-kink-helix motif essential for protein stability and survival promoting activity of DJ-1. J Biol Chem 282: 13680–13691.
64. Lin J, Prahlad J, Wilson MA (2012) Conservation of oxidative protein stabilization in an insect homologue of parkinsonism-associated protein DJ-1. Biochemistry 51: 3799–3807.
65. Blackinton J, Lakshminarasimhan M, Thomas KJ, Ahmad R, Greggio E, et al. (2009) Formation of a stabilized cysteine sulfinic acid is critical for the mitochondrial function of the parkinsonism protein DJ-1. J Biol Chem 284: 6476–6485.
66. Kim SJ, Park YJ, Oh YJ (2012) Proteomic analysis reveals a protective role for DJ-1 during 6-hydroxydopamine-induced cell death. Biochem Biophys Res Commun 422: 8–14.
67. Jeong HJ, Kim DW, Kim MJ, Woo SJ, Kim HR, et al. (2012) Protective effects of transduced Tat-DJ-1 protein against oxidative stress and ischemic brain injury. Exp Mol Med 44: 586–593.
68. Robert G, Puissant A, Dufies M, Marchetti S, Jacquel A, et al. (2012) The caspase 6 derived N-terminal fragment of DJ-1 promotes apoptosis via increased ROS production. Cell Death Differ 19: 1769–1778.
69. Yu HH, Xu Q, Chen HP, Wang S, Huang XS, et al. (2013) Stable overexpression of DJ-1 protects H9c2 cells against oxidative stress under a hypoxia condition. Cell Biochem Funct.
70. Nowak JZ (2006) Age-related macular degeneration (AMD): pathogenesis and therapy. Pharmacol Rep 58: 353–363.
71. Ding X, Patel M, Chan CC (2009) Molecular pathology of age-related macular degeneration. Prog Retin Eye Res 28: 1–18.

72. Kinnunen K, Petrovski G, Moe MC, Berta A, Kaarniranta K (2012) Molecular mechanisms of retinal pigment epithelium damage and development of age-related macular degeneration. Acta Ophthalmol 90: 299–309.
73. Mohan R, Sivak J, Ashton P, Russo LA, Pham BQ, et al. (2000) Curcuminoids inhibit the angiogenic response stimulated by fibroblast growth factor-2, including expression of matrix metalloproteinase gelatinase B. J Biol Chem 275: 10405–10412.
74. Schutt F, Volcker HE, Dithmar S (2007) [N-acetylcysteine improves lysosomal function and enhances the degradation of photoreceptor outer segments in cultured RPE cells]. Klin Monbl Augenheilkd 224: 580–584.
75. Chan CM, Huang JH, Lin HH, Chiang HS, Chen BH, et al. (2008) Protective effects of (−)-epigallocatechin gallate on UVA-induced damage in ARPE19 cells. Mol Vis 14: 2528–2534.
76. Cao GF, Liu Y, Yang W, Wan J, Yao J, et al. (2011) Rapamycin sensitive mTOR activation mediates nerve growth factor (NGF) induced cell migration and pro-survival effects against hydrogen peroxide in retinal pigment epithelial cells. Biochem Biophys Res Commun 414: 499–505.
77. Chong EW, Wong TY, Kreis AJ, Simpson JA, Guymer RH (2007) Dietary antioxidants and primary prevention of age related macular degeneration: systematic review and meta-analysis. BMJ 335: 755.
78. Parisi V, Tedeschi M, Gallinaro G, Varano M, Saviano S, et al. (2008) Carotenoids and antioxidants in age-related maculopathy italian study: multifocal electroretinogram modifications after 1 year. Ophthalmology 115: 324–333 e322.
79. Bandopadhyay R, Kingsbury AE, Cookson MR, Reid AR, Evans IM, et al. (2004) The expression of DJ-1 (PARK7) in normal human CNS and idiopathic Parkinson's disease. Brain 127: 420–430.
80. Jarrett SG, Lin H, Godley BF, Boulton ME (2008) Mitochondrial DNA damage and its potential role in retinal degeneration. Prog Retin Eye Res 27: 596–607.
81. Turrens JF (2003) Mitochondrial formation of reactive oxygen species. J Physiol 552: 335–344.
82. Shabalina IG, Nedergaard J (2011) Mitochondrial ('mild') uncoupling and ROS production: physiologically relevant or not? Biochem Soc Trans 39: 1305–1309.
83. Santos JH, Hunakova L, Chen Y, Bortner C, Van Houten B (2003) Cell sorting experiments link persistent mitochondrial DNA damage with loss of mitochondrial membrane potential and apoptotic cell death. J Biol Chem 278: 1728–1734.
84. Feher J, Kovacs I, Artico M, Cavallotti C, Papale A, et al. (2006) Mitochondrial alterations of retinal pigment epithelium in age-related macular degeneration. Neurobiol Aging 27: 983–993.
85. Nordgaard CL, Berg KM, Kapphahn RJ, Reilly C, Feng X, et al. (2006) Proteomics of the retinal pigment epithelium reveals altered protein expression at progressive stages of age-related macular degeneration. Invest Ophthalmol Vis Sci 47: 815–822.
86. Nordgaard CL, Karunadharma PP, Feng X, Olsen TW, Ferrington DA (2008) Mitochondrial proteomics of the retinal pigment epithelium at progressive stages of age-related macular degeneration. Invest Ophthalmol Vis Sci 49: 2848–2855.
87. SanGiovanni JP, Arking DE, Iyengar SK, Elashoff M, Clemons TE, et al. (2009) Mitochondrial DNA variants of respiratory complex I that uniquely characterize haplogroup T2 are associated with increased risk of age-related macular degeneration. PLoS One 4: e5508.
88. Kenney MC, Atilano SR, Boyer D, Chwa M, Chak G, et al. (2010) Characterization of retinal and blood mitochondrial DNA from age-related macular degeneration patients. Invest Ophthalmol Vis Sci 51: 4289–4297.
89. Mueller EE, Schaier E, Brunner SM, Eder W, Mayr JA, et al. (2012) Mitochondrial haplogroups and control region polymorphisms in age-related macular degeneration: a case-control study. PLoS One 7: e30874.
90. Stenirri S, Santambrogio P, Setaccioli M, Erba BG, Pia Manitto M, et al. (2012) Study of FTMT and ABCA4 genes in a patient affected by age-related macular degeneration: identification and analysis of new mutations. Clin Chem Lab Med 50: 1021–1029.
91. Blasiak J, Glowacki S, Kauppinen A, Kaarniranta K (2013) Mitochondrial and nuclear DNA damage and repair in age-related macular degeneration. Int J Mol Sci 14: 2996–3010.
92. Kenney MC, Hertzog D, Chak G, Atilano SR, Khatibi N, et al. (2013) Mitochondrial DNA haplogroups confer differences in risk for age-related macular degeneration: a case control study. BMC Med Genet 14: 4.
93. Crabb JW, Miyagi M, Gu X, Shadrach K, West KA, et al. (2002) Drusen proteome analysis: an approach to the etiology of age-related macular degeneration. Proc Natl Acad Sci U S A 99: 14682–14687.
94. Bando H, Shadrach KG, Rayborn ME, Crabb JW, Hollyfield JG (2007) Clathrin and adaptin accumulation in drusen, Bruch's membrane and choroid in AMD and non-AMD donor eyes. Exp Eye Res 84: 135–142.
95. Hageman GS, Mullins RF, Russell SR, Johnson LV, Anderson DH (1999) Vitronectin is a constituent of ocular drusen and the vitronectin gene is expressed in human retinal pigmented epithelial cells. FASEB J 13: 477–484.
96. Mullins RF, Russell SR, Anderson DH, Hageman GS (2000) Drusen associated with aging and age-related macular degeneration contain proteins common to extracellular deposits associated with atherosclerosis, elastosis, amyloidosis, and dense deposit disease. FASEB J 14: 835–846.
97. Anderson DH, Ozaki S, Nealon M, Neitz J, Mullins RF, et al. (2001) Local cellular sources of apolipoprotein E in the human retina and retinal pigmented epithelium: implications for the process of drusen formation. Am J Ophthalmol 131: 767–781.
98. Malek G, Li CM, Guidry C, Medeiros NE, Curcio CA (2003) Apolipoprotein B in cholesterol-containing drusen and basal deposits of human eyes with age-related maculopathy. Am J Pathol 162: 413–425.
99. Shimwell NJ, Ward DG, Mohri Y, Mohri T, Pallan L, et al. (2012) Macrophage migration inhibitory factor and DJ-1 in gastric cancer: differences between high-incidence and low-incidence areas. Br J Cancer 107: 1595–1601.
100. Lisitskaia KV, Eremina LS, Ivanov AV, Kovaleva MA, Okhrits VE, et al. (2011) [Study of Dj-1 protein in tissue specimens, cultured cells and serum of prostate cancer patients]. Biomed Khim 57: 392–401.
101. Chen Y, Kang M, Lu W, Guo Q, Zhang B, et al. (2012) DJ-1, a novel biomarker and a selected target gene for overcoming chemoresistance in pancreatic cancer. J Cancer Res Clin Oncol 138: 1463–1474.
102. Zeng HZ, Qu YQ, Zhang WJ, Xiu B, Deng AM, et al. (2011) Proteomic Analysis Identified DJ-1 as a Cisplatin Resistant Marker in Non-Small Cell Lung Cancer. Int J Mol Sci 12: 3489–3499.
103. Pardo M, Garcia A, Thomas B, Pineiro A, Akoulitchev A, et al. (2006) The characterization of the invasion phenotype of uveal melanoma tumour cells shows the presence of MUC18 and HMG-1 metastasis markers and leads to the identification of DJ-1 as a potential serum biomarker. Int J Cancer 119: 1014–1022.
104. Oda M, Makita M, Iwaya K, Akiyama F, Kohno N, et al. (2012) High levels of DJ-1 protein in nipple fluid of patients with breast cancer. Cancer Sci 103: 1172–1176.
105. Hong Z, Shi M, Chung KA, Quinn JF, Peskind ER, et al. (2010) DJ-1 and alpha-synuclein in human cerebrospinal fluid as biomarkers of Parkinson's disease. Brain 133: 713–726.
106. Shi M, Furay AR, Sossi V, Aasly JO, Armaly J, et al. (2012) DJ-1 and alphaSYN in LRRK2 CSF do not correlate with striatal dopaminergic function. Neurobiol Aging 33: 836 e835–837.
107. Salvesen L, Bech S, Lokkegaard A, Hjermind LE, Nielsen JE, et al. (2012) The DJ-1 concentration in cerebrospinal fluid does not differentiate among Parkinsonian syndromes. Parkinsonism Relat Disord 18: 899–901.
108. Abdalla MA, Haj-Ahmad Y (2012) Promising Urinary Protein Biomarkers for the Early Detection of Hepatocellular Carcinoma among High-Risk Hepatitis C Virus Egyptian Patients. J Cancer 3: 390–403.
109. Davis AA, Bernstein PS, Bok D, Turner J, Nachtigal M, et al. (1995) A human retinal pigment epithelial cell line that retains epithelial characteristics after prolonged culture. Invest Ophthalmol Vis Sci 36: 955–964.
110. Nandrot EF, Kim Y, Brodie SE, Huang X, Sheppard D, et al. (2004) Loss of synchronized retinal phagocytosis and age-related blindness in mice lacking alphavbeta5 integrin. J Exp Med 200: 1539–1545.
111. Bonilha VL, Shadrach KG, Rayborn ME, Li Y, Pauer GJ, et al. (2013) Retinal deimination and PAD2 levels in retinas from donors with age-related macular degeneration (AMD). Exp Eye Res 111C: 71–78.

Experimental Eye Research 111 (2013) 71–78

Contents lists available at SciVerse ScienceDirect

Experimental Eye Research

journal homepage: www.elsevier.com/locate/yexer

# Retinal deimination and PAD2 levels in retinas from donors with age-related macular degeneration (AMD)

Vera L. Bonilha [a,*], Karen G. Shadrach [a], Mary E. Rayborn [a], Yong Li [a,1], Gayle J.T. Pauer [a], Stephanie A. Hagstrom [a], Sanjoy K. Bhattacharya [b], Joe G. Hollyfield [a]

[a] *Department of Ophthalmology, The Cole Eye Institute(i31), Cleveland Clinic Lerner College of Medicine, 9500 Euclid Avenue, Cleveland, OH 44195, USA*
[b] *Bascom Palmer Eye Institute, University of Miami, Miami, FL 33136, USA*

## ARTICLE INFO

*Article history:*
Received 14 November 2012
Accepted in revised form 22 March 2013
Available online 3 April 2013

*Keywords:*
posttranslational modifications
protein deimination
immunohistochemistry
AMD
retina
retinal pigment epithelium

## ABSTRACT

Deimination is a form of protein posttranslational modification carried out by the peptidyl arginine deiminases (PADs) enzymes. PAD2 is the principal deiminase expressed in the retina. Elevated levels of PAD2 and protein deimination are present in a number of human neurological diseases, with or without ocular manifestation. To define the association of deimination with the pathogenesis of age-related macular degeneration (AMD), we studied protein deimination and PAD2 levels in retinas of AMD donor eyes compared to age-matched non-AMD retinas. Eyes from non-AMD and AMD donors were fixed in 4% paraformaldehyde and 0.5% glutaraldehyde in phosphate buffer. Retina and retinal pigment epithelium (RPE) from donor eyes were processed for immunohistochemical detection and western blotting using antibodies to PAD2 and citrulline residues. The ganglion cell, inner plexiform, inner nuclear and outer nuclear layers were labeled by both PAD2 and citrulline antibodies. Changes in the localization of deiminated residues and PAD2 were evident as the retinal layers were remodeled coincident with photoreceptor degeneration in AMD retinas. Immunodetection of either PAD2 or citrulline residues could not be evaluated in the RPE layer due to the high autofluorescence levels in this layer. Interestingly, higher deimination immunoreactivity was detected in AMD retinal lysates. However, no significant changes in PAD2 were detected in the AMD and non-AMD retinas and RPE lysates. Our observations show increased levels of protein deimination but not PAD2 in AMD retinas and RPE, suggesting a reduced rate of turnover of deiminated proteins in these AMD retinas.

## 1. Introduction

Posttranslational modifications (PTMs) of proteins allow the incorporation of more structural and functional diversity in protein than is possible with only variations in amino acid residues. In turn PTMs become important as signals in the regulation of many cellular activities. Protein deimination, often referred to as citrullination, is a PTM that is carried out by peptidyl arginine deiminases (PADs) upon increase of intracellular calcium levels and involves conversion of arginine residues to citrulline (Vossenaar et al., 2003). Deimination of proteins induces a decrease in the charge of the modified proteins with major consequences on their conformation, stability and/or interactions with other proteins, and therefore on their functions (Gyorgy et al., 2006; Mechin et al., 2011). Mammalian cells possess five protein deiminases, PAD1-4 and 6 (Vossenaar et al., 2003).

PAD2 is considered the most prevalent isotype expressed in the central nervous system. Hence, elevated levels of PAD2 and protein deimination have been reported in a number of human neurological diseases including autoimmune encephalomyelitis (Nicholas et al., 2005), multiple sclerosis (Moscarello et al., 2007), Alzheimer's disease (Ishigami et al., 2005; Louw et al., 2007; Mohlake and Whiteley, 2010; Acharya et al., 2012), Parkinson's disease (Nicholas, 2011), amyotrophic lateral sclerosis (Chou et al., 1996), and glaucoma (Bhattacharya et al., 2006a, 2006b; Cafaro et al., 2010). Elevated levels of PADs and protein deimination have also been linked to the pathogenesis of autoimmune diseases such as rheumatoid arthritis (Yamada et al., 2005; Harris et al., 2008; Kochi, 2010; Kochi et al., 2011; Giles et al., 2012).

Previously, it was reported that human brain from multiple sclerosis donors displayed increased deimination in comparison to brain from control and donors with other neurological diseases

---

[*] Corresponding author. Tel.: +1 216 445 7690; fax: +1 216 445 3670.
*E-mail address:* bonilhav@ccf.org (V.L. Bonilha).

[1] Present address: Department of Neurological Surgery, Case Western Reserve University, Cleveland, OH, USA.

0014-4835/$ – see front matter © 2013 Elsevier Ltd. All rights reserved.
http://dx.doi.org/10.1016/j.exer.2013.03.017

(Moscarello et al., 1994). The same study also found that infants possess higher levels of deimination compared to normal adults and that the relative proportion of relative deiminated protein in both multiple sclerosis and infant brain tissue was similar (Moscarello et al., 1994). We recently reported reduced levels of deimination in the retina, optic nerve, and blood of older F344BN rats compared to young animals. These observations were in concert with reduced mRNA and protein levels and activity for PAD2 in the retina and optic nerve of older rats compared to those from young rats (Bhattacharya et al., 2008). We also reported decreased deimination in ganglion cell layer together with increased deimination in other retinal layers to occur in a mouse model of demyelination (Pelizaeus-Merzbacher disease termed ND4 mice). These findings were accompanied by a decrease in inner retinal function indicating loss of vision in ND4 mice. In these mice, local restoration of deimination dramatically improved retinal function (Enrique-Algeciras et al., 2013). Taken together, these findings suggest the cell-specific regulation of deimination may be a previously unrecognized indicator of retinal function. For example, increased deimination in astrocytes and decreased deimination in ganglion cells occurs in neurodegenerative disease. In contrast, increased deimination occurs in developing ganglion cells in infants. These results are consistent with our conjecture pertaining to differences in deimination in disease and development (Bhattacharya, 2009).

Age-related macular degeneration (AMD) is the most common cause of irreversible blindness in the elderly population in industrialized countries. AMD is characterized by progressive loss of photoreceptors in the macula secondary to dysfunction of the retinal pigment epithelium (RPE) in the setting of prominent extracellular lesions. Late AMD can manifest in two forms, geographic atrophy or “dry AMD” and neovascular or “wet” AMD. Geographic atrophic (GA) is characterized by focal death of RPE, photoreceptors and choriocapillaris in the macula often together with large and abundant drusen accumulation (Biarnés et al., 2011). The “wet”, neovascular form, occurs when new abnormal blood vessels, originating from the choroid, penetrate Bruch’s membrane causing damage to the RPE and overlying photoreceptors and resulting in vascular leakage, hemorrhage, and scarring (Freund et al., 2010). Dry AMD is much more common than wet, but choroidal neovascularization (CNV) in wet AMD accounts for the majority of vision loss (Bressler et al., 1988). The purpose of this study was to define the distribution of protein deimination and PAD2 in eyes from donors with AMD and to compare this with the distribution in age-matched non-AMD eyes. We found that the amount of protein deimination but not the levels of PAD2 was significantly increased in retinal and RPE lysates from AMD donor eyes, as compared to that observed from non-AMD eyes. All together our data suggests that strict, localized regulation of deimination levels is essential for retinal function.

## 2. Material and methods

### 2.1. Human eye tissue

Donor eyes were obtained from the Cleveland Eye Bank or through the Foundation Fighting Blindness Eye (FFB) Donor Program (Columbia, MD). Tissue from 41 different donors was analyzed. Among those, 16 samples were from non-AMD donors and 25 were from AMD donors. The analyzed tissue included FFB donations # 703, 704, 711, 714, 716, 722, 723, 728, 745, 758, 781. The donor ages varied between 35 and 91 years and the interval between time of death and tissue processing varied between 4 and 35.5 h. Additional information about the donors is provided in Table 1. Eye bank records accompanying the donor eyes indicated whether the donor had AMD or no known eye diseases. One eye from each donor was used in our analysis. Globes were cut through the *ora serrata* and individually assessed for gross pathology using a Zeiss Universal S3 surgical microscope with an OPMI MD Microscopic Head equipped with a Xenon Light Source. Upon dissection, the fundus of each eye was analyzed, and graded according to the AREDS disease stage using the Minnesota grading system for postmortem eyes as defined by the location and area of drusen distribution (Olsen and Feng, 2004). In our samples we could not determine if subretinal drusenoid deposits were present. Fixed eyes were analyzed intact, with the retina on top of the RPE, while unfixed tissue had the retina mechanically removed from the RPE before grading the eyes. Of the AMD eyes used in this analysis, 7 had advanced AMD, defined as either neovascular AMD or geographic atrophy (GA) involving the center of the macula, and the remaining eyes were either stage 2 or 3. Non-AMD control eyes did not have any drusen in the macular area nor did they display any grossly visible AMD features. The immunohistochemical and Western blot analysis of these eyes is exempt of IRB approval.

**Table 1**
AMD and non-AMD human donor additional information.

| Donor ID | Age[a] | Gender[b] | Race[c] | PMI[d] | Donor type |
|---|---|---|---|---|---|
| 1 | 84 | M | C | 10 | AMD |
| 2 | 92 | F | C | 10 | AMD |
| 3 | 75 | M | C | 10 | AMD |
| 4 | 83 | M | C | 10 | NON-AMD |
| 5 | 91 | F | C | 10 | NON-AMD |
| 6 | 73 | M | C | 10 | NON-AMD |
| 7 | 63 | M | C | 8 | NON-AMD |
| 8 | 74 | F | AA | 8.5 | NON-AMD |
| 9 | 79 | F | C | 11 | AMD |
| 10 | 83 | M | C | 7.5 | AMD |
| 11 | 87 | F | C | 4 | AMD |
| 12 | 93 | M | C | 4.5 | AMD |
| 13 | 97 | M | C | 6 | AMD |
| 14 | 70 | F | C | 6 | AMD |
| 15 | 80 | M | C | <6 | NON-AMD |
| 16 | 80 | M | C | 5 | AMD |
| 17 | 80 | M | C | 4.5 | NON-AMD |
| 18 | 80 | M | C | 2.5 | NON-AMD |
| 19 | 82 | M | C | 12 | AMD |
| 20 | 81 | M | C | 8 | NON-AMD |
| 21 | 91 | M | C | <6 | NON-AMD |
| 22 | 35 | M | C | 7 | NON-AMD |
| 23 | 72 | M | C | 12 | AMD |
| 24 | 80 | M | C | 2 | AMD |
| 25 | 82 | F | C | 9 | NON-AMD |
| 26 | 81 | F | C | 4.5 | NON-AMD |
| 27 | 72 | F | C | 5.1 | NON-AMD |
| 28 | 50 | F | C | 8.5 | NON-AMD |
| FFB#703 | 23 | M | C | 19 | AMD |
| FFB#704 | 93 | U | U | 8.5 | AMD |
| FFB#711 | 83 | U | U | 13 | AMD |
| FFB#714 | 82 | F | C | 6.5 | AMD |
| FFB#716 | 80 | F | C | 35.5 | NON-AMD |
| FFB#722 | 90 | M | C | 22 | AMD |
| FFB#723 | 76 | M | C | 9.5 | AMD |
| FFB#728 | 91 | M | C | 7.5 | AMD |
| FFB#745 | 65 | F | C | 7.5 | NON-AMD |
| FFB#758 | 91 | F | C | 7 | AMD |
| FFB#781 | 80 | F | C | 9 | AMD |

[a] Age: age at death (years).
[b] Gender: M = Male, F = Female, U = Unknown.
[c] Race: C = Caucasian, AA = African American, U = Unknown.
[d] Interval from death to preservation (hrs).

Macroscopic fundus images were collected using a Zeiss AxioCam MRC5 camera equipped with a macro video lens. Prior to imaging, the cornea and lens were removed leaving only the posterior pole. Remaining eyecups were filled with PBS to eliminate specular reflections and improve contrast and image quality.

### 2.2. Preparation of human RPE and retina lysates

RPE cells (Table 1) were isolated using the protocol initially described with mechanical removal of the retina and brushing of the RPE from the choroid in PBS (Nakata et al., 2005). RPE cells suspended in PBS were pelleted, the PBS was aspirated from the tube and fresh PBS containing protease inhibitors was added to the cells. The RPE cells were kept at −80 °C until used. RPE lysates were diluted 1:1 with 2× radioimmunoprecipitation buffer (RIPA) (0.2% SDS, 2% Triton X 100, 2% deoxycholate, 0.15 M NaCl, 4 mM EDTA, 50 mM Tris pH 7.4) containing a cocktail of protease and phosphatase inhibitors (Sigma, St. Louis, MO, USA). Pieces of retinas collected from human donor eyes were collected into eppendorff tubes and lysed in 1× RIPA buffer. Cells were lyzed for 1 h at 4 °C in a rotator, centrifuged for 10 min at 14000 rpm and the supernatants were transferred to clean tubes. The protein concentration was determined using the MicroBCA kit (Pierce Biotechnology, Inc., Rockford, IL) according to the manufacture's directions.

### 2.3. Western blot analysis of lysates

Protein from each sample (40 μg) was boiled in SDS sample buffer (62.5 mM Tris-HCl (pH 6.8), 25% glycerol, 0.01% bromophenol blue, and 2% SDS), separated on a 10–20% Novex®-Tris-Glycine gel (Invitrogen Corporation, Carlsbad, CA) and electrotransferred to Immobilon PVDF membranes (Millipore, Bedford, MA) using a Bio-Rad Semi-Dry Electrophoretic Transfer Cell (20 min transfer at 18 V). Membranes were incubated with antibodies to modified citrulline (#17-347, from the Anti-Citrulline (modified) Detection Kit, EMD Millipore, Lake Placid, NY) and PAD2 (ab16478, Abcam, Cambridge, MA) in Blotto A buffer (20 mM Tris/HCl, 0.9% NaCl, 0.05% Tween 20 (TBST), 5% skimmed milk) for 1 h. For detection of deimination, PVDF membranes were incubated at 37 °C overnight without agitation with modification buffer, prepared by mixing 1 part of reagent A (0.025% $FeCl_3$ in a solution of sterile, distilled water/98%$H_2SO_4$/85%$H_3PO_4$ (55%/25%/20%)) and 1 part of reagent B (0.5% 2,3-butanedione monoxime, 0.25% antipyrine, 0.5 M acetic acid) as described in the anti-citrulline (modified) detection kit (Millipore). After extensive washing and blocking, membranes were reacted with secondary antibodies conjugated to peroxidase and signal was visualized using chemiluminescence Reagent Plus (NEN™ Life Science Products, Inc., Boston, MA) detection system.

The gels were stained with Gelcode Blue (Thermo Scientific, Rockford, IL), after partial transfer to PVDF membranes to serve as a reference for the load homogeneity of the samples as previously described (Bando et al., 2007; Bonilha et al., 2008). Briefly, both gel and blot were digitized using a densitometer (BIO-RAD GS800), and the density of the gel and bands was measured and transferred to pixels using Quantity One 4.6.8. A rectangular area was drawn around the most intense band signal in the scanned blots and used as a template to determine the number of pixels in these areas. Plotted signals represent pixel intensity for each band after subtraction from the background signal. The total protein pixel number from each donor lane stained with Gelcode Blue in the transferred gel was quantified. The previously determined number of pixels in the Western blot was divided by the pixels in the Gelcode Blue lane, and these then were used to establish the pixel count per sample. The average pixel count was determined as a mean of all the AMD and non-AMD samples. Standard error and *t*-test were calculated using GraphPad Software (http://www.graphpad.com/quickcalcs/ttest1.cfm) and are presented in Section 3.

### 2.4. Immunohistology of tissue

The presence of deiminated proteins was investigated in cryosections of AMD and non-AMD eyes in the perifoveal area (between the fovea and the optic nerve head). Eye pieces of retina-RPE-choroid were cut and fixed by immersion in 4% paraformaldehyde made in PBS overnight at 4 °C, quenched with 50 mM $NH_4Cl$ made in PBS for 1 h at 4 °C, infused successively with 10% and 20% sucrose made in the same buffer and with Tissue-Tek "4583" (Miles Inc., Elkhart, IN). 10–12 μm cryosections were cut on a cryostat HM 505E (Microm, Walldorf, Germany) equipped with a CryoJane Tape-Transfer system (Instrumedics, Inc., Hackensack, NJ, USA). For detection of protein deimination, cryosections of retina-RPE-choroid were processed and labeled using anti-citrulline (modified) detection kit as described in western blot analysis. Briefly, cryosections of retina-RPE-choroid were hydrated, the freezing medium (3 parts of 20% sucrose made in PBS to 7 parts of Tissue-Tek "4583") was removed and cryosections of retina-RPE-choroid were treated with freshly made modification buffer for 30 min at 37 °C. Tissue was blocked in PBS supplemented with +1% BSA (PBS/BSA) for 30 min, and incubated with the antibodies to protein deimination (Millipore) and PAD2. The monoclonal PAD2 antibody has been previously described and characterized in rat retinas (Koike et al., 1994; Bhattacharya et al., 2008). Cell nuclei were labeled with TO-PRO®-3 iodide (Molecular Probes). Secondary antibody (goat anti-rabbit IgG; 1:1000) was labeled with Alexa Fluor 488. Sections were analyzed using a Leica laser scanning confocal microscope (TCS-SP2, Leica, Exton, PA). A series of 1 μm *xy* (*en face*) sections were collected. Each individual *xy* image of the retinas stained represents a three-dimensional projection of the entire cryosection (sum of all images in the stack). Microscopic panels were composed using Adobe Photoshop CS3 (Adobe, San Jose, CA). The labeling controls were incubated with secondary antibodies only.

### 2.5. Genetic analysis of AMD samples

Several of the donor samples (11 non-AMD and 25 AMD) were genotyped for single nucleotide polymorphisms (SNPs) previously shown to be associated with the development and progression of AMD. DNA was extracted from blood or eye tissue by means of the Gentra Systems PUREGENE DNA Purification kit (Qiagen, Minneapolis, MN). Samples were genotyped for SNPs rs1061170 (*CFH*), rs10490924 (*ARMS2*), rs11200638 (*HTRA1*), and rs2230199 (*C3*), using TaqMan SNP genotyping assays.

## 3. Results

### 3.1. Immunolocalization of deimination in retinas of AMD donors

To define the localization of deiminated proteins and PAD2 in the retina of AMD donors several samples were analyzed. Representative fundus images are presented in Fig. 1 of one non-AMD eye (Fig. 1A) and four advanced AMD eyes (Fig. 1B–E). Evidence for GA (Fig. 1B–C) and neovascular AMD (Fig. 1D–E) can be observed in the areas selected for histological analysis (Fig. 1, rectangles).

The distribution of deiminated proteins from perifovea of non-AMD (Fig. 2A and D) and in AMD retinas (Fig. 2B, C, E and F) is illustrated in Fig. 2. Analysis of the retinal sections showed that the localization of immunoreactivity of deiminated proteins in AMD retinas was similar to that observed in non-AMD retinas. Specifically, labeling was observed in ganglion cell, inner nuclear layer and outer nuclear layer as well as the choroid in non-AMD retinas (Fig. 2A) when deimination labeling was overlaid on differential contrast images (DIC) of the retina. Interestingly, deimination immunoreactivity was mostly localized to the nuclei of cells in each of these locations. A disorganized distribution of deiminated proteins was evident in the degenerated areas of the retinas of AMD donors due to retina modeling as evidenced by the retina morphology (Fig. 2B, C, E and F, braces). Non-AMD (Fig. 2D) and AMD (data not shown) retinas labeled only with the secondary antibody did not display any deiminated protein labeling.

### 3.2. *Similar immunolocalization of PAD2 in retinas of several AMD donors*

The distribution of PAD2 was also analyzed in the perimacula of AMD and non-AMD retinas (Fig. 3). Interestingly, PAD2 immunoreactivity was stronger and more abundant than deimination. PAD2 was detected in all retinal lamina in both non-AMD (Fig. 3A) and AMD retinas from several donors (Fig. 3B, C, E and F). PAD2 also localized to the nuclei of cells in the ganglion cell layer, and the inner and outer nuclear layer. A disorganized distribution of PAD2 was evident in the degenerated areas of the retinas of AMD donors (Fig. 3B, C, E and F, braces). Non-AMD (Fig. 3D) and AMD (data not shown) retinas labeled only with the secondary antibody did not display any PAD2 labeling; non-AMD retina displayed typical laminar organization.

### 3.3. *Protein deimination in RPE and retina lysates of AMD donors*

The intensity of immunoreactivity of deiminated protein within the AMD and non-AMD RPE and retinas were separately analyzed by western blot analysis using anti-modified citrulline antibody and comparison to gels stained with Gelcode blue after partial transfer to PVDF membranes to serve as reference for the load homogeneity of the samples (Fig. 4A and D). Our analysis revealed significant increase in the immunoreactivity in AMD RPE lysates (Fig. 4B, lane 5–8) when compared to non-AMD retinas (Fig. 4B, lane 1–4). The specificity of the immunoreactivity was demonstrated by reacting Drosophila (canton S strain) whole extract, which lacks PADs (Fig. 4B, lane 9), and Drosophila whole extract that has been subjected to citrullination with PAD2 incubation (Fig. 4B, lane 10). Significant increase in the deiminated immunoreactivity was also observed in AMD (Fig. 4E, lane 5–8) and non-AMD retinal lysates (Fig. 4E, lane 1–4). The deiminated proteins in RPE lysates showed several prominent protein bands (ca. between 82 and 49 kDa and ~200 kDa, Fig. 4B). In contrast, the retinal lysates displayed several major bands in the molecular weight range 37–64 kDa (Fig. 4E). Immunoblot quantification of RPE and retina lysates obtained from AMD donor eyes displayed significant increase in protein deimination immunoreactivity intensity (Fig. 4C and F). Quantitation of these blots showed that protein deimination immunoreactivity was upregulated 1.8 fold in AMD RPE and 2.2 fold in AMD retina samples when compared with non-AMD samples. These differences were statistically significant ($p = 0.0164$ in the RPE and $p = 0.0481$ in the retinas) (Fig. 4C and F).

### 3.4. *PAD2 in RPE and retina lysates of AMD donors*

The differences in immunoreactivity of PAD2 within the AMD and non-AMD RPE and retinas were addressed by Western

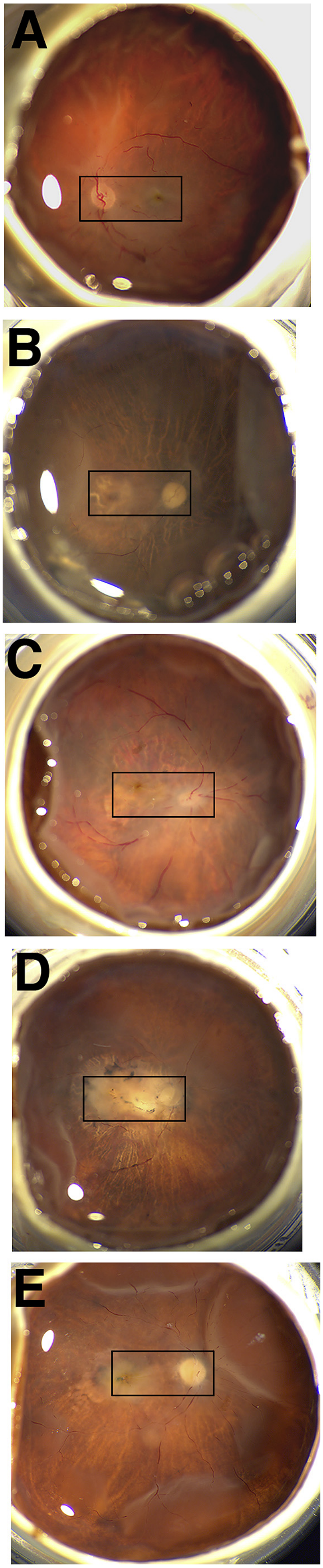

**Fig. 1.** *In situ* imaging of whole AMD and age-matched non-AMD donor eyes. The optic nerve head, macula and retinal veins were visible in the macroscopic fundus image of the non-AMD eye (A). AMD samples displayed typical geographic atrophy (B, D) and exudate accumulation around the macula (C–E). Rectangles highlight the areas selected for histological analysis.

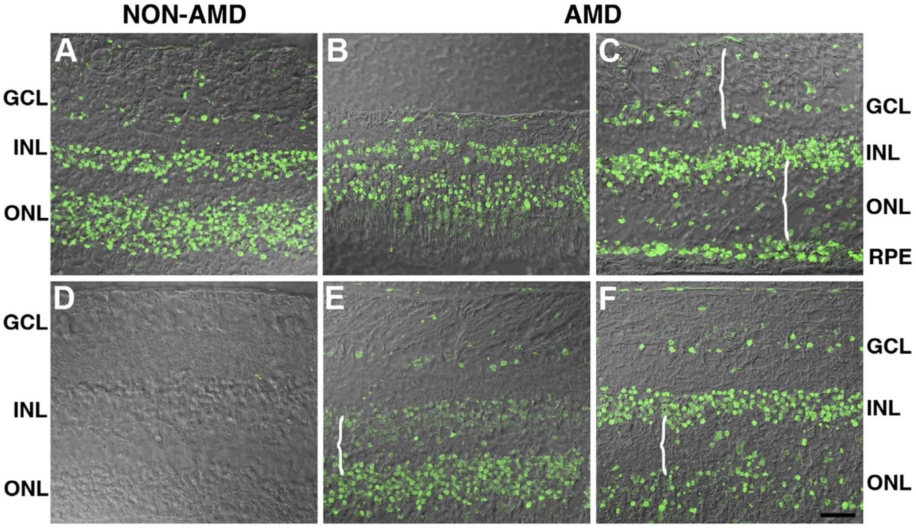

**Fig. 2.** Protein deimination localization is similar in the retinas of AMD and non-AMD donors. The levels of protein deimination staining were analyzed in the perifovea of non-AMD (A) and AMD retinas (B, C, E, F). Immunoreactivity was overlaid on differential contrast images (DIC) of the retina. Analysis of the AMD retinal sections showed that the levels of deiminated proteins observed were similar to the levels observed in non-AMD retinas. Specifically, non-AMD retinas displayed protein deimination in the ganglion cell layer (GCL), inner nuclear layer (INL), outer nuclear layer (ONL). Interestingly, deimination was frequently localized to the nuclei of cells in these layers of both AMD and non-AMD. A disorganized distribution of deiminated proteins was visible in the degenerated areas of the retinas of AMD donors (braces). Non-AMD (D) and AMD (data not shown) retinas labeled only with the secondary antibody did not display any deiminated protein labeling bar. Bar = 40 μm.

analysis. Whole RPE (Fig. 5A–C) and retina (Fig. 5D–F) lysates were harvested, resolved in an SDS-PAGE and transferred to a membrane and reacted with PAD2 antibody. Western blot using anti-PAD2 antibody revealed no significant differences in the immunoreactivity between non-AMD (Fig. 5B, lane 1–4) and AMD (Fig. 5B, lane 5–8) RPE lysates. Similar observations were also made for non-AMD (Fig. 5E, lane 1–4) and AMD retinal (Fig. 5E, lane 5–8) lysates probed with anti-PAD2 antibody. Quantitation of these blots showed PAD2 immunoreactivity was upregulated 1.2 fold in both AMD RPE and retina samples when compared with non-AMD samples. However, these differences were not statistically significant ($p = 0.2193$ in RPE and $p = 0.4535$ in retinas) (Fig. 5C and F).

### 3.5. *No differential genetic association in AMD compared to non-AMD donors*

Among the donor tissue studied, 11 non-AMD and 25 AMD were genotyped for four SNPs previously associated with the risk and progression of AMD. These included: (1) complement factor H (*CFH*) Y402H (rs1061170), (2) age-related maculopathy susceptibility 2 (*ARMS2*, also called LOC387715) A69S (rs10490924), (3) high temperature requirement factor A1 (*HTRA1*) (rs11200638), and (4) complement component 3 (*C3*) R80G (rs2230199). The minor allele frequencies for each SNP are shown in Table 2. There was no significant difference between the AMD samples and the non-AMD samples at any of the SNPs.

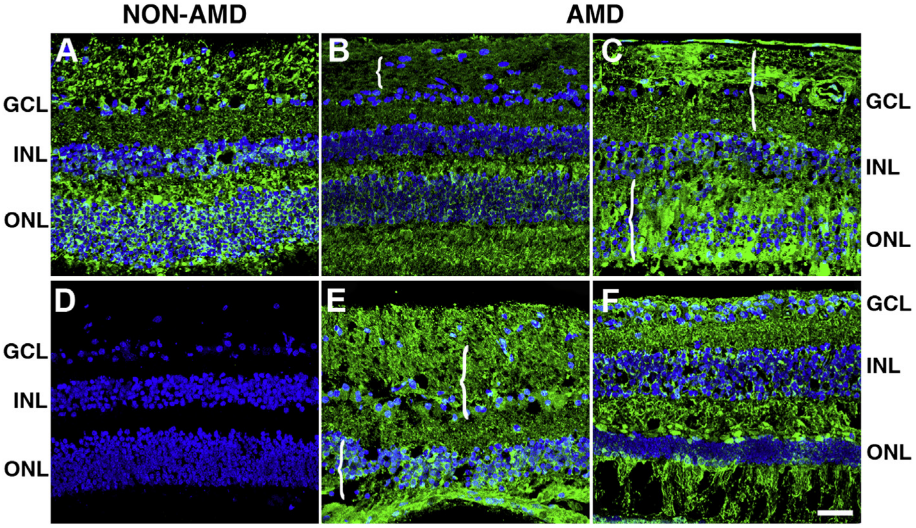

**Fig. 3.** PAD2 levels are similar in the retinas of AMD and non-AMD donors. The levels of PAD2 were analyzed in the perifovea of non-AMD (A, D) and AMD retinas (B, C, E, F). Nuclei were labeled with TO-PRO3 and are shown in blue to serve as a reference for the retinal layers. Analysis of the AMD retinal sections showed that the levels of PAD2 were similar to the levels observed in non-AMD retinas. Immunolocalization of PAD2 was present in all retinal layers, namely, ganglion cell layer (GCL), inner nuclear layer (INL), outer nuclei layer (ONL). Interestingly, PAD2 was frequently localized to the nuclei of cells in the GCL and INL. A disorganized distribution of PAD2 was visible in the degenerated areas of the retinas of AMD donors (braces) Non-AMD (D) and AMD (data not shown) retinas labeled only with the secondary antibody did not display any deiminated protein labeling. Bar = 40 μm.

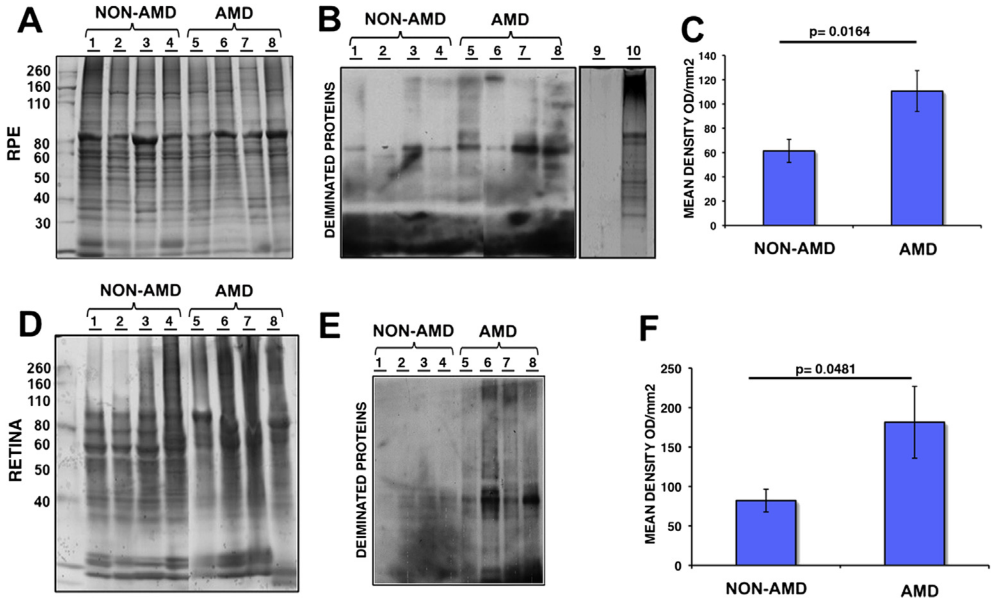

**Fig. 4.** Increased expression of deiminated proteins in RPE and retina lysates of AMD and non-AMD donors. RPE (A–C) and retinas (D–F) from several AMD donors were harvested and lysed. A representative gel is shown stained with Gelcode blue after partial transfer to PVDF membranes to serve as a reference for the load homogeneity of the samples (A, D). The same samples are also shown after immunoreactivity with the anti-citrulline antibody (B, E). Drosophila whole extracts (which lacks PADs) before (B, lane 9) and after (B, lane 10) incubation with PAD2 provided controls for anti-citrulline antibody immunoreactivity. In C, and F, the mean signal intensity was plotted for AMD and non-AMD samples ± error bars. Protein deimination immunoreactivity was approximately 1.8 fold higher in AMD RPE compared with non-AMD RPE ($p = 0.\ 0164$ by Student's *t*-test, $n = 10$). In addition, protein deimination immunoreactivity was approximately 2.2 fold higher in AMD retinas compared with non-AMD retinas ($p = 0.0481$ by Student's *t*-test, $n = 7$).

## 4. Discussion

Deimination is a form of protein PTM involving conversion of arginine residues into citrulline. This reaction is carried out by PAD2 in the retina. Previously, we observed lower levels on proteins deimination in the retina and optic nerve as well as reduced blood levels in older rats compared to young animals. The purpose of this investigation was to define the distribution and relative levels of protein deimination and PAD2 in retinal tissues from AMD donor eyes for comparison with these tissues from age-matched non-AMD eyes. We found that deiminated proteins were highest in AMD tissues, but PAD2 levels were not increased above those present in non-AMD tissues. To our knowledge this is the first report on citrullination in retinas of donors with AMD.

The calcium-dependent enzymatic deimination of peptidyl-arginine to peptidyl-citrulline, leads to a decrease in the charge of

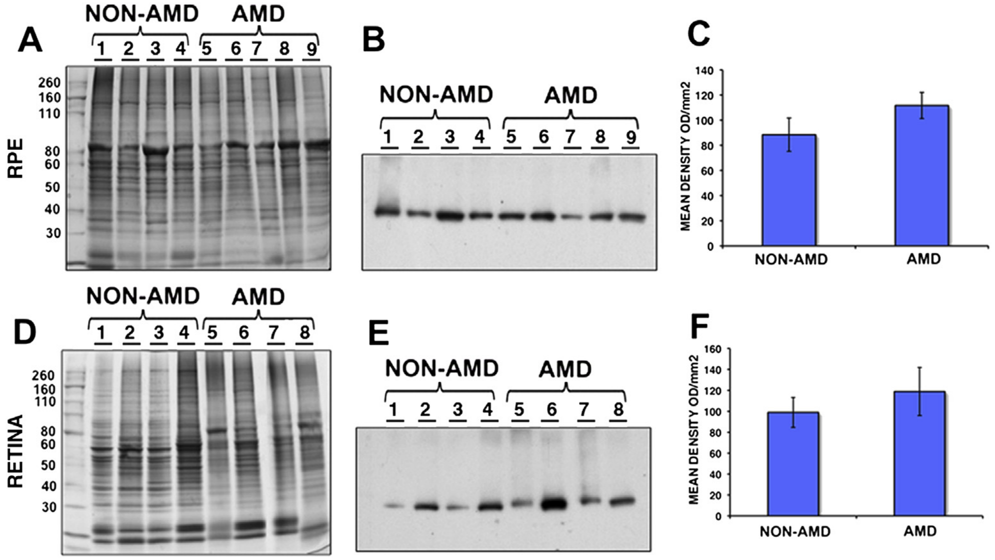

**Fig. 5.** Similar expression of PAD2 in RPE and retina lysates of AMD and non-AMD donors. RPE (A–C) and retinas (D–F) from AMD donors were harvested and lysed. A representative gel is shown stained with Gelcode blue after partial transfer to PVDF membranes to serve as a reference for the load homogeneity of the samples (A, D). The same samples are also shown after immunoreactivity of samples with the anti-PAD2 antibody (B, E). In C, and F, the mean signal intensity was plotted for AMD and non-AMD samples ± error bars. PAD2 immunoreactivity was approximately 1.2 fold higher in AMD RPE compared with non-AMD RPE ($p = 0.2193$ by Student's *t*-test, $n = 10$). PAD2 immunoreactivity was also approximately 1.2 fold higher in AMD retinas compared with non-AMD retinas ($p = 0.4535$ by Student's *t*-test, $n = 9$).

**Table 2**
Minor allele frequencies (MAF) for the SNPs genotyped in AMD and non-AMD donor eyes.

| SNP | Risk allele | MAF AMD | MAF Non-AMD | *p*-value |
|---|---|---|---|---|
| rs1061170 (*CFH*) | C | 0.40 | 0.36 | 1.000 |
| rs10490924 (*ARMS2*) | T | 0.28 | 0.23 | 0.772 |
| rs11200638 (*HTRA1*) | A | 0.28 | 0.23 | 0.772 |
| rs2230199 (*C3*) | G | 0.19 | 0.15 | 1.000 |

the modified proteins with major consequences on their conformation, stability and/or interactions. In turn, this affects their functions (Mechin et al., 2011). The physiologic significance of deimination is yet to be defined.

It has been reported that PAD2 activity in damaged neuronal tissue is often triggered by calcium imbalance (Asaga and Ishigami, 2001; Asaga et al., 2002). We did not specifically measure $Ca^{2+}$ levels in the samples analyzed. However, several reports suggest that changes in $Ca^{2+}$-signaling are observed in AMD retinas and may be a factor modulating PAD2 activity in AMD retinas (Spraul and Grossniklaus, 1997; Li et al., 2010; Vogt et al., 2011; Chen et al., 2012). First, oxidative stress, an important cause of retinal pigment epithelium death and subsequent AMD, induces calcium overload and leads to cell injury (Li et al., 2010). Second, it has been shown that all-trans-retinal-mediated photoreceptor degeneration *in vivo* is associated with changes in $PLC/IP_3/Ca^{2+}$ signaling (Chen et al., 2012). Third, calcification of Bruch's membrane has been reported in postmortem eyes from AMD donors (Spraul and Grossniklaus, 1997) and is increased in geographic atrophy eyes (Vogt et al., 2011). Fourth, calcification is an end-stage of drusen (Rudolf et al., 2008).

Variability was observed in the PAD2 immunoreactivity and protein deimination in the AMD and non-AMD retinal lysates. This observation may be related to different genetic markers and environmental factors associated with each sample. Indeed, it is known that genetic factors and environment influence susceptibility to AMD (Smith et al., 2001; Chen et al., 2010, 2011; Choudhury et al., 2011; Seddon et al., 2011). However, our analysis of the four SNPs that are consistently shown to have the strongest associations with the development and progression of AMD revealed no difference between AMD and non-AMD samples. These results suggest that genetic risk factors do not influence deimination of proteins in AMD retinas. Environmental factors such as smoking have been linked to deimination in both rheumatoid arthritis and multiple sclerosis (Klareskog et al., 2006a, 2006b; Mahdi et al., 2009; Kochi et al., 2011). However, the information available for the tissue analyzed did not include donors smoking habits.

Our unpublished data determined that the levels of PAD1, PAD3 and PAD4 remains unchanged in the AMD tissue compared to controls using quantitative amplified message (real time PCR). In addition, almost none or very low levels of PAD1 and PAD3 protein were detected in RPE lysates. Therefore, the changes in citrullination reported here are likely related to PAD2 activity.

In conclusion, we found that protein deimination but not PAD2 was significantly increased in AMD retinas and RPE lysates. While PAD2 levels were not significantly increased in AMD tissue, it is possible that its enzymatic activity is different in AMD samples, while the level of PAD2 remains the same. It is also possible that in AMD samples, the deiminated proteins accumulate due to reduced turnover/lysosomal and/or proteasomal function. Indeed, RPE lysosomal activity is a cellular function reported to be altered in AMD (Beatty et al., 2000; Mettu et al., 2012). In addition, increased expression of proteins involved in the proteasomal pathway was also reported in the retinas of AMD donors (Ethen et al., 2006, 2007).

Our results, suggest that protein deimination may have a role in the pathology of AMD and that deiminated proteins might become a useful biomarker for neurodegeneration in this disease. Our experiments did not address the identity of proteins deiminated in the AMD retinas. Previously, immunoprecipitation and mass spectrometry have identified about 36 proteins that potentially undergo deimination in the human retina (Bhattacharya, 2009). Several of these proteins could be citrullinated in AMD retinas leading to changes in their biological activity. Alternatively, it is possible that molecules involved in soft tissue calcification such as pyrophosphate, fetuin A, matrix gla protein, vitamin K, and ATP-binding cassettes 6, among other proteins may be regulated through deimination in the retina.

## Acknowledgments

Supported by NIH grants EY014240 (JGH), a Research Center Grant from the Foundation Fighting Blindness (JGH), a Challenge Grant from Research to Prevent Blindness (JGH) and Research to Prevent Blindness career award (SKB).

## References

Acharya, N.K., Nagele, E.P., Han, M., Coretti, N.J., DeMarshall, C., Kosciuk, M.C., Boulos, P.A., Nagele, R.G., 2012. Neuronal PAD4 expression and protein citrullination: possible role in production of autoantibodies associated with neurodegenerative disease. J. Autoimmun. 38, 369–380.

Asaga, H., Ishigami, A., 2001. Protein deimination in the rat brain after kainate administration: citrulline-containing proteins as a novel marker of neurodegeneration. Neurosci. Lett. 299, 5–8.

Asaga, H., Akiyama, K., Ohsawa, T., Ishigami, A., 2002. Increased and type II-specific expression of peptidylarginine deiminase in activated microglia but not hyperplastic astrocytes following kainic acid-evoked neurodegeneration in the rat brain. Neurosci. Lett. 326, 129–132.

Beatty, S., Koh, H., Phil, M., Henson, D., Boulton, M., 2000. The role of oxidative stress in the pathogenesis of age-related macular degeneration. Surv. Ophthalmol. 45, 115–134.

Bando, H., Shadrach, K.G., Rayborn, M.E., Crabb, J.W., Hollyfield, J.G., 2007. Clathrin and adaptin accumulation in drusen, Bruch's membrane and choroid in AMD and non-AMD donor eyes. Exp. Eye Res. 84, 135–142.

Bhattacharya, S.K., Bhat, M.B., Takahara, H., 2006a. Modulation of peptidyl arginine deiminase 2 and implication for neurodegeneration. Curr. Eye Res. 31, 1063–1071.

Bhattacharya, S.K., Crabb, J.S., Bonilha, V.L., Gu, X., Takahara, H., Crabb, J.W., 2006b. Proteomics implicates peptidyl arginine deiminase 2 and optic nerve citrullination in glaucoma pathogenesis. Invest. Ophthalmol. Vis. Sci. 47, 2508–2514.

Bhattacharya, S.K., Sinicrope, B., Rayborn, M.E., Hollyfield, J.G., Bonilha, V.L., 2008. Age-related reduction in retinal deimination levels in the F344BN rat. Aging Cell 7, 441–444.

Bhattacharya, S.K., 2009. Retinal deimination in aging and disease. IUBMB Life 61, 504–509.

Biarnés, M., Monés, J., Alonso, J., Arias, L., 2011. Update on geographic atrophy in age-related macular degeneration. Optom. Vis. Sci. 88, 881–889.

Bonilha, V.L., Rayborn, M.E., Shadrach, K.G., Li, Y., Lundwall, A., Malm, J., Hollyfield, J.G., 2008. Semenogelins in the human retina: differences in distribution and content between AMD and normal donor tissues. Exp. Eye Res. 86, 150–156.

Bressler, N.M., Frost, L.A., Bressler, S.B., Murphy, R.P., Fine, S.L., 1988. Natural course of poorly defined choroidal neovascularization associated with macular degeneration. Arch. Ophthalmol. 106, 1537–1542.

Cafaro, T.A., Santo, S., Robles, L.A., Crim, N., Urrets-Zavalia, J.A., Serra, H.M., 2010. Peptidylarginine deiminase type 2 is over expressed in the glaucomatous optic nerve. Mol. Vis. 16, 1654–1658.

Chen, Y., Bedell, M., Zhang, K., 2010. Age-related macular degeneration: genetic and environmental factors of disease. Mol. Interv. 10, 271–281.

Chen, Y., Okano, K., Maeda, T., Chauhan, V., Golczak, M., Maeda, A., Palczewski, K., 2012. Mechanism of all-trans-retinal toxicity with implications for stargardt disease and age-related macular degeneration. J. Biol. Chem. 287, 5059–5069.

Chen, Y., Zeng, J., Zhao, C., Wang, K., Trood, E., Buehler, J., Weed, M., Kasuga, D., Bernstein, P.S., Hughes, G., Fu, V., Chin, J., Lee, C., Crocker, M., Bedell, M., Salasar, F., Yang, Z., Goldbaum, M., Ferreyra, H., Freeman, W.R., Kozak, I., Zhang, K., 2011. Assessing susceptibility to age-related macular degeneration with genetic markers and environmental factors. Arch. Ophthalmol. 129, 344–351.

Chou, S.M., Wang, H.S., Taniguchi, A., 1996. Role of SOD-1 and nitric oxide/cyclic GMP cascade on neurofilament aggregation in ALS/MND. J. Neurol. Sci. 139 (Suppl.), 16–26.

Choudhury, F., Varma, R., McKean-Cowdin, R., Klein, R., Azen, S.P., 2011. Risk factors for four-year incidence and progression of age-related macular degeneration: the los angeles latino eye study. Am. J. Ophthalmol. 152, 385–395.

Enrique-Algeciras, M., Ding, D., Mastronardi, F.G., Marc, R.E., Porciatti, V., Bhattacharya, S.K., 2013. Deimination restores inner retinal visual function in a demyelinating disease. J. Clin. Inv. 123 (2), 646–656.

Ethen, C.M., Reilly, C., Feng, X., Olsen, T.W., Ferrington, D.A., 2006. The proteome of central and peripheral retina with progression of age-related macular degeneration. Invest. Ophthalmol. Vis. Sci. 47, 2280–2290.

Ethen, C.M., Hussong, S.A., Reilly, C., Feng, X., Olsen, T.W., Ferrington, D.A., 2007. Transformation of the proteasome with age-related macular degeneration. FEBS Lett. 581, 885–890.

Freund, K.B., Zweifel, S.A., Engelbert, M., 2010. Do we need a new classification for choroidal neovascularization in age-related macular degeneration? Retina 30, 1333–1349.

Giles, J.T., Fert-Bober, J., Park, J.K., Bingham 3rd, C.O., Andrade, F., Fox-Talbot, K., Pappas, D., Rosen, A., van Eyk, J., Bathon, J.M., Halushka, M.K., 2012. Myocardial citrullination in rheumatoid arthritis: a correlative histopathologic study. Arthritis Res. Ther. 14, R39.

Gyorgy, B., Toth, E., Tarcsa, E., Falus, A., Buzas, E.I., 2006. Citrullination: a post-translational modification in health and disease. Int. J. Biochem. Cell. Biol. 38, 1662–1677.

Harris, M.L., Darrah, E., Lam, G.K., Bartlett, S.J., Giles, J.T., Grant, A.V., Gao, P., Scott Jr., W.W., El-Gabalawy, H., Casciola-Rosen, L., Barnes, K.C., Bathon, J.M., Rosen, A., 2008. Association of autoimmunity to peptidyl arginine deiminase type 4 with genotype and disease severity in rheumatoid arthritis. Arthritis Rheum. 58, 1958–1967.

Ishigami, A., Ohsawa, T., Hiratsuka, M., Taguchi, H., Kobayashi, S., Saito, Y., Murayama, S., Asaga, H., Toda, T., Kimura, N., Maruyama, N., 2005. Abnormal accumulation of citrullinated proteins catalyzed by peptidylarginine deiminase in hippocampal extracts from patients with Alzheimer's disease. J. Neurosci. Res. 80, 120–128.

Klareskog, L., Padyukov, L., Lorentzen, J., Alfredsson, L., 2006a. Mechanisms of disease: genetic susceptibility and environmental triggers in the development of rheumatoid arthritis. Nat. Clin. Pract. Rheumatol. 2, 425–433.

Klareskog, L., Stolt, P., Lundberg, K., Kallberg, H., Bengtsson, C., Grunewald, J., Ronnelid, J., Harris, H.E., Ulfgren, A.K., Rantapaa-Dahlqvist, S., Eklund, A., Padyukov, L., Alfredsson, L., 2006b. A new model for an etiology of rheumatoid arthritis: smoking may trigger HLA-DR (shared epitope)-restricted immune reactions to autoantigens modified by citrullination. Arthritis Rheum. 54, 38–46.

Kochi, Y., 2010. Genetic background of tolerance breakdown in rheumatoid arthritis. Nihon Rinsho Meneki Gakkai Kaishi 33, 48–56.

Kochi, Y., Thabet, M.M., Suzuki, A., Okada, Y., Daha, N.A., Toes, R.E., Huizinga, T.W., Myouzen, K., Kubo, M., Yamada, R., Nakamura, Y., Yamamoto, K., 2011. PADI4 polymorphism predisposes male smokers to rheumatoid arthritis. Ann. Rheum. Dis. 70, 512–515.

Koike, H., Sase, K., Uchida, H., Sudo, T., Shiraiwa, M., Sugawara, K., Takahara, H., 1994. Production and epitope specificity of monoclonal antibody against mouse peptidylarginine deiminase type II. Biosci. Biotechnol. Biochem. 58, 2286–2287.

Li, G.Y., Fan, B., Zheng, Y.C., 2010. Calcium overload is a critical step in programmed necrosis of ARPE-19 cells induced by high-concentration $H_{(2)}O_{(2)}$. Biomed. Environ. Sci. 23, 371–377.

Louw, C., Gordon, A., Johnston, N., Mollatt, C., Bradley, G., Whiteley, C.G., 2007. Arginine deiminases: therapeutic tools in the etiology and pathogenesis of Alzheimer's disease. J. Enzym. Inhib. Med. Chem. 22, 121–126.

Mahdi, H., Fisher, B.A., Kallberg, H., Plant, D., Malmstrom, V., Ronnelid, J., Charles, P., Ding, B., Alfredsson, L., Padyukov, L., Symmons, D.P., Venables, P.J., Klareskog, L., Lundberg, K., 2009. Specific interaction between genotype, smoking and autoimmunity to citrullinated alpha-enolase in the etiology of rheumatoid arthritis. Nat. Genet. 41, 1319–1324.

Mechin, M.C., Nachat, R., Coudane, F., Adoue, V., Arnaud, J., Serre, G., Simon, M., 2011. Deimination or citrullination, a post-translational modification with many physiological and pathophysiological facets. Med. Sci. (Paris) 27, 49–54.

Mettu, P.S., Wielgus, A.R., Ong, S.S., Cousins, S.W., 2012. Retinal pigment epithelium response to oxidant injury in the pathogenesis of early age-related macular degeneration. Mol. Aspects Med. 33, 376–398.

Mohlake, P., Whiteley, C.G., 2010. Arginine metabolising enzymes as therapeutic tools for Alzheimer's disease: peptidyl arginine deiminase catalyses fibrillogenesis of beta-amyloid peptides. Mol. Neurobiol. 41, 149–158.

Moscarello, M.A., Wood, D.D., Ackerley, C., Boulias, C., 1994. Myelin in multiple sclerosis is developmentally immature. J. Clin. Invest. 94, 146–154.

Moscarello, M.A., Mastronardi, F.G., Wood, D.D., 2007. The role of citrullinated proteins suggests a novel mechanism in the pathogenesis of multiple sclerosis. Neurochem. Res. 32, 251–256.

Nakata, K., Crabb, J.W., Hollyfield, J.G., 2005. Crystallin distribution in Bruch's membrane-choroid complex from AMD and age-matched donor eyes. Exp. Eye Res. 80, 821–826.

Nicholas, A.P., 2011. Dual immunofluorescence study of citrullinated proteins in Parkinson diseased substantia nigra. Neurosci. Lett. 495, 26–29.

Nicholas, A.P., Sambandam, T., Echols, J.D., Barnum, S.R., 2005. Expression of citrullinated proteins in murine experimental autoimmune encephalomyelitis. J. Comp. Neurol. 486, 254–266.

Olsen, T.W., Feng, X., 2004. The Minnesota Grading System of eye bank eyes for age-related macular degeneration. Invest. Ophthalmol. Vis. Sci. 45, 4484–4490.

Rudolf, M., Clark, M.E., Chimento, M.F., Li, C.M., Medeiros, N.E., Curcio, C.A., 2008. Prevalence and morphology of druse types in the macula and periphery of eyes with age-related maculopathy. Invest. Ophthalmol. Vis. Sci. 49, 1200–1209.

Seddon, J.M., Reynolds, R., Yu, Y., Daly, M.J., Rosner, B., 2011. Risk models for progression to advanced age-related macular degeneration using demographic, environmental, genetic, and ocular factors. Ophthalmology 118, 2203–2211.

Smith, W., Assink, J., Klein, R., Mitchell, P., Klaver, C.C., Klein, B.E., Hofman, A., Jensen, S., Wang, J.J., de Jong, P.T., 2001. Risk factors for age-related macular degeneration: pooled findings from three continents. Ophthalmology 108, 697–704.

Spraul, C.W., Grossniklaus, H.E., 1997. Characteristics of Drusen and Bruch's membrane in postmortem eyes with age-related macular degeneration. Arch. Ophthalmol. 115, 267–273.

Vogt, S.D., Curcio, C.A., Wang, L., Li, C.M., McGwin Jr., G., Medeiros, N.E., Philp, N.J., Kimble, J.A., Read, R.W., 2011. Retinal pigment epithelial expression of complement regulator CD46 is altered early in the course of geographic atrophy. Exp. Eye Res. 93, 413–423.

Vossenaar, E.R., Zendman, A.J., van Venrooij, W.J., Pruijn, G.J., 2003. PAD, a growing family of citrullinating enzymes: genes, features and involvement in disease. Bioessays 25, 1106–1118.

Yamada, R., Suzuki, A., Chang, X., Yamamoto, K., 2005. Citrullinated proteins in rheumatoid arthritis. Front. Biosci. 10, 54–64.

# Chapter 60
# Imaging Human Postmortem Eyes with SLO and OCT

**Nika Bagheri, Brent A. Bell, Vera L. Bonilha, and Joe G. Hollyfield**

**Keywords** Scanning laser ophthalmoscope • Optical coherence tomography • Macular hole • Retinal pigment epithelium detachment • Age-related macular degeneration • Retinitis pigmentosa

## 60.1 Introduction

The confocal scanning laser ophthalmoscope (SLO) and the spectral-domain optical coherence tomography (OCT) are two imaging systems that have rapidly revolutionized clinical ophthalmology. SLO is a noncontact, high-resolution imaging system that is now a worldwide standard in macular diagnostics. It has multiple imaging modes that provide contrast for imaging a variety of retinal conditions (Sharp and Manivannan 1997). Currently, SLO is used to evaluate a wide spectrum of retinal and choroidal diseases (Hassenstein and Meyer 2009). OCT provides in-depth structural detail of retinal morphology with an axial resolution of several microns. Today, this "noninvasive optical-biopsy" is used extensively for early diagnosis and precise monitoring of glaucoma and retinal diseases (Geitzenauer et al. 2010). These two instruments continue to make substantial advances in clinical ophthalmology (Da Pozzo et al. 2009; Wolf-Schnurrbusch et al. 2008; Imamura et al. 2009).

Here, we describe the use of SLO and OCT as the initial assessment to (1) screen "normal" postmortem eyes for retinal lesions, and (2) better characterize retinal lesions in eyes with suspected pathology prior to histological analysis. Just as the combination of SLO and OCT provides a comprehensive diagnostic assessment in the clinic, the combination of these two modalities ensures comprehensive characterization of retinal lesions prior to histopathology.

---

N. Bagheri • B.A. Bell • V.L. Bonilha • J.G. Hollyfield (✉)
Department of Ophthalmology, Cole Eye Institute (i31),
Cleveland Clinic Lerner College of Medicine, Cleveland, OH 44195, USA
e-mail: hollyfj@ccf.org

M.M. LaVail et al. (eds.), *Retinal Degenerative Diseases*, Advances in Experimental Medicine and Biology 723, DOI 10.1007/978-1-4614-0631-0_60,

## 60.2 Materials and Methods

### *60.2.1 Tissue Preparation*

Postmortem human eyes were obtained through the donor eye program of the Foundation Fighting Blindness (donations #777, #779, #784, #846, #908). Five donors (6 eyes) are described (Table 60.1). The first three donors' eyes had no grossly visible pathology. #846 had a fibrovascular scar consistent with end-stage age-related macular degeneration (AMD). #908 had extensive degeneration from retinitis pigmentosa (RP). Globes were initially fixed in 4% paraformaldehyde and 0.5% glutaraldehyde in 0.1 M phosphate buffer and later stored in 2% paraformaldehyde in the same buffer. Globes were bisected near the equator, dividing the globe into an anterior and posterior pole; the latter was used in this analysis.

### *60.2.2 Bright-Field Macroscopic Imaging*

Prior to imaging, each eye was placed in a custom holder to stabilize the posterior pole; this allows it to be immersed in phosphate buffered saline, minimizing surface reflectance artifact. The first set of images collected used conventional bright-field macrophotography with a Zeiss AxioCam MRC5 camera equipped with a Zoom 7000 Navitar macro video lens. Illumination was accomplished using a flexible, bifurcated fiber-optic coupled to a tungsten-halogen light source. Images were taken using Zeiss AxioVision AC Rel 4.5 software.

### *60.2.3 Scanning Laser Ophthalmoscope*

The next set of images was collected using SLO Heidelberg Retina Angiograph 2 (HRA2, Heidelberg Engineering, Inc.) equipped with a 55° wide field objective. The SLO housing was positioned so that the lens was directed down onto the aqueous surface for optimal imaging of the fundus. A 1,000 ± 2.5 μm ruby sphere was placed on the optic nerve head to provide a reference scale. Autofluorescence (AF) and infrared (IR) images were obtained. Lesion areas were estimated based on the mean of five separate hand drawn outlines using ImageJ software.

**Table 60.1** Human donor eye information

| Donation # | 779 | 777 | 784 | 846 | 908 |
|---|---|---|---|---|---|
| Eye(s) | OD | OD | OU | OD | OD |
| Age (years) | 74 | 74 | 95 | 71 | 79 |
| Gender | Female | Female | Female | Male | Male |
| Postmortem interval | 10.5 h | 6.5 h | 4 h | 7 h | 11 h |

### 60.2.4 Optical Coherence Tomography

The final set of images was collected using Spectral-domain OCT (Bioptigen, Inc.) operating at a peak wavelength of 840 and a 55 nm bandwidth with a 50° field of view (300 A-scans/B-scan by 300 B-scans/volume). The eye was positioned directly below the OCT objective.

## 60.3 Results

### 60.3.1 Normal Retina

Fundus images of #779 show an opaque appearance around the fovea consistent with edema (Fig. 60.1a). SLO AF images collect lipofuscin autofluorescence signal from the RPE. IR images penetrate farther into tissue, showing choroidal vasculature.

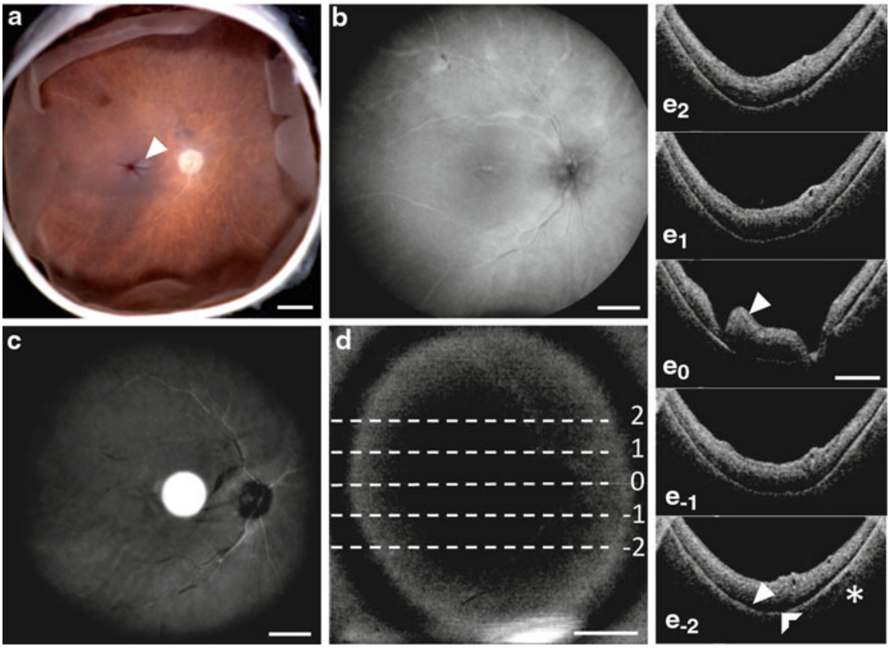

**Fig. 60.1** Imaging characterizes a normal donor eye. (**a**) Macroscopic fundus image shows an opaque appearance around the fovea consistent with edema (*closed arrow*). (**b**, **c**) SLO AF and IR images show no pathology. (**d**) *Dashed lines* on OCT fundus image indicate B-scan image planes. ($E_2$–$E_{-2}$) OCT is unremarkable at levels shown in (**d**) except for mild macular edema at 0 (*closed arrow*). The inner retina becomes opaque postmortem making retinal lamina difficult to differentiate; however, the photoreceptor layer (*closed arrow*), RPE (*open arrow*), and choroid (*asterisk*) remain visible. Scale = 2 mm

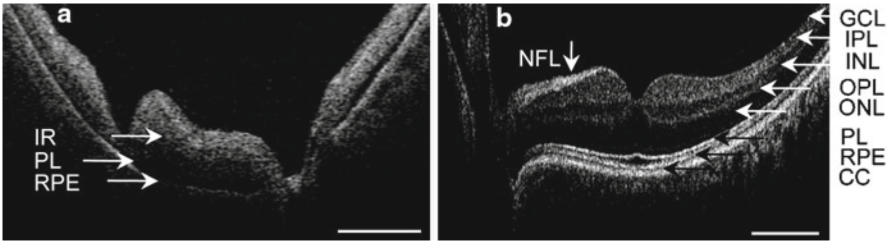

**Fig. 60.2** Postmortem (**a**) and in vivo (**b**) OCT B-scans of normal human retinas. *IR* inner retina; *NFL* nerve fiber layer; *GCL* ganglion cell layer; *IPL* inner plexiform layer; *INL* inner nuclear layer; *OPL* outer plexiform layer; *ONL* outer nuclear layer; *ELM* external limiting membrane; *PL* photoreceptor inner and outer segments; *RPE* retinal pigment epithelium; *CC* choriocapillaris. Scale = 2 mm

SLO imaging is unremarkable (Fig. 60.1b, c). OCT shows minor macular edema (Fig. 60.1d, 60.1$E_2$–$E_{-2}$). However, comparison of OCT from in vivo eyes with OCT from postmortem eyes shows that postmortem changes are accompanied by the loss of distinct retinal lamella (compare Fig. 60.2a, b).

### 60.3.2 Macular Hole

Fundus images of #777 show an opaque appearance around the fovea consistent with edema. In addition, exudate is seen around the optic nerve (Fig. 60.3a). SLO AF images show decreased autofluorescence around the optic nerve and macula (Fig. 60.3b). SLO IR images show increased reflectance around the optic nerve and within an oval-shaped area at the center of the macula (Fig. 60.3c). OCT imaging reveals a macular hole (Fig. 60.3d). At the center of the macular hole, an isolated retinal fragment corresponds to the small area of decreased autofluorescence in Fig. 60.3b. The hole corresponds to the oval-shaped area of increased reflectance in Fig. 60.3c. The perimacular area of decreased reflectance in Fig. 60.3c is due to increased scattering of light from retinal elevation surrounding the macular hole, which attenuates signal from the choroid.

### 60.3.3 RPE Detachment

Fundus images of #784 OD and OS show prominent choroidal vessels and exudate around the optic nerve (Fig. 60.4a). SLO AF images of both eyes have a subtle, halo-shaped area of increased autofluorescence at the fovea (Fig. 60.4b). OCT imaging reveals bilateral, focal RPE detachment centered on the fovea (Fig. 60.4c, d). The halo-shaped area of increased autofluorescence corresponds to changes in the elevation of the RPE in the region of detachment. The AF laser penetrates the epithelial

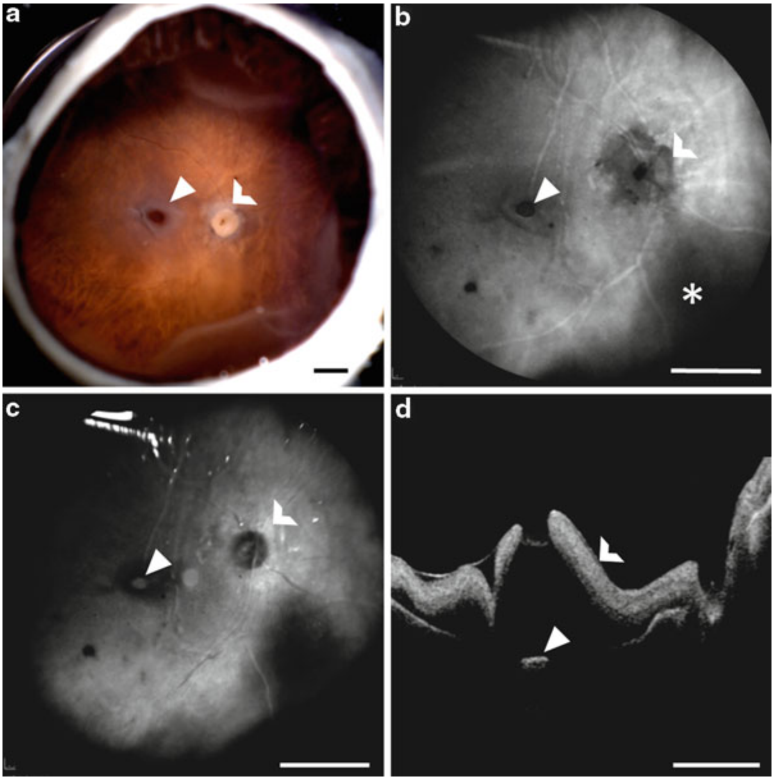

**Fig. 60.3** Imaging of normal donor eye reveals macular hole. (**a**) Macroscopic fundus image shows an opaque appearance around the fovea consistent with edema (*closed arrow*) and exudate around the optic nerve (*open arrow*). (**b**) SLO AF image shows a small area of decreased autofluorescence at the macula (*closed arrow*) and a well-demarcated area of decreased autofluorescence around the optic nerve (*open arrow*). *Dark areas* in periphery are due to retinal detachment (*asterisk*). (**c**) SLO IR image shows increased reflectance around the optic nerve corresponding to the region in (**b**) and consistent with RPE degeneration (*open arrow*). An oval-shaped area of increased reflectance at the center of the macula (*closed arrow*) is surrounded by a larger area of decreased reflectance. (**d**) OCT B-scan of the optic nerve and fovea reveals a macular hole with a piece of detached retina (*closed arrow*) and retinal elevation surrounding the hole (*open arrow*). Scale = 2 mm

surface at a tangential angle rather than a right angle, appearing as if the retinal thickness is increased adjacent to the detachment.

### 60.3.4 AMD Retina

Fundus images of #846 show a fibrovascular scar consistent with end-stage AMD (Fig. 60.5a). SLO AF imaging shows absence of autofluorescence in a large, central area similar to the fibrovascular scar (Fig. 60.5b). However, macroscopic image

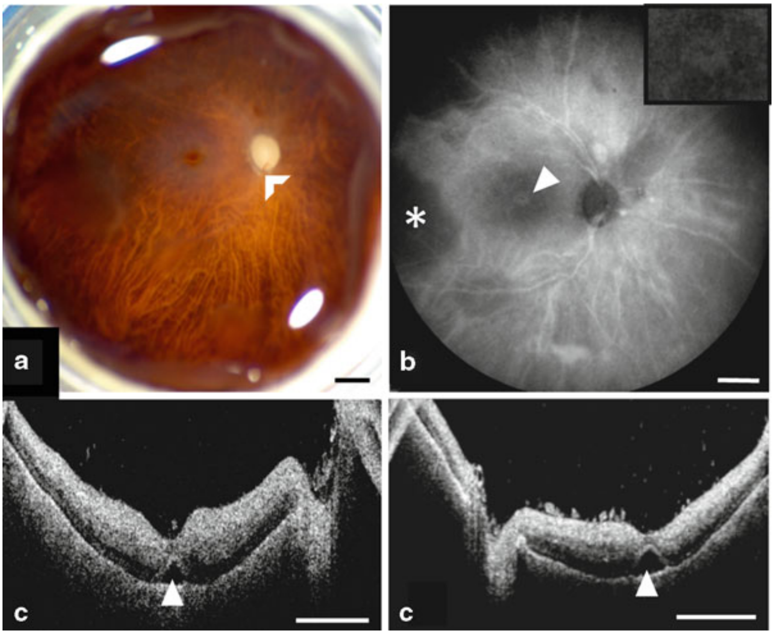

**Fig. 60.4** Imaging a pair of eyes from a normal donor reveals bilateral RPE detachment. (**a**) Macroscopic fundus images show RPE atrophy allowing for visualization of choroidal vessels and exudate around the optic nerve (*open arrow*) (OS not shown). (**b**) SLO AF images of both eyes have a subtle, halo-shaped area of increased autofluorescence at the fovea (*closed arrow*, *inset*) (OS not shown). Dark areas in periphery are due to retinal detachment (*asterisk*). (**c**, **d**) OCT B-scan of the optic nerve and fovea shows bilateral, focal RPE detachment centered on the fovea (*closed arrows*). Scale = 2 mm

estimates the lesion area to be 66.0 ± 1.22 $mm^2$ whereas AF image estimates the lesion area to be 75.9 ± 0.60 $mm^2$. SLO shows a 13% larger lesion than conventional bright-field macrophotography. A *t* test of the macroscopic lesion estimate versus the AF lesion estimate shows a significant difference ($p < 0.0001$) likely due to improved contrast with SLO. OCT also reveals areas with subretinal fibrosis (Fig. 60.5$C_2$–$C_{-2}$).

## 60.3.5 RP Retina

Fundus images of #908 show prominent choroidal vessels indicating atrophy of the overlying RPE and numerous bone spicule pigment deposits in the periphery encroaching on the macula (Fig. 60.6a). SLO AF imaging shows loss of autofluorescence consistent with RPE atrophy (Fig. 60.6b). OCT reveals thinning, degenerate retina toward the periphery and RPE detachment (Fig. 60.6$C_2$–$C_{-2}$). Bone spicule pigment deposits are not evident with OCT.

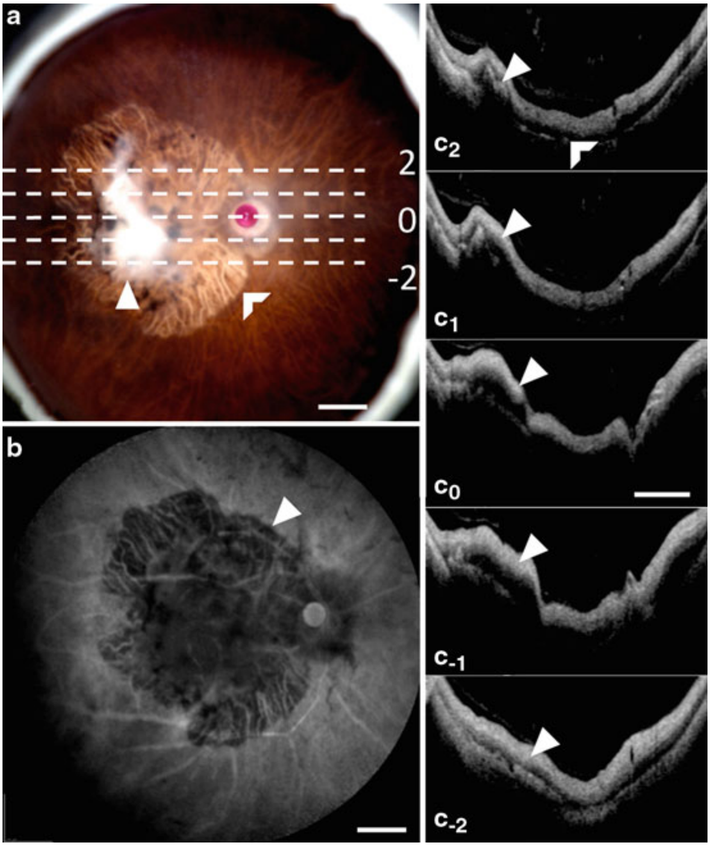

**Fig. 60.5** Imaging characterizes an end-stage AMD eye. (**a**) Macroscopic fundus image shows a fibrovascular scar (*closed arrow*) and a central area of RPE atrophy allowing visualization of choroidal vessels (*open arrow*). The ruby sphere is placed on the optic nerve head for magnification reference. *Dashed lines* indicate OCT image planes. (**b**) SLO AF image shows a large, well-defined area of decreased autofluorescence encompassing the optic nerve and macula (*closed arrow*) which corresponds to the central lesion in (**a**). Areas with autofluorescence correspond to the remaining area with RPE. $C_2$–$C_{-2}$: OCT B-scans indicated in (**a**) reveal bright collections directly above the RPE which raise the inner retinal layer and are consistent with fibrovascular scar (*closed arrows*). Small, *dome-shaped* irregularities below the RPE layer may be drusen (*open arrow*). Scale = 2 mm

## 60.4 Discussion

Although human donor eyes are invaluable to research, the vast majority are received with minimal clinical history and usually without fundus images. Here, we have attempted to address this perpetual challenge by applying the same technology used in the clinic to postmortem eyes.

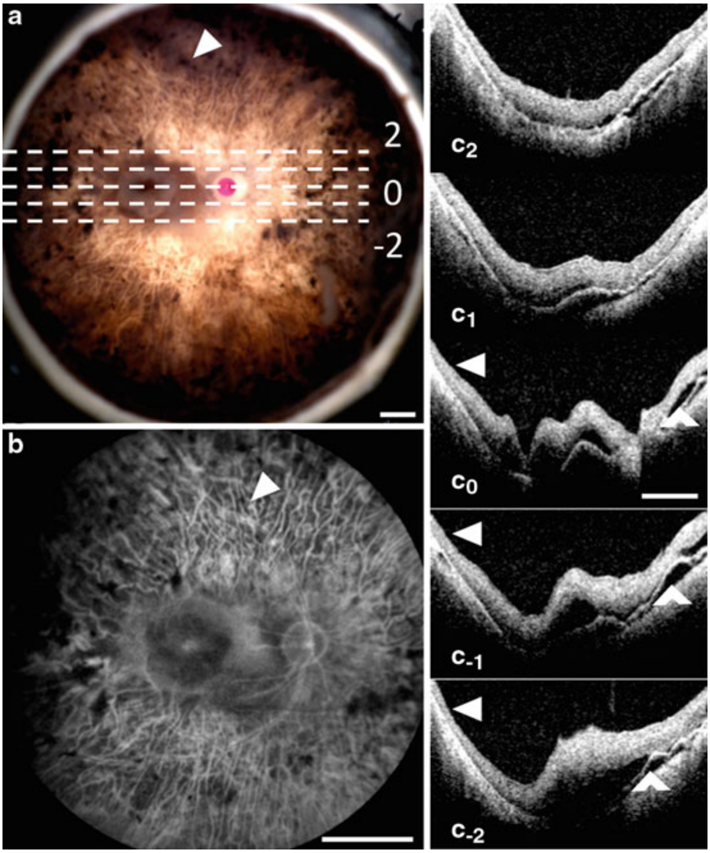

**Fig. 60.6** Imaging characterizes an RP eye. (**a**) Macroscopic fundus image shows prominent choroidal vessels indicative of RPE atrophy and bone spicule pigment deposits (*closed arrow*) in the periphery. The ruby sphere is placed on the optic nerve head for magnification reference. *Dashed lines* indicate OCT image planes. (**b**) SLO AF image shows loss of autofluorescence indicating RPE atrophy (*closed arrow*), particularly in the periphery and mid-periphery. $C_2$–$C_{-2}$: OCT B-scans indicated in (**a**) reveal thin, degenerate retina at the margins (*closed arrows*). RPE detachment is also seen (*open arrows*). Scale = 2 mm

In vivo imaging with SLO allows for angiography and provides detailed retinal and choroidal vasculature (Jorzik et al. 2005). Postmortem imaging with the AF and IR modes of SLO identifies areas with absent or atrophied RPE. SLO imaging with AF and IR of postmortem eyes reveals features of RPE and choroid similar to those of in vivo eyes. Potential retinal detachment, however, substantially reduces the quality of images of postmortem eyes as compared to in vivo eyes. Tissue fixatives may further exacerbate the degree of retinal detachment from the RPE-choroid complex. In addition, the retina becomes less transparent in postmortem eyes. Both conditions compromise signal collection from structures underlying the retina and contribute to reduced image quality in postmortem eyes.

In vivo imaging with OCT shows detailed retinal architecture, including distinct retinal lamina (Yaqoob et al. 2005). It also resolves localized changes in retinal thickness between the macula and periphery. Postmortem changes mask the lamellar features of the inner retina, and allow resolution only of the photoreceptor layer, RPE, and choroid. Figure 60.2 clearly shows a difference in resolution of retinal lamina in in vivo and postmortem images. Despite the stark contrast in image quality, OCT imaging of postmortem eyes shows the thickness of the inner retina and RPE, and visualizes changes at sections throughout tissue with an in-depth resolution of several microns.

In vivo imaging is optimal; however, postmortem imaging with SLO and OCT provides more detail than the standard photographic image of the posterior pole. Information obtained from imaging regarding the location and size of retinal lesions also allows for targeted histopathology. To the best of our knowledge, the use of SLO for retinal imaging in human postmortem eyes has been reported only by two other groups (Bindewald et al. 2004; Olsen 2008). These earlier studies, however, removed the neural retina prior to imaging to improve visualization of the RPE-choroid complex. The removal of the neural retina for imaging limits the usefulness of the procedure when subsequent histology of the specimens is required. OCT has been used on human postmortem eyes primarily for corneal studies (Wolf et al. 2004; Johnson et al. 2007). OCT also has been used for retinal imaging of human postmortem eyes (Chauhan and Marshall 1999; Ugarte et al. 2006). However, this is the first time OCT has been routinely applied in conjunction with SLO and macroscopic imaging to screen and characterize a range of retinal pathology in postmortem donor eyes.

In summary, the use of both SLO and OCT in the initial assessment of postmortem eyes prior to histological analysis provides useful information about locations and types of different retinal lesions. As described above, #777 and #784 appeared normal in macroscopic fundus images, but in fact were found to have a macular hole and bilateral RPE detachment, respectively. Without knowing the clinical history of #777, it is impossible to determine if the isolated retinal fragment at the base of the macular hole was present at the time of death or if it was an artifact of fixation. Similarly, it is unknown if the bilateral RPE detachments were present at the time of death or were fixation artifacts. Aside from finding lesions that were not detected by macroscopic imaging, SLO and OCT further characterized known retinal lesions. The combination of SLO and OCT shows the full extent of retinal pathology and clarifies the locations of specific inclusions. Despite the valuable information imaging provides, it is important to be wary of using a single imaging instrument which may provide an incomplete picture of retinal pathology. The combination of SLO and OCT is critical to accurately interpreting pathology, and provides a more thorough means to identify retinal lesions in donor eyes.

**Acknowledgments** This work was supported by the Foundation Fighting Blindness, Columbia, MD and Research to Prevent Blindness, New York, NY. Figure 60.2b was reprinted with permission from Bioptigen, Inc. The authors thank Charlie Kaul and Dr. Lisa Kuttner-Kondo for their constructive comments and enthusiastic support.

# References

Bindewald A, Jorzik JJ, Loesch A et al (2004) Visualization of retinal pigment epithelial cells in vivo using digital high-resolution confocal scanning laser ophthalmoscopy. Am J Ophthalmol 137:556–558

Chauhan DS, Marshall J (1999) The interpretation of optical coherence tomography images of the retina. Invest Ophthalmol Vis Sci 40:2332–2342

Da Pozzo S, Marchesan R, Ravalico G (2009) Scanning laser polarimetry - a review. Clin Experiment Ophthalmol 37:68–80

Geitzenauer W, Hitzenberger CK, Schmidt-Erfurth UM (2010)Retinal optical coherence tomography: past, present and future perspectives. Br J Ophthalmol

Hassenstein A, Meyer CH (2009) Clinical use and research applications of Heidelberg retinal angiography and spectral-domain optical coherence tomography - a review. Clin Experiment Ophthalmol 37:130–143

Imamura Y, Fujiwara T, Margolis R et al (2009) Enhanced depth imaging optical coherence tomography of the choroid in central serous chorioretinopathy. Retina 29:1469–1473

Johnson CS, Mian SI, Moroi S et al (2007) Role of corneal elasticity in damping of intraocular pressure. Invest Ophthalmol Vis Sci 48:2540–2544

Jorzik JJ, Bindewald A, Dithmar S et al (2005) Digital simultaneous fluorescein and indocyanine green angiography, autofluorescence, and red-free imaging with a solid-state laser-based confocal scanning laser ophthalmoscope. Retina 25:405–416

Olsen TW (2008) The Minnesota Grading System using fundus autofluorescence of eye bank eyes: a correlation to age-related macular degeneration (an AOS thesis). Trans Am Ophthalmol Soc 106:383–401

Sharp PF, Manivannan A (1997) The scanning laser ophthalmoscope. Phys Med Biol 42:951–966

Ugarte M, Hussain AA, Marshall J (2006) An experimental study of the elastic properties of the human Bruch's membrane-choroid complex: relevance to ageing. Br J Ophthalmol 90:621–626

Wolf AH, Neubauer AS, Priglinger SG et al (2004) Detection of laser in situ keratomileusis in a postmortem eye using optical coherence tomography. J Cataract Refract Surg 30:491–495

Wolf-Schnurrbusch UE, Enzmann V, Brinkmann CK et al (2008) Morphologic changes in patients with geographic atrophy assessed with a novel spectral OCT-SLO combination. Invest Ophthalmol Vis Sci 49:3095–3099

Yaqoob Z, Wu J, Yang C (2005) Spectral domain optical coherence tomography: a better OCT imaging strategy. Biotechniques 39:S6–13

# Histopathology and Functional Correlations in a Patient with a Mutation in *RPE65*, the Gene for Retinol Isomerase

*Vera L. Bonilha,*[1] *Mary E. Rayborn,*[1] *Yong Li,*[1,2] *Gregory H. Grossman,*[1] *Eliot L. Berson,*[3] *and Joe G. Hollyfield*[1]

**Purpose.** Here the authors describe the structural features of the retina and retinal pigment epithelium (RPE) in postmortem donor eyes of a 56-year-old patient with a homozygous missense *RPE65* mutation (Ala132Thr) and correlate the pathology with the patient's visual function last measured at age 51.

**Methods.** Eyes were enucleated within 13.5 hours after death. Representative areas from the macula and periphery were processed for light and electron microscopy. Immunofluorescence was used to localize the distribution of RPE65, rhodopsin, and cone arrestin. The autofluorescence in the RPE was compared with that of two normal eyes from age-similar donors.

**Results.** Histologic examination revealed the loss of rods and cones across most areas of the retina, attenuated retinal vessels, and RPE thinning in both eyes. A small number of highly disorganized cones were present in the macula that showed simultaneous labeling with cone arrestin and red/green or blue opsin. RPE65 immunoreactivity and RPE autofluorescence were reduced compared with control eyes in all areas studied. Rhodopsin labeling was observed in rods in the far periphery. The optic nerve showed a reduced number of axons.

**Conclusions.** The clinical findings of reduced visual acuity, constricted fields, and reduced electroretinograms (ERGs) 5 years before death correlated with the small number of cones present in the macula and the extensive loss of photoreceptors in the periphery. The absence of autofluorescence in the RPE suggests that photoreceptor cells were probably missing across the retina for extended periods of time. Possible mechanisms that could lead to photoreceptor cell death are discussed. (*Invest Ophthalmol Vis Sci.* 2011;52:8381–8392) DOI:10.1167/iovs.11-7973

Leber congenital amaurosis (LCA) comprises a group of genetic disorders in which visual loss or dysfunction is present at birth. Patients typically have hyperopia and nystagmus and reduced electroretinograms (ERGs). The extent of visual loss varies from patient to patient but is usually severe. Mutations have been identified in 15 genes in persons with LCA, each of which is a recessive disorder.[1,2]

Mutations in the *RPE65* gene account for approximately 7% of LCA. *RPE65* is uniquely expressed in the retinal pigment epithelium (RPE), where the protein, an enzyme, binds and converts all-*trans* retinyl ester to 11-*cis* *ret*inol.[3–5] Retinol isomerization is an essential enzymatic step required for functional vision to occur in rod and cone photoreceptors.[6,7] More than 60 mutations in the *RPE65* gene have been documented in LCA patients. Mutations have been reported in each of the 14 exons of the *RPE65* gene and its boundaries.[8–14] Typically, mutations in the *RPE65* gene result in impaired vision from birth and typically progress to legal blindness in the third decade of life.[9,11,12,15,16]

Mutations in *RPE65* do not necessarily result in early loss of photoreceptors. For example, studies of dog retinas with a naturally occurring *RPE65* mutation and mouse retinas that are missing the *RPE65* gene show structurally intact photoreceptors visible by optical coherence tomography that appear nonfunctional because of the inability of the RPE to generate 11-*cis* retinal. The sparing of photoreceptors has allowed *RPE65* gene replacement therapy to restore this critical retinol isomerase activity to the RPE with the accompanying restoration of visual function.[17,18]

In this report we describe the pathology and clinical findings in a woman with a homozygous mutation (Ala132Thr) in the *RPE65* gene.[12] Unlike most persons with RPE65 mutations, this patient retained some vision into her early fifties. To our knowledge this is the first study of adult postmortem donor eyes from a patient with a homozygous recessive mutation in the *RPE65* gene.

## Methods

Clinical evaluations were carried out at the Harvard Medical School, Massachusetts Eye and Ear Infirmary (Boston, MA). The research conformed to the tenets of the Declaration of Helsinki.

### Tissue Acquisition and Fixation

The patient was a registered eye donor with the Foundation Fighting Blindness and the Berman-Gund Laboratory. Eyes were enucleated 13.5 hours postmortem and fixed in 4% paraformaldehyde and 0.5% glutaraldehyde in phosphate buffer. After 1 month in fixative, the globes were transferred and stored in 2% paraformaldehyde in PBS. Normal postmortem donor eyes from a 60-year-old woman and a 61-year-old man were used as controls.

---

From the [1]Cole Eye Institute, Department of Ophthalmology, Cleveland Clinic Lerner College of Medicine, Cleveland, Ohio; and the [3]Berman-Gund Laboratory for the Study of Retinal Degenerations, Harvard Medical School, Massachusetts Eye and Ear Infirmary, Boston, Massachusetts.

[2]Present affiliation: Department of Neurological Surgery, Case Western Reserve University, Cleveland, Ohio.

Supported by The Foundation Fighting Blindness Histopathology Grant F-OH01-1102-0231 (JGH), Research Center Grants from The Foundation Fighting Blindness (JGH, ELB), Research to Prevent Blindness Unrestricted Grants (JGH), and National Institutes of Health Grants R01EY014240-08 (JGH) and 3R21EY017153-02S1 (VLB).

Submitted for publication June 1, 2011; revised August 9 and September 1, 2011; accepted September 5, 2011.

Disclosure: **V.L. Bonilha**, None; **M.E. Rayborn**, None; **Y. Li**, None; **G.H. Grossman**, None; **E.L. Berson**, None; **J.G. Hollyfield**, None

Corresponding author: Vera L. Bonilha, Department of Ophthalmic Research, The Cole Eye Institute, Cleveland Clinic, 9500 Euclid Avenue, Cleveland, OH 44195; bonilhav@ccf.org.

Investigative Ophthalmology & Visual Science, October 2011, Vol. 52, No. 11

## Immunohistochemistry

Small areas from the macula (OD and OS) and peripheral eye wall (OD) were cut and infused successively with 10% and 20% sucrose in PBS, and embedded in optimum temperature cutting compound (Tissue-Tek 4583; Miles Inc., Elkhart, IN). Ten-micrometer cryosections were cut on a cryostat (HM 505E; Microm, Walldorf, Germany) equipped with a tape-transfer system (CryoJane; Instrumedics, Inc., Hackensack, NJ). Before labeling, embedding medium was removed through two consecutive PBS incubations for 20 minutes. The tissue was then processed for immunofluorescence labeling. Sections

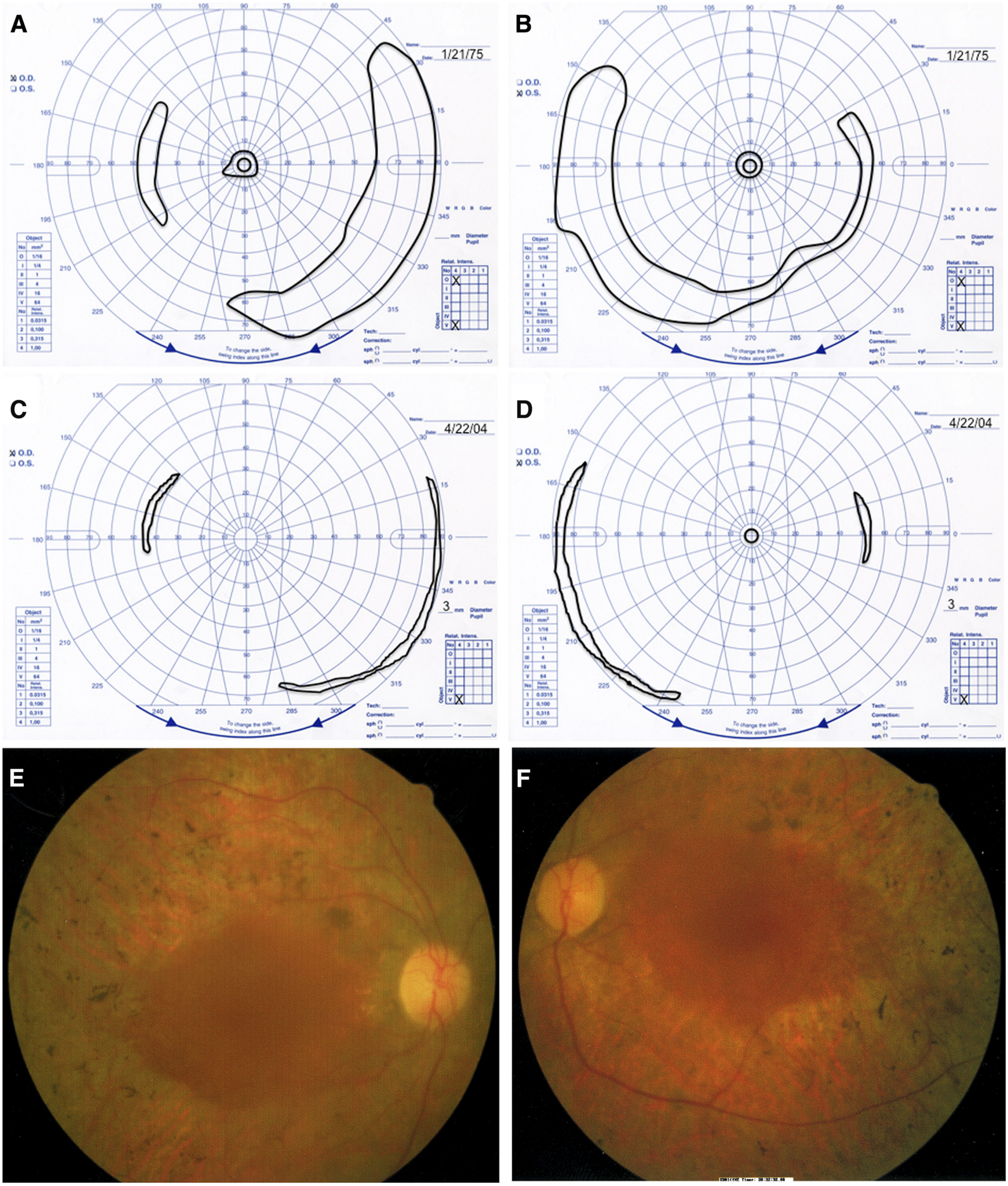

**FIGURE 1.** Findings in patient with RPE65 gene mutation. (**A**, **B**) Goldmann visual fields to a V-4e white test light and I-4e white test light at age 22. (**C**, **D**) Goldmann visual fields to a V-4e white test light at age 51. (**E**, **F**) Fundus photographs OD and OS at age 51.

were blocked in PBS supplemented with 1% BSA (PBS/BSA) for 30 minutes and incubated with monoclonal antibody B6–30N to rhodopsin (1:100; from Paul Hargrave, University of Florida, Gainesville, FL) and polyclonal antibodies PETLET to RPE65 (1:500; from Rosalie Crouch, University of South Carolina, Charleston, SC), to red/green (AB5405, 1:1200; Chemicon), and to blue (AB5407, 1:1200; Chemicon, Temecula, CA) opsin, and monoclonal antibody 7G6 to cone arrestin (1:100; from Peter MacLeish, Morehouse School of Medicine, Atlanta, GA) in PBS/BSA overnight at 4°C. Cell nuclei were labeled with iodide (TO-PRO-3; blue, 1 mg/mL; Molecular Probes, Eugene, OR). Secondary antibody goat anti-mouse IgG (1:1000) was labeled with Alexa Fluor 488 (green; Molecular Probes) while goat anti-rabbit IgG was labeled with Alexa Fluor 488 or 594 (red) for 1 hour at room temperature. Sections were analyzed using a laser scanning confocal microscope (TCS-SP2; Leica, Exton, PA). A series of 1-$\mu$m *x-y* (en face) sections were collected. Each individual x-y image of the retinas stained represented a three-dimensional projection of the entire cryosection (sum of all images in the stack). Microscopic panels were composed using image editing software (Photoshop CS3; Adobe, San Jose, CA).

### Immunofluorescence Montages

Sections labeled with antibodies to cones and rods were stained as described and were imaged with a fluorescence microscope (BX-61; Olympus, Tokyo, Japan) equipped with a charge-coupled device monochrome camera (Hamamatsu Photonics, Bridgewater, NJ). Each montage image represented a composition of a series of individual photomicrographs collected throughout the whole tissue with 10× and 20× objectives using a computer-controlled motorized x-y stage (Proscan II; Prior Scientific Inc., Rockland, MA) and reconstructed into one image (SlideBook software, version 4.2; Intelligent Imaging Innovations, Denver, CO).

### Semithin Epon Sections and Ultrastructural Analysis

A small area of the retina/RPE/choroid tissue from both the macular region (OS) and the periphery (OD) of the RPE65 donor and matched-controls were fixed in 2.5% glutaraldehyde in 0.1 M cacodylate buffer, sequentially dehydrated in ethanol, and embedded in Epon. One-micrometer plastic sections of both samples were stained with toluidine blue and examined and photographed by light microscopy with a microscope (Axiophot; Carl Zeiss, Jena, Germany) equipped with a high-sensitivity charge-coupled device camera (C5810; Hamamatsu Photonics, Hamamatsu, Japan). Thin sections were prepared, and electron micrographs were taken on a 200-kV digital electron microscope (Tecnai 20; Philips, Hillsboro, OR) using a Gatan (Pleasanton, CA) image filter and a digital camera at 3600 diameters and were printed at identical magnifications.

## RESULTS

### Clinical Findings

The patient was first examined by one of the authors (ELB) at age 22, at which time she reported night blindness and limited side vision since childhood. At the initial examination, she had best-corrected visual acuity of 20/40 (right eye, OD) and 20/30 (left eye, OS). Her visual fields were constricted to 11° diameter centrally, with peripheral islands in both eyes with a V-4e white test light (Figs. 1A, 1B). Slit lamp examination showed clear lenses in both eyes (OU). Fundus examination showed a normal disc, retinal arteriolar attenuation, and bone spicule pigmentation around the midperiphery in each eye. Dark adaptation OS with an 11° diameter white test light showed a threshold 3.5 log units above normal after 45 minutes of dark adaptation. Rod and cone responses were nondetectable (<10 $\mu$V) with conventional full-field ERG testing. With narrow bandpass filtering and computer averaging, full-field 30-Hz cone responses were 8.4 $\mu$V OU (lower normal is 50 $\mu$V).

She was most recently examined by us at age 51, 5 years before her death. At that time, she had hand motions vision OD and 20/200 OS. Visual field testing showed reduction of the temporal island in each eye, no detectable central field OD, and only a 4° central field diameter OS (Figs. 1C, 1D). Slip lamp examination revealed central posterior subcapsular cataracts in both eyes. Fundus examination of each eye showed slight waxy pallor of the disc, a granular macula, attenuated retinal vessels, and bone spicule pigmentation

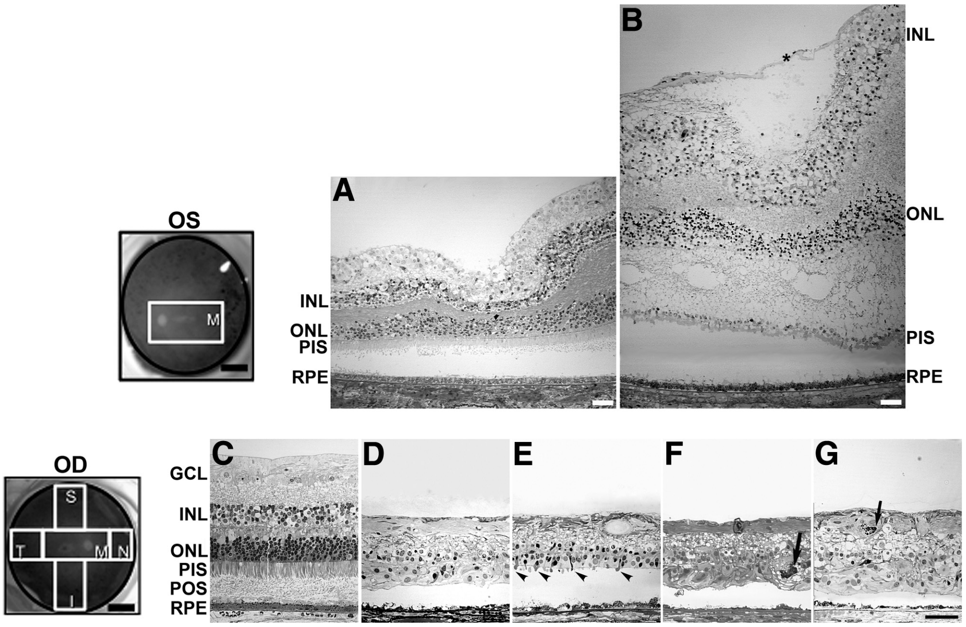

FIGURE 2. Degeneration in the retina of an RPE65 donor. Fundus images of both eyes with disc and macula delineated; schematic drawing of the regions cut and processed for cryosectioning (*far left, top and bottom*). One-micrometer plastic sections of both matched control (**A**, **C**) and RPE65 donor (**B**, **D**–**G**) postmortem retinas stained with toluidine blue. The macula of the left eye of the RPE65 donor (**B**) displayed edema. It contained a prominent preretina (epiretinal) membrane composed of fibroblastlike cells that were vitread to a connective tissue lamina (*). In the periphery, the retina of the RPE65 donor (**D**–**G**) displayed different degrees of retinal degeneration in all quadrants observed. Sparse inner and outer nuclear layers with stunted photoreceptor inner and outer segments are evident in the superior quadrant (**E**, *arrowheads*). A few pigmented cells are seen invading the degenerating retina of the temporal (**F**) and nasal quadrant (**G**, *arrows*). Finally, a thin, continuous area of pigmented RPE cells was present. Quadrants: M, macula; I, inferior; S, superior; T, temporal; N, nasal. RPE, retinal pigment epithelium; POS, photoreceptor outer segment; PIS, photoreceptor inner segment; ONL, outer nuclear layer; INL, inner nuclear layer; GCL, ganglion cell layer. Scale bars: 0.5 cm (fundus images *upper* and *lower left*); 400 $\mu$m (**A**, **B**); 200 $\mu$m (**C**–**G**).

around the periphery (Figs. 1E, 1F). A small central macular hole could be visualized OD. No macular edema could be seen. Dark-adaptation OS showed a final threshold still elevated 3.5 log units above normal. Narrow band-passed, computer-averaged, 30-Hz cone ERGs were now only 0.50 μV (OD) and 0.67 μV (OS). Applanation tensions of 10 mm Hg (OD) and 12 mm Hg (OS) were recorded during her visit at age 51.

## Histopathology of the Retina and Optic Nerve

Semithin sections of Epon-embedded RPE65 eye tissue were analyzed and compared with equivalent areas in an age-similar control eye (Fig. 2). A schematic drawing of the postmortem donor eye under study depicts the regions harvested and processed for both histologic and immunohistologic analysis: inferior (I), superior (S), temporal (T), nasal (N), retina, and macula (M). The macula of the left eye (Fig. 2B) was swollen. It contained a prominent preretinal (epiretinal) membrane composed of fibroblastlike cells that were vitreal to a connective tissue lamina. In each quadrant of the periphery, the retina (Figs. 2D–G) displayed different degrees of degeneration when compared with the morphology of the control retina in the periphery (Fig. 2C) and macula (Fig. 2A). No layers of nuclei (ganglion, inner, and outer) were evident in any of the quadrants of the retinal periphery analyzed. Nuclei were randomly distributed throughout the disorganized retina. The inner and outer plexiform layers were also not evident. An occasional stunted photoreceptor inner and outer segment projecting from the outer retinal surface was evident in the superior quadrant (Fig. 2E, arrowheads). A few pigmented cells were observed invading the degenerate retina of the temporal and nasal quadrants (Figs. 2F, 2G, arrows). The vitreal surface of the retina was formed of glial fibers ending at the inner limiting membrane. The RPE layer was continuous below the degenerate retina, but RPE cells had reduced apical to basal height compared with the RPE in age-similar control eyes.

Cross-sections of the optic nerve were taken approximately 1 mm behind the lamina cribrosa (Fig. 3). A few myelinated axons were found in the optic nerve of the RPE65 donor (Figs. 3B, 3D) compared with sections from the control nerves at equivalent retrolaminar locations (Figs. 3A, 3C). Only a few nuclei (possible astrocytes) were evident (Fig. 3D), and the diameters of the central retinal artery and vein were severely reduced in diameter (Fig. 3F) compared with control (Fig. 3E). The paucity of axons in the optic nerve was consistent with the absence of distinct ganglion cells in the RPE65 donor retina.

## Immunohistocytochemistry Studies

The RPE65 postmortem donor eye displayed a continuous but much decreased signal of RPE65 immunoreactivity in the macula compared with the control eye (Figs. 4A–D). In some areas of the macula, multilayered RPE65-positive cells could be observed bulging into the subretinal space (Figs. 4E, 4F). In the peripheral retina, RPE65 immunoreactivity was patchy and sparse, probably related to the RPE attenuation and thinning (Figs. 4G, 4H).

To follow some of the specific molecular changes in the remaining photoreceptors, the retina of the postmortem RPE65 donor was also evaluated for the distribution of cone arrestin in the macula of each eye (Fig. 5) and in the periphery (Fig. 6). Cone arrestin distribution was compared with that in a control eye in similar regions. Individual images collected throughout the whole tissue length were acquired and reconstructed into a montage. In the RPE65 donor retina, a small cluster of foveal cones was still present in both eyes; these were highly disorganized and lacked distinct cone synaptic terminals (Fig. 5). In addition, cone arrestin–positive cells were rarely observed in any peripheral retinal quadrant studied (Fig. 6). Therefore, our immunohistologic observations cannot account for the difference in vision acuity recorded when the patient was tested 5 years earlier.

In control retinas, cone arrestin antibody labeled the entire cone cell body in all retinal areas studied (Fig. 7). Observation at higher magnification showed that cone arrestin antibody labeled the few remaining cones in the fovea of the RPE65 eye, but cone pedicles were not labeled and could not be identified (Fig. 7B). Cone arrestin immunoreactivity was rarely encountered in the peripheral retina, which was consistent with the absence of all photoreceptor types in these locations. The few remaining cones exhibited amorphous morphology and expansion of the retina horizontally (Figs. 7C–F). Moreover, there was a paucity of nuclei in the outer nuclear layer labeled with iodide (TO-PRO-3; Molecular Probes) in the RPE65 eye compared with the control eye.

Cones were further characterized through double labeling of the macula (Fig. 8) and periphery (Supplementary Fig. S1; http://www.iovs.org/lookup/suppl/doi:10.1167/iovs.11-7973/-/DCSupplemental) with red/green or blue opsin and cone arrestin antibodies. As described, cone arrestin is distributed through the entire cytoplasm of cones (Figs. 8A, 8G; Supplementary Figs. S1A, S1G; http://www.iovs.org/lookup/suppl/doi:10.1167/iovs.11-7973/-/DCSupplemental) whereas red/green opsin (Fig. 8B; Supplementary Fig. S1B; http://www.iovs.org/lookup/suppl/doi:10.1167/iovs.11-7973/-/DCSupplemental) and blue opsin (Fig. 8H; Supplementary Fig. S1H; http://www.iovs.org/lookup/suppl/doi:10.1167/iovs.11-7973/-/DCSupplemental) are restricted to the outer segment in

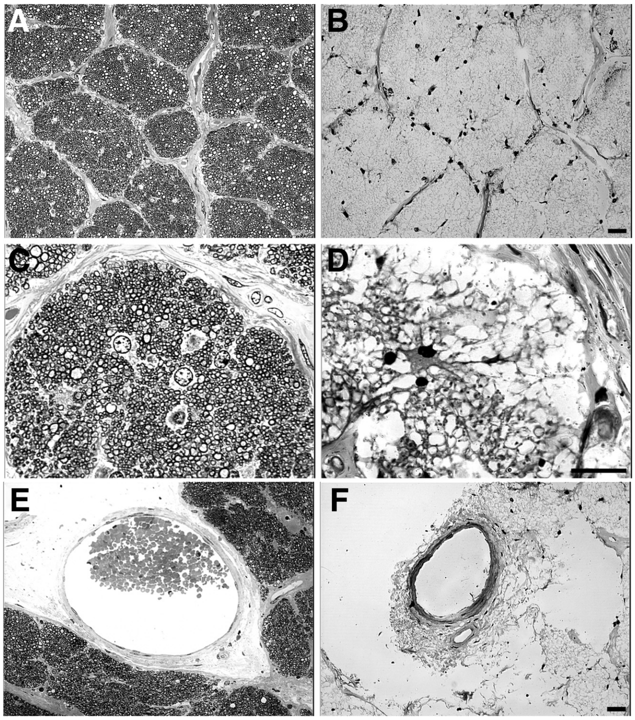

**Figure 3.** Degeneration in the optic nerve of the RPE65 donor. Light microscopy of 1-μm plastic sections of optic nerve from both a matched control (**A**, **C**, **E**) and the RPE65 donor (**B**, **D**, **F**) stained with toluidine blue. Analysis of the optic nerve of the RPE65 donor in both low (**B**) and high (**D**) magnification showed the absence of myelinated axons when compared with the control (**A**, **C**). Only a few nuclei (astrocytes?) are evident (**D**). There is a paucity of axons consistent with the loss of ganglion cells in the retina. Finally, the RPE65 donor displayed a severely reduced central retinal vessel diameter (**F**). Scale bars, 200 μm.

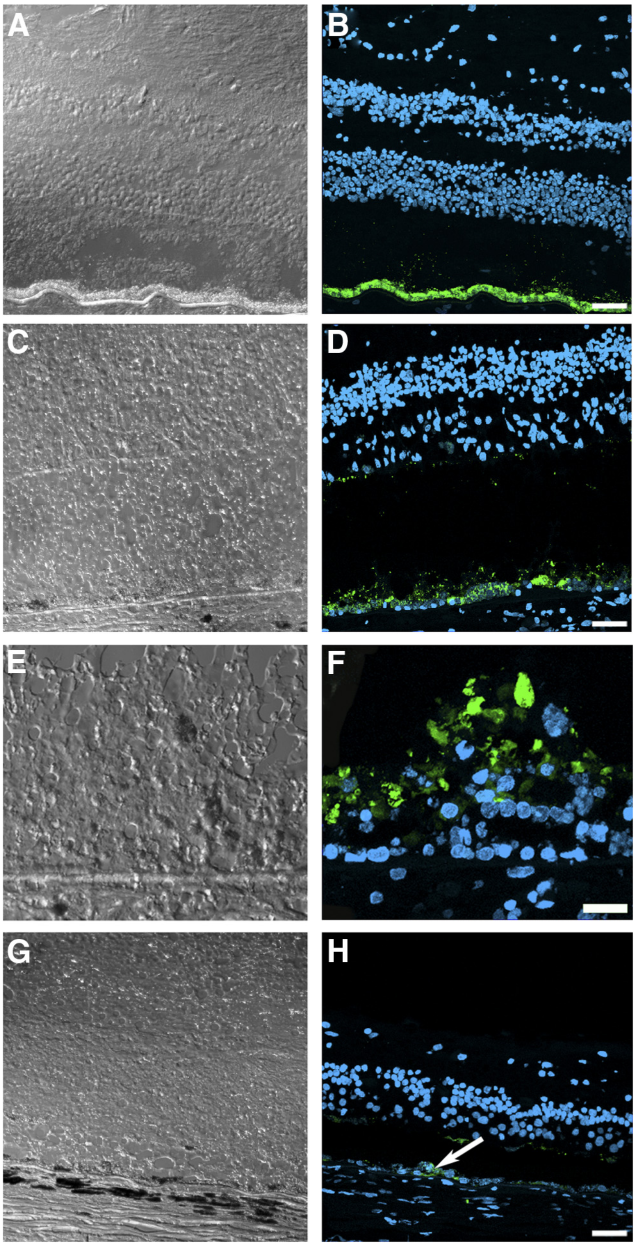

**FIGURE 4.** Presence of remaining RPE cells expressing RPE65 in the postmortem eyes from an RPE65 donor. A continuous layer of cells was observed expressing RPE65 in the control (**B**) and in the macula of the RPE65 donor (**D**); however, the RPE65 donor expression was substantially lower than that observed in the control tissue. In a few areas in the macula of the RPE65 donor (**F**), several layers of RPE65-positive cells were observed in the RPE65 donor retina. In the periphery of the RPE65 donor retina, very few cells were detected expressing RPE65 (**H**, *arrow*). **A**, **C**, **E**, and **G** are differential interference contrast microscopy images of the same field shown in **B**, **D**, **F**, and **H**. Scale bars, 40 $\mu$m (**B**, **D**, **H**); 20 $\mu$m (**F**).

control eyes. In the RPE65 eye, red/green opsin displayed a diffuse, cytoplasmic distribution in the macula (Fig. 8E) and retinal periphery (Supplementary Fig. S1E; http://www.iovs.org/lookup/suppl/doi:10.1167/iovs.11-7973/-/DCSupplemental). Interestingly, blue opsin displayed a decreased but membrane-associated distribution in the macula (Fig. 8K) and periphery (Supplementary Fig. S1K; http://www.iovs.org/lookup/suppl/doi:10.1167/iovs.11-7973/-/DCSupplemental) compared with the control tissue distribution. As described, cone arrestin labeling in the RPE65 donor eye macula highlighted the abnormal distribution of cones (Figs. 8D, 8J) whereas in the periphery only severely degenerate cones remained (Supplementary Figs. S1D, S1J; http://www.iovs.org/lookup/suppl/doi:10.1167/iovs.11-7973/-/DCSupplemental).

Rod photoreceptors were identified with a rhodopsin antibody. After antibody labeling, individual overlapping images were collected throughout the entire tissue expanse from each retinal quadrant studied and were used to construct a montage (Fig. 9). Comparison of the samples showed that rhodopsin labeling was mostly absent in the RPE65 eye. A few rods were detected in the far periphery of the temporal quadrant of the RPE65 eye (Fig. 9D, arrows).

Rhodopsin is normally localized only to the outer segment (Fig. 10A), but in the few rods found in the RPE65 eye, rhodopsin was distributed throughout the entire cell body (Figs. 10B–F). Comparison of the samples showed that rods were significantly decreased in all the observed regions; the remaining rods had lost the normal rodlike shape and were much shorter than rods in control retinas. Additionally, rhodopsin-labeled neuritelike processes were commonly observed extending into the inner retina.

Photoactivation of rhodopsin and cone opsin results in the isomerization of 11-*cis* retinal to all-*trans* retinal, which is then recycled to the RPE for regeneration in a pathway termed the retinoid visual cycle. During aging, a functional visual cycle is necessary for the RPE to accumulate lipofuscin, the fluorescent storage material that accumulates in RPE cells. We compared the relative amount of autofluorescence in the RPE postmortem donor eye with control RPE. RPE in the macula (Fig. 11B) showed a substantial decrease of autofluorescence compared with RPE in the macula of the age-similar control eyes (Fig. 11A). Finally, in the periphery, the RPE in the RPE65 donor retina showed a paucity of autofluorescence (Figs. 11D–G) compared with an age-similar control RPE (Fig. 11C).

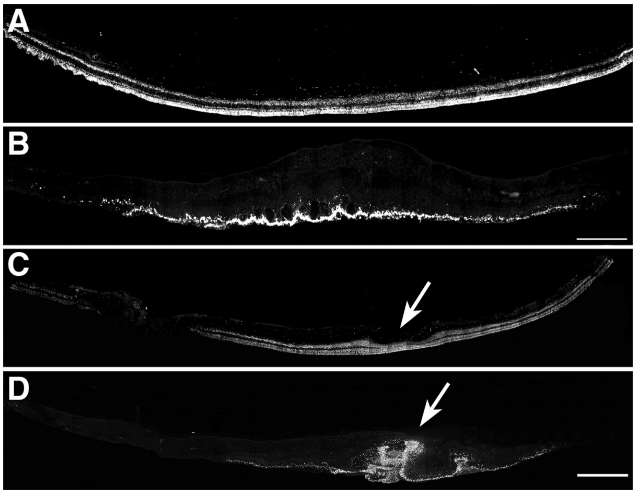

**FIGURE 5.** Presence of disorganized cones in the macular region of both postmortem eyes from an RPE65 donor. Montages of photomicrographs of the macular region of both the right (**B**) and the left (**D**) postmortem eyes from the RPE65 donor and control eyes (**A**, **C**) were analyzed using a cone arrestin antibody (7G6). Observations showed that in the RPE65 postmortem donor eyes, cones were still present in the macula but were highly disorganized and synapses were absent. (*arrows*) Macula pit. Scale bar, 500 $\mu$m.

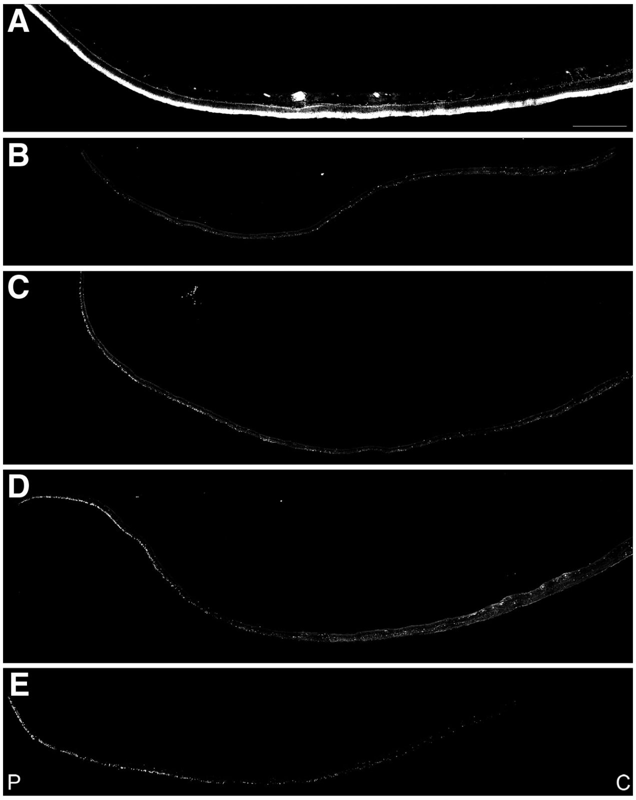

**Figure 6.** Significant reduction in the cones in the periphery of an RPE65 postmortem donor eye. Montages of photomicrographs of the periphery tissue from the RPE65 donor (**B–E**) and control eyes (**A**) were analyzed using a cone arrestin antibody (7G6). Comparison of the samples showed that cones were mostly absent in the affected retina in inferior (**B**), superior (**C**), temporal (**D**), and nasal (**E**) regions. P, periphery; C, central. Scale bar, 500 μm.

## Ultrastructural Studies of the RPE and Bruch's Membrane

Transmission electron microscopy of RPE and Bruch's membrane in the fovea (Figs. 12C, 12D) and periphery (Figs. 12E–H) of the RPE65 donor and an age-similar control eye (Figs. 12A, 12B) was performed, and findings were compared. The control RPE displayed the expected apical microvilli (Fig. 12A) and basal infoldings (Fig. 12B). In contrast, the RPE65 postmortem donor eye showed degenerative changes in the RPE in each quadrant studied. In the macula, apical microvilli were absent, and pleomorphic inclusions were common (Figs. 12C, 12D). In the nasal quadrant, apical microvilli were present (Fig. 12E); however, the basal region was characterized by the presence of electron-dense material beneath the RPE cells (Fig. 12F). In the inferior quadrant, inflammatory cells were present above the RPE in some areas (data not shown). A few short microvilli remained on their apical surface (Fig. 12G). Examination of the RPE basal surface revealed a complete absence of basal infoldings and the presence of a debris zone beneath the RPE. Bruch's membrane had lost the pentalaminate structure and was disorganized in this area (Fig. 12H).

## Discussion

This study reveals for the first time the histologic changes present in an adult retina of a patient with an RPE65 mutation. The Ala132Thr site mutation in exon 5 of the *RPE65* gene was previously identified in this patient and several family members.[12] The functional consequence of this specific RPE65 mutation was also studied previously in vitro, in 293 cells.[5] Data showed that mutation to threonine at residue 132 lead to 50% reduction in the activity of isomerization potential of RPE65. Some remaining activity of RPE65 enzyme most likely contributed to the long retention of vision measured in this patient.

Several studies[19–21] have evaluated the retinas in RPE65-deficient (LCA) patients in vivo through the use of optical coherence tomography combined with visual function. These studies determined that despite severely reduced early loss of cone vision, many persons with *RPE65* mutations had near-normal foveal microstructure but most were lacking rods.[19–21] Observation of the fovea also showed that patients with RPE65 deficiency exhibited some cone photoreceptor loss, even at the youngest ages. However, residual cone photoreceptor function persisted for decades.[20] In fact, these patients have differing amounts of cone function, with some older patients having more function than younger patients.[20,22,23] Based on these studies it is likely that gene therapy will have to be targeted to different regions, possibly on a case-by-case basis.

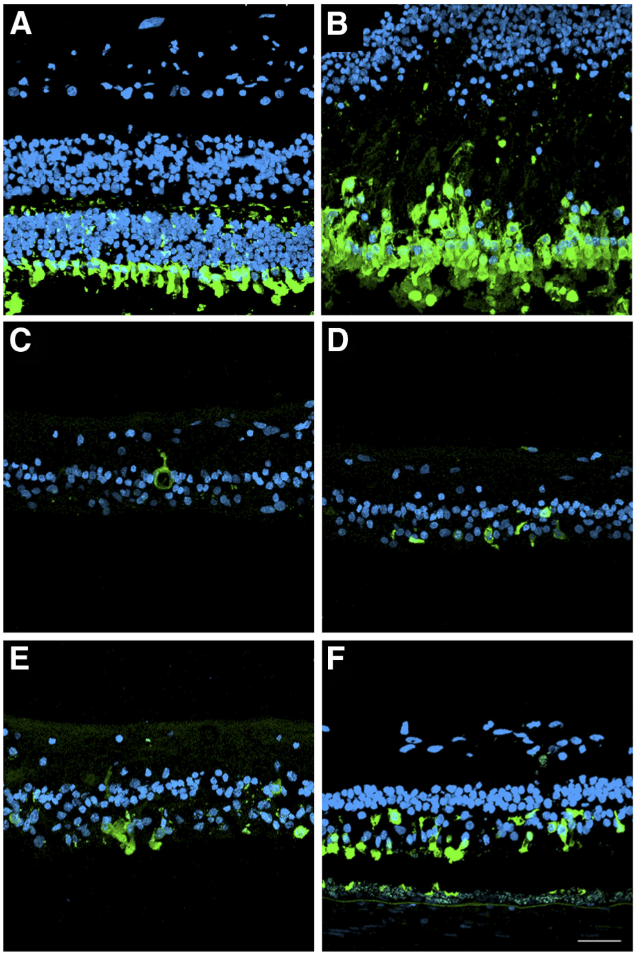

**Figure 7.** Disorganized morphology of the cones remaining in the retina of an RPE65 postmortem donor eye. High-magnification comparison of the control and RPE65 donor retina showed that cone arrestin was distributed along the entire plasma membrane of this cone type, from the tip of the outer segment to the synaptic base in the control retina (**A**). Cones were present in the macula of the RPE65 donor, but synapses were not visualized (**B**). On the other hand, cones were mostly absent in the periphery of the RPE65 mutant retina in the inferior (**C**), superior (**D**), temporal (**E**), and nasal (**F**) quadrants. Scale bar, 40 μm.

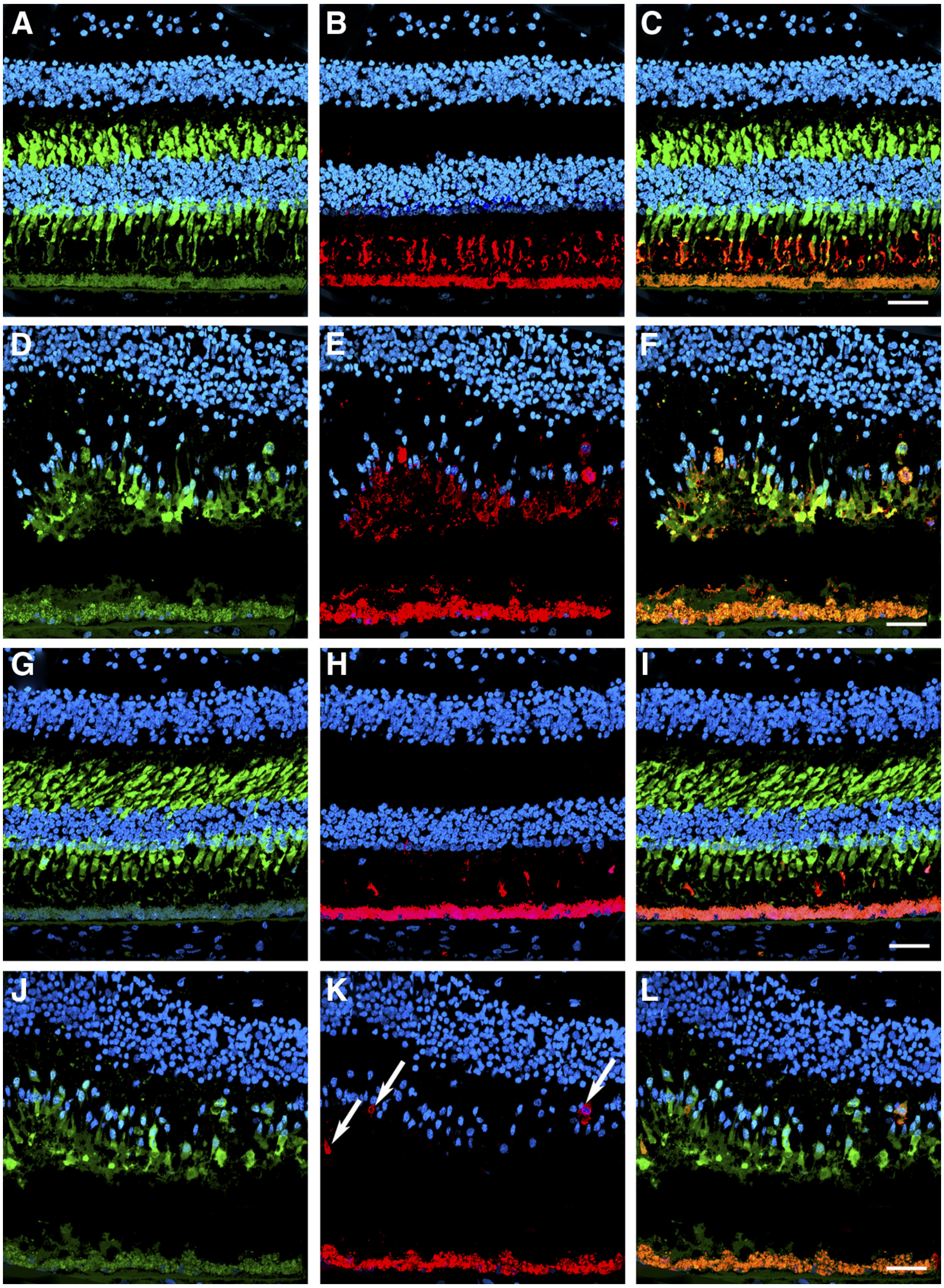

**Figure 8.** Disorganized expression of red/green and blue opsins in the cones in the macula of an RPE65 postmortem donor eye. The distribution of cones was also analyzed in control and RPE65 eyes labeled with the cone arrestin (7G6), red/green opsin (AB5405), and blue opsin (AB5407) antibodies. Control retinas displayed cone arrestin distributed along the entire cone cell body (**A**, **G**), however the RPE65 donor retina displayed disorganized cones (**D**, **J**). In the control eyes, red/green (**B**) and blue (**H**) opsins were restricted to the cone outer segments. In the RPE65 eyes, the red/green opsin displayed a more diffuse staining (**E**) that overlapped with cone arrestin. However, blue opsin localization was mostly to the cone cell boundaries (**K**, *arrows*). Overlaid images are shown in **C**, **F**, **I**, **L**. Scale bar, 40 $\mu$m.

Data presented in this study demonstrated that the RPE65 donor retinas showed generalized loss of rod and cone photoreceptors except in the central macula, with RPE thinning in most regions of the peripheral retina. Together with the data reported on LCA patients, the findings we report here, though of interest, cannot necessarily be regarded as representative of the pathology in all RPE65 mutations.

Our study probed the distribution of cone arrestin, red/green opsin, and blue opsin in the RPE65 eye and compared it with the distribution in control eyes. A previous study has shown that abnormal cones, from RP donor eyes with rhodopsin mutations, displayed loss of immunolabeling with anti–cone arrestin.[24] However, in the present RPE65 donor eye, virtually all cones that labeled with anti–cone arrestin also showed labeling with the red/green or blue opsin antibodies. This difference in cone labeling may be attributed to different pathogenic mechanisms of the involved retinal degenerations.

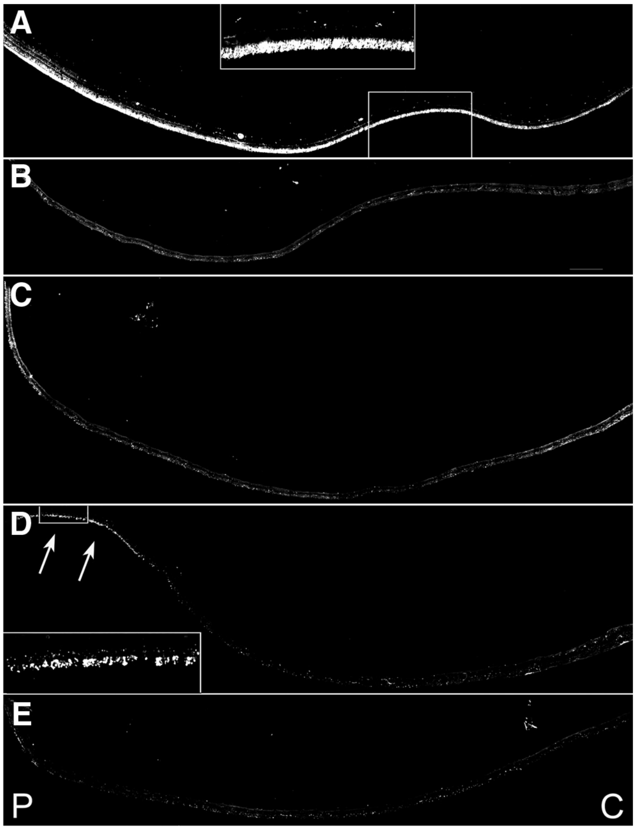

**Figure 9.** Absence of rhodopsin in the rods in the periphery of an RPE65 postmortem donor eye. Montages of photomicrographs of the periphery tissue from the RPE65 donor (**B–E**) and control eyes (**A**) were analyzed using a rhodopsin antibody (B630N). Comparison of the samples showed that rhodopsin was mostly absent in the affected retina in the inferior (**B**), superior (**C**), and nasal (**E**) regions. A few rods were still present in the far periphery of the temporal region of the RPE65 mutant retina (**D**, *inset* and *arrows*). P, periphery; C, central. Scale bar, 500 μm.

Our data show that the better visual acuity the patient had in the right eye when tested 5 years earlier suggests that very few cones are required for 20/200 vision. In addition, we observed degeneration of the optic nerve and an indistinct ganglion cell layer. This is consistent with previous reports describing optic atrophy or optic pallor as one of the features associated with some forms of LCA.[15,25–31]

Previously, Porto et al.[32] published a histopathologic description of a voluntarily aborted 33-week-old fetus with LCA caused by a homozygous Cyst330Tyr missense mutation in RPE65. The fetal retina displayed reduced photoreceptor density, a thin ONL, decreased rod and cone opsin immunoreactivity, and aberrant synaptic and inner retinal organization. Ultrastructural examination revealed the presence of lipid and vesicular inclusions not seen in normal RPE. In addition, the Cyst330Tyr eyes demonstrated thickening, detachment, and collagen fibril disorganization in the underlying Bruch's membrane. The choroid was distended and abnormally vascularized compared with controls.[32]

The clinical findings when the patient was last examined at age 51 could be correlated with retinal histologic findings studied at age 56. The patient reported lower acuity in the right than in the left eye, probably because of the presence of a central macular hole in the right eye and optic nerve changes. The constricted fields with temporal islands and reduced full-field cone ERGs are consistent with the observation of cone photoreceptors only in the macula and far periphery. In addition, the near absence of rods was observed in the periphery of each eye, which is consistent with the elevated final dark-adaptation threshold of 3.5 log units. The decrease in the size of the full-field 30-Hz cone ERGs from 8.0 to 0.5 μV over 28 years suggested an exponential rate of decline of approximately 10% loss of remaining cone function per year that has been described for persons with retinitis pigmentosa.[33] The clinical description of our patient is similar to that of other RPE65 LCA patients previously described and includes measurable visual acuities, Goldmann visual fields, and small ERG amplitudes followed by slow deterioration of their visual function when measured over 20 years.[8,15]

Our study revealed a significant decrease in the accumulation of autofluorescent material in the RPE in the macula and periphery and is in agreement with observations carried out in LCA patients and in RPE65 knockout mice. Autofluorescence measures lipofuscin accumulation in the RPE, which is related to shed photoreceptor disc segments and requires vitamin A derivatives (retinoids). It allows for the visualization of disease-specific distributions of lipofuscin in the RPE, often not visible on ophthalmoscopy. Lorenz et al.[34] found absent or minimal autofluorescence in all LCA patients with compound heterozygous or homozygous RPE65 mutations, whereas autofluores-

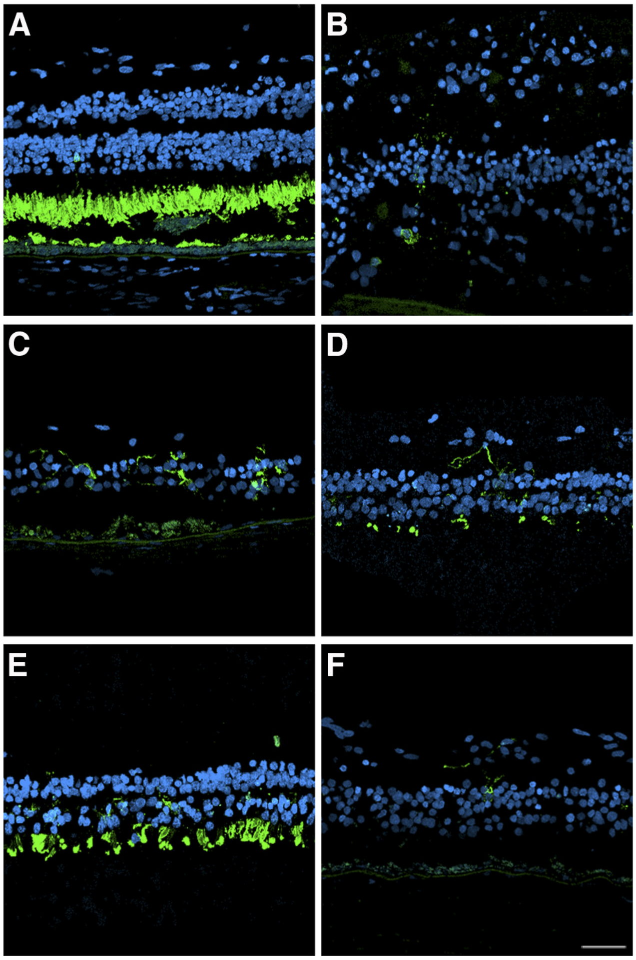

**Figure 10.** Disorganized morphology of the rods remaining in the retina of an RPE65 postmortem donor eye. High-magnification comparison of the control and RPE65 donor retina showed that rhodopsin was restricted to the rod outer segments in the control retina (**A**). In the RPE65 donor, rods were significantly decreased in the affected retina in the macula (**B**) and periphery in the inferior (**C**), superior (**D**), temporal (**E**), and nasal (**F**) quadrants, with the remaining rods expanding horizontally into the RPE65 mutant retina. Scale bar, 40 μm.

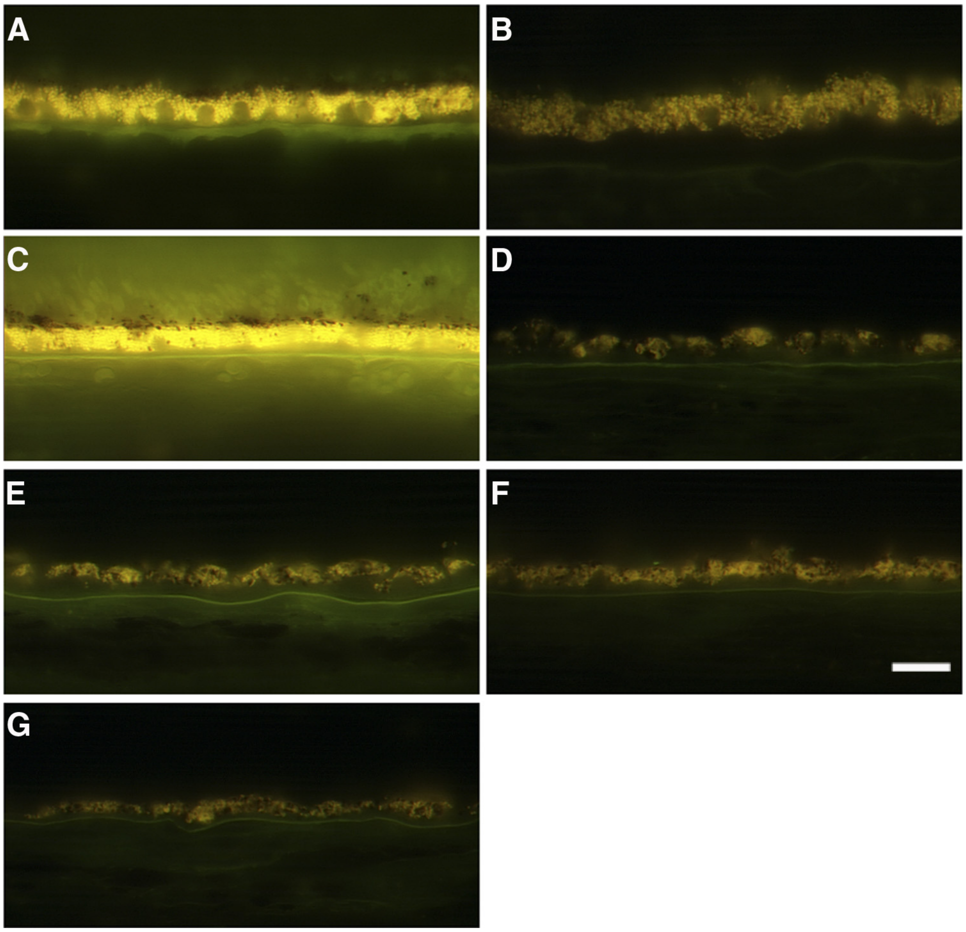

**FIGURE 11.** Significant decrease in the accumulation of autofluorescent material in the RPE of an RPE65 postmortem donor eye. Human cryosections of both a matched control (**A**, **C**) and an affected RPE65 donor (**B**, **D**–**G**) were observed on epifluorescence in the green channel (FITC filter, excitation 495 nm/emission 519 nm). RPE from the RPE65 mutant retina displayed significantly decreased autofluorescent granules in the macula (**B**) and periphery in the inferior (**D**), superior (**E**), temporal (**F**), and nasal (**G**) quadrants when compared with the control RPE (**A**). Scale bar, 200 $\mu$m.

cence was normal in the heterozygous parents and in LCA patients without mutations in RPE65 but with GUCY2D mutations. In the *Rpe65* knockout mice, RPE lipofuscin fluorophore accumulation was almost abolished in 12- to 13-month-old mice, indicating that the formation of RPE lipofuscin fluorophores is almost completely dependent on a normal visual cycle.[35,36]

The immunoreactivity of the RPE in the RPE65 postmortem donor eye when probed with the RPE65 antibody clearly indicates that RPE65 protein was present in this tissue. Although the functional consequences of the Ala132Thr substitution in the protein caused by the specific mutation in the *RPE65* gene of this donor are unknown, the severe progressive loss of rod and cone photoreceptors documented during her life suggests that this mutation results in the production of nonfunctional or minimally functional retinol isomerase by the RPE cells. Because some functional vision was retained in the remaining cones of the macula, a question arises about the source of the retinol isomerase that produces the chromophore used by these foveal cones. Recent studies[37,38] provide evidence that in addition to the retinol isomerase in the RPE (RPE65), there is another pathway in the outer retina for the generation of 11-*cis* retinoid used by cone photoreceptors that is independent of RPE65 activity. It is possible that some foveal cones in this RPE65 postmortem donor eye retained function because of the presence of this other pathway for the generation of a photoactive chromophore. Alternatively, although all cones failed comparably, the fovea failed last possibly because the density of cones was highest in this region.

Recently, two-photon microscopy revealed specialized storage sites for retinyl esters that were referred to as retinosomes or retinyl ester storage particles, taking advantage of the intrinsic fluorescence of all-*trans* retinyl esters in the living mouse eye.[39–41] Retinosomes were shown to correspond to vacuole-like structures, with translucent inclusions observed with electron microscopy. Our observations of the ultrastructure in this RPE65 donor eye revealed the presence of several cytoplasmic pleomorphic inclusions similar in structure to the retinosomes described in the RPE of wild-type and RPE65$^{-/-}$ mice. However, because the detection of retinosomes is carried out in vivo, we could not confirm the presence of these structures in the RPE of the RPE65 postmortem donor eye.

Several animal models with RPE65 mutations have been characterized and used in studies that have advanced our knowledge of LCA. In the knockout mouse model of the *RPE65* gene, RPE$^{-/-}$, rods and cones are present at birth and appear normal with intact outer segments until 15 weeks; however, the outer nuclear layer displays only seven layers at 28 weeks. The rod ERG is absent from the beginning, but the cone ERG is intact. Furthermore, the rhodopsin molecule is absent.[6] Therefore, the RPE$^{-/-}$ mouse model likely represents a rod-cone degeneration, with much more rod than cone dis-

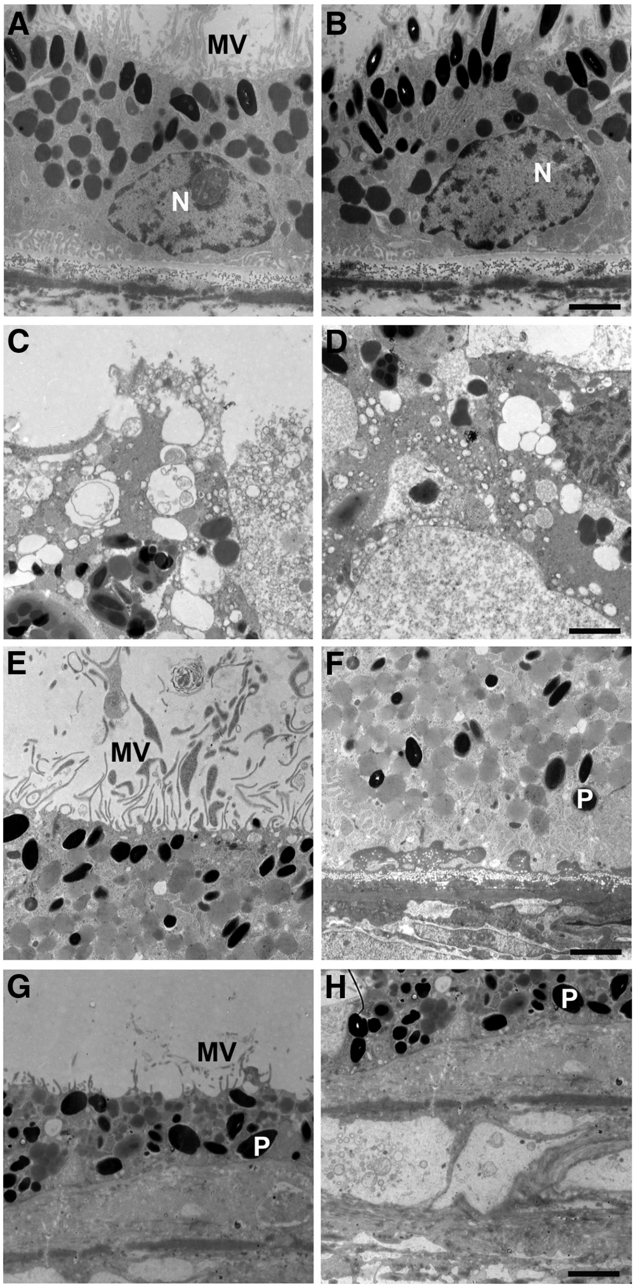

**Figure 12.** RPE degeneration in an RPE65 postmortem donor eye. Electron micrographs of the RPE from the control (**A**, **B**) and the RPE65 donor (**C**–**H**). The control RPE displayed apical microvilli (**A**) and basal infoldings (**B**). The ultrastructure of the RPE65 donor RPE showed degenerating changes in the different quadrants studied. In the macula, apical microvilli were absent, and pleomorphic inclusions were common (**C**). The basal surface was characterized by the absence of infoldings and pleomorphic inclusions (**D**). In the nasal quadrant, apical microvilli were present (**E**). However, the basal surface was characterized by the presence of electron-dense material beneath the RPE cells (**F**). In the inferior quadrant, the RPE was discontinuous, and in some areas short apical microvilli were still present above the RPE (**G**) and a debris zone was present below it (**H**). N, nucleus; P, pigment; MV, microvilli. Scale bars, 2 $\mu$m.

ease, and therefore is a good model for human LCA. On the other hand, the Briard dog displays a natural knockout of the *RPE65* gene that includes a 4-bp deletion of the gene.[42,43] In this model the retinal appearance of young animals is mostly normal, with the exception of the presence of inclusion bodies in the RPE layer; however, the ERG of both cones and rods is undetectable. This model is characterized by a very slow progressive retinal degeneration with outer segment shortening and retinal thinning.

In animals with RPE65 deficiency, gene transfer resulted in efficient RPE transduction, close to normal levels of rhodopsin and 11-*cis* retinal, and improved ERG responses with consequent improved visual acuity and visual guided behavior leading the way to consideration of human trials for this potentially reversible biochemical defect.[17,44–55] At first, three clinical trials involved the administration of adenoassociated virus vectors to replace for RPE65 deficiency and included nine patients.[56–58] All the trials targeted the clinically worse eye of adult patients with advanced disease. The short-term results from these ongoing trials were recently reported with improvements in light sensitivity, ambulation through an obstacle course, and nystagmus frequency in some patients, but the results were less promising in other patients. All patients still had nonrecordable ERGs, which was in clear contrast to the results obtained in the treatment studies using the canine model of RPE65 deficiency.[56–58]

Since the first clinical trial results were reported,[56–58] clinical data on >30 patients are now available. As expected, the clinical benefit remained stable in all patients, and no severe adverse effects were observed.[59,60] Overall, younger patients responded better to treatment and had greater improvements in light sensitivity than older patients.[60,61] Because of the extensive loss of photoreceptors, the degeneration of the optic nerve, and the indistinct ganglion cell layer observed in the retina of the RPE65 donor described here, it seems unlikely that gene therapy would result in extensive recovery of vision in a patient with retinal degeneration this advanced.

## *References*

1. Cremers FP, van den Hurk JA, den Hollander AI. Molecular genetics of Leber congenital amaurosis. *Hum Mol Genet.* 2002;11:1169–1176.
2. den Hollander AI, Roepman R, Koenekoop RK, Cremers FP. Leber congenital amaurosis: genes, proteins and disease mechanisms. *Prog Retin Eye Res.* 2008;27:391–419.
3. Jin M, Li S, Moghrabi WN, Sun H, Travis GH. Rpe65 is the retinoid isomerase in bovine retinal pigment epithelium. *Cell.* 2005;122: 449–459.
4. Moiseyev G, Chen Y, Takahashi Y, Wu BX, Ma JX. RPE65 is the isomerohydrolase in the retinoid visual cycle. *Proc Natl Acad Sci U S A.* 2005;102:12413–12418.
5. Redmond TM, Poliakov E, Yu S, Tsai JY, Lu Z, Gentleman S. Mutation of key residues of RPE65 abolishes its enzymatic role as isomerohydrolase in the visual cycle. *Proc Natl Acad Sci U S A.* 2005;102:13658–13663.
6. Redmond TM, Yu S, Lee E, et al. Rpe65 is necessary for production of 11-cis-vitamin A in the retinal visual cycle. *Nat Genet.* 1998;20: 344–351.
7. Woodruff ML, Olshevskaya EV, Savchenko AB, et al. Constitutive excitation by Gly90Asp rhodopsin rescues rods from degeneration caused by elevated production of cGMP in the dark. *J Neurosci.* 2007;27:8805–8815.
8. Dharmaraj SR, Silva ER, Pina AL, et al. Mutational analysis and clinical correlation in Leber congenital amaurosis. *Ophthalmic Genet.* 2000;21:135–150.
9. Marlhens F, Bareil C, Griffoin JM, et al. Mutations in RPE65 cause Leber's congenital amaurosis. *Nat Genet.* 1997;17:139–141.
10. Perrault I, Rozet JM, Ghazi I, et al. Different functional outcome of RetGC1 and RPE65 gene mutations in Leber congenital amaurosis. *Am J Hum Genet.* 1999;64:1225–1228.
11. Gu SM, Thompson DA, Srikumari CR, et al. Mutations in RPE65 cause autosomal recessive childhood-onset severe retinal dystrophy. *Nat Genet.* 1997;17:194–197.
12. Morimura H, Fishman GA, Grover SA, Fulton AB, Berson EL, Dryja TP. Mutations in the RPE65 gene in patients with autosomal re-

cessive retinitis pigmentosa or Leber congenital amaurosis. *Proc Natl Acad Sci U S A.* 1998;95:3088–3093.

13. Thompson DA, Gal A. Vitamin A metabolism in the retinal pigment epithelium: genes, mutations, and diseases. *Prog Retin Eye Res.* 2003;22:683–703.
14. Cai X, Conley SM, Naash MI. RPE65: role in the visual cycle, human retinal disease, and gene therapy. *Ophthalmic Genet.* 2009;30:57–62.
15. Lorenz B, Gyurus P, Preising M, et al. Early-onset severe rod-cone dystrophy in young children with RPE65 mutations. *Invest Ophthalmol Vis Sci.* 2000;41:2735–2742.
16. Paunescu K, Wabbels B, Preising MN, Lorenz B. Longitudinal and cross-sectional study of patients with early-onset severe retinal dystrophy associated with RPE65 mutations. *Graefes Arch Clin Exp Ophthalmol.* 2005;243:417–426.
17. Acland GM, Aguirre GD, Ray J, et al. Gene therapy restores vision in a canine model of childhood blindness. *Nat Genet.* 2001;28:92–95.
18. Dejneka NS, Surace EM, Aleman TS, et al. In utero gene therapy rescues vision in a murine model of congenital blindness. *Mol Ther.* 2004;9:182–188.
19. Jacobson SG, Aleman TS, Cideciyan AV, et al. Identifying photoreceptors in blind eyes caused by RPE65 mutations: prerequisite for human gene therapy success. *Proc Natl Acad Sci U S A.* 2005;102: 6177–6182.
20. Jacobson SG, Aleman TS, Cideciyan AV, et al. Human cone photoreceptor dependence on RPE65 isomerase. *Proc Natl Acad Sci U S A.* 2007;104:15123–15128.
21. Jacobson SG, Cideciyan AV, Aleman TS, et al. RDH12 and RPE65, visual cycle genes causing Leber congenital amaurosis, differ in disease expression. *Invest Ophthalmol Vis Sci.* 2007;48:332–338.
22. Jacobson SG, Cideciyan AV, Aleman TS, et al. Photoreceptor layer topography in children with Leber congenital amaurosis caused by RPE65 mutations. *Invest Ophthalmol Vis Sci.* 2008;49:4573–4577.
23. Jacobson SG, Aleman TS, Cideciyan AV, et al. Defining the residual vision in Leber congenital amaurosis caused by RPE65 mutations. *Invest Ophthalmol Vis Sci.* 2009;50:2368–2375.
24. John SK, Smith JE, Aguirre GD, et al. Loss of cone molecular markers in rhodopsin-mutant human retinas with retinitis pigmentosa. *Mol Vis.* 2000;6:204–215.
25. Gillespie FD. Congenital amaurosis of Leber. *Am J Ophthalmol.* 1966;61:874–880.
26. Flynn JT, Cullen RF. Disc oedema in congenital amaurosis of Leber. *Br J Ophthalmol.* 1975;59:497–502.
27. Noble KG, Carr RE. Peripapillary pigmentary retinal degeneration. *Am J Ophthalmol.* 1978;86:65–75.
28. Moore A. Inherited retinal dystrophies. In: Taylor D, ed. *Pediatric Ophthalmology.* Boston: Blackwell Scientific Publications; 1990: 376–406.
29. Koenekoop RK. An overview of Leber congenital amaurosis: a model to understand human retinal development. *Surv Ophthalmol.* 2004;49:379–398.
30. Booij JC, Florijn RJ, ten Brink JB, et al. Identification of mutations in the AIPL1, CRB1, GUCY2D, RPE65, and RPGRIP1 genes in patients with juvenile retinitis pigmentosa. *J Med Genet.* 2005;42: 1–8.
31. Sullivan TJ, Lambert SR, Buncic JR, Musarella MA. The optic disc in Leber congenital amaurosis. *J Pediatr Ophthalmol Strabismus.* 1992;29:246–249.
32. Porto FB, Perrault I, Hicks D, et al. Prenatal human ocular degeneration occurs in Leber's congenital amaurosis (LCA2). *J Gene Med.* 2002;4:390–396.
33. Berson EL. Long-term visual prognoses in patients with retinitis pigmentosa: the Ludwig von Sallmann lecture. *Exp Eye Res.* 2007; 85:7–14.
34. Lorenz B, Wabbels B, Wegscheider E, Hamel CP, Drexler W, Preising MN. Lack of fundus autofluorescence to 488 nanometers from childhood on in patients with early-onset severe retinal dystrophy associated with mutations in RPE65. *Ophthalmology.* 2004; 111:1585–1594.
35. Katz ML, Redmond TM. Effect of Rpe65 knockout on accumulation of lipofuscin fluorophores in the retinal pigment epithelium. *Invest Ophthalmol Vis Sci.* 2001;42:3023–3030.
36. Katz ML, Wendt KD, Sanders DN. RPE65 gene mutation prevents development of autofluorescence in retinal pigment epithelial phagosomes. *Mech Ageing Dev.* 2005;126:513–521.
37. Mata NL, Radu RA, Clemmons RC, Travis GH. Isomerization and oxidation of vitamin a in cone-dominant retinas: a novel pathway for visual-pigment regeneration in daylight. *Neuron.* 2002; 36:69–80.
38. Mata NL, Ruiz A, Radu RA, Bui TV, Travis GH. Chicken retinas contain a retinoid isomerase activity that catalyzes the direct conversion of all-trans retinol to 11-cis retinol. *Biochemistry.* 2005;44: 11715–11721.
39. Imanishi Y, Batten ML, Piston DW, Baehr W, Palczewski K. Noninvasive two-photon imaging reveals retinyl ester storage structures in the eye. *J Cell Biol.* 2004;164:373–383.
40. Imanishi Y, Gerke V, Palczewski K. Retinosomes: new insights into intracellular managing of hydrophobic substances in lipid bodies. *J Cell Biol.* 2004;166:447–453.
41. Imanishi Y, Lodowski KH, Koutalos Y. Two-photon microscopy: shedding light on the chemistry of vision. *Biochemistry.* 2007;46: 9674–9684.
42. Wrigstad A, Narfstrom K, Nilsson SE. Slowly progressive changes of the retina and retinal pigment epithelium in Briard dogs with hereditary retinal dystrophy: a morphological study. *Doc Ophthalmol.* 1994;87:337–354.
43. Aguirre GD, Baldwin V, Pearce-Kelling S, Narfstrom K, Ray K, Acland GM. Congenital stationary night blindness in the dog: common mutation in the RPE65 gene indicates founder effect. *Mol Vis.* 1998;4:23.
44. Narfstrom K, Katz ML, Ford M, Redmond TM, Rakoczy E, Bragadottir R. In vivo gene therapy in young and adult RPE65−/− dogs produces long-term visual improvement. *J Hered.* 2003;94:31–37.
45. Lai CM, Yu MJ, Brankov M, et al. Recombinant adeno-associated virus type 2-mediated gene delivery into the Rpe65−/− knockout mouse eye results in limited rescue. *Genet Vaccines Ther.* 2004;2:3.
46. Acland GM, Aguirre GD, Bennett J, et al. Long-term restoration of rod and cone vision by single dose rAAV-mediated gene transfer to the retina in a canine model of childhood blindness. *Mol Ther.* 2005;12:1072–1082.
47. Narfstrom K, Vaegan, Katz M, Bragadottir R, Rakoczy EP, Seeliger M. Assessment of structure and function over a 3-year period after gene transfer in RPE65−/− dogs. *Doc Ophthalmol.* 2005;111:39–48.
48. Bemelmans AP, Kostic C, Crippa SV, et al. Lentiviral gene transfer of RPE65 rescues survival and function of cones in a mouse model of Leber congenital amaurosis. *PLoS Med.* 2006;3:e347.
49. Nusinowitz S, Ridder WH 3rd, Pang JJ, et al. Cortical visual function in the rd12 mouse model of Leber congenital amaurosis (LCA) after gene replacement therapy to restore retinal function. *Vision Res.* 2006;46:3926–3934.
50. Pang JJ, Chang B, Kumar A, et al. Gene therapy restores vision-dependent behavior as well as retinal structure and function in a mouse model of RPE65 Leber congenital amaurosis. *Mol Ther.* 2006;13:565–572.
51. Rolling F, Le Meur G, Stieger K, et al. Gene therapeutic prospects in early onset of severe retinal dystrophy: restoration of vision in RPE65 Briard dogs using an AAV serotype 4 vector that specifically targets the retinal pigmented epithelium. *Bull Mem Acad R Med Belg.* 2006;161:497–508, discussion 508–499.
52. Aguirre GK, Komaromy AM, Cideciyan AV, et al. Canine and human visual cortex intact and responsive despite early retinal blindness from RPE65 mutation. *PLoS Med.* 2007;4:e230.
53. Le Meur G, Stieger K, Smith AJ, et al. Restoration of vision in RPE65-deficient Briard dogs using an AAV serotype 4 vector that specifically targets the retinal pigmented epithelium. *Gene Ther.* 2007;14:292–303.
54. Roman AJ, Boye SL, Aleman TS, et al. Electroretinographic analyses of Rpe65-mutant rd12 mice: developing an in vivo bioassay for human gene therapy trials of Leber congenital amaurosis. *Mol Vis.* 2007;13:1701–1710.
55. Bennicelli J, Wright JF, Komaromy A, et al. Reversal of blindness in animal models of Leber congenital amaurosis using optimized AAV2-mediated gene transfer. *Mol Ther.* 2008;16:458–465.

56. Bainbridge JW, Ali RR. Success in sight: the eyes have it! Ocular gene therapy trials for LCA look promising. *Gene Ther.* 2008;15: 1191–1192.
57. Hauswirth WW, Aleman TS, Kaushal S, et al. Treatment of Leber congenital amaurosis due to RPE65 mutations by ocular subretinal injection of adeno-associated virus gene vector: short-term results of a phase I trial. *Hum Gene Ther.* 2008;19:979–990.
58. Maguire AM, Simonelli F, Pierce EA, et al. Safety and efficacy of gene transfer for Leber's congenital amaurosis. *N Engl J Med.* 2008;358:2240–2248.
59. Cideciyan AV, Hauswirth WW, Aleman TS, et al. Human RPE65 gene therapy for Leber congenital amaurosis: persistence of early visual improvements and safety at 1 year. *Hum Gene Ther.* 2009; 20:999–1004.
60. Simonelli F, Maguire AM, Testa F, et al. Gene therapy for Leber's congenital amaurosis is safe and effective through 1.5 years after vector administration. *Mol Ther.* 2010;18:643–650.
61. Maguire AM, High KA, Auricchio A, et al. Age-dependent effects of RPE65 gene therapy for Leber's congenital amaurosis: a phase 1 dose-escalation trial. *Lancet.* 2009;374:1597–1605.

Ophthalmic Genetics, 30(4), 172–180, 2009

ISSN: 1381-6810 print/ 1744-5094 online
DOI: 10.3109/13816810903176765

informa
healthcare

ORIGINAL ARTICLE

# Retinal pathology of a patient with Goldmann-Favre Syndrome

Vera L. Bonilha[1], Gerald A. Fishman[2], Mary E. Rayborn[1], and Joe G. Hollyfield[1]

[1]*The Cole Eye Institute, The Cleveland Clinic Foundation, Cleveland, Ohio, USA*
[2]*Department of Ophthalmology and Visual Sciences, University of Illinois, Chicago, Illinois, USA*

## ABSTRACT

*Purpose:* To define the retinal pathology in an 88-year-old male affected with Goldmann-Favre syndrome with a 2bp 5′ A>C splice site mutation in the NR2E3 gene.
*Methods:* Retinal tissue from the macula and periphery was processed for immunohistochemistry. Perimacular retina was processed for transmission electron microscopy. Cryosections were studied by indirect immunofluorescence, using well-characterized antibodies to rhodopsin, cone cytoplasm, and cone opsins. The affected donor eye was compared to a postmortem matched normal eye.
*Results:* The retina was highly disorganized without laminar organization. The RPE was discontinuous in some perimacular regions. Large (>1mm) spherical electrondense melanosomes were observed in the RPE and choroid by TEM. Rods were virtually absent in the affected retina. Cones were present in the macula, but were mostly absent from the retinal periphery. In addition, cone rosettes were observed in the perimacular area. Both red/green and blue cone opsins were distributed along the entire cellular expanse of the cone photoreceptors in the affected eye, but were restricted to the cone outer segments in the control retina.
*Conclusions:* The histological data obtained from the retina of an elderly male patient with Goldmann-Favre syndrome showed an absence of rods and abnormal distribution of red/green and blue cone opsins.

**KEYWORDS:** Goldmann-Favre syndrome; Cone opsins; Histology; Immunohistochemistry; Pigment clumping; Retinal degeneration; Rhodopsin

## INTRODUCTION

The Goldmann-Favre syndrome (GFS) is an autosomal recessive distinctive vitreoretinal degenerative disorder initially described in two separate reports in 1957[1] and 1958.[2] GFS is characterized by night blindness, pigmentary degeneration, macular and peripheral retinoschisis, posterior subcapsular cataract, markedly abnormal or nondetectable electroretinograms, and degenerative vitreous changes, such as liquefaction, and the presence of strands and/or bands. Since the original description, a number of other cases have been reported confirming that this is a clinically recognizable disease but it is now known that the specific clinical features vary among pedigrees.[3–9]

More recently, it was proposed that the GFS is a phenotypic variant of the enhanced S-cone syndrome, since in both retinal dysfunctions the patients display hypersensitivity to short-wavelength and their electroretinograms have greater amplitudes to short-wavelength (eg, blue) light flashes than to long-wavelength (eg, orange) light flashes.[10]

The GFS is caused by loss-of-function mutations in the *NR2E3* gene (also known as *PNR*). The *NR2E3* gene encodes a retinal nuclear receptor recently discovered to be a ligand-dependent transcription factor[11] specifically found in photoreceptors. Although the morphology and physiology of photoreceptors

Received 14 April 2009; revised 26 May 2009; accepted 06 July 2009

Correspondence: Vera L. Bonilha, PhD, Cleveland Clinic Foundation, The Cole Eye Institute, 9500 Euclid Avenue, i31, Cleveland, OH 44195. E-mail: bonilhav@ccf.org

are well documented, the developmental pathways from a multipotent retinal progenitor to a committed precursor and a terminally differentiated photoreceptor are only beginning to be elucidated. It is thought that *NR2E3* controls photoreceptor differentiation by repressing the expression of cone-specific genes in rods.[12,13] However, it is not known how the mutation in this gene leads to the degeneration of the RPE and retina.

Previously, a histopathological analysis from a full-thickness eye-wall biopsy of the eye of a young patient affected by GFS was reported.[5] In the present study we analyzed the morphology of the retina and the distribution of photoreceptor markers in a donor eye from a male donor affected by GFS. To our knowledge this is the first immunohistological study performed in a GFS affected eye.

## MATERIALS AND METHODS

### Patient Information

The donor was an 88-year-old man who died from congestive heart failure. He was an affected member of a family with autosomal recessive Goldmann-Favre syndrome. The eyes were obtained through the National Retinitis Pigmentosa Foundation Donor Program (donation number #816). The donor had an ocular exam 1 year prior to his death.

The clinical evaluation of the patient was carried out at the University of Illinois with the approval of the Institutional Review Board (IRB) at the University of Illinois Medical Center. However, since this is a single case report, IRB approval was not needed for this project.

### Histopathology

The immunocytochemistry analysis was performed at the Cleveland Clinic, where use of human tissues obtained after death is exempt from IRB approval. The donor globes were fixed 12 hrs postmortem in a mixture of 4% paraformaldehyde and 0.5% glutaraldehyde made in 0.1M phosphate buffer, pH 7.3. After 1 month in fixative, the globes were transferred and stored in 2% paraformaldehyde prepared in the same buffer. The eyes from a 78-year-old male and a 91-year-old male were used as controls, and were fixed 4.5 hr and 8.5 hr postmortem in 2% paraformaldehyde made in the same buffer. Tissue from the macula and periphery were cut, and the tissue was infused successively with 10% and 20% sucrose in PBS, and embedded in Tissue-Tek '4583' (Miles Inc., Elkhart, IN). Ten µm cryosections were cut on a cryostat HM 505E (Microm, Walldorf, Germany) equipped with a CryoJane Tape-Transfer system (Instrumedics, Inc., Hackensack, NJ).

Prior to labeling, embedding medium was removed through two consecutive PBS incubations for 20 min. The tissue was then processed for immunofluorescence labeling as previously described.[14] Briefly, tissues were blocked in PBS supplemented with 1% BSA (PBS/BSA) for 30 min and incubated with the antibodies in PBS/BSA overnight at 4°C. Cryosections of both the matched control and affected donor tissues were labeled with the following antibodies: rabbit polyclonal antibody AB5407 to blue cone opsin (1: 1200, Chemicon International, Inc., Temecula, CA), rabbit polyclonal antibody AB5405 to red/green cone opsins (1: 1200, Chemicon International, Inc., Temecula, CA), monoclonal antibody B6-30N to rhodopsin (1:50, from Dr. P. Hargrave, University of Florida, Gainesville, FL, U.S.A.), and the monoclonal antibody 7G6 to cone arrestin (1:100, from Dr. P. MacLeish, Morehouse School of Medicine, Atlanta, GA).[15] Cell nuclei were labeled with TO-PRO®-3 iodide (1mg/ml, Molecular Probes, Eugene, OR). Secondary antibodies (goat anti-mouse or anti-rabbit IgG; 1:1000) were labeled with Alexa Fluor 488 (green; Molecular Probes). Sections were analyzed using a Leica laser scanning confocal microscope (TCS-SP2, Leica, Exton, PA). A series of 1 µm *xy* (*en face*) sections were collected. Each individual *xy* image of the retinas stained represents a three-dimensional projection of the entire cryosection (sum of all images in the stack). Microscopic panels were composed using AdobePhotoshop CS3 (Adobe, San Jose, CA).

### Ultrastructural Analysis

A small area of the retina/RPE/choroid tissue from the perimacula region of the affected donor and matched-controls (78- and 91-year-old males with 4.5 and 7.5 hr postmortem) were fixed in 2.5% glutaraldehyde and 0.1M cacodylate buffer, sequentially dehydrated in ethanol and embedded in Epon as previously reported.[16] One µm plastic sections of both samples were stained with toluidine blue and examined and photographed by light microscopy with a Zeiss Axiophot microcroscope (Zeiss) equipped with a Hamamatsu C5810 camera (Hamamatsu Photonics, Bridgewater, NJ, USA). Thin sections were prepared and electron micrographs were taken on a Tecnai 20 200 kV digital electron microscope (Philips, Hillsboro, OR) using a Gatan image filter and digital camera (Gatan, Inc., Warrendale, PA, USA) at 3600 diameters and were printed at identical magnifications.

# RESULTS

## Clinical Findings

The patient was initially seen at age 57 years with a history of poor night vision for as long as he could remember. He also complained of blurred central vision and impairment of his peripheral visual field. His family pedigree showed that of five siblings, a deceased sister was known to have had poor vision from an early age.

He was last seen for a follow-up eye examination in February 2006 at 87 years of age which was 1 year prior to his death. At that time, his visual acuity was correctable to 20/400 in the right eye and 20/200 in the left. The corneas were clear and he had bilateral posterior capsule intraocular lens implants. Ocular pressures by applanation were 15 mmHg in each eye.

His retinal examination showed atrophic-appearing changes in the macula of each eye. The retinal vessels were attenuated and the optic disc in each eye showed a ‘waxy’ appearing atrophy. The peripheral retina showed extensive pigment clumping, which was spherical in appearance and present for 360°. Predominantly in the inferotemporal quadrant, there was a peripheral retinoschisis in each eye. Goldmann kinetic visual fields obtained 4 years prior to his death showed severe concentric restriction to even a large V4e test target in each eye.

A 2bp 5′ A>C splice site mutation in the NR2E3 gene had been previously identified.

## Morphologic Study

Semi-thin sections of epon-embedded GFS donor tissue were analyzed and compared to age-similar controls (Figure 1). The fundus image of the posterior pole of the GFS patient is depicted in Figure 1A, highlighting hyperpigmentation (white arrowheads) and peripheral retinoschisis (white *) (A); both periphery and perimacular tissues were harvested and processed for observation in both the morphological and ultrastructural assays. The retina of the GFS affected donor displayed different degrees of retinal degeneration in each of the regions observed when compared to the morphology of the control retina in the perimacular (Figure 1B) region of the eye. Observation at low magnification of both perimacula (Figure 1C) and periphery tissue (Figure 1E) demonstrated sparse inner and outer nuclear layers with stunted photoreceptor inner and outer segments. A thin, restricted area of pigmented RPE cells was observed in the perimacular retina (Figure 1, C and D, arrows) while a continuous layer of pigmented RPE cells was observed in the periphery (Figure 1E) of the affected donor. High magnification observation of the affected retina in the periphery (Figure 1F, arrowheads) but not in the perimacular region (Figure 1D) showed the presence of several areas of pigment clumping. In addition, tissue from the inferotemporal quadrant was also evaluated (Figures 1, G and H). This region contained a prominent pre-retina (epiretinal) membrane composed of a monolayer of fibroblast-like cells that were separated from the retina by a connective tissue-like matrix that was free of cells (Figures 1, H and G, *). The separation of this membrane from the retinal surface varied from 10 to 40μm. This membrane was not observed in the other areas of the retina examined.

## Immunofluorescence Study

To further understand some of the molecular changes associated with the GFS phenotype in this affected donor, tissue from the periphery and macula of his right eye was processed for cryosectioning and immunofluorescence. Initially, the distribution of rhodopsin was analyzed in both the symptomatic carrier and a matched-control eye (Figure 2, A–D). Rhodopsin was absent in both the periphery (Figure 2B) and perimacular (Figures 2, C and D) area of the GFS affected retina. This observation was in sharp contrast to the presence of rhodopsin in the outer segments observed in the control retina (Figure 2A).

In addition, cryosections were also labeled with cone specific markers. Initially, the distribution of the cone cytoplasmic marker 7G6 was analyzed in both the GFS affected donor and a matched-control eye (Figures 3, A–D). In the GFS affected retina, a complete absence of cones was observed in the periphery (Figure 3B). However, in the perimacular area, a high density of cones (Figure 3C) was observed together with the presence of several rosettes (Figure 3D). In contrast to cones in the control sample (Figure 3A), the cones in the GFS affected retina did not display a synaptic base (Figures 3, B–D). Moreover, cell nuclei, labeled with TO-PRO-3, displayed a significant difference in the organization of the all retinal cell types when compared to the matched control.

Additional characterization of the GFS affected donor also included the labeling of this retina with antibodies directed to red/green cone opsin. The control retina displayed the red/green cone opsin restricted to its outer segments (Figure 4A). However, a striking abnormal distribution of the red/green opsins throughout the entire cone cell body was observed in the perimacular regions of the affected

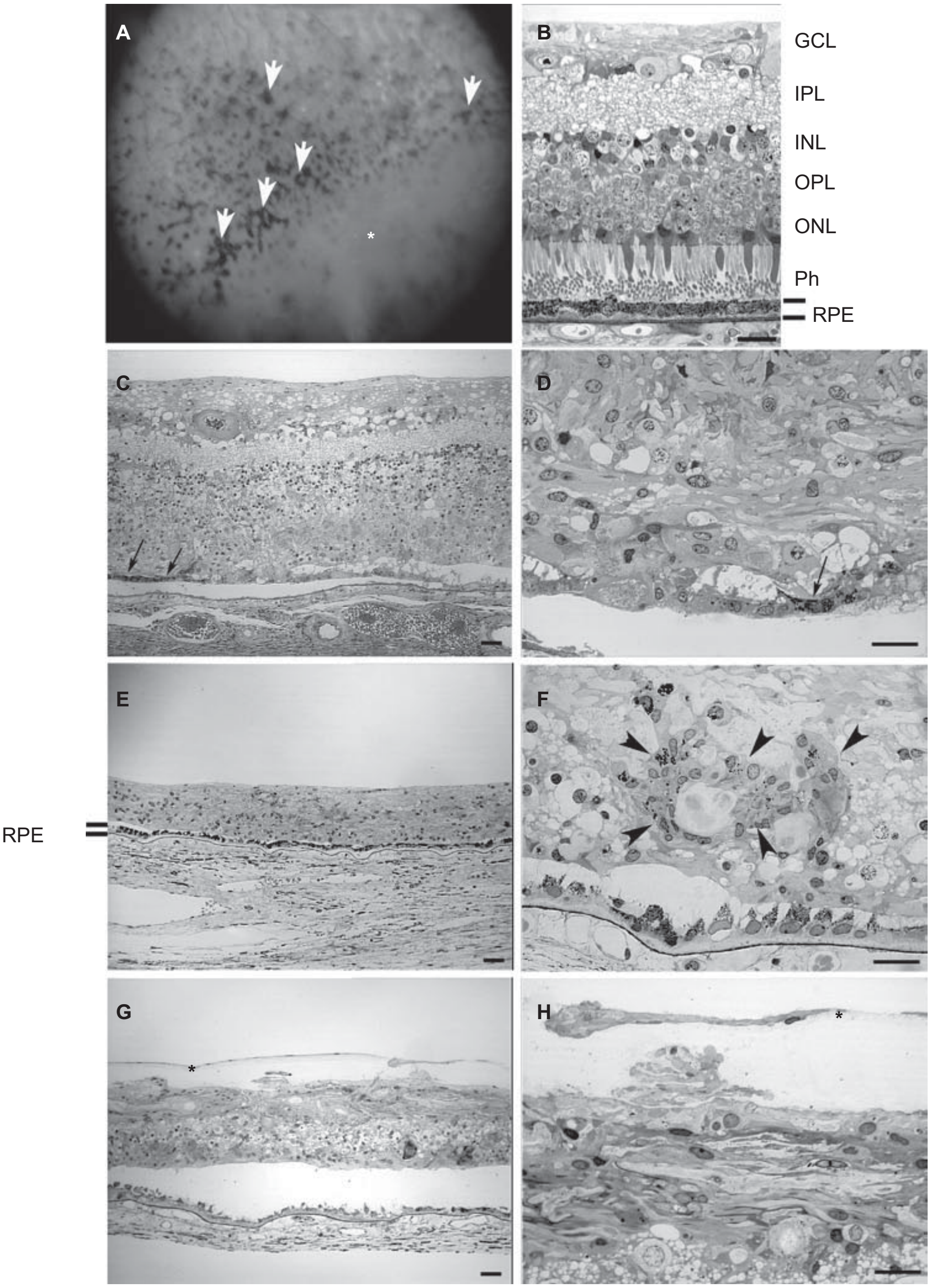

FIGURE 1 Degeneration in the retina of a Goldmann-Favre syndrome (GFS) affected donor. Human 1µm plastic sections of both a matched control (B) and the affected GFS (C-F) retinas stained with toluidine blue. Top panel corner depicts a fundus image of the patient's left eye, showing hyperpigmentation (white arrowheads) and peripheral retinoschisis (white *) (A). (B) Morphology of perimacular region of the control eye (C–F). The retina of the affected GFS donor displayed different degrees of retinal degeneration. Observation at low magnification of both perimacular region (C) and peripheral tissue (E) demonstrated sparse inner and outer nuclear layers with stunted photoreceptor inner and outer segments. A thin, restricted area of pigmented RPE cells was observed in the perimacular retina (C, arrows) while a continuous layer of pigmented RPE cells was observed in the periphery (E) of the affected donor. High magnification observation of the affected retina in the periphery (F) but not in the perimacular region (D) showed the presence of several clumps of pigment (arrowheads). In addition, tissue from the inferotemporal quadrant was also evaluated (G, H). This region contained a prominent pre-retina (epiretinal) compartment composed of a monolayer of fibroblast-like cells that were separated from the retina by a connective tissue-like matrix that was free of cells (H, G, *). RPE= retinal pigment epithelium; Ph=photoreceptors; ONL= outer nuclear layer; OPL= outer plexiform layer; INL= inner nuclear layer; IPL= inner plexiform layer; GCL= ganglion cell layer. Scale bars C, E, G=40µm; B, D, F, H= 20µm.

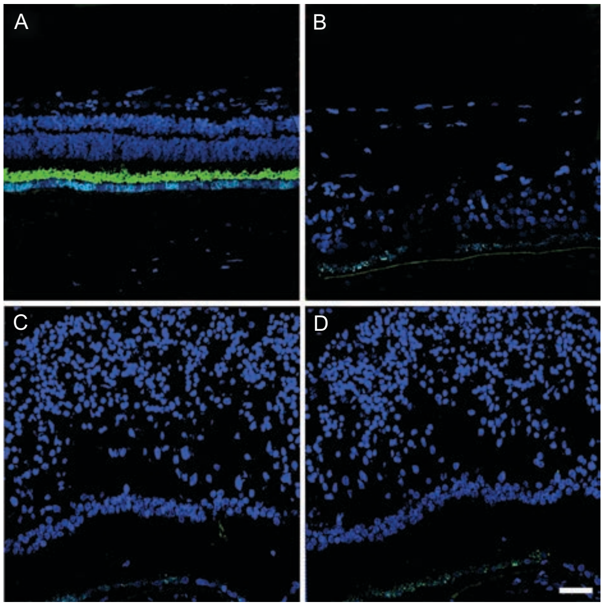

FIGURE 2 Absence of rhodopsin in the rods in a GFS affected donor. Human cryosections of both a matched control (A) and affected GFS donor (B–D) were labeled with antibodies specific to rhodopsin (Alexa488, green) while cell nuclei were labeled with TO-PRO-3 (blue). Sections were analyzed using a Leica laser scanning confocal microscope. Comparison of the samples showed that rhodopsin was absent in the affected retina in all the regions observed. Scale bar = 40µm.

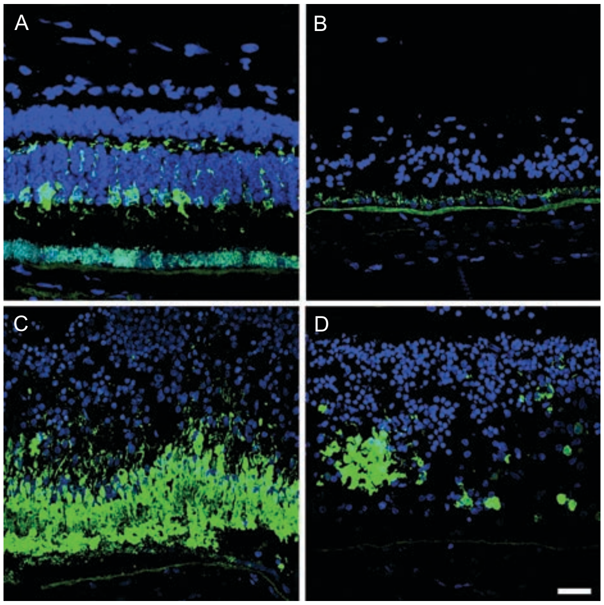

FIGURE 3 Significant absence of cones in the periphery together with the presence of rosettes of cones in the perimacular region of a GFS affected donor. Human cryosections of both a matched control (A) and a GFS affected donor (B–D) were labeled with antibodies specific to cone cytoplasm (7G6, Alexa488, green) while cell nuclei were labeled with TO-PRO-3 (blue). Sections were analyzed using a Leica laser scanning confocal microscope. Comparison of the samples showed that cones were almost absent in the periphery (B) while in the perimacular region they were present in high density (C). Cones were also distributed in rosettes in the perimacular region (D). Scale bar = 40µm.

retina (Figure 4C); the abnormal distribution was also observed in rosettes within the perimacular region (Figure 4D). On the other hand, red/green opsins were mostly absent in the periphery of the affected retina (Figure 4B).

Both a matched control and affected GFS donor eyes were labeled with antibodies specific to blue cone opsins (Figure 5). The control retina displayed the blue cone opsin restricted to its outer segments (Figure 5A). However, a significant increase in blue cone opsin was observed in all regions of the cone structure in the GFS affected eye (Figure 5, B–D) where the blue cone opsin was distributed along the entire plasma membrane of this cone type; the abnormal distribution was also observed in rosettes in the perimacular region (Figure 5D).

### Ultrastructural Pathology

The ultrastructure of RPE and Bruch's membrane in the perimacula tissue was analyzed by TEM (Figure 6). Observation at both low (Figures 6, B and C) and high (Figure 6D) magnification showed a collapsed RPE apical surface mostly deprived of apical microvilli; no photoreceptor outer segments were observed anterior to the RPE apical surface. Moreover, observation of the RPE's basal surface showed an absence of basal infoldings (Figure 6D, arrows); Bruch's membrane was notably disorganized (Figure 6, B and C) when compared to control sample (Figure 6A). Some areas displayed multilayers of pigmented cells (Figure 6C). Interestingly, the presence of desmosomes (Figures 6, C and D, arrowheads) was noticed between adjacent cells. The cytoplasm of RPE cells was filled with abnormally large (>1mm) spherical electrondense melanosomes (Figures 6, B and C) when compared to control RPE cells (Figure 6A).

## DISCUSSION

Histopathological analysis of the GFS affected retina showed the presence of different degrees of photoreceptor cell degeneration in both the peripheral and perimacular regions. In this affected donor, RPE degeneration was also observed and documented.

Differentiation of the vertebrate retina is guided by complex interactions between intrinsic genetic programs and extrinsic regulatory factors, entailing

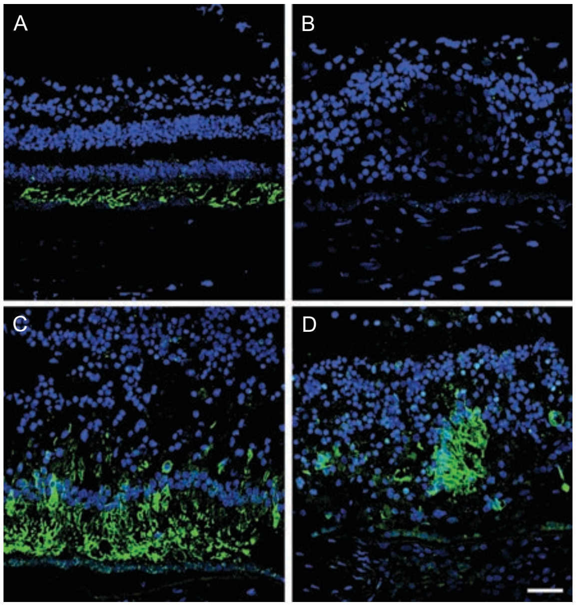

FIGURE 4 Red/green cone opsin is distributed along the entire plasma membrane of this cone type in a GFS affected donor. Human cryosections of both a matched control (A) and affected GFS donor (B–D) were labeled with antibodies specific to red/green cone opsins (Alexa488, green) while cell nuclei were labeled with TO-PRO-3 (blue). Sections were analyzed using a Leica laser scanning confocal microscope. Comparison of the samples showed that red/green cone opsins were distributed along the entire plasma membrane of this cone type in the perimacular region (C, D); this abnormal distribution was also observed in rosettes in a perimacular location (D). On the other hand, red/green opsins were mostly absent in the periphery of the affected retina (B). Scale bar = 40μm.

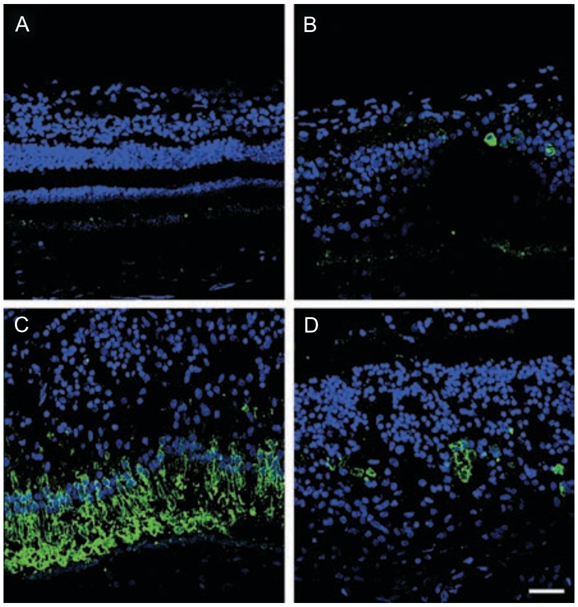

FIGURE 5 Blue cone opsin is significantly increased and distributed along the entire plasma membrane of this cone type in a GFS affected donor. Human cryosections of both a matched control (A) and affected GFS donor (B–D) were labeled with antibodies specific to blue cone opsins (Alexa488, green) while cell nuclei were labeled with TO-PRO-3 (blue). Sections were analyzed using a Leica laser scanning confocal microscope. Comparison of the samples showed that blue cone opsins were significantly increased both in the periphery (B) and perimacular region (C, D) of the affected eye, where blue cone opsins were distributed along the entire plasma membrane of this cone type; the abnormal distribution was also observed in rosettes in a perimacular location (D). Scale bar = 40μm.

precise coordination between withdrawal from the cell cycle and differentiation.[17–21] Acquisition of functional specificity depends on precise spatially and temporally gene expression patterns that are in turn dictated by complex transcriptional regulatory networks.[22–24] In the mammalian retina rod and cone photoreceptors are generated from common pool(s) of neuroepithelial progenitors. Cone-rod homeobox (CRX), neural retina leucine zipper (NRL) and rod-specific orphan nuclear receptor (NR2E3) are key transcriptional regulators that control photoreceptor differentiation.[11,25–27]

Enhanced S cone syndrome (ESCS) patients, as well as patients with Goldman-Favre syndrome and some patients with clumped pigmentary retinal degeneration, carry mutations in the NR2E3 gene. Specifically, loss-of-function mutations in this gene cause a disorder of human retinal photoreceptor development characterized by hyperfunction and excess of the normally minority S (short wavelength or blue) cone photoreceptor type together with near absence of function of the majority of rod receptors.[12,28–31] Moreover, multiple mutations in the mouse Nr2e3 gene were identified in the rd7 mouse model.[32,33] The rd7 mice exhibit a progressive rod degeneration accompanied by 1.5–2 fold increase in the number of S-cones.[32–34]

The human retina is composed of roughly 90% red/green and 10% blue cones.[35–37] However, the data obtained in the analysis of the GFS affected retina revealed a significant increase in blue cone opsins both in the periphery and perimacular region. A high proportion of rods over cones (over 95%) also characterize the normal human retina. The GFS affected retina was characterized by an almost complete absence of rods. The photoreceptor phenotypes described above are in agreement with the previously described Nr2e3 mutations in humans and rodents, which led to excess of the minority of the S (short-wavelength or blue) cone photoreceptor type together with near absence of rod function.

In the present case, a striking cone abnormality was the presence of both red/green and blue opsins throughout the entire cone cell body instead of the usual restriction to the outer segment. A previous

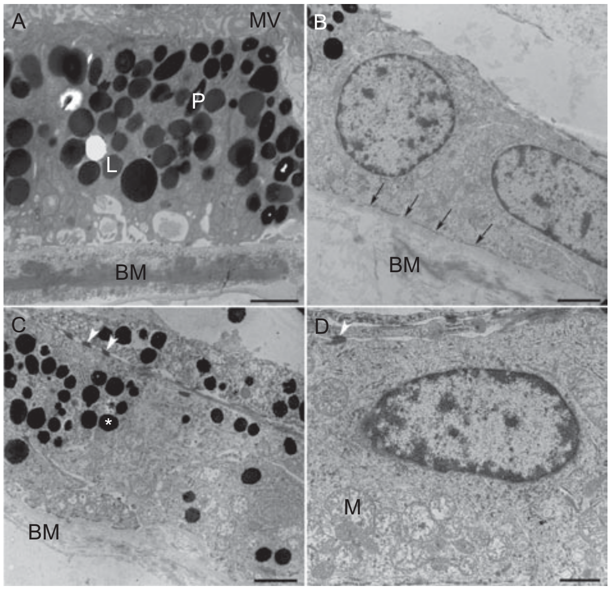

FIGURE 6 Ultrastructural evidence of RPE degeneration in a GFS affected donor. The ultrastructure of perimacular tissue was analyzed by TEM. Observation at both low (B, C) and high (D) magnification showed a collapsed RPE apical surface mostly deprived of apical microvilli; no photoreceptor outer segments are observed on top of the RPE apical surface. Moreover, observation of RPE's basal surface showed absence of basal infoldings (arrows); Bruch's membrane was very disorganized (B, C) when compared to control sample (A). Some areas displayed multilayers of pigmented cells (C). The presence of desmosomes (C, D, arrowheads) was noticed between adjacent cells. The cytoplasm of RPE cells was filled with abnormally large (>1mm) spherical electrondense melanosomes (B, C, *) when compared to a control RPE cell (A). Electron micrographs were taken on a Tecnai 20, 200 kv digital electron microscope using a Gatan image filter. N= nucleus; M= mitochondria; MV= microvilli; BM= Bruch's membrane; L= lipofuscin granules; P=pigment. Scale bars: A, B, C = 2μm and D = 1μm.

study of enhanced S-cone syndrome donor eyes reported the presence of abnormal distribution of both S- (blue) and L/M- (red/green) cone opsins along the entire plasma membranes of the cells, including their inner segments, cell bodies, axon and pedicles.[28] More recently, an affected member of a clinically well characterized family with an autosomal dominant form of cone dystrophy was also shown to exhibit distribution of the red/green cone opsin from the tip of the outer segment to the pedicle.[35] Moreover, a recent retinitis pigmentosa GTPase regulator (RPGR)-deficient murine model was also shown to have initial ectopic or unrestricted distribution of both red/green and blue opsins and a reduced level of rhodopsin followed by the subsequent degeneration of cones and rods.[38] That report suggested that mislocalization of cone opsins may precede cone cell death. Finally, a recent report described red/green opsin distribution throughout the cell membrane of the heterozygous P23H-3 rhodopsin rat transgenic retinas from postnatal day 16 to 500.[39]

Another unique phenotype of the GFS affected retina was the presence of rosettes of both red/green and blue cone opsin in the perimacular region. The rd7 mouse model is characterized histologically by retinal dysplasia manifesting as folds and whorls labeled with blue cone opsin antibody in the photoreceptor layer.[33] The authors that described the retinal dysplasia speculated that Nr2e3 might function by regulating genes involved in cone cell proliferation. Further studies will be necessary to unravel the function of Nr2e3 in the generation of retinal folds or rosettes.

The processing of visual information from the environment begins at the output of the photoreceptor synapse with neurons in the inner layers of the retina. No cone pedicles were observed in the GFS affected retina when labeled with the cone arrestin antibody, in contrast to what was observed in control retinas. Therefore, it is possible that the GFS affected retina could not effectively process visual information.

In the GFS affected retina, the RPE cells were significantly different from control matched RPE cells. A thin, restricted area of pigmented RPE cells was observed in the perimacular retina while a continuous layer of pigmented RPE cells was observed in the periphery; these pigmentary changes are likely associated with the clinical clumped pigmentary retinal findings frequently reported in Goldmann-Favre patients. The ultrastructural observation of the perimacular area revealed a collapsed RPE apical surface mostly deprived of apical microvilli and basal infoldings. Moreover, Bruch's membrane was extensively disorganized. Some areas displayed multilayers of pigmented cells where the presence of desmosomes was noticed between adjacent cells. The cytoplasm of RPE and choroidal cells was filled with abnormally large (>1mm) spherical electrondense melanosomes. Further analysis of these melanosomes is needed for a better understanding of their role in the pathologic changes observed. A previous histopathologic analysis of a full-thickness eye-wall biopsy obtained from the eye of a young patient with Goldmann-Favre syndrome, from a 4 mm peripheral area, displayed diffuse degenerative changes involving predominantly the sensory retinal layers with a relatively normal pigment epithelium and choroid.[5]

In conclusion, we report here the clinical findings and abnormal distribution of the red/green and blue cone opsins throughout the entire cone cell bodies together with absence of rhodopsin in the retina from a donor diagnosed with GFS. The red/green and blue cones were also observed in rosettes uniquely present in the perimacular area. These results are important to our understanding of one of possibly several molecular mechanisms underlying this disease. It also suggests that vision loss in this patient may result not only from abnormal Nr2e3 but also from secondary neuronal death and corrupted retinal circuitry due to the irreversible effects of retinal remodeling.

## ACKNOWLEDGMENTS

This work was presented at the Association for Research in Vision and Ophthalmology Annual Meeting, May, 2008 and at the XIIIth International Symposium on Retinal Degeneration Meeting, September, 2008 and at XVIII ICER08.
The authors thank Dr. Peter MacLeish (Morehouse School of Medicine, Atlanta, GA) for providing us with the antibody to cone arrestin (7G6), Dr. Paul Hargrave (University of Florida, Gainesville, FL) for providing us with the antibody to rhodopsin (B6-30N). This work was supported by The Foundation Fighting Blindness, Owings Mills, MD, NIH infrastructure grant EY015638 and an unrestricted grant from Research to Prevent Blindness.

***Declaration of interest*:** The authors report no conflict of interest.

## REFERENCES

1. Goldmann H. Présentation du rapport sur la biomicroscopie du du corps vitré et du fond d'oeil. Bull Mem Soc Fr Ophtalmol. 1957;70:265–272.
2. Favre M. Two cases of hyaloid-retinal degeneration. Ophthalmologica. 1958;135:604–609.
3. Fishman GA, Jampol LM, Goldberg MF. Diagnostic features of the Favre-Goldmann syndrome. Br J Ophthalmol. 1976;60:345–353.
4. Schmidt B., Weinberg M. Atypical retinopathia pigmentosa with central retinoschisis (Goldmann-Favre). Klin Monatsbl Augenheilkd. 1976;169:508–512.
5. Peyman GA, Fishman GA, Sanders DR, Vlchek J. Histopathology of Goldmann-Favre syndrome obtained by full-thickness eye-wall biopsy. Ann Ophthalmol. 1977;9:479–484.
6. Izumi K, Matsuhashi M. Goldmann-Favre syndrome in a four-year-old-girl. Doc Ophthalmol. 1977;66:219–226.
7. Nasr YG, Cherfan GM, Michels RG, Wilkinson CP. Goldmann-Favre maculopathy. Retina. 1990;10:178–180.
8. Garweg J, Bohnke M, Mangold I. Treatment of Goldmann-Favre syndrome with cyclosporin A and bromocriptine. Klin Monatsbl Augenheilkd. 1991;199:199–205.
9. Ikaheimo K, Tuppurainen K, Mantyjarvi M. Clinical features of Goldmann-Favre syndrome. Acta Ophthalmol Scand. 1999;77:459–461.
10. Jacobson SG, Roman AJ, Roman MI, Gass JDM, Parker JA. Relatively enhanced S cone function in the Goldmann-Favre syndrome. Am J Ophthalmol. 1991;111:446–453.
11. Kobayashi M, Takezawa S, Hara K, Yu RT, Umesono Y, Agata K, Taniwaki M, Yasuda K, Umesono K. Identification of a photoreceptor cell-specific nuclear receptor. Proc Natl Acad Sci USA. 1999;96:4814–4819.
12. Haider NB, Jacobson SG, Cideciyan AV, Swiderski R, Streb LM, Searby C, Beck G, Hockey R, Hanna DB, Gorman S, Duhl D, Carmi R, Bennett J, Weleber RG, Fishman GA, Wright AF, Stone EM, Sheffield VC. Mutation of a nuclear receptor gene, NR2E3, causes enhanced S cone syndrome, a disorder of retinal cell fate. Nat Genet. 2000;24:127–131.
13. Cheng H, Aleman TS, Cideciyan AV, Khanna R, Jacobisn SG, Swaroop A. In vivo function of the orphan nuclear receptor NR2E3 in establishing photoreceptor identity during mammalian retinal development. Hum Mol Genet. 2006;15:2588–2602.
14. Bonilha VL, Hollyfield JG, Grover S, Hollyfield JG. Abnormal distribution of red/green cone opsins in a patient with an autosomal dominant cone dystrophy. Ophthalmic Genet. 2005;26:69–76.
15. Zhang H, Cuenca N, Ivanova T, Church-Kopish J, Frederick JM, MacLeish PR, Baebr W. Identification and light-dependent translocation of a cone-specific antigen, cone arrestin, recognized by monoclonal antibody 7G6. Invest Ophthalmol Vis Sci. 2003:44:2858–2867.
16. Bonilha VL, Trzupek KM, Li Y, et al. Choroideremia: analysis of the retina from a female symptomatic carrier. Ophthalmic Genet. 2008;29:99–110.
17. Ericson J, Morton S, Kawakami A, Roelink H, Jessell TM. Two critical periods of Sonic Hedgehog signaling required for the specification of motor neuron identity. Cell. 1996;87:661–673.
18. Desai AR, McConnell SK. Progressive restriction in fate potential by neural progenitors during cerebral cortical development. Development. 2000;127:2863–2872.
19. Levine EM, Fuhrmann S, Reh TA. Soluble factors and the development of rod photoreceptors. Cell Mol Life Sci. 2000;57:224–234.
20. Dyer MA, Cepko CL. Regulating proliferation during retinal development. Nat Rev Neurosci. 2001;2:333–342.
21. Ohnuma S, Harris WA. Neurogenesis and the cell cycle. Neuron. 2003;40:199–208.
22. Brivanlou AH, Darnell JE Jr. Signal transduction and the control of gene expression. Science. 2002;295:813–818.
23. Marquardt T, Gruss P. Generating neuronal diversity in the retina: one for nearly all. Trends Neurosci. 2002;25:32–38.
24. Levine M, Davidson EH. Gene regulatory networks for development. Proc Natl Acad Sci U S A. 2005;102: 4936–4942.
25. Swaroop A, Xu JZ, Pawar H, Jackson A, Skolnick C, Agarwal N. A conserved retina-specific gene encodes a basic motif/leucine zipper domain. Proc Natl Acad Sci U S A. 1992;89:266–270.
26. Chen S, Wang QL, Nie Z, Sun H, Lennon G, Copeland NG, Gilbert DJ, Jenkins NA, Zack DJ. Crx, a novel Otx-like paired-homeodomain protein, binds to and transactivates photoreceptor cell-specific genes. Neuron. 1997;19: 1017–1030.
27. Furukawa T, Morrow EM, Cepko CL. Crx, a novel otx-like homeobox gene, shows photoreceptor-specific expression and regulates photoreceptor differentiation. Cell. 1997;91:531–541.

28. Milam AH, Rose L, Cideciyan AV, Barakat MR, Tang WX, Gupta N, Aleman TS, Wright AF, Stone EM, Sheffield VC, Jacobson SG. The nuclear receptor NR2E3 plays a role in human retinal photoreceptor differentiation and degeneration. Proc Natl Acad Sci U S A. 2002;99:473–478. Epub 2002 Jan 2.
29. Sharon D, Sandberg MA, Caruso RC, Berson EL, Dryja TP. Shared mutations in NR2E3 in enhanced S-cone syndrome, Goldmann-Favre syndrome, and many cases of clumped pigmentary retinal degeneration. Arch Ophthalmol. 2003;121:1316–1323.
30. Wright AF, Reddick AC, Schwartz SB, Ferguson JS, Aleman TS, Kellner U, Jurklies B, Schuster A, Zrenner E, Wissinger B, Lennon A, Shu X, Cideciyan AV, Stone EM, Jacobson SG, Swaroop A. Mutation analysis of NR2E3 and NRL genes in Enhanced S Cone Syndrome. Hum Mutat. 2004;24:439.
31. Jacobson SG, Sumaroka A, Aleman TS, et al. Nuclear receptor NR2E3 gene mutations distort human retinal laminar architecture and cause an unusual degeneration. Hum Mol Genet. 2004;13:1893–1902.
32. Akhmedov NB, Piriev NI, Chang B, Rapoport AL, Hawes NL, Nishina PM, Nusinowitz S, Heckenlively JR, Roderick TH, Kozak CA, Dacinger M, Davisson MT, Farber DB. A deletion in a photoreceptor-specific nuclear receptor mRNA causes retinal degeneration in the rd7 mouse. Proc Natl Acad Sci U S A. 2000;97:5551–5556.
33. Haider NB, Naggert JK, Nishina PM. Excess cone cell proliferation due to lack of a functional NR2E3 causes retinal dysplasia and degeneration in rd7/rd7 mice. Hum Mol Genet. 2001;10:1619–1626.
34. Curcio CA, Allen KA, Sloan KR, Lerea CL, Hurley JB, Klock IB, Milam AH. Distribution and morphology of human cone photoreceptors stained with anti-blue opsin. J Comp Neurol. 1991;312:610–624.
35. Chen J, Rattner A, Nathans J. Effects of L1 retrotransposon insertion on transcript processing, localization and accumulation: lessons from the retinal degeneration 7 mouse and implications for the genomic ecology of L1 elements. Hum Mol Genet. 2006;15:2146–2156.
36. Roorda A, Metha AB, Lennie P, Williams DR. Packing arrangement of the three cone classes in primate retina. Vision Res. 2001;41:1291–1306.
37. Roorda A, Williams DR. The arrangement of the three cone classes in the living human eye. Nature. 1999;397:520–522.
38. Hong DH, Pawlyk BS, Shang J, Sandberg MA, Berson EL, Li T. A retinitis pigmentosa GTPase regulator (RPGR)-deficient mouse model for X-linked retinitis pigmentosa (RP3). Proc Natl Acad Sci U S A. 2000;97:3649–3654.
39. Chrysostomou V, Stone J, Valter K. Life history of cones in the rhodopsin-mutant P23H-3 rat: evidence of long term survival. Invest Ophthalmol Vis Sci. 2008; Epub 2008 Dec 30.

Ophthalmic Genetics, 29:99–110, 2008
Copyright © Informa Healthcare USA, Inc.
ISSN: 1381-6810 (print) / 1744-5094 (online)
DOI: 10.1080/13816810802206499

RESEARCH ARTICLE

# Choroideremia: Analysis of the Retina from a Female Symptomatic Carrier

**Vera L. Bonilha**
*The Cole Eye Institute, The Cleveland Clinic Foundation, Cleveland, Ohio, USA*

**Karmen M. Trzupek**
*Casey Eye Institute, Oregon Health & Science University, Portland, Oregon, USA*

**Yong Li**
*The Cole Eye Institute, The Cleveland Clinic Foundation, Cleveland, Ohio, USA*

**Peter J. Francis**
*Casey Eye Institute, Oregon Health & Science University, Portland, Oregon, USA*

**Joe G. Hollyfield and Mary E. Rayborn**
*The Cole Eye Institute, The Cleveland Clinic Foundation, Cleveland, Ohio, USA*

**Nizar Smaoui**
*NEI DNA Diagnostic Laboratory, National Institutes of Health, Bethesda, Maryland, USA*

**Richard G. Weleber**
*Casey Eye Institute, Oregon Health & Science University, Portland, Oregon, USA*

***Purpose*: To define the retinal pathology in a 91 year-old affected matriarch of a three-generation choroideremia family with multiple manifesting carriers. *Methods*: Tissue from three different retinal areas was processed for immunohistochemistry. The macular area was processed for transmission electron microscopy. Cryosections were studied by indirect immunofluorescence, using well-characterized antibodies to cone cytoplasm, rhodopsin and cone opsins. The affected donor eyes were compared to a postmortem matched normal eye. *Results*: The retina displayed areas of severe degeneration, with no photoreceptor outer segments, photoreceptor nuclear atrophy, and atrophy of the inner retina. Other retinal areas were near to normal. The RPE was severely degenerated, with thinning, pigment clumping and sub-epithelial debris deposition in all the areas examined. The choroid displayed depigmentation. Labeling with cone opsin antibodies revealed that cones were drastically affected: blue opsin was almost completely absent, while red/green opsins were distributed along the entire plasma membrane of the cell. Rhodopsin was also distributed along the entire rod plasma membrane. Ultrastructural analysis of the affected macula revealed the absence of RPE apical microvilli and basal infoldings. Instead, RPE's basal surface and choroid displayed the presence of banded fibers composed of clumps of wide-spacing collagen. Bruch's membrane was filled with vesicular structures, some smooth and others with bristle-like projections. *Conclusions*: The histological data suggests that the clinical manifestation in this donor is related to degenerative changes in the retina, RPE, and choroid.***

**Keywords** choroideremia; carrier state; immunohistochemistry; cone opsins; rhodopsin

## INTRODUCTION

Choroideremia is a rare (1:50,000 males) X-linked recessive degeneration characterized by progressive atrophy of the photoreceptors, RPE, and choroid in affected males. Vision loss in males is similar to that observed in X-linked retinitis pigmentosa,

---

Received 14 May 2008; accepted 14 May 2008.

Address correspondence to: Vera L. Bonilha, Cleveland Clinic Foundation, The Cole Eye Institute, 9500 Euclid Avenue, i31, Cleveland, OH 44195, USA. E-mail: bonilhav@ccf.org

with night blindness, severe peripheral vision loss, and central visual acuity loss late in the course of the disease.

Female carriers of choroideremia often demonstrate characteristic fundus changes including patchy depigmentation of the RPE and coarse pigmentary granularity in the periphery. However, most carriers retain good visual function throughout life, with either no symptoms or mild to moderate night blindness. Significant visual impairment in female carriers of choroideremia is uncommon, and typically attributed to skewed X-inactivation leading to a high percentage of cells expressing the mutant X chromosome,[1] although subretinal neovascularization or fibrosis has been reported in at least 2 cases.[2,3] Full-field ERG recordings in carrier females are typically normal or very mildly reduced[4,5]; multifocal ERGs may be more sensitive given the patchy nature of cellular loss in the carrier state.[6]

Pathologically, male patients with choroideremia show complete loss of the choroid and outer retina, displaying a thin line of atrophic inner retina lying against the sclera.[7–9] The complete atrophy of the retina and choroid in male patients precludes identification of the primary defect in these structures. However, the milder changes in female patients present an opportunity for understanding of the mechanisms involved in this pathological process.

Choroideremia is caused by mutations in the *CHM* gene, which encodes component A of Rab geranylgeranyl-transferase, referred to as Rab escort protein (REP-1).[10–12] However, it is still unclear how mutations in this protein lead to the degeneration of the choroid, RPE and retina. In the present study we analyzed the retina, RPE and choroid morphology and the distribution of photoreceptor markers in a donor eye from a female symptomatic carrier of X linked choroideremia.

## MATERIALS AND METHODS

### Patient Information

The clinical evaluation of the affected members was carried out at the Casey Eye Institute at Oregon Health & Science University in Portland, Oregon with the approval of the OHSU Institutional Review Board (IRB). The donor requested eye donation prior to her death; organ donation was coordinated through National Retinitis Pigmentosa Foundation Donor Program (donation number #788).

The patient and several other affected members in the family were clinically evaluated.

### Molecular Genetics

Genomic DNA was prepared from peripheral blood lymphocytes using a commercially available kit Gentra DNA kit (Puregene; Gentra Systems, Minneapolis, MN). All fifteen exons of the *CHM* gene and their respective splice site junctions were PCR amplified and sequenced by bi-directional fluorescence sequencing using BigDye Terminator cycle sequencing version 3.1 and the model ABI 3130 sequencer according to the manufacturer's recommendations (Applied Biosystems, Foster City, CA). Primers sequences and PCR conditions are shown in Table 1.

### Histopathology

The immunocytochemistry analysis was performed in the Cleveland Clinic Foundation and is exempt of IRB approval. The donor globes were fixed 8 hrs post-mortem in a mixture of 4% paraformaldehyde and 0.5% glutaraldehyde made in 0.1 M phosphate buffer, pH 7.3. After 1 month in fixative, the globes were transferred and stored in 2% paraformaldehyde prepared in the same buffer. The eyes from a 68-year-old female and a 91-year-old male were used as controls, and were fixed 14.5 hr and 7.5 hr post-mortem in 2% paraformaldehyde made in the same buffer. Tissue from three different retinal areas were cut, dehydrated through a series of ethanol solutions and embedded in paraffin using an automated tissue processor (Leica Microsystems TP1020, Benneck Burn, IL). 7–8 $\mu$m sections were cut on a Leica RM2125 microtome (Leica Microsystems) and sections were collected on Superfrost/Plus Slides (Fisher Scientific, Pittsburgh, PA, USA).

Sections were stretched on the slides on water and adhered to the slides by room temperature incubation overnight followed by 2 hrs incubation in a HI1210 slide warmer at 60°C (Fisher Scientific). Prior to labeling, paraffin was removed through two consecutive xylene incubations for 10 min. The tissue was then gradually rehydrated by sequential incubation of ethanol 100, 90, 70, 50, and 30% for 5 min. each and processed for immunofluorescence labeling as previously described.[13]

Briefly, tissues were blocked in PBS supplemented with 1% BSA (PBS/BSA) for 30 min and incubated with the antibodies in PBS/BSA overnight at 4°C. Cryosections of both the matched control and affected donor tissues were labeled with the following antibodies: rabbit polyclonal antibody AB5407 to blue cone opsin (1: 1200, Chemicon International, Inc., Temecula, CA, USA), rabbit polyclonal antibody AB5405 to red/green cone opsins (1: 1200, Chemicon International, Inc., Temecula, CA), monoclonal antibody B6-30N to rhodopsin (1:50, from Dr. P. Hargrave, University of Florida, Gainesville, FL, USA.), and the monoclonal antibody 7G6 to cone cytoplasm (1:100, from Dr. P. MacLeish, Morehouse School of Medicine, Atlanta, GA, USA).

Cell nuclei were labeled with TO-PRO-3 iodide (1mg/ml, Molecular Probes, Eugene, OR, USA). Secondary antibodies (goat anti-mouse or anti-rabbit IgG; 1:1000) were labeled with Alexa Fluor 488 (green; Molecular Probes). Sections were analyzed using a Leica laser scanning confocal microscope (TCS-SP2, Leica, Exton, PA, USA). A series of 1 $\mu$m *xy* (*en face*) sections were collected. Each individual *xy* image of the retinas stained represents a three-dimensional projection of the entire cryosection (sum of all images in the stack). Microscopic panels were composed using AdobePhotoshop 5.5 (Adobe, San Jose, CA, USA).

TABLE 1
Primers and conditions used for mutation detection in the CHM gene

| Exon | Primer | Sequence: 5’>3’ | Amplicon size | Tm |
|---|---|---|---|---|
| 1 | EX1FW | GACCTTCCACCCAAGAACTAC | 218 | 55 |
| | EX1RV | ACAGTCTTCCTAAACTTTGTCC | | |
| 2 | EX2FW | AGGATGGGTCTCTTTGGTGGTT | 497 | 55 |
| | EX2RV | GGGGCAGGCATGAGGTTTC | | |
| 3 | EX3FW | CTTTTAGCCTACCACTTCCACTTA | 468 | 55 |
| | EX3RV | CGCACCCGAGCTCTATTTAT | | |
| 4 | EX4FW | TTGCATGTTTCACACTGCCCAC | 222 | 55 |
| | EX4RV | AGTCATTAATTTAGTTTACCTGCAG | | |
| 5 | EX5AFW | CCCTGTCTGTCTTAAATTCTCAAAA | 1096 | 60 |
| | EX5BRV | TATCCCTTCCCTAACCCCCAACC | | |
| 6 | EX6FW | CCAATTTTTCTACTATTTCAAC | 214 | 55 |
| | EX6RV | AACTTAAGCTGATGCCCAGT | | |
| 7 | EX7FW | GCCTGGCTAGAGTGGAAACGAT | 473 | 55 |
| | EX7RV | ATGGGAGCCCTTGAAATACAGC | | |
| 8 | EX8FW | AGTTTAGTTCTGATTTTAAGTG | 309 | 55 |
| | EX8RV | CACTTTTAGAAGGGACAAGAA | | |
| 9 | EX9bFW | TTTCGGGGGATAATTGGCTCTTG | 387 | 53 |
| | EX9RV | TATATATGAAGGTTACTTATATC | | |
| 10 | EX10FW | AAGCCCTCAAAATAGCAACAAGAA | 567 | 55 |
| | EX10RV | TCACCTCCCAAAACCAAGTCAAGT | | |
| 11 | EX11FW | CGAAACTTATCCATGGAATC | 204 | 55 |
| | EX11RV | GTGTAGTGATTAGTTCACCA | | |
| 12 | EX12FW | ATGTCCCTAATCTGAATATCTAAAATC | 580 | 55 |
| | EX12RV | ATCTCTACAAATACAACCTTCACAACT | | |
| 13 | EX13FW | GCTCAGCTCTCTATTATCCAT | 254 | 55 |
| | EX13RV | GAAGATTATGATGGTTACAT | | |
| 14 | EX14FW | TAGGCTACACAGTGTAGTAA | 317 | 55 |
| | EX14RV | GACTTCTCTCCTCCCAGAGG | | |
| 15 | EX15FW | TGAACACTTGATAATGAACCTGATG | 588 | 55 |
| | EX15RV | CCCTTTTGGATTTCTATTACCTATT | | |

### Ultrastructural Analysis

A small area of the retina/RPE/choroid tissue from the macula of the affected choroideremia donor and matched-controls (88- and 91-year-old males with 7.5 and 12 hr post-mortem) were fixed in 2.5% glutaraldehyde in 0.1M cacodylate buffer, sequentially dehydrated in ethanol and embedded in Epon as previously reported (Bonilha et al., *J. Cell Biol.* 1999). Thin sections were prepared and electron micrographs were taken on a Tecnai 20 200 kV digital electron microscope (Philips, Hillsboro, OR, USA) using a Gatan image filter and digital camera at 3600 diameters and are printed at identical magnifications.

## RESULTS

### Clinical Findings

Figure 1 shows the pedigree of the family affected with an X-linked choroideremia. The donor (III-4 of Figure 1) first presented to the Ophthalmic Genetics Clinic at the Casey Eye Institute at the age of 77 with a visual acuity of 20/25 OD, 20/30 OS, and no subjective limitation of night vision or peripheral vision. Fundus examination disclosed a striking reticular pigmentary dispersion with fine clumping, but no frank bone spicule pigmentation, in the mid and far periphery of each eye.A large pigmented retinal scar was observed temporal to the right macula OD. Full field electroretinography was normal. Over the ensuing 14 years, her night vision and central vision gradually decreased; by 91, her family reports that she was significantly visually impaired from loss of central vision.

The donor’s family history is unique in that several of the female members appear to be affected to an equal, if not greater degree than the men. The donor’s daughter (IV-2 of Figure1) was initially diagnosed with retinitis pigmentosa in her early 20’s. When she presented to ophthalmic genetics at the age of 41, she suffered from reduced night vision and blurred central vision (20/40-2, 20/25-2). Full-field ERG responses were mildly subnormal. By the age of 54, acuity worsened to 20/300, 20/60+1,

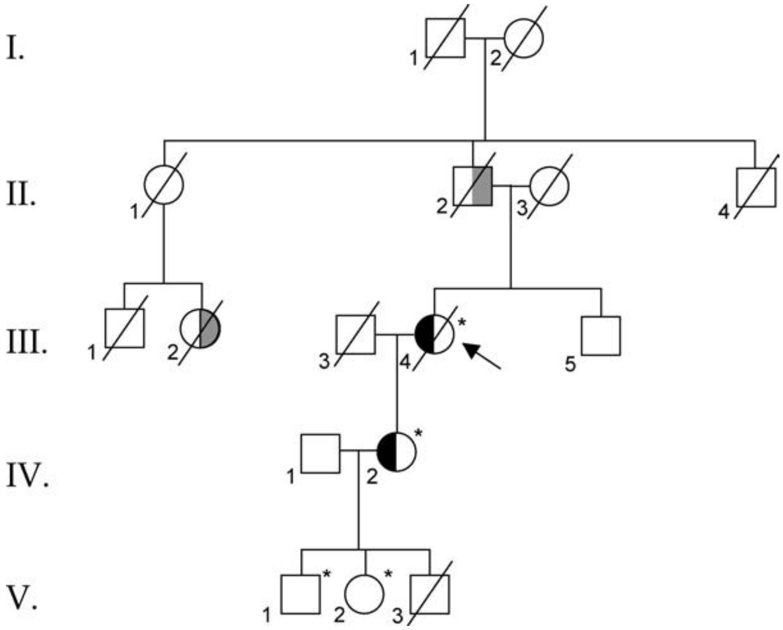

FIG. 1. Pedigree of a family with an X-linked choroideremia showing the symptomatic carrier member (III-4) on whom the postmortem analysis was performed. *Molecularly confirmed to carry 1413 + 1 G > A in *CHM;* II-2: By report, totally blind by early 50's;III-2: By report, legally blind in adulthood; III-4: Propositus. Night blindness and central vision loss late in life (>75yo); IV-2: Night blindness and significant central vision loss in 50s. Abnormal rod and cone responses on ERG; V-1: Salt and pepper retinopathy; asymptomatic at 34 years old; V-2: Mottling of inferior RPE; asymptomatic at 33 years old.
The symbol ∗ indicates patients examined personally; hatched symbols, patients who are affected by history but not personally examined; arrow, proband; single oblique line, deceased.

and she was unable to drive. ERG responses decreased to approximately one-third of those in the earlier study.

Her son and daughter (V-1 and V-2 of Figure 1), who both carry the familial CHM mutation, remain asymptomatic at the age of 35 and 34 years, respectively. The donor, her daughter, and her granddaughter and grandson were molecularly confirmed to carry a splice site mutation on the 5' *splice* site (donor site) of intron 11 in the *CHM* gene c1413 + 1G>. This mutation is expected either to cause the retention of intron 11 or skipping of exon 11 which in either case will produce an unstable mRNA leading to a nonsense-mediated mRNA decay (NMD) and the absence of the *REP-1*.

## Morphological Pathology

Semi-thin sections of epon-embedded tissue were analyzed and compared to matched controls (Figure 2A, B). In female patients, the severity of disease expression is related to the proportion of cells expressing the mutant X chromosome. As a consequence, we focused our observations in three different regions in the periphery of the donor. The schematic drawing in the upper corner of this figure depicts the regions harvested and processed for observation in both the morphological and immunohistological assays (periphery regions 1, 2, and 3 and macular region 4). The retina of the affected donor displayed different degrees of photoreceptor degeneration in each of the regions observed when compared to the morphology of the control retina in the periphery (Figure 2A) and macular (Figure 2B) region of the eye. Extensive degeneration could be observed in all retinal layers in all analyzed regions (Figures 2C1, D2, E3).

Some pigmented cells are seen invading the degenerating retina (Figure 2C1, arrowheads). The RPE of the affected donor displayed typical thinning, pigment clumping and basal laminar deposits (Figures 2F1, G2, H3) when compared to the matched control (Figure 2A and B). Extensive accumulation of amorphous material underneath the RPE layer was observed (Figure 2G2,*) while in another area the presence of inflammatory cells (Figure 2H3, small arrows) was observed in the choroid. In the macula, the RPE was thinned with pigment clumping, soft and hard drusen deposits (Figure 2I4, J4, K4, large arrows), widespread photoreceptor degeneration, and giant lipophilic drops in the choroid when compared to the matched control (Figure 2B).

## Histological Pathology

To further understand some of the molecular changes associated with this X-linked choroideremia phenotype in this family, tissue from the same regions described above (regions 1–3 in Figure 2) were also processed for paraffin embedding and

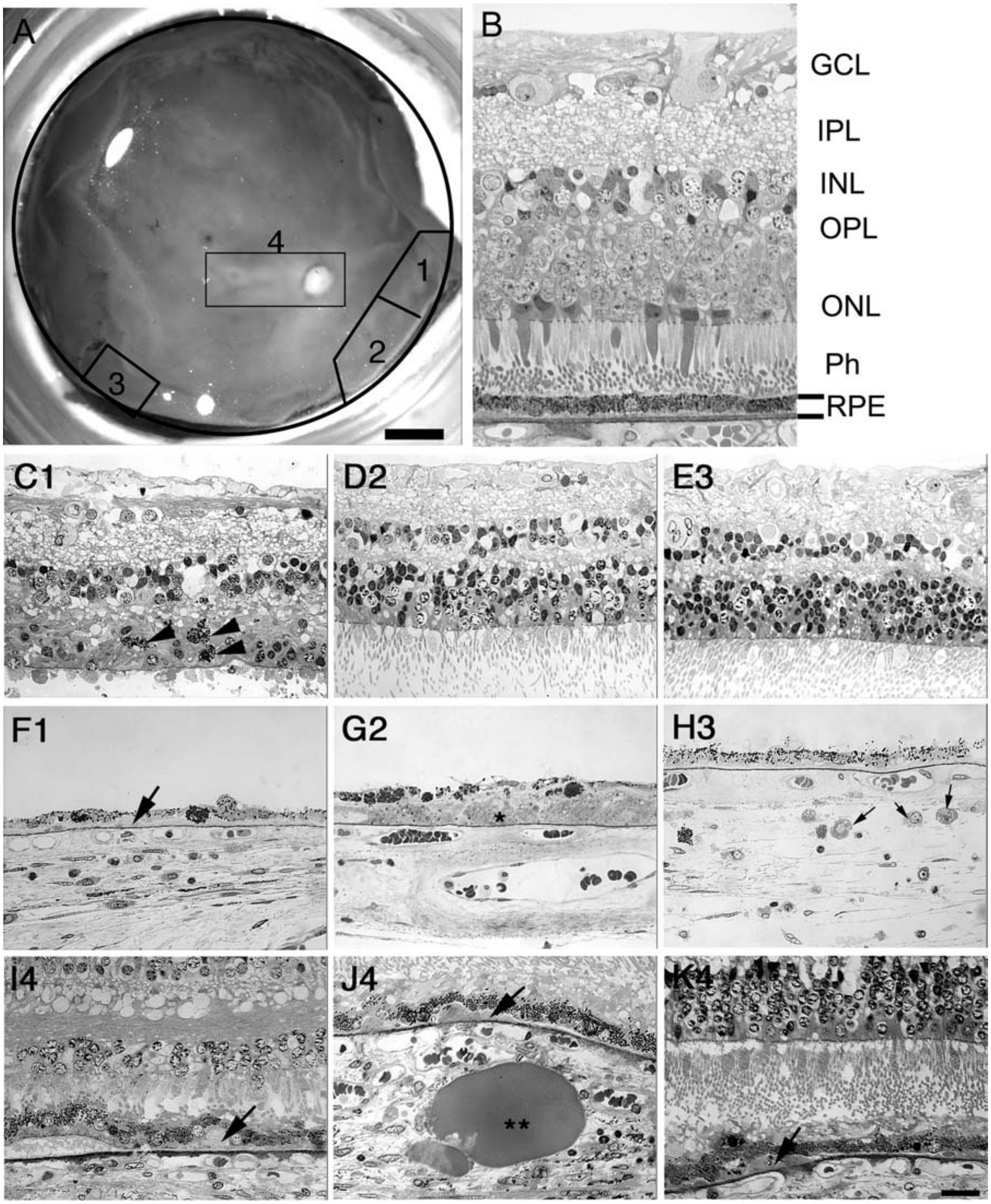

FIG. 2. Degeneration in the retina of a female symptomatic carrier of choroideremia. Human 1 $\mu$m plastic sections of both a matched control and an affected choroideremia stained with toluidine blue. Top panel corner depicts a fundus image of the studied eye with a schematic drawing of the regions cut and processed for cryosectioning (A). Morphology of control retina in the perimacular region (B). (C1, D2, E3) The retina of the affected donor displayed different degrees of photoreceptor degeneration in each of the regions observed. In C1 some pigmented cells are seen invading the degenerating retina (arrowheads). (F1, G2, H3) RPE of the affected donor displayed typical thinning, pigment clumping, basal laminar deposits. In G2 extensive accumulation of amorphous material underneath the RPE layer is observed ($*$) while in H3 the presence of inflammatory cells (small arrows) is observed in the choroid. (I4, J4, K4) Different areas of the affected donor displaying deposition of drusen under the RPE (large arrows), RPE thinning and pigment clumping, photoreceptor degeneration and the presence of giant lipophilic drops in the choroid ($**$). *RPE = retinal pigment epithelium; Ph = photoreceptors; ONL = outer nuclear layer; OPL = outer plexiform layer; INL = inner nuclear layer; IPL = inner plexiform layer; GCL = ganglion cell layer*. Bar = 200 $\mu$m.

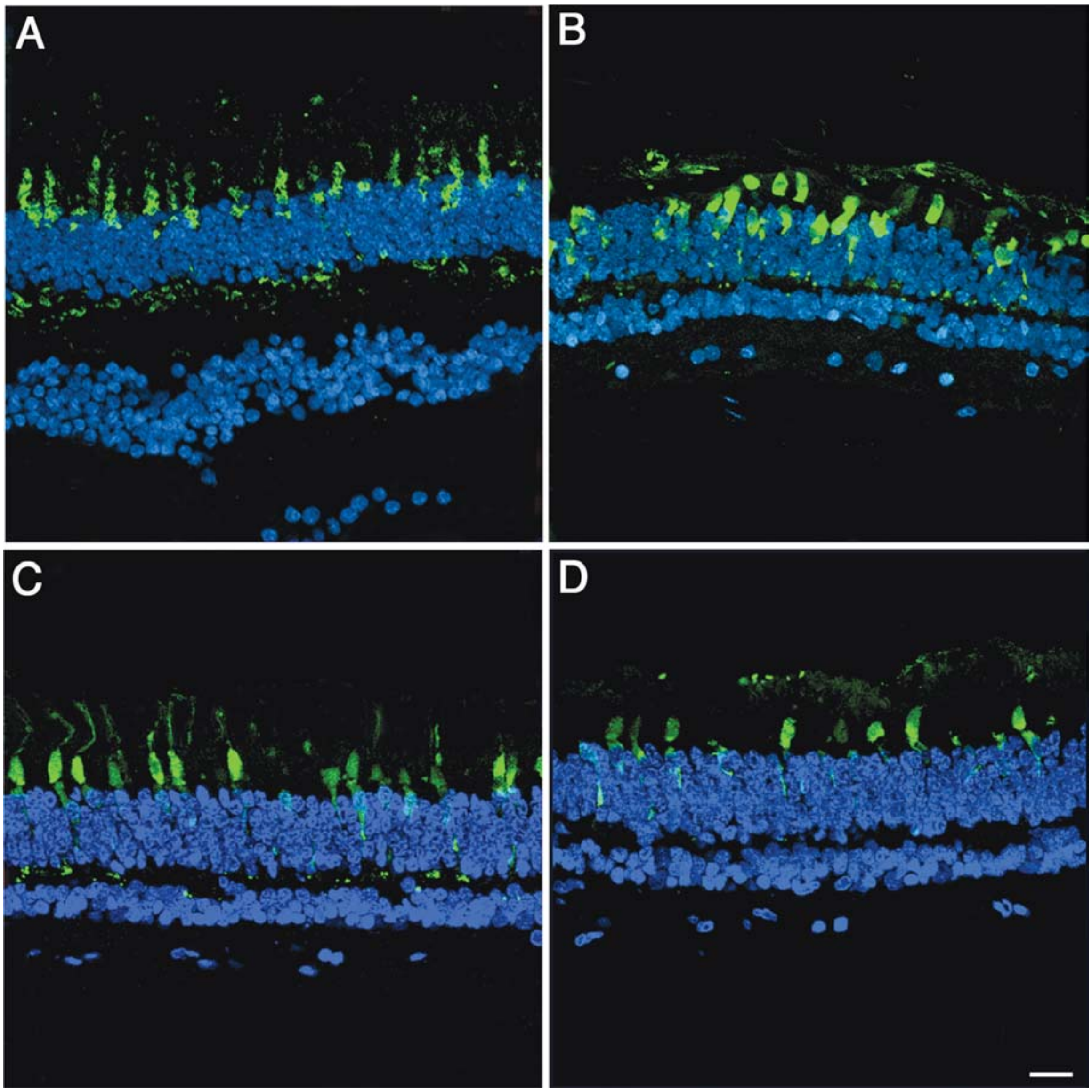

FIG. 3. Cone cytoplasmic marker distribution is normal in a female symptomatic carrier of choroideremia. Human paraffin sections of both a matched control (A) and affected choroideremia donor (B, C, D) were labeled with an antibody specific to cone cytoplasm (green) while cell nuclei were labeled with TO-PRO-3 (blue). Sections were analyzed using a Leica laser scanning confocal microscope. Comparison of the samples showed that there was no significant difference in the overall morphology of the control and affected donor cones. Bar = 40 $\mu$m.

immunofluorescence. Initially, the distribution of the cone cytoplasmic marker 7G6 was analyzed in both the symptomatic carrier and a matched-control eye (Figure 3A–D). No significant differences were observed between the control sample (Figure 3A) and all the three other areas observed in the affected donor (Figure 3B–D) with cones displaying normal morphologic characteristics of cone photoreceptors. Moreover, cell nuclei, labeled with TO-PRO-3, did not display any significant difference to the matched control.

However, a striking abnormal distribution of the red/green opsins throughout the entire cone cell body was observed in all the affected donor regions (4B–D) when compared to the matched control eye (Figure 4A). This abnormal distribution was observed from the outer segments to the cone pedicles in the inner nuclear region of the retina of the affected donor.

In contrast, the blue cone opsin of the affected donor eye (Figure 5 B–D) was almost completely abolished when compared to the matched-control eye (Figure 5A). However, region 2 displayed a few cones that still expressed blue opsin distributed throughout the inner and outer segments of this cone type (Figure 5B, arrow).

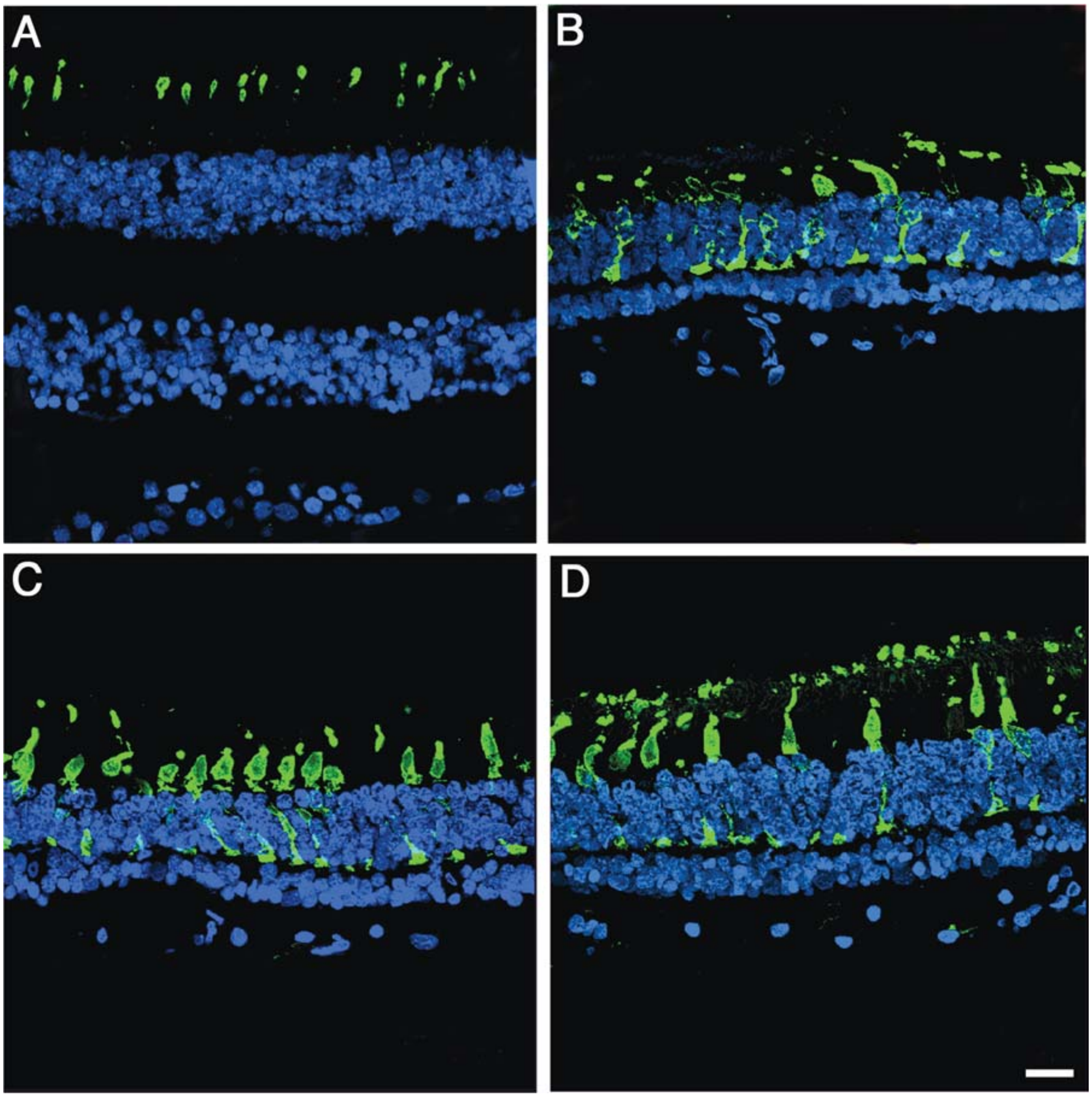

FIG. 4. Red/Green cone opsins are distributed along the entire plasma membrane of this cone type in a female symptomatic carrier of choroideremia. Human paraffin sections of both a matched control (A) and affected choroideremia donor (B, C, D) were labeled with antibodies specific to red/green cone opsins (green) while cell nuclei were labeled with TO-PRO-3 (blue). Sections were analyzed using a Leica laser scanning confocal. Comparison of the samples showed that red/green cone opsins are distributed along the entire plasma membrane of this cone type, from the tip of the outer segment to the synaptic base in all the observed regions of the affected eye. Bar = 40 $\mu$m.

The rod outer segments were visualized through labeling with rhodopsin antibodies. Similar to the red/green opsin, a striking unrestricted distribution of rhodopsin was observed throughout the entire rod cell body of the affected eye (Figure 6B–D) when compared to the control-matched eye (Figure 6A).

## Ultrastructural Pathology

The ultrastructure of RPE and Bruch's membrane in the macular area was analyzed by TEM. Observation at low magnification showed photoreceptor outer segments (POS) lying on top of a collapsed RPE apical surface. No RPE microvilli are visible on the RPE apical surface. Moreover, the RPE cytoplasm is filled with small vacuoles and pigments (P) (Figure 7A). Examination of the RPE's basal surface revealed complete absence of basal infoldings and the presence of banded fibers composed of clumps of banded material with 1000Å periodicity consistent with long spaced collagen (Figure 7B–D, arrows, B, C, D). The choroid, Bruch's membrane, and the space between

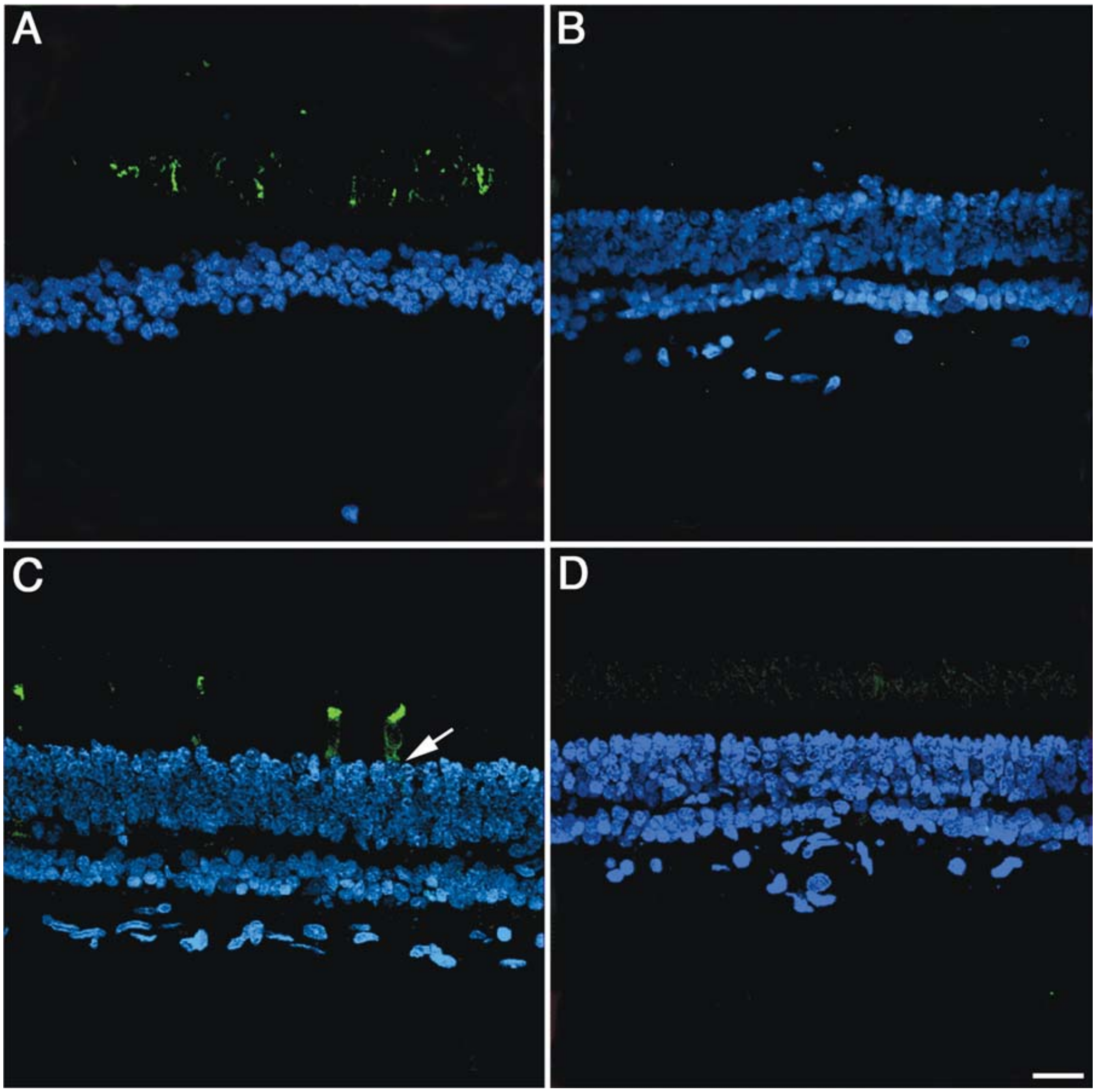

FIG. 5. Blue cone opsins are significantly decreased in this cone type in a female symptomatic carrier of choroideremia. Human paraffin sections of both a matched control (A) and affected choroideremia donor (B, C, D) were labeled with antibodies specific to blue cone opsins (green) while cell nuclei were labeled with TO-PRO-3 (blue). Sections were analyzed using a Leica laser scanning confocal microscope. Comparison of the samples showed that blue cone opsins are significantly decreased in all the observed regions of the affected eye. Region 2 displays a few cones that still express blue opsin but it is distributed throughout the inner and outer segments of the cones (arrow). Bar = 40 $\mu$m.

the RPE basal membrane was filled with vesicular structures, some smooth and others like bristle-coated vesicles (Figure 7B and C). Higher magnification of this area is shown in Figure 7C. Beneath the RPE, the banded fibers composed of clumps of wide-spacing collagen are continuous with a drusen characterized by the presence of residual bodies, vesicular material and filaments (Figure 7D). The basement membrane is not visible in this area.

## DISCUSSION

This study demonstrated substantial redistribution in the photoreceptor proteins, specifically red/green cone opsin and rhodopsin, as compared to normal control tissues. These changes included loss of opsin restriction to the cone and rod outer segment resulting in its distribution throughout the entire cell body. Moreover, the blue cone opsin was significantly decreased in the affected retina. With the exception of one of the three

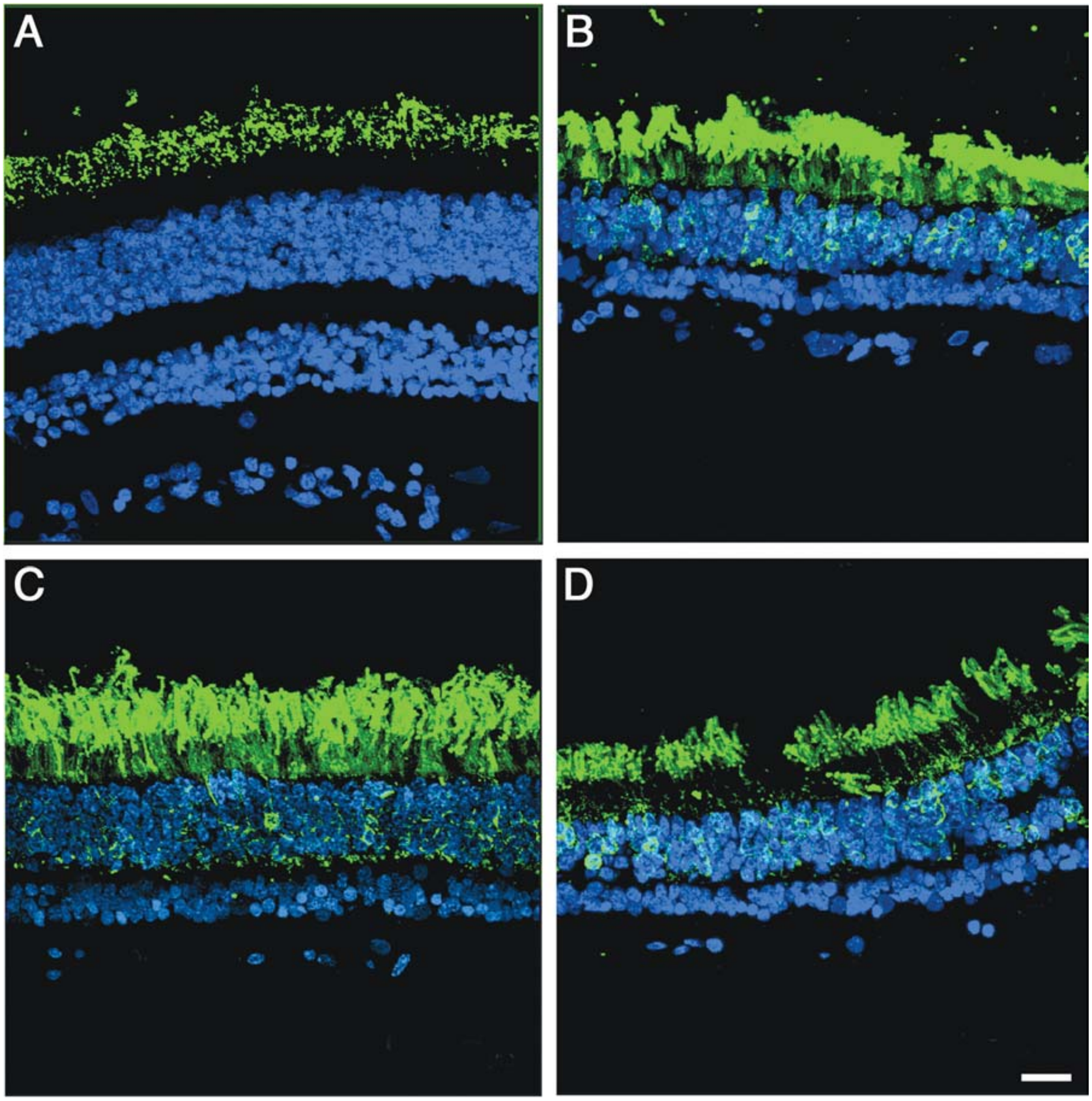

FIG. 6. Rhodopsin is distributed along the entire plasma membrane of the rods in a female symptomatic carrier of choroideremia. Human paraffin sections of both a matched control (A) and affected choroideremia donor (B, C, D) were labeled with antibodies specific to rhodopsin (green) while cell nuclei were labeled with TO-PRO-3 (blue). Sections were analyzed using a Leica laser scanning confocal microscope. Comparison of the samples showed that rhodopsin is distributed along the entire plasma membrane of rods, from the tip of the outer segment to the synaptic base in all the observed regions of the affected eye. Bar = 40 $\mu$m.

observed areas, no blue opsin was detected in the affected retina. Rhodopsin was also found to be distributed along the entire cell body.

Opsins are the protein component of the photopigments, which absorb photons of light. This reaction leads to a change in molecular shape and the subsequent release of energy, the first step in the visual transduction cascade. Two families of opsins are generally recognized due to different spatial expression and evolutionary histories. Rhodopsin, which is used in night vision, is a high-sensitivity, low-acuity opsin found in the rod photoreceptor cells.

Cone opsins, employed in color vision, are low-sensitivity, high-acuity opsins located in the cone photoreceptor cells. Cone opsins are further subdivided according to their absorption maxima ($\lambda_{\max}$), the wavelength at which the highest light absorption is observed. Evolutionary relationships, deduced using the amino acid sequence of the opsins, are also frequently used to categorize cone opsins into their respective group. Both

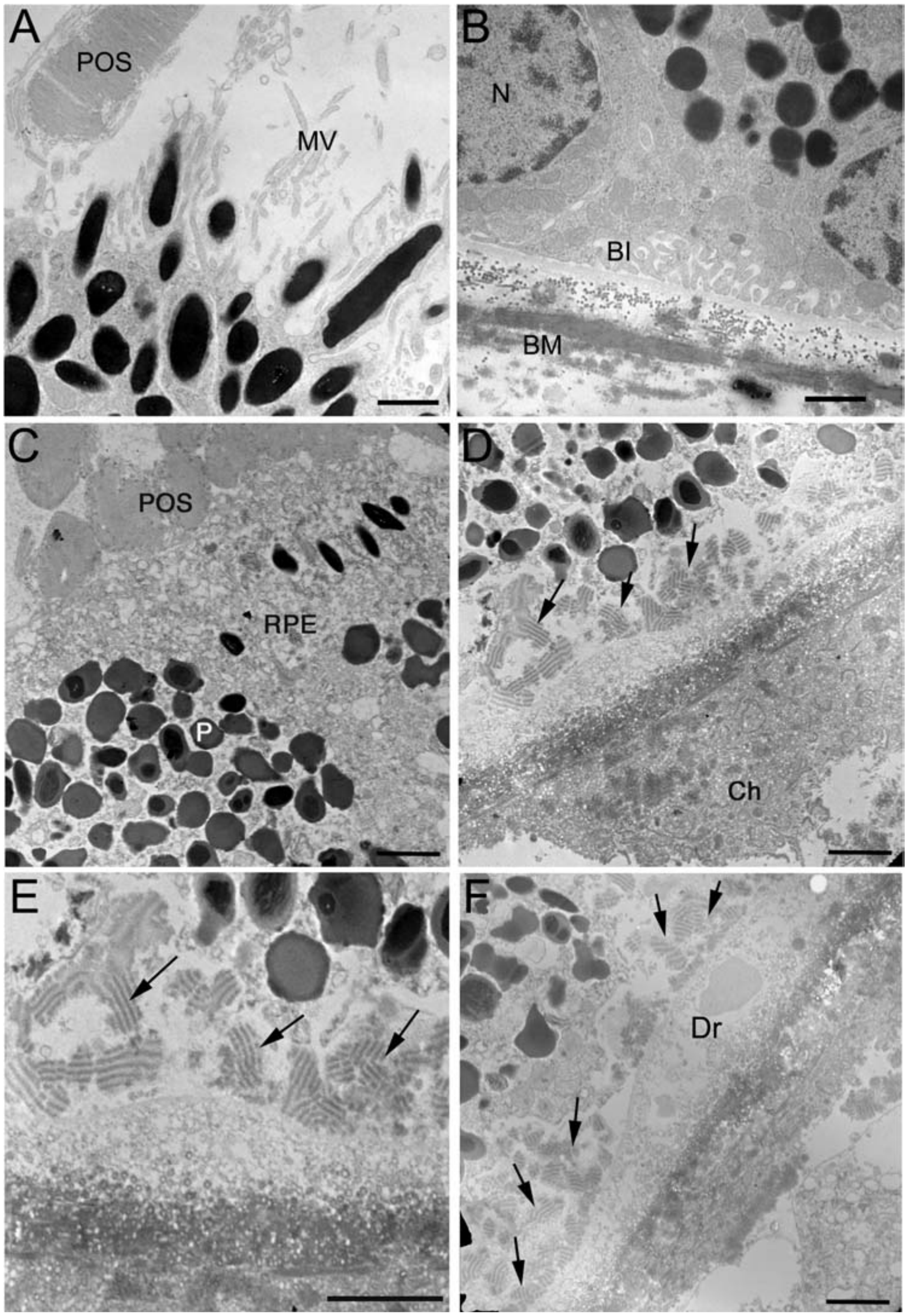

FIG. 7. Ultrastructural evidence of RPE degeneration in a female symptomatic carrier of choroideremia. The ultrastructure of RPE and Bruch's membrane was analyzed by TEM. Observation at low magnification showed photoreceptor outer segments (POS) lying on top of a collapsed RPE apical surface while a control-matched eye displayed several apical microvilli supporting the POS (A). The matched control displayed extensive basal infoldings (BI) in their basal surface on top of a well-structured aged Bruch's membrane (BM). The choroideremia donor cytoplasm was filled with small vacuoles and pigments (P) (C). Observation of RPE's basal surface in the choroideremia donor revealed absence of basal infoldings and the presence of banded fibers composed of clumps of wide-spacing collagen (arrows, D, E, F). The choroid (Ch), Bruch's membrane (BM) and the space between the RPE basal membrane was filled with vesicular structures, some smooth and others like bristle-coated vesicles (D, E). Higher magnification of this area is shown in E. Another area of the choroideremia donor eye displayed drusen (Dr) and beneath it Bruch's membrane contained residual bodies, vesicular material and filaments (F). Bars: C, D, F =2 $\mu$m and A, B, E = 1 $\mu$m.

methods predict four general cone opsin groups in addition to rhodopsin.[14] Our immunofluorescence studies were carried out with antibodies specific to both red/green and the blue cone opsins. Our labeling of the red/green opsins detected a large population of these cone types throughout the entire retina when compared to those with blue cone opsin. This result is in agreement with several reports demonstrating that the human retina is composed of roughly 90% red/green and 10% blue cones.[15–18]

In the present case, a striking cone abnormality was the presence of red/green opsins throughout the entire cone cell body instead of the usual restriction to the outer segment. A previous study of enhanced S-cone syndrome donor eyes reported the presence of abnormal distribution of both S- (blue) and L/M- (red/green) cone opsins along the entire plasma membranes of the cell, including their inner segments, cell bodies, axon and pedicles.[19]

Moreover, a patient with X-linked cone degeneration (a known 6.5-kilobase deletion in the red cone pigment gene) showed a significant diminution of the red and green cone population when compared with an age-matched control eye. However, some remaining red and green cones without outer segments did stain weakly with the antibody to red and green opsin in the inner segments.[20] More recently, an affected member of a clinically well characterized family with an autosomal dominant form of cone dystrophy was also shown to exhibit distribution of the red/green cone opsin from the tip of the outer segment to the synaptic base of this cone type.[13]

A recent retinitis pigmentosa GTPase regulator (RPGR)-deficient murine model was also shown to have initial ectopic or unrestricted distribution of both red/green and blue opsins and a reduced level of rhodopsin followed by the subsequent degeneration of cones and rods.[21] This report suggested that mislocalization of cone opsins may precede cone cell death. This conclusion was strengthened by data from another report showing that both rod- and cone-mediated function declined with age as did the central retinal thickness in a group of clinically defined and genotyped patients studied.[22]

Although the molecular mechanism of visual excitation in the cone is not as well understood as in the rod, it is generally thought to involve a cone-specific G protein (cone transducin) that couples the cone visual pigment to a cGMP phosphodiesterase. The functional significance of the red/green opsin delocalization is not known but it could result in a major loss of sensitivity, which, in turn, could lead to sufficient cone degeneration to cause the visual symptoms experienced by the donor.

Mura et al.[5] performed light- and dark-adapted thresholds in an obligate CHM carrier, and found that while most of the 500-nm dark-adapted thresholds were within reference limits, 650-nm fully dark-adapted thresholds were significantly elevated at all loci tested. The authors suggest that impaired cone function in the dark-adapted state is the most likely explanation for reduced night vision in symptomatic carriers of CHM. In this context, our present observations might contribute to the night vision and central vision loss observed in this donor.

The blue cone opsin reactivity was significantly diminished in the affected donor. To our knowledge this is the first report of such pathology in the retina of a choroideremia patient. One of the possible explanations for this observation is that the antigenic epitopes might be masked in this donor since there was no alteration of the labeling with the cone cytoplasmic marker. Another possibility is loss of blue cones in this donor. This case was also characterized by the striking abnormal distribution of rhodopsin throughout the entire rod cell body. A previous study carried out in a female carrier of choroideremia also detected patchy ectopic distribution of rhodopsin.[23]

It has been shown that choroideremia is caused by mutations in the REP-1 gene that encodes component A of *Rab* geranylgeranyl-transferase or REP-1, a protein involved in intracellular vesicular transport.[10–12,24] However, little is known about how mutations cause disease and degeneration of the choroid, RPE and retina. Rab geranylgeranyl-transferase A–B holoenzyme attaches (3)H-geranylgeranyl groups to Rab GTPases, a reaction which regulates Rab intracellular trafficking since the mutation in Rep1 prevents the modification of Rab proteins, thereby disrupting Rab-mediated intracellular trafficking.[25]

Recently, REP-1 was localized to rod inner segments, cell bodies and synapses suggesting that rods are the primary site of degeneration in this disease.[23] Our observations of cone degeneration suggest an important role of cones in the choroideremia pathology. Also recently, the retinal pathology of zebrafish rep1 mutants carrying a nonsense mutation in the homologous REP1 gene was described.[26] However, the author did not see any abnormal distribution of rhodopsin, red/green and blue opsins in the photoreceptor cells of the mutant zebrafish.

The ultrastructural observation of the affected macula revealed absence of RPE apical microvilli and basal infoldings. Moreover, the RPE's donor basal surface was dominated by the presence of banded fibers composed of clumps of wide-spacing collagen. Bruch's membrane was filled with vesicular structures, some smooth and others like bristle-coated vesicles. Similar findings were previously reported when the functions of the RPE begin to fail in the senile maculopathies.[27] The reported RPE ultrastructure is consistent with RPE cells that are not able to carry out several of their nurturing functions.

In conclusion, we report here the clinical findings and abnormal distribution of the red/green cone opsins and rhodopsin throughout the entire cone and rod cell bodies from a member of a family with an X-linked recessive retinal degeneration. The blue cones were also affected since they exhibited very low reactivity to the blue cone opsin antibody. These results are important to our understanding of one of likely several molecular mechanisms underlying choroideremia in the context of high clinical variability. It also suggests that vision loss in choroideremia may result not only from abnormal REP-1 but also from secondary neuronal death and corrupted retinal circuitry due to the irreversible effects of retinal remodeling.

## ACKNOWLEDGMENT

The authors thank Dr. Peter MacLeish (Morehouse School of Medicine, Atlanta, GA, USA) for providing us with the antibody to cone cytoplasmic marker (7G6), Dr. Paul Hargrave (University of Florida, Gainesville, FL, USA) for providing us with the antibody to rhodopsin (B6-30N). This work was supported by The Foundation Fighting Blindness, Owings Mills, MD, USA (Trzupek, Francis, Hollyfield, Weleber), NIH infrastructure grant EY015638 (Hollyfield), and a Career Development Award (Francis) and an unrestricted grant (Weleber, Hollyfield) from Research to Prevent Blindness. This work was presented at the Association for Research in Vision and Ophthalmology Annual Meeting, May 2007.

## REFERENCES

1. Lyon M. Gene action in X chromosome of mouse (*Mus musculus L.*). *Nature*. 1961;190:372–373.
2. Endo K, Yuzawa M, Ohba N. Choroideremia associated with subretinal neovascular membrane. *Acta Ophthalmol Scand*. 2000; 78:483–486.
3. Potter MJ, Wong E, Szabo SM, McTaggart KE. Clinical findings in a carrier of a new mutation in the choroideremia gene. *Ophthalmology*. 2004;111:1905–1909.
4. Rubin ML, Fishman RS, McKay RA. Choroideremia: Study of a family and literature review. *Arch Ophthalmol*. 1966;76:563–574.
5. Mura M, Sereda C, Jablonski MM, MacDonald IM, Iannaccone A. Clinical and functional findings in choroideremia due to complete deletion of the CHM gene. *Arch Ophthalmol*. 2007;125:1107–1113.
6. Cheung MC, Nune GC, Wang M, McTaggart KE, MacDonald IA IM, Duncan JL. Detection of localized retinal dysfunction in a choroideremia carrier. *Am J Ophthalmol*. 2004;137:189–191.
7. Ghosh M, McCulloch JC. Pathological findings from two cases of choroideremia. *Can J Ophthalmol*. 1987;15:147–153.
8. Cameron JG, Fine BS, Shapiro I. Histopathologic observations in choroideremia with emphasis on vascular changes of the uveal tract. *Ophthalmology*. 1987;94:187–196.
9. Rodrigues MM, Ballintine ES, Wiggert BN. Choroideremia: A clinical, electron microscopic, and biochemical report. *Ophthalmology*. 1984;91:873–883.
10. Seabra MC, Brown MS, Goldstein JL. Retinal degeneration in choroideremia: deficiency of Rab geranylgeranyl transferase. *Science*. 1993;259:377–381.
11. Seabra MC, Ho YK, Anant JS. Deficient geranylgeranylation of Ram/Rab27 in choroideremia. *J Biol Chem*. 1995;270:24420–24427.
12. van den Hurk JAJM, Schwartz M, van Bokhoven H. Molecular basis of choroideremia (CHM): mutations involving the Rab escort protein-1 (REP-1) gene. *Hum Mutat*. 1997;9:110–117.
13. Bonilha VL, Hollyfield JG, Grover S, Fishman GA. Abnormal distribution of red/green cone opsins in a patient with an autosomal dominant cone dystrophy. *Ophthalmol Genet*. 2005;26:69–76.
14. Terakita A. The Opsins. *Genome Biol*. 2005;6:213.1–213.9.
15. Curcio CA, Allen KA, Sloan KR, Lerea CL, Hurley JB, Klock IB, Milam AH. Distribution and morphology of human cone photoreceptors stained with anti-blue opsin. *J Comp Neurol*. 1991;312:610–624.
16. Roorda A, Williams DR. The arrangement of the three cone classes in the living human eye. *Nature*. 1999;397:520–522.
17. Takada Y, Ohhashi T, Suzuki M, Kitahara K, Kobayashi M. Immunohistochemical detection of retinal cones in monkey retina: light and electron microscopic study. *Jpn J Ophthalmol*. 2000;44:503–510.
18. Roorda A, Metha AB, Lennie P, Williams DR. Packing arrangement of the three cone classes in primate retina. *Vision Res*. 2001;41:1291–1306.
19. Milam AH, Rose L, Cideciyan AV, Barakat MR, Tang WX, Gupta N, Aleman TS, Wright AF, Stone EM, Sheffield VC, Jacobson SG. The nuclear receptor NR2E3 plays a role in human retinal photoreceptor differentiation and degeneration. *Proc Natl Acad Sci USA*. 2002;99:473–478. Epub 2002 Jan 2002.
20. To KW, Adamian M, Jakobiec FA, Berson EL. Histopathologic and immunohistochemical study of an autopsy eye with X-linked cone degeneration. *Arch Ophthalmol*. 1998;116:100–103.
21. Hong DH, Pawlyk BS, Shang J, Sandberg MA, Berson EL, Li T. A retinitis pigmentosa GTPase regulator (RPGR)-deficient mouse model for X-linked retinitis pigmentosa (RP3). *Proc Natl Acad Sci USA*. 2000;97:3649–3654.
22. Duncan JL, Aleman TS, Gardner LM, De Castro E, Marks DA, Emmons JM, Bieber ML, Steinberg JD, Bennett J, Stone EM, MacDonald IM, Cideciyan AV, Maguire MG, Jacobson SG. Macular pigment and lutein supplementation in choroideremia. *Exp Eye Res*. 2002;74:371–381.
23. Syed N, Smith JE, John SK, Seabra MC, Aguirre GD, Milam AH. Evaluation of retinal photoreceptors and pigment epithelium in a female carrier of choroideremia. *Ophthalmology*. 2001;108:711–720.
24. MacDonald IM, Mah DY, Ho YK, Lewis RA, Seabra MC. A practical diagnostic test for choroideremia. *Ophthalmology.* 1998;105:1637–1640.
25. Preising M, Ayuso C. Rab escort protein 1 (REP1) in intracellular traffic: A functional and pathophysiological overview. *Ophthalmol Genet*. 2004;25:101–110.
26. Krock BL, Bilotta J, Perkins BD. Noncell-autonomous photoreceptor degeneration in a zebrafish model of choroideremia. *Proc Natl Acad Sci USA*. 2007;104:4600–4605.
27. Hogan MJ. Role of the retinal pigment epithelium in macular disease. *Trans Am Acad Ophthalmol Otoryngol*. 1972;76:64–80.

# Age and disease-related structural changes in the retinal pigment epithelium

Vera L Bonilha

Cole Eye Institute, The Cleveland Clinic, Cleveland, OH, USA

**Abstract:** As the retinal pigment epithelium (RPE) ages, a number of structural changes occur, including loss of melanin granules, increase in the density of residual bodies, accumulation of lipofuscin, accumulation of basal deposits on or within Bruch's membrane, formation of drusen (between the basal lamina of the RPE and the inner collagenous layer of Bruch's membrane), thickening of Bruch's membrane, microvilli atrophy and disorganization of the basal infoldings. Although these changes are well known, the basic mechanisms involved in them are frequently poorly understood. These age-related changes progress slowly and vary in severity in different individuals. These changes are also found in age-related macular degeneration (AMD), a late onset disease that severely impacts the RPE, but they are much more pronounced than during normal aging. However, the changes in AMD lead to severe loss of vision. Given the many supporting functions which the RPE serves for the retina, it is important to decipher the age-related changes in this epithelium in order to understand age-related changes in vision.

**Keywords:** retinal pigment epithelium, aging, age-related macular degeneration (AMD), ocular disorders, retinal disease

## Age-related changes in the RPE

The retinal pigment epithelium (RPE) performs highly specialized metabolic and transport functions essential for homeostasis of the neural retina (Bok 1993). These include phagocytosis of photoreceptor-shed outer segments, transport of nutrients into and removal of waste products from photoreceptor cells and retinoid transport and regeneration. The RPE is a low cuboidal epithelium containing very long thin and sheet-like microvilli on its apical surface that project into the interphotoreceptor matrix where they interact with the tips of the rod and cone photoreceptor outer segments (Bok 1993). The apical surface of RPE cells supports and carries out the diurnal phagocytic removal of spent photoreceptor tips. One RPE cell supports 30–50 photoreceptors, which shed daily ~5% of their outer segment mass (Zinn and Benjamin-Henkind 1979). The basal surface of RPE cells displays highly convoluted basal infoldings that attach to a specialized Bruch's basement membrane, an acellular layer separating the RPE from the choriocapillaris. The RPE's basal surface participates in extensive metabolic exchanges with the blood vessels in the underlying choriocapillaris.

An accumulation of discrete but pronounced structural changes occurs in aging eyes. In the aged retina, an overall thinning is apparent, due to loss of neurons from all the neuronal cells and also shortening of photoreceptor cells. The RPE specifically is known to undergo several structural changes, including loss of melanin granules, increase in the number of residual bodies, accumulation of the age pigment lipofuscin, accumulation of basal deposits on or within Bruch's membrane (BM), formation of drusen (between the basal lamina of the RPE and the inner collagenous layer of BM), thickening of BM, RPE microvilli atrophy and disorganization of basal infoldings (Boulton and Dayhaw-Barker 2001). Some of these changes are shown in Figure 1

Correspondence: Vera L Bonilha
Cole Eye Institute (i31), The Cleveland Clinic, 9500 Euclid Avenue, Cleveland, OH 44195, USA
Tel +1 216 445 7690
Fax +1 216 445 3670
Email bonilhav@ccf.org

Clinical Ophthalmology 2008:2(2) 413–424

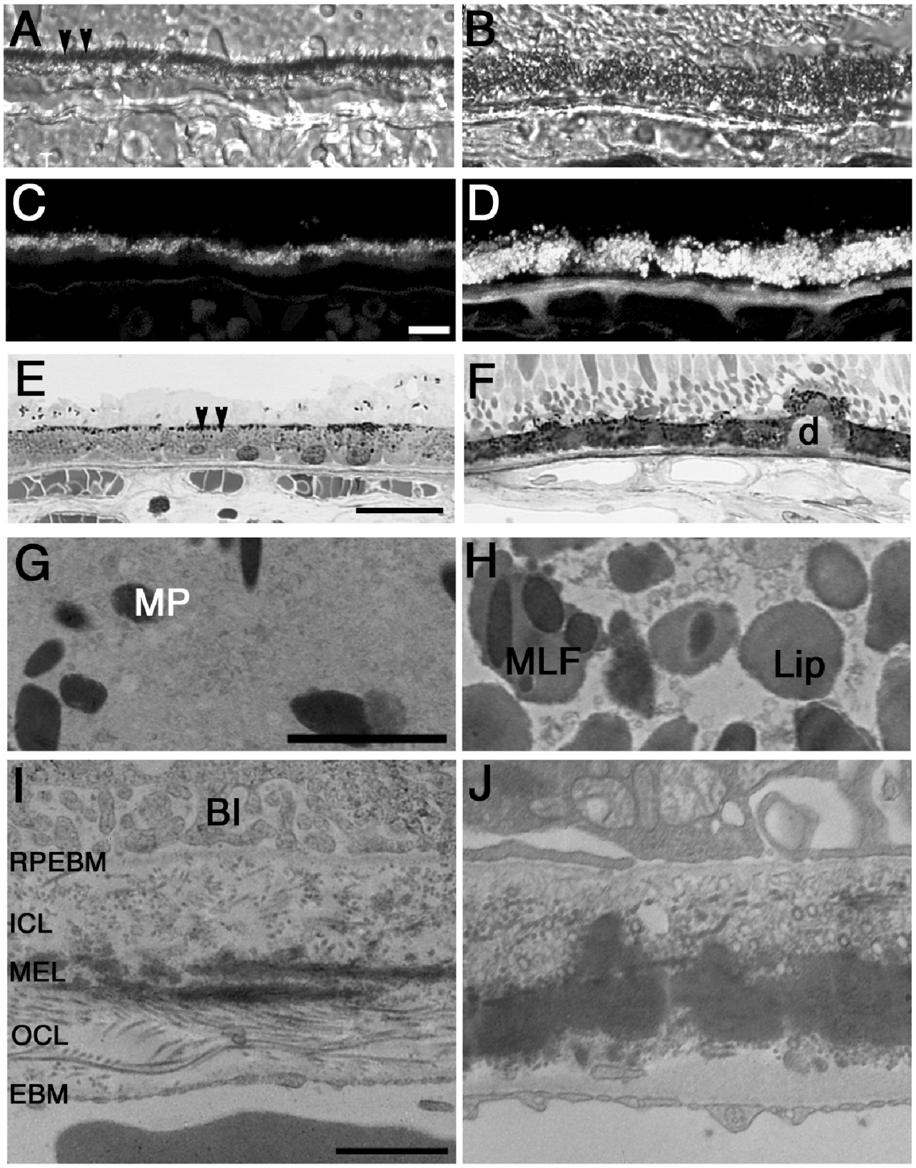

**Figure 1** Age-related changes in human RPE. Observation of the structural differences in RPE from young (23 year-old, **A**, **C**, **E**, **G**, **I**) and aged (75 and 88 year-old, **B**, **D**, **F**, **H**, **J**) human donors. Aged RPE from human donors displays loss of melanin granules (MP, arrowheads in **A**, **E**) and accumulation of the age pigment lipofuscin (Lip) (**B**, **D**), as observed by the presence of increased autofluorescent granules when observed on epifluorescence in the green channel (FITC filter: excitation 495 nm/emission 519 nm) in aged RPE (**D**) when compared to young RPE (**C**). Additional observation of the aged RPE displayed formation of drusen (**D**) (between the basal lamina of the RPE and the inner collagenous layer of Bruch's membrane) (**F**), thickening of Bruch's membrane and basal infoldings disorganization (**J**) when processed and analyzed by electron microscopy. In addition, in the aged RPE cells melanin granules are frequently seen in association with lipofuscin (melanolipofuscin, MLF) granules (**H**). Young RPE displays melanin pigments on their apical surface (**A**, **E**, **G**) while aged RPE contains mostly lipofuscin granules (**B**, **H**). Differential interference contrast microscopy images (**A**, **B**). Semi-thin epon sections stained with toluidine blue of young (**E**) and aged RPE (**F**) examined in bright field.

**Abbreviations:** BI, basal infoldings; RPEBM, RPE basement membrane; ICL, inner collagenous layer; MEL, middle elastic layer; OCL, outer collagenous layer; EBM, choroidal endothelial cell basement membrane; Bars: (**A** to **D**), 10 μm; (**E**, **F**), 200 μm; (**G**, **H**), 2 μm; (**I**, **J**), 1 μm.

(B, D, F, H, J) and they will be discussed in detail in the following text. The RPE aging changes progress slowly and are of varying severity in different eyes.

The RPE contains two kinds of pigment, namely lipofuscin and melanin. Melanin is an insoluble high molecular weight polymer derived from the enzymatic oxidation of tyrosine and dihydroxyphenylalanine, linked to proteins and contained in membrane-limited granules in the RPE melanosomes. Recently a comprehensive determination of the protein composition of melanosomes isolated from human melanoma cells was reported using proteomics (Chi et al 2006). The identified proteins included 16 homologs to mouse coat color genes, many associated with human pigmentary diseases, pigment epithelium-derived factor (PEDF) and SLC24A5 (sodium/potassium/calcium exchanger 5, NCKX5). However, these melanosomes may be different from the ones present in the RPE. RPE melanin originates from neural ectoderm, whereas the one in melanocytes originates from neural crest (Feeney 1978). In aged RPE cells melanin granules are frequently seen in association with lysosomes (melanolysosomes, MLL) and lipofuscin granules (melanolipofuscin, MLF; Figure 1H), which suggests that any protein bound to melanin may be degraded. In addition, melanosomes may undergo photobleaching with aging, which can diminish the antioxidant efficiency of melanin (Sarna et al 2003). Altogether, these observations suggest that changes in melanin granules possibly contribute to some of the senile changes evident in the RPE. A recent manuscript observed the accumulation of MLF in human RPE from different decades of life and assessed their phototoxicity to RPE cultures *in vitro*. The analysis of the composition of MLF granules suggested that, in contrast to lipofuscin, they do not contain photoreceptor-specific proteins. The authors suggest that MLF may not originate from photoreceptor outer segments phagocytosis but that MLF accumulates as a result of the melanosomal autophagocytosis of RPE cells (Warburton et al 2006).

Accumulation of secondary lysosomes and residual bodies containing lipofuscin, known as dense bodies, has been observed in post-mitotic and intermitotic cells during aging (Schmucker and Sachs 2002; Morales et al 2004; Kubasik-Juraniec et al 2004). The general consensus is that the accumulation of these dense bodies represents lysosomal aging and is a universal index of cellular senescence (Schmucker and Sachs 2002; Terman et al 2007). It has been well established that the RPE has an extremely active lysosomal system capable of degrading thousands of phagocytosed outer segment disks per day (Young 1971; Zinn and Benjamin-Henkind 1979). The aged RPE accumulates indigested residues of this phagocytic process as residual bodies (Feeney-Burns et al 1987).

Lipofuscin pigment has been described as intracellular yellow-brown autofluorescent granules exhibiting sudanophilic, osmiophilic, argyrophilic and periodic acid-Schiff-positive and acid-fast staining characteristics (Feeney 1978). Lipofuscin is a heterogeneous material composed of a mixture of lipids and different fluorescent compounds, the main fluorophore of which has been identified as the pyridinium bis-retinoid, *N*-retinylidene-*N*-retinylethanolamine (A2E), a derivative of vitamin A. RPE lipofuscin is unique because it originates mainly from the phagocytosed photoreceptor outer segments as was demonstrated in early studies. For instance, analysis of the chemical composition of RPE cells revealed that it is different from the photoreceptor outer segments (Berman et al 1974). In addition, investigations undertaken on the Royal College of Surgeons (RCS) rats showed that in this strain, which fails to phagocytose shed outer segments, lipofuscin is significantly diminished (Katz et al 1986; Eldred and Lasky 1993). Moreover, the accumulation of autofluorescent debris was observed in a transgenic mouse line expressing a mutated form of cathepsin D that is enzymatically inactive, thereby impairing the processing of phagocytosed photoreceptor outer segments by the RPE cells (Rakoczy et al 2002). A recent study established the presence of extragranular material present in preparations of lipofuscin routinely isolated by sucrose density gradient centrifugation. In this study, the lipofuscin granules were isolated and further purified by digestion of the extragranular material with proteinase K or by wash with SDS detergent. Raw and purified granules were tested for their protein content. The results demonstrated that: debris-free granules contain little or no protein; the protein associated with lipofuscin granules is essentially all extra-granular and appears to be significantly modified by posttranslational modifications (Renganathan et al 2007). Lipofuscin granules first appear in the basal portions of RPE cells of young eyes (1st decade, Figure 1C), whereas in older eyes (9th decade, Figure 1D), lipofuscin granules form into clumps and fill the entire RPE cell cytoplasm (Wing et al 1978). It is suggested that the accumulation of lipofuscin in aged RPE is connected to RPE functional degeneration either by "clogging" of the cytoplasm or by increased oxidative stress in the cell. Support for the first mechanism (clogging of the cytoplasm) comes from a recent study, which implanted glycoxidized microspheres (Glycox-MS) as imitation for lipofuscin into the subretinal space of 10–12 week-old rabbits. Observations were carried out from 1 to 16 weeks after subretinal implantation. Glycox-MS stagnated for a prolonged period in the cytoplasm of RPE cells and eyes implanted with glycox-MS produced drusen-like deposits at a significantly higher frequency (Yasukawa et al 2007). Support for the second mechanism (increased oxidative stress in the RPE cells) comes from observations that lipofuscin is a photoinducible generator of superoxide anion, singlet oxygen and hydrogen peroxide (Boulton et al 1993; Gaillard et al 1995; Rozanowska et al 1995, 1998). Thus, visible-light irradiation (400–1100 nm) of lipofuscin granules results in extra-granular oxidation of lipids and inactivation of lysosomal and antioxidant enzymes (Wassel et al 1999). In addition, it was shown that A2E has phototoxic and detergent properties and is capable of inducing disintegration of membrane-bound organelles in RPE cultures. Finally, lipofuscin can also interfere with the antioxidant properties of melanin (Boulton et al 1993; Rozanowska et al 1995; Schutt et al 2001, 2002; Wang et al 2006). The aged RPE displays increased intracellular accumulation of the blue-shifted autofluorescence lipofuscin granules, which coincides with the depletion of melanin pigments (Feeney-Burns 1984; Han et al 2007). RPE lipofuscin granules exhibit a broad band emission spectrum with a peak at 600 nm and subsidiary shoulders located at 470 and 550 nm when excited at 364 nm; a 680 peak appears with increasing age (Boulton et al 1990).

Bruch's membrane (BM) is a pentalaminar structure composed of the RPE basement membrane, inner collagenous layer, middle elastic layer, outer collagenous layer, and the choroidal endothelial cell basement membrane (Hogan and Alvarado 1967). This acellular extracellular meshwork found between the RPE and the choroid, which is 2–4 μm thick is known to undergo increased thickening (Figure 1J), chemical reconfiguration of both proteins and lipids, and debris accumulation during aging (Pauleikhoff et al 1990; Okubo et al 1999; Zarbin 2004). The aged BM displays an exponential increase in phospholipids, triglycerides, fatty acids, and free cholesterol content (Sheraidah et al 1993). Protein reconfiguration in the form of post-translational modifications has been reported in the BM. Immunoreactivity to some of the advanced glycation end product (AGE) adducts increases in the aged BM (Farboud et al 1999; Handa et al 1999). Although the precise contribution of AGEs to the retinal pathology remains to be elucidated, AGEs are recognized as important initiators of age-related dysfunction, inasmuch as they are known to cause protein cross-linking, reduced solubility, enzymatic dysfunction, and loss of receptor recognition (Baynes 2001). A recent study combined both Raman microscopy and specific chemical quantification to assess defined AGE adducts and quantify AGE-related spectral alterations in aged BM of postmortem eyes (Glenn et al 2007). The analysis showed that the AGEs pentosidine, carboxymethyllysine (CML), and carboxyethyllysine (CEL) occurred at significantly higher levels in BM-Ch with age (Glenn et al 2007). In addition, several recent studies demonstrated that tissue metalloproteinase inhibitor 3 (TIMP-3), vitronectin, annexins, crystallins, clathrin and adaptin proteins were crosslinked as evidenced from western blots that showed the presence of these proteins at several regions of the gel (Nakata et al 2005; Rayborn et al 2006; Bando et al 2007).

In addition, BM is under constant cycles of pressure-induced stress as a result of the choroidal flow oscillating with the cardiac rhythm. The mechanical properties of BM are critical determinants of its physiology. Specifically, the elastic properties of BM will determine its ability to sustain potentially damaging stress and strain perturbations. Recently the mechanical properties of isolated human BM were investigated and related to aging. This study demonstrated that the elasticity of human BM-Ch complex decreased linearly with aging after the age of 21 with an approximate reduction of 1% per year. On the other hand, the recoil capacity of Bruch's membrane-choroid was not affected by aging (Ugarte et al 2006).

Drusen are debris-like deposits that accumulate below the RPE along BM (Figure 1F). Clinically, they are characterized by the terms "hard" and "soft" according to their size and their appearance in fluorescein angiography. Hard drusen are small, hard, round and have well defined borders (Marshall et al 1998). Hard drusen occur in 80% of postmortem eyes, and are usually small, they are hyperfluorescent on fluorescein angiography, a characteristic that may be related to the fact that they are enriched in phospholipids (Bird and Marshall 1986; Pauleikhoff et al 1992; Arnold et al 1997). On the other hand, soft drusen are extensive, diffuse, large deposits, which have borders not sharply defined, and rarely occur before the age of 55 (Garner et al 1994; Marshall et al 1998). Soft drusen are hypofluorescent in fluorescein angiography and display a high content of neutral fats (Pauleikhoff et al 1992; Arnold et al 1997), vesicles, membranous debris, and wide-spaced collagen. Generally, hard drusen do not lead to loss of vision, but soft drusen are considered contributors to the pathology of age-related macular degeneration (AMD). Soft drusen deposition in the macula precedes visual loss; it defines the early stages of AMD together with pigmentary changes of the RPE. Deposition of soft drusen in the macula is considered the precursor lesion that leads to the development of geographic atrophy (dry AMD) and choroidal neovascularization (wet AMD), which are the late forms of AMD. The different types of AMD will be discussed in detail in the following text.

A recent proteomic study carried out on isolated drusen from both AMD and normal donors found up to 65% of the proteins identified common to both donor types. TIMP-3, clusterin, vitronectin, and serum albumin were the most common proteins observed in normal donor drusen, whereas crystallin was detected more frequently in AMD donor drusen. In addition, protein from both normal and AMD donors such as vitronectin, TIMP-3, clusterin, complement C9, lysosyme C, serum amyloid P, and apolipoprotein E migrated in multiple mass ranges from the top to the bottom of the gel, suggesting the presence of covalent crosslinks (Crabb et al 2002).

Recent work from several groups also suggests that local inflammation plays a role in drusen formation in a process analogous to that which occurs in other age-related diseases such as Alzheimer's disease and atherosclerosis, in which there is an accumulation of extracellular plaques and deposits causing a local chronic inflammatory response which in turn exacerbates the effects of the primary stimuli (Hageman et al 2001; Johnson et al 2001; Anderson et al 2002). This hypothesis is supported by evidence revealing the localization of several proteins involved in the immune system such as immunoglobulins; components of complement cascade (such as C5b-9 complex, complement factor F); MHC class II antigens; cell-associated molecules, including HLA-DR and specific CD antigens (Mullins et al 2000; Hageman et al 2001; Johnson et al 2001; Anderson et al 2002).

Few studies have demonstrated age-related effects on RPE microvilli. A finding common to all of them was the shortening of the RPE microvilli (Katz and Robison 1984; Lai and Rana 1986; Weisse 1995). Previously, we have been able to isolate intact RPE microvilli from mice (Bonilha et al 2004) and characterize its content using proteomics. Several of the identified proteins in the microvilli fraction are antioxidant enzymes and have been shown to undergo specific modulation during aging. These include lactate dehydrogenase, glutathione S-transferase, peroxiredoxin, ceruloplasmin, and superoxide dismutase. Our data are supported by several reports, which identified the presence of antioxidative enzymes in the microvilli of kidney (Davies et al 1993; Muse et al 1994), respiratory tract epithelium (Coursin et al 1992), and intestine (Davis et al 1989), among others. Oxidation is a very important mechanism in aging (Kohen and Nyska 2002; Balazy and Nigam 2003; Van Remmen et al 2003; Kregel and Zhang 2007). RPE apical microvilli shortening is also expected to affect several of the key functions carried out by the apical surface. Examples of these include phagocytosis of shed photoreceptor outer segments through the receptors $\alpha v\beta 5$ vitronectin receptor and the Mer tyrosine kinase (MerTK) receptor protein; apical transport involving transporters such as Na,K-ATPase, the glucose transporter (Glut-1), monocarboxylate transporter 1 (MCT1), basigin, the Kir7.1 K+ channel, chloride intracellular channel 6, carbonic anhydrase XIV, among others; and visual cycle function through the involvement of CRALBP, RPE65, IRBP, and CRBP (Rayborn et al 2005). These changes could alter the retinal metabolic equilibrium and accelerate degenerative processes in the aging retina. Our ongoing research aims to identify a protein profile that is uniquely present in aged RPE cells. Our findings will lead to future studies on the functional consequence of these proteins and to a more complete understanding of the pathogenesis of AMD.

## Animal models in RPE aging studies

A good animal model should reduplicate biochemical, morphological, and molecular changes shown in humans during aging. Much of our understanding of the biological changes that occur with aging has come from studies using rodents. Similarities in the physiology and cell biology of aging in humans and rodents make rodents a valuable model with which to test therapeutic interventions for aging, and they are small enough to allow for the use of statistically robust sample sizes. There are several rodent models to choose from. The National Institute on Aging (NIA) supports many resources to facilitate the use of animal models for biogerontological research, including aged rodent colonies, the aged rodent tissue bank, and tissue arrays from aged rodents (Nadon 2006). One of the rodent models available for aging studies is the rat $F_1$ F344/BN hybrid. The aged (24–25 month-old) F344/BN rat displays several of the RPE age-related changes described above; specifically, BM thickening, lipofuscin accumulation, accumulation of residual bodies, decrease in RPE density and microvilli atrophy when compared to young (3–4 month-old) rats (Figure 2).

## Age-related changes in RPE density

Numerous studies have been undertaken to determine changes in RPE density with age. However, previous studies yielded contradictory results: Some found that RPE density increased with age (Tso and Friedman 1968; Harman et al 1997; Leung et al 2004). Others found that it decreased (Streeten 1969; Gao and Hollyfield 1992; Watzke et al 1993); while yet another study found that it did not change with age at all (Dorey et al 1989). The discrepancies among these studies can be explained by the number of eyes analyzed and by the nature of the analyses which were carried out. Use of cross-sections allows analysis of a restricted number of cells, whereas whole-mount preparations allows analysis of the whole population of cells in the tissue. One study (Gao and Hollyfield 1992) investigated this issue analyzing eyes from donors from the 2nd to the 9th decade. Tissue fragments were obtained and analyzed as whole-mounts from the fovea and the retinal equator. Observations suggested that foveal RPE is denser, with cells smaller and more homogeneous, independent of the age of the donor, as shown in Figure 3A and C. Linear regression of the obtained data yielded a significant negative slope of RPE density in the retinal equator, suggesting a uniform rate of equatorial RPE loss during aging.

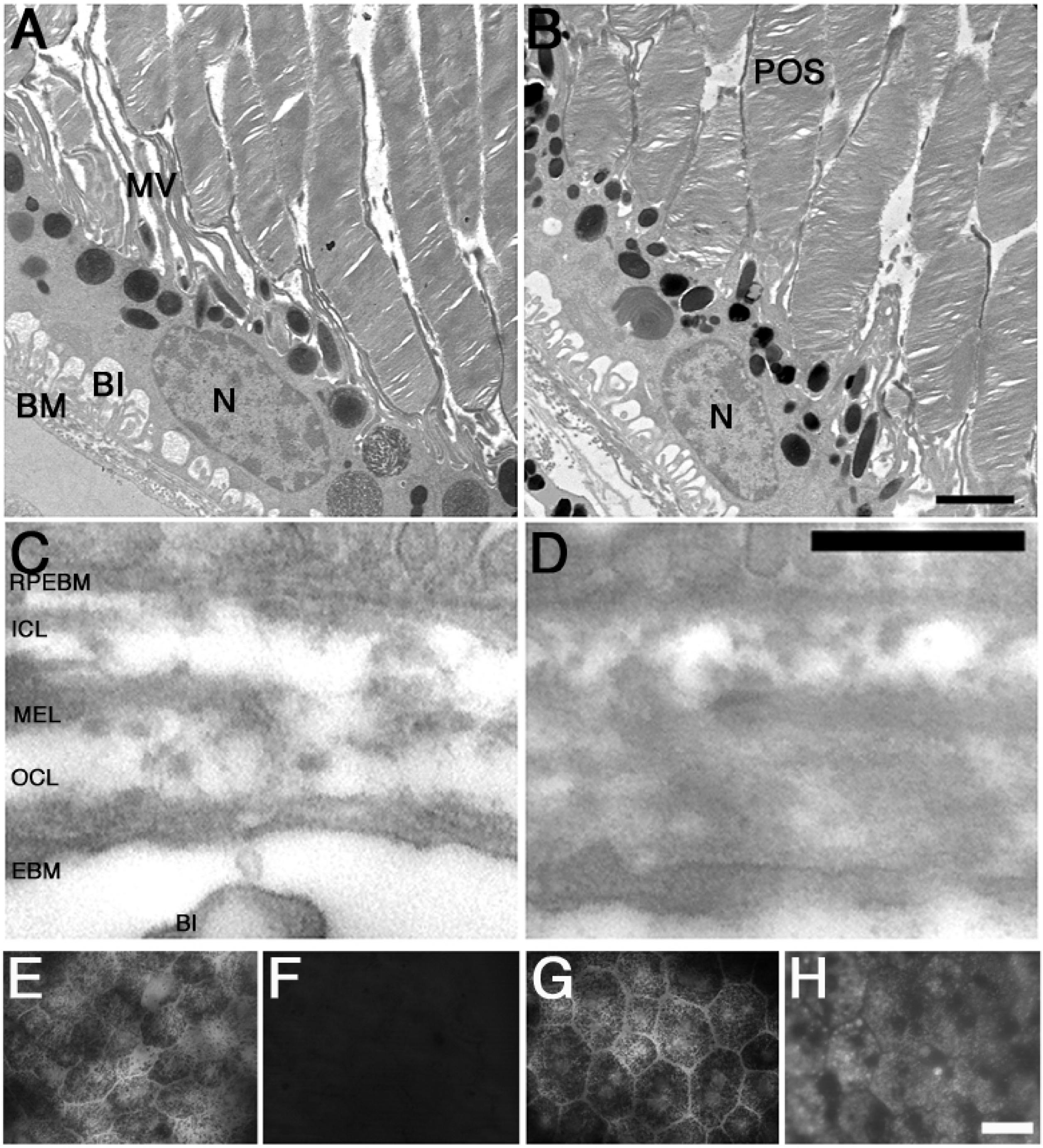

**Figure 2** Age-related changes in F1 F344BN hybrid rat RPE. Observation of young (3–4 month-old, **A**) and aged (24–25 month-old, **B**) F1 F344BN hybrid rats reveals several of the RPE age-related changes previously described. These include: Bruch's membrane thickening (**D**), accumulation of residual bodies, and microvilli atrophy (**B**). In addition, bright-field analysis of aged RPE whole-mounts reveals decrease in RPE density (**G**) while epifluorescence in the green channel (FITC filter: excitation 495 nm/emission 519 nm) reveals increased lipofuscin accumulation (**H**) when compared to the young RPE cells (**E** and **F**). **A**–**D**. Transmission electron microscopy.

**Abbreviations:** BI, basal infoldings; MV, microvilli; POS, photorecptor outer segments; RPEBM, RPE basement membrane; ICL, inner collagenous layer; MEL, middle elastic layer; OCL, outer collagenous layer; EBM, choroidal endothelial cell basement membrane; Bars: (**A** and **B**), 1 μm; (**C** and **D**), 2 μm; and (**C** to **F**), 200 μm.

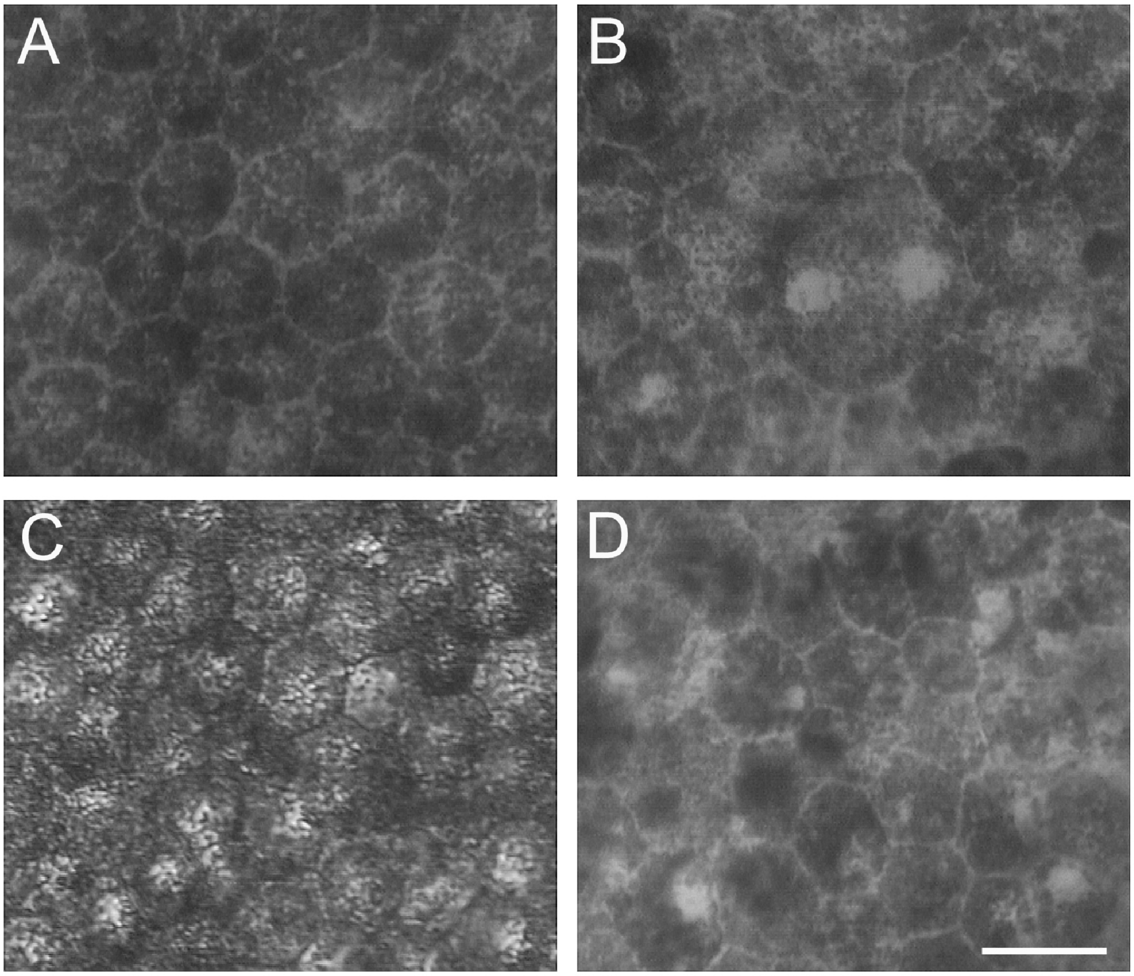

**Figure 3** Age-related changes in RPE density. Bright-field micrographs of RPE whole- mounts from both young (**A** and **B**) and aged (**C** and **D**) donor eyes. Observations were carried out both in the fovea (**A** and **C**) and periphery (**B** and **D**) of the eyes. Foveal RPE cells are smaller and more homogeneous than the peripheral RPE cells independent of the age of the donor. Bas, 200 μm.

On the other hand, foveal RPE density was relatively stable from the 2nd through the 9th decades, with no significant decrease in cell density (Gao and Hollyfield 1992).

Another study investigated the age-related changes in RPE in an even larger number of eyes from donors from the 2nd to the 9th decade (Panda-Jones et al 1996). Using a 3 mm trephine the authors collected RPE/retina/choroid in the fovea and in the superior, inferior, temporal, and nasal meridians in 6 rings that were arranged concentrically around the fovea. These samples were also analyzed as whole-mount preparations. As in the previous study, the authors concluded that RPE density at the foveal center was the highest and that it decreased significantly from the fovea to the mid-retinal periphery. In the periphery, RPE density was the highest in the nasal region. The age-related loss was most marked in the fovea and the mid periphery. The authors determined that RPE cell density in the fovea decreased significantly by about 0.3% per year with increasing age.

The elderly suffer from loss of visual acuity (Weale 1975; Del Viva and Agostini 2007), color perception (Ohta and Kato 1975; Page and Crognale 2005), and dark-adaptation sensitivity (McFarland et al 1960; Werner 2005). These conditions are probably associated with age-related death of RPE and photoreceptors. It is important to understand the mechanisms involved in these cell deaths. One study specifically addressed this issue by analyzing age-related RPE apoptosis through terminal deoxynucleotidyl transferase-mediated dUTP nick end (TUNEL)-labeling in whole-mount preparations of eyes divided into 4 concentric regions centered on the fovea. Overall, analysis showed that TUNEL-positive RPE cells were uncommon. There was a significant positive correlation between the donor's age and the number of apoptotic cells. Analysis of the individual regions revealed that within zone 1 (0–1.5 mm radius) the proportion of apoptotic RPE cells started to increase in the 6th decade. There was also an age-dependent increase in apoptosis within zone 2 (1.5–3.0 mm radius, at a much lower number) (Del Priore et al 2002).

## RPE changes and loss in AMD

AMD is the most common cause of irreversible blindness in the elderly population in industrialized countries (Leibowitz et al 1980; Klein et al 1995; Kelin et al 2004). Although aging is an important event that contributes to the pathogenesis of AMD, it does not directly lead to the occurrence of AMD (Sarks 1976; Young 1987). AMD occurs in two forms: neovascular or exudative (wet) and atrophic (dry) AMD. Neovascular AMD is characterized by abnormal growth of capillaries from the choroid into the Bruch's membrane and RPE and by subsequent exudation of fluid, lipid, and blood. It results ultimately in a disciform scar in the macula and is responsible for severe, sudden visual loss (Holloway and Verhoeff 1929; Verhoeff and Grossman 1937). Atrophic AMD, also known as geographic atrophy (GA) is characterized by a progressing course leading to degeneration of RPE and photoreceptors. Studies have shown that the atrophy initially tends to develop in the perifoveal area, while the fovea may be spared until later during the clinical course (Sarks et al 1988; Sunness 1999). GA is characterized by a loss of the outer neurosensory retina, the RPE, and the choriocapillaris (Figure 4). The primary dysfunction and cell death of the RPE cells is thought to occur initially, followed by collateral loss of neighboring photoreceptor cells and choriocapillaris (Sarks et al 1988; Roth et al 2004). Previous studies have shown that photoreceptor apoptosis is involved in AMD pathology (Green and Enger 1993; Xu et al 1996). Recently, another study quantified the number of TUNEL-positive cells in each retinal layer in cryosections of AMD and control eyes. The authors showed that maculas with AMD had a statistically significant increase in TUNEL-positive RPE cells compared with the control ones. In the GA eyes, TUNEL-positive rods and RPE nuclei were present near the edges of RPE atrophy (Dunaief et al 2002). Additional data also suggest that A2E, a lipofuscin component, induces apoptosis in RPE cultures (Suter et al 2000). Finally, apoptosis was also observed in surgically excised choroidal neovascular (CNV) membranes from AMD-affected eyes (Hinton et al 1998).

Clinical features common in both types of AMD include the presence of drusen and hypo- and hyperpigmentation of the RPE. Histological features of RPE in AMD include accumulation of lipofuscin, formation of drusen and of basal deposits in the BM, and alteration in the BM extracellular matrix (Hogan 1972; Sarks 1976; Young 1987; Green and Enger 1993; Roth et al 2004; Nowak 2006). As mentioned above, these features are also observed, with lower intensity, in the aging RPE. However, the changes in AMD lead to severe loss of vision.

AMD is a multifactor disease with genetic components (Klaver and Allikmets 2003; Gold et al 2006; Hageman et al 2006; Scholl et al 2007). However, exogenous factors such as light exposure, a high fat diet, high blood pressure, and smoking (Leibowitz et al 1980; Cruickshanks et al 1993; Cousins et al 2002) are known to modulate its pathogenesis. In addition, abnormal regulation of the complement system, likely caused by the Y402H polymorphism in the complement factor H gene on 1q, is a recognized risk factor for AMD, as is the A69S variant in the poorly characterized LOC387715 gene and the serine protease HTRA1 in multiple populations (Edwards et al 2005; Haines et al 2005; Jakobsdottir et al 2005; Klein et al 2005; Rivera et al 2005; Dewan et al 2006;

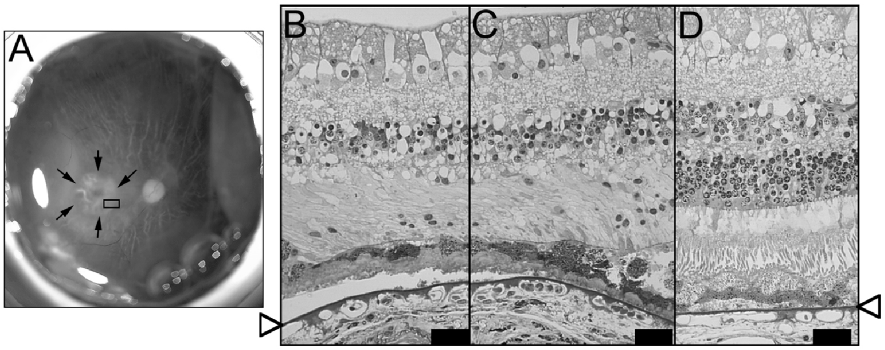

**Figure 4** RPE cell loss in geographic atrophy. Gross photomicrography of a postmortem eye from an AMD donor with geographic atrophy (GA) (**A**). Arrows indicate the edges of GA; inset indicates the region cut and processed for transmission electron microscopy. Semi-thin epon sections stained with toluidine blue of this region demonstrates extensive RPE, photoreceptors and choroids atrophy in the GA region (**B**) while the edge of GA displays more RPE cells and the presence of some photoreceptor outer segments (**C**). In the region outside of the GA the RPE layer is continuous and the photoreceptors' inner and outer segments can be observed (**D**). Arrowheads point to Bruch's membrane. Debris accumulation is observed underneath the RPE cells in all regions observed. Bars 200 μm.

Yang et al 2006). On the other hand, polymorphisms in the factor B and complement component 2 are associated with decreased susceptibility to AMD (Gold et al 2006; Spencer et al 2007). Previous studies had identified the genes ABC4, APOE, TLR4, and FBLN5 as being associated with susceptibility to AMD. However, the fraction of AMD patients carrying sequence changes in these genes was very small (Scholl et al 2007).

As mentioned above, complement activation has been implicated in susceptibility to AMD, mainly through complement factor H. It is synthesized mainly in the liver and released into the blood where it is transported to other tissues. However, high levels of complement factor H are detected in the retina-choroid interface (Mandal and Ayyagari 2006; Chen et al 2007). This expression increases with age (Mandal and Ayyagari 2006). In addition, it was suggested that the RPE synthesizes complement factor H locally (Hageman et al 2005). The RPE production of factor H would increase the local concentration of complement regulators and provide protection to inappropriate complement activation at sites of infection and inflammation (Rodriguez et al 2004). This mechanism would be particularly important in the retina, as the complement factors supplied by the blood may be restricted through the blood-brain barrier (Mandal and Ayyagari 2006).

Several reports have shown that oxidative mechanisms constitute the initial stimulus that triggers apoptosis, thereby contributing to the progression of AMD. The retina is highly susceptible to photo-oxidative damage due to its high oxygen demand, life-long exposure to light and the presence of polyunsaturated fatty acids highly enriched in the photoreceptor outer segments (Beatty et al 2000; Roth et al 2004). This scenario is aggravated with age, for there is a reduction in the local antioxidative enzymes in the RPE and a decrease in macular pigment density, which serves not only as a filter for short-wavelength light, but also as an antioxidant, through its two constituents, lutein and zeaxanthin. The age-related increase in oxidative stress leads to cellular events which in turn induce the histopathological changes associated with AMD, as described above. An animal model recently described the connection between oxidation, inflammation and pathology of AMD. In this model, mice were injected with mouse serum albumin adducted with carboxyethylpyrrole, an oxidation fragment generated from the protoreceptor-enriched lipid docosahexaenoic acid. Injected mice develop antibodies to this hapten, fix high amounts of complement component 3 in Bruch's membrane, accumulate drusen below the RPE, and develop lesions in the RPE-photoreceptor interface that mimic AMD (Hollyfield et al 2007). The severity of the cellular lesions correlated with the antibody production titer.

## Outlook

The aged RPE is characterized by several structural changes, which are exacerbated in AMD. These structural changes are known to be associated with an increase in oxidative stress and general decline of basic functions. Recently, it became evident that RPE and choriocapillaris express many if not all of the components and regulators of the complement cascade. Moreover, the RPE also plays an important role in the development of immune and inflammatory responses in the posterior part of the eye through production of cytokines. However, little is known about it in aging. The connection between oxidation and immune system in aging will provide a powerful approach for the elucidation of the many senile degenerative macular and peripheral retinal diseases such as AMD.

## Acknowledgments

The author thanks Mary E Rayborn for critical review of the manuscript and for the help with electron microscopy and Joe G Hollyfield for critical comments on the manuscript and constant support. Human eyes used in this review were obtained through the Retinitis Pigmentosa Foundation Donor Program (Owings Mills, Maryland USA). Research was supported by NIH grants R21EY017153; a Research Center grant from the Foundation Fighting Blindness; a Challenge Grant from Research to Prevent Blindness; and an NEI infrastructure grant (EY015638).

## References

Anderson DH, Mullins RF, Hageman GS, et al. 2002. A role for local inflammation in the formation of drusen in the aging eye. *Am J Ophthalmol*, 134:411–30.

Arnold JJ, Quaranta M, Soubrane G, et al. 1997. Indocyanine green angiography of drusen. *Am J Ophthalmol*, 124:344–56.

Bando H, Shadrach KG, Rayborn ME, et al. 2007. Clathrin and adaptin accumulation in drusen, Bruch's membrane and choroid in AMD and non-AMD donor eyes. *Exp Eye Res*, 84:135–42.

Baynes JW. 2001. The role of AGEs in aging: causation or correlation. *Exp Gerontol*, 36:1527–37.

Beatty S, Koh H-H, Phil M, et al. 2000. The role of oxidative stress in the pathogenesis of age-related macular degeneration. *Surv Ophthalmol*, 45:115–34.

Berman ER, Schwell H, Feeney L. 1974. The retinal pigment epithelium. chemical composition and structure. *Invest Ophthalmol Vis Sci*, 13:675–87.

Bird AC, Marshall J. 1986. Retinal pigment epithelial detachments in the elderly. *Trans Ophthalmol Soc U K*, 105:674–82.

Bok D. 1993. The retinal pigment epithelium: a versatile partner in vision. *J Cell Sci Suppl*, 17:189–95.

Bonilha VL, Bhattacharya SK, West KA, et al. 2004. Proteomic characterization of isolated retinal pigment epithelium microvilli. *Mol Cell Proteomics*, 11:1119–27.

Boulton M, Dayhaw-Barker P. 2001. The role of the retinal pigment epithelium: topographical variation and ageing changes. *Eye*, 15:384–9.

Boulton M, Docchio F, Dayhaw-Barker P, et al. 1990. Age-related changes in the morphology, absorption and fluorescence of melanosomes and lipofuscin granules of the retinal pigment epithelium. *Vision Res*, 30:1291–303.

Boulton M, Dontsov A, Jarvis-Evans J, et al. 1993. Lipofuscin is a photoinducible free radical generator. *J Photochem Photobiol B*, 19:201–4.

Chen M, Forrester JV, Xu H. 2007. Synthesis of complement factor H by retinal pigment epithelial cells is down-regulated by oxidized photoreceptor outer segments. *Exp Eye Res*, 84:635–45.

Chi A, Valencia JC, Hu ZZ, et al. 2006. Proteomic and bioinformatic characterization of the biogenesis and function of melanosomes. *J Proteome Res*, 5:3135–44.

Coursin DB, Cihla HP, Oberley TD, et al. 1992. Immunolocalization of antioxidant enzymes and isozymes of glutathione S-transferase in normal rat lung. *Am J Physiol*, 263:L679–91.

Cousins SW, Espinosa-Heidmann DG, Alexandridou A, et al. 2002. The role of aging, high fat diet and blue light exposure in an experimental model for basal laminar deposit formation. *Exp Eye Res*, 75:543–53. Erratum in: *Exp Eye Res*, 2003. 76:517.

Crabb JW, Miyagi M, Gu X, et al. 2002. Drusen proteome analysis: an approach to the etiology of age-related macular degeneration. *Proc Natl Acad Sci USA*, 99:14682–7.

Cruickshanks KJ, Klein R, Klein BE. 1993. Sunlight and age-related macular degeneration. The Beaver Dam Eye Study. *Arch Ophthalmol*, 111:514–18.

Davies SJ, D'Sousa R, Philips H, et al. 1993. Localisation of alpha, mu and pi class glutathione S-transferases in kidney: comparison with CuZn superoxide dismutase. *Biochim Biophys Acta*, 1157:204–8.

Davis WL, Matthews JL, Shibata K, et al. 1989. The immunocytochemical localization of superoxide dismutase in the enterocytes of the avian intestine: the effect of vitamin D3. *Histochem J*, 21:194–202.

Del Piore LV, Kuo Y-H, Tezel TH. 2002. Age-related changes in human RPE cell density and apoptosis. *Invest Ophthalmol Vis Sci*, 43:3312–18.

Del Viva MM, Agostini R. 2007. Visual spatial integration in the elderly. *Invest Ophthalmol Vis Sci*, 48:2940–6.

Dewan A, Liu M, Hartman S, et al. 2006. HTRA1 promoter polymorphism in wet age-related macular degeneration. *Science*, 314:989–92.

Dorey CK, Wu G, Eberstein D, et al. 1989. Cell loss in the aging retina: relationship to lipofuscin accumulation and macular degeneration. *Invest Ophthalmol Vis Sci*, 30:1691–9.

Dunaief JL, Dentchev T, Ying G-S, et al. 2002.The role of apoptosis in age-related macular degeneration. *Arch Ophthalmol*, 120:1435–42.

Edwards AO, Ritter R III, Abel KJ, et al. 2005. Complement factor H polymorphism and age-related macular degeneration. *Science*, 308:421–4.

Eldred GE, Lasky MR. 1993. Retinal age pigments generated by self-assembling lysosomotrophic detergents. *Nature*, 361:724–6.

Farboud B, Aotaki-Kee A, Miyata et al. 1999. Development of a polyclonal antibody with broad epitope specificity for advanced glycation endproducts and localization of these epitopes in Bruch's membrane of the aging eye. *Mol Vis*, 5:11.

Feeney L. 1978. Lipofuscin and melanin of human retinal pigment epithelium. Fluorescence, enzyme cytochemical and ultrastructural studies. *Invest Ophthalmol Vis Sci*, 17:583–600.

Feeney-Burns L, Gao CL, Tidwell M. 1987. Lysosomal enzyme cytochemistry of human RPE, Bruch's membrane and drusen. *Invest Ophthalmol Vis Sci*, 28:1138–47.

Feeney-Burns L, Hilderbrand ES, Eldridge S. 1984. Aging human RPE: Morphometric analysis of macular, equatorial, and peripheral cells. *Invest Ophthalmol Vis Sci*, 25:195–200.

Gao H, Hollyfield JG. 1992. Aging of the human retina: differential loss of neurons and retinal pigment epithelial cells. *Invest Ophthalmol Vis Sci*, 33:1–17.

Gaillard ER, Atherton SJ, Eldred G, et al. 1995. Photophysical studies on human retinal lipofuscin. *Photochem Photobiol*, 61:448–53.

Garner A, Sarks S, Sarks JP. 1994. Degenerative and related disorders of the retina and choroid. In: Garner A, and Klintworth GK ed. Pathobiology of ocular diseases: a dynamic approach, 2nd ed, New York, NY: Marcel Dekker. pp. 631–74.

Glenn JV, Beattie JR, Barret L, et al. 2007. Confocal raman microscopy can quantify advanced glycation end product (AGE) modifications in Bruch's membrane leading to accurate, nondestructive prediction of ocular aging. *Faseb J*, 21:1–11.

Gold B, Merriam JE, Zernant J, et al. 2006. Variation in factor B (BF) and complement component 2 (C2) genes is associated with age-related macular degeneration. *Nat Genet*, 38:458–62.

Green RW, Enger C. 1993. Age-related macular degeneration histopathologic studies. The 1992 Lorenz E. Zimmerman Lecture. *Ophthalmology*, 100:1519–34.

Hageman GS, Anderson DH, Johnson LV, et al. 2005. A common haplotype in the complement regulatory gene factor H (HF1/CFH) predisposes individuals to age-related macular degeneration. *Proc Natl Acad Sci USA*, 102:7227–32.

Hageman GS, Hancox LS, Taibr AJ, et al. 2006. Extended haplotypes in the complement factor H (CFH) and CFH-related (CFHR) family of genes protect against age-related macular degeneration: characterization, ethnic distribution and evolutionary implications. *Ann Med*, 38:592–604.

Hageman GS, Luthert PJ, Victor Chong NH, et al. 2001. An integrated hypothesis that considers drusen as a biomarker of immune-mediated processes at the RPE-Bruch's membrane interface in aging and age-related macular degeneration. *Prog Ret Eye Res*, 20:705–32.

Haines JL, Hauser MA, Schmidt S, et al. 2005. Complement factor H variant increases risk of age-related macular degeneration. *Science*, 308:419–21.

Han M, Giese G, Schmitz-Valckenberg S, et al. 2007. Age-related structural abnormalities in the human retina-choroid complex revealed by two-photon excited autofluorescence imaging. *J Bio Optics,* 12:024012–1–7.

Handa JT, Verzijl N, Matsunaga H, et al. 1999. Increase in the advanced glycation end product pentosidine in Bruch's membrane with age. *Invest Ophthalmol Vis Sci*, 40:775–9.

Harman AM, Fleming PA, Hoskins RV, et al. 1997. Development and aging of cell topography in the human retinal pigment epithelium. *Invest Ophthalmol Vis Sci*, 38:2016–26.

Hinton DR, He S, Lopez PF. 1998. Apoptosis in surgically excised choroidal neovascular membranes in age-related macular degeneration. *Arch Ophthalmol*, 116:203–9.

Hogan MJ. 1972. Role of the retinal pigment epithelium in macular disease. *Trans Am Acad Ophthalmol Otolaryngol*, 76:64–80.

Hogan MJ. and Alvarado J. 1967. Studies on the human macula. IV. Aging changes in Bruch's membrane. *Arch Ophthalmol,* 77:410–20.

Hollyfield JG, Rayborn ME, Yang X, et al. 2007. Identification of an inflammatory signal from the outer retina causing age-related macular degeneration [abstract]. *ARVO*, 2356.

Jakobsdottir J, Conley YP, Weeks DE, et al. 2005. Susceptibility genes for age-related maculopathy on chromosome 10q26. *Am J Hum Genet*, 77:389–407.

Johnson LV, Leiter WP, Staples MK, et al. 2001. Complement activation and inflammatory response in drusen formation and age-related macular degeneration. *Exp Eye Res*, 73:887–96.

Katz ML , Drea CM, Eldred GE, et al. 1986. Influence of early photoreceptor degeneration on lipofuscin in the retinal pigment epithelium. *Exp Eye Res*, 43:561–73.

Katz ML, Robison WG Jr. 1984. Age-related changes in the retinal pigment epithelium of pigmented rats. *Exp Eye Res*, 38:137–51.

Klaver CC, Allikmets R. 2003. Genetics of macular dystrophies and implications for age-related macular degeneration. In: Wissinger B, Kohl S, Langenbeck U eds. Genetics in Ophthalmology. *Dev Ophthalmol,* Basel, Karger, 37:155–69.

Kelin R, Peto T, Bird A, et al. 2004. The epidemiology of age-related macular degeneration. *Am J Ophthalmol*, 137:486–95.

Kelin R, Wang Q, Klein BEK, et al. 1995. The relationship of age-related maculopathy, cataract, and glaucoma to visual acuity. *Invest Ophthalmol Vis Sci*, 36:182–91.

Klein RJ, Zeiss C, Chew EY, et al. 2005. Complement factor H polymorphism in age-related macular degeneration. *Science*, 308:385–9.

Kohen R, Nyska A. 2002. Oxidation of biological systems: oxidative stress phenomena, antioxidants, redox reactions, and methods for their quantification. *Toxicol Pathol*, 30:620–50.

Kregel KC, Zhang HJ. 2007. An integrated view of oxidative stress in aging: basic mechanisms, functional effects, and pathological considerations. *AM J Physiol Regul Integr Comp Physiol*, 292:R18–36.

Kubasik-Juraniec J, Kmieć Z, Tukaj C, et al. 2004. The effect of fasting and refeeding on the ultrastructure of the hypothalamic paraventricular nucleus in young and old rats. *Folia Morphol (Warsz),* 63:25–35.

Lai YL, Rana MW. 1986. A study of photoreceptor-retinal pigment epithelium complex: age-related changes in monkeys. *Proc Soc Exp Biol Med*, 181:371–81.

Leibowitz HM, Krueger DE, Maunder LR, et al. 1980. The Framingham Eye Study monograph: An ophthalmological and epidemiological study of cataract, glaucoma, diabetic retinopathy, macular degeneration, and visual acuity in a general population of 2631 adults, 1973–1975. *Surv Ophthalmol*, 24:335–610.

Leung IY-F, Sandstrom MM, Zucker CL, et al. 2004. Nutrional manipulation of primate retinas, II: Effects of age, n-3 fatty acids, lutein, and zeaxanthin on retinal pigment epithelium. *Invest Ophthalmol Vis Sci*, 45:3244–56.

Mandal MN, Ayyagari R. 2006. Complement factor H: spatial and temporal expression and localization in the eye. *Invest Ophthalmol Vis Sci*, 47:4091–7.

Marshall J, Hussain AA, Starita C, et al. 1998. Aging and Bruch's membrane. In: Marmor MF, Wolfensberger TJ ed. The Retinal Pigment Epithelium. New York, NY: Oxford University Press, pp. 669–92.

McFarland RA, Domey RG, Warren AB, et al. 1960. Dark adaptation as a fuction of age: I. Statistical analysis. *J Gerontol*, 15:149–54.

Morales E, Horn R, Pastor LM, et al. 2004. Involution of seminiferous tubules in aged hamsters: an ultrastructural, immunohistochemical and quantitative morphological study. *Histol Histopathol,* 19:445–55.

Mullins R, Aptsiauri N, Hageman GS. 2000. Dendritic cells and proteins associated with immune-mediated processes are associated with drusen and may play a central role in drusen biogenesis. *Invest Ophthalmol Vis Sci*, 41:S24.

Muse KE, Oberley TD, Sempf JM, et al. 1994. Immunolocalization of antioxidant enzymes in adult hamster kidney. *Histochem J*, 26:734–53.

Nadon N. 2006. Exploiting the rodent model for studies on the pharmacology of lifespan extension. *Aging Cell*, 5:9–15.

Nakata K, Crabb JW, Holyyfield JG. 2005. Crystallin distribution in Bruch's membrane-choroid complex from AMD and age-matched donor eyes. *Exp Eye Res*, 80:821–6.

Nowak JZ. 2006. Age-related macular degeneration (AMD): pathogenesis and theraphy. *Pharmacol Rep*, 58:353–63.

Ohta Y, Kato H. 1975. Colour perception changes with age. *Mod Prob Ophthalmol,* 17:345.

Okubo A, Rosa RH Jr, Bunce CV, et al. 1999. The relashionships of age changes in retinal pigment epithelium and Bruch's membrane. *Invest Ophthalmol Vis Sci*, 40:443–9.

Page JW, Crognale MA. 2005. Differential aging of chromatic and achromatic visual pathways: behavior and electrophysiology. *Vis Res*, 45:1481–9.

Panda-Jones S, Jonas JB, Jakobczyk-Zmija M. 1996. Retinal pigment epithelial cell count, distribution, and correlations in normal human eyes. *Am J Ophthalmol*, 121:181–9.

Pauleikhoff D, Harper CA, Marshall, et al. 1990. Aging changes in Bruch's membrane. A histochemical and morphologic study. *Ophthalmology*, 97:171–8.

Pauleikhoff D, Zuels S, Sheraidah GS, et al. 1992. Correlation between biochemical composition and fluorescein binding of deposits in Bruch's membrane. *Ophthalmology,* 99:1548–53.

Renganathan K, Ng KP, Davies M, et al. 2007. Does lipofuscin contain protein? amino acid, protein and ultrastructural analysis of human lipofuscin [abstract]. *ARVO*, 5059.

Rakoczy PE, Zhang D, Robertson T, et al. 2002. Progressive age-related changes similar to age-related macular degeneration in a transgenic mouse model. *Am J Pathol*, 161:1515–24.

Rayborn ME, Sakagushi H, Shadrach KG, et al. 2006. Annexins in Bruch's membrane and drusen. *Adv Exp Med Biol*, 572:75–8.

Rayborn ME, Hollyfield JG, Bonilha VL. 2005. Age-related changes in the retinal pigment epithelium apical surface [abstract]. *ARVO*, 3049.

River A, Fisher SA, Fritscher LG, et al. 2005. Hypothetical LOC387715 is a second major susceptibility gene for age-related macular degeneration, contributing independently of complement factor H to disease risk. *Hum Mol Genet*, 14:3227–36.

Rodriguez DC, Esparza-Gordillo J, Goicoechea DJ, et al. 2004. The human complement factor H: functional roles, genetic variations and disease associations. *Mol Immunol*, 41:355–67.

Roth F, Bindewald A, Holz FG. 2004. Key pathophysiologic pathways in age-related macular disease. *Graefe's Arch Clin Exp Ophthalmol*, 242:710–16.

Rozanowska M, Jarvis-Evans J, Korytowski W, et al. 1995. Blue light-induced reactivity of retinal age pigment. In vitro generation of oxygen-reactive species. *J Biol Chem*, 270:18825–30.

Rozanowska M, Wessels J, Boulton M, et al. 1998. Blue light-induced singlet oxygen generation by retinal lipofuscin in non-polar media. *Free Rad Biol Med*, 24:1107–12.

Sarks SH. 1976. Aging and degeneration in the macular region: a clinico-pathological study. *Br J Ophthalmol*, 60:324–41.

Sarks JP, Sarks SH, Killingsworth MC. 1988. Evolution of geographic atrophy of the retinal pigment epithelium. Evolution of geographic atrophy of the retinal pigment epithelium. *Eye*, 2:552–77.

Sarna T, Burke JM, Korytowski W, et al. 2003. Loss of melanin from human RPE with aging: possible role of melanin photooxidation. *Exp Eye Res*, 76:89–98.

Schmucker DL, Sachs H. 2002. Quantifying dense bodies and lipofuscin during aging: a morphologist's perspective. *Arch Gerontol Geriatr*, 34:249–61.

School HPN, Fleckenstein M, Issa PC, et al. 2007. An update on the genetics of age-related macular degeneration. *Mol Vis*, 13:196–0205.

Schutt F, Davies S, Kopitz J, et al. 2001. Photodamage to human RPE cells by A2-E, a retinoid component of lipofuscin. *Invest Ophthalmol Vis Sci*, 41:2303–8.

Schutt F, Bergmann M, Holz FG, et al. 2002. Isolation of intact lysosomes from human RPE cells and effects of A2-E on the integrity of the lusosomal and other cellular membranes. *Graefes Arch Clin Exp Ophthalmol*, 240:983–8.

Sheraidah G, Steinmetz R, Maguire J, et al.1993. Correlation between lipids extracted from Bruch's membrane and age. *Ophthalmology*, 100:47–51.

Spencer KL, Hauser MA, Olson LM, et al. 2007. Protective effect of complement factor B and complement component 2 variants in age-related macular degeneration. *Hum Mol Genet*, 16:1986–92.

Sunness JS. 1999. The natural history of geographic atrophy, the advanced atrophic form of age-related macular degeneration. *Mol Vis*, 5:25.

Suter M, Reme C, Grimm C, et al. 2000. Age-related macular degeneration. The lipofuscin component N-retinyl-N-retinylidene ethanolamine detaches proapoptotic proteins from the mitochondria and induces apoptosis in mammalian retinal pigment epithelial cells. *J Biol Chem*, 275:39625–30.

Streeten BW. 1969. Development of the human retinal pigment epithelium and the posterior segment. *Arch Ophthalmol*, 81:383–94.

Terman A, Gustafsson B, Brunk UT. 2007. Autophagy, organelles and ageing. *J Pathol*, 211:134–43.

Tso MOM, Friedman E. 1968. The retinal pigment epithelium: III. Growth and development. *Arch Ophthalmol*, 80:214–16.

Ugarte M, Hussain AA, Marshall J. 2006. An experimental study of the elastic properties of the human Bruch's membrane-choroid complex: relevance to ageing. *Br J Ophthalm*, 90:621–6.

Van Remmen H, Hamilton ML, Richardson A. 2003. Oxidative damage to DNA and aging. *Exerc Sport Sci Rev*, 31:149–53.

Wang Z, Dillon J, Gaillard ER. 2006. Antioxidant properties of melanin in retinal pigment epithelial cells. *Photochem Photobiol*, 82:474–9.

Warrburton S, Davis WE, Southwick K, et al. 2007. Proteomic and phototoxic characterization of melanolipofuscin: correlation to disease and model for its origin. *Mol Vis*, 13:318–29.

Wassell J, Davies S, Bardsley W, et al. 1999. The photo-reactivity of the retinal age pigment lipofuscin. *J Biol Chem*, 274:23828–32.

Watzke RC, Soldevilla JD, Trune DR. 1993. Morphometric analysis of human retinal pigment epithelium: correlation with age and location. *Curr Eye Res*, 12:133–42.

Weale RA. 1975. Senile changes in visual acuity. *Trans Ophthalmol Soc UK*, 95:36–8.

Weisse I. 1995. Changes in the aging rat retina. *Ophthalmic Res*, 27:154–63.

Werner JS. 2005. Night vision in the elderly: consequences for seeing through a "blue filtering" intraocular lens. *Br J Ophthalmol*, 89:1518–21.

Wing GL, Blanchard GC, Weiter JJ. 1978. The topography and age relationship of lipofuscin concentration in the retinal pigment epithelium. *Invest Ophthalmol Vis Sci*, 17:601–7.

Xu GZ, Li WW, Tso MOM. 1996. Apoptosis in human retinal degenerations. *Trans Am Ophthalmol Soc,* 94:411–31.

Yang Z, Cammp NJ, Sun H, et al. 2006. A variant of the HTRA1 gene increases susceptibility to age-related macular degeneration. *Science*, 314:992–3.

Yasukawa T, Wiedemann P, Hoffman S, et al. 2007. Glycoxidized particles mimic lipofuscin accumulation in aging eyes: a new age-related macular degeneration model in rabbits. *Graefes Arch Clin Exp Ophthalmol*, 245:1475–85.

Young RW. 1987. Pathophysiology of age-related macular degeneration. *Surv Ophthalmol,* 31:291–306.

Zarbin MA. 2004. Current concepts in the pathogenesis of age-related macular degeneration. *Arch Ophthalmol*, 122:598–614.

Zinn KM, Benjamin-Henkind JV. 1979. Anatomy of the human retinal pigment epithelium. In: Zinn KM and Marmor MF ed. The Retinal Pigment Epithelium. Cambridge, MA: Harvard University Press, pp. 3–31.

Available online at www.sciencedirect.com
ScienceDirect
Experimental Eye Research 86 (2008) 150–156
EXPERIMENTAL EYE RESEARCH
www.elsevier.com/locate/yexer

# Semenogelins in the human retina: Differences in distribution and content between AMD and normal donor tissues

Vera L. Bonilha [a,*], Mary E. Rayborn [a], Karen G. Shadrach [a], Yong Li [a], Åke Lundwall [b], Johan Malm [b], Joe G. Hollyfield [a]

[a] Department of Ophthalmology, The Cole Eye Institute, Cleveland Clinic Lerner College of Medicine, 9500 Euclid Avenue, Cleveland, OH 44195, USA
[b] Department of Laboratory Medicine, Lund University, University Hospital, MAS, S-205 02 Malmö, Sweden

Received 13 August 2007; accepted in revised form 17 October 2007
Available online 25 October 2007

## Abstract

The two cellular targets of interest in age-related macular degeneration (AMD) are the photoreceptors and the RPE. However, the mechanisms involved in AMD pathology are not yet fully understood. In the present report, we extend our previous studies on semenogelin proteins (Sgs) in normal human retina and compare these with the distribution in retinas from AMD donor eyes. Semenogelins I (SgI) and II (SgII) are the major structural protein components of semen coagulum, but have been recently found in non-genital tissues as well. Cryo and paraffin sections of human retina were processed for both immunofluorescence and DAB reaction with a specific antibody. The presence of SgI was analyzed in retina and RPE total lysates and SgI was detected by western blot in human retina and RPE. The intensity of immunoreactivity was significantly reduced in the AMD eyes. SgI is expressed in the normal human retina and in the retina of AMD donor eyes, where localization was detected in the photoreceptors and in a few ganglion cells. We find the distribution of SgI in the AMD retinas substantially lower than observed in normal retina. SgI localization to photoreceptors and the RPE suggests a possible function related to the ability of these cells to sequester zinc.

*Keywords:* semenogelins; zinc; immunohistochemistry; AMD; retina

## 1. Introduction

Semenogelin proteins I and II are the major secretory products from the glandular epithelium of the seminal vesicles and the epididymis (Bjartell et al., 1996). Semenogelin I (SgI) is a non-glycosylated protein with a molecular mass of 50 KDa (Lilja et al., 1989; Lilja and Lundwall, 1992). Semenogelin II (SgII) has a molecular mass of 63 KDa (Lilja and Lundwall, 1992); it has a potential site for N-linked glycosylation. Approximately half of the SgII molecules in seminal plasma are glycosylated, yielding two molecular species with an apparent mass difference of 5 KDa (Lilja and Laurell, 1985). Studies have indicated a role of semenogelin proteins (Sgs) related to capacitation and motility of sperm (Robert and Gagnon, 1996; de Lamirande et al., 2001; de Lamirande, 2007). More recently, high $Zn^{2+}$-binding capacity of both SgI and SgII (Jonsson et al., 2005) was demonstrated, suggesting that Sgs might function as important regulators of extracellular $Zn^{2+}$ homeostasis.

Recently, Sgs expression was characterized in non-genital tissues like trachea, bronchi, skeletal muscle cells, and cells in the central nervous system (Lundwall et al., 2002), suggesting additional yet unknown functions for these molecules. Our recent studies of normal human retina showed that both Sgs are found in this tissue (Bonilha et al., 2006).

Earlier clinical trial data found a significant decrease in the progression of age-related macular degeneration (AMD) in individuals supplemented with antioxidants and zinc (Age-Related Eye Disease Study Research Group, 2001; Clemons et al., 2005; Schmidt-Erfurth, 2005). The cellular targets in AMD are the RPE and macular photoreceptors (Penfold et al., 2001). Our observations that Sgs are localized to

---

* Corresponding author. Tel.: +1 216 445 7690; fax: +1 216 445 3670.
*E-mail address:* bonilhav@ccf.org (V.L. Bonilha).

0014-4835/$ - see front matter © 2007 Elsevier Ltd. All rights reserved.
doi:10.1016/j.exer.2007.10.006

photoreceptors and the RPE may point to a function related to the ability of these cells to sequester $Zn^{2+}$ for protection against AMD. In this regard, we decided to define the distribution of Sgs in the eyes from donors with diagnosed AMD.

The purpose of this investigation was to define the distribution of SgI in the eyes from donors with diagnosed AMD and to compare this with the distribution in normal eyes. We found that the content of SgI in the AMD eyes was substantially lower than that observed in the normal retina.

## 2. Material and methods

### 2.1. Human eye tissue

Donor eyes were obtained from the Cleveland Eye Bank or through the Foundation for Fighting Blindness Eye Donor Program (Owings Mills, MD). Tissue from 20 different donors was analyzed. The donor ages varied between 35 and 97. The interval between death and tissue processing varied between 4 and 14 h. The records received from the eye banks stated the donor eyes as AMD and non-AMD. Upon dissection the eyes were imaged and further classified as AMD or not. There were three eyes with GA, two with end-stage AMD displaying fibrovascular scar and the remaining eyes were either stage 2 or 3. Control eyes did not have any drusen in the macular area. The immunocytochemistry and Western analysis are exempts from IRB approval.

### 2.2. Preparation of human RPE and retina lysates

RPE cells were isolated using the protocol initially described (Nakata et al., 2005) with mechanical removal of the retina and brushing of the RPE from the choroid. RPE cells were pelleted down, the PBS was removed and the fresh PBS containing protease inhibitors was added to the cells. The RPE cells were kept at −80 °C until used. When ready to use, RPE lysates were diluted 1:1 with 2× radioimmunoprecipitation buffer (RIPA) (0.2% SDS, 2% Triton-X100, 2% deoxycholate, 0.15 M NaCl, 4 mM EDTA, 50 mM Tris pH 7.4) containing a cocktail of protease and phosphatase inhibitors (Sigma, St. Louis, MO, USA). Pieces of retinas collected from human donor eyes were collected into eppendorff tubes and lysed in 1× RIPA buffer. Cells were lyzed for 1 h at 4 °C in the rotator, centrifuged for 10 min at 14,000 rpm and the supernatants were transferred to clean tubes and the protein concentration was determined using the MicroBCA kit (Pierce Biotechnology, Inc., Rockford, IL) according to the manufacturer's directions.

### 2.3. Western blot analysis of lysates

Forty micrograms of protein of each sample was boiled in SDS sample buffer (62.5 mM Tris−HCl (pH 6.8), 25% glycerol, 0.01% bromophenol blue, and 2% SDS), separated on a 10−20% Novex®-Tris-Glycine gel (Invitrogen Corporation, Carlsbad, CA) and electro-transferred to Immobilon PVDF membranes (Millipore, Bedford, MA) using a Bio-Rad Semi-Dry Electrophoretic Transfer Cell (20 min transfer at 18 V). Positive control was unliquefied seminal fluid in buffer containing 4 M urea. Membranes were incubated with antibodies to SgI (cross reactivity with SgII ∼ 5%) in Blotto A buffer (20 mM Tris/HCl, 0.9% NaCl, 0.05% Tween 20 (TBST), 5% skimmed milk) for 1 h. Protein detection was performed with secondary antibodies conjugated to peroxidase and visualized using chemiluminescence Reagent Plus (NEN™ Life Science Products, Inc., Boston, MA) detection system. PVDF membranes were exposed to film, films were scanned and figures were composed using Adobe Photoshop 5.5.

The gels were stained with Gelcode Blue (Pierce), after partial transfer to PVDF membranes to serve as a reference for the load homogeneity of the samples as previously described (Bando et al., 2007). Briefly, both gel and blot were digitized using a densitometer, and the density of the gel and bands was measured and transferred to pixels using Quantity One 4.2.3. A rectangular area was drawn around the most intense band signal in the scanned blots and used as a template to measure the pixel intensity in each band. A rectangular area was drawn around each gel lanes and used to determine the number of pixels in these areas. Plotted signals represent pixel intensity for each band subtracted from the background signal. The total protein pixel density from each donor lane stained with Gelcode Blue in the transferred gel was quantitated. The previously determined number of pixels in the Western blot was divided by the pixels in the Gelcode Blue lane, and these were then used to establish the pixel count per sample. The average pixel count was determined as a mean of all the AMD and non-AMD samples. Standard deviation, standard error and *t*-test were calculated and are presented in Section 3.

### 2.4. Immunohistology of tissue

To determine the localization of SgI in AMD eyes, immunohistochemical assays were performed using cryo and paraffin sections of human eyes and paraffin section of isolated human Bruch's membrane/choroid in the perimacular area. Eye pieces were cut and fixed by immersion in 4% paraformaldehyde made in PBS for 3 h at 4 °C. For isolated Bruch's membrane-choroid, a 2 × 10-mm strip was isolated from the eyecups as previously described (Bando et al., 2007) and fixed by immersion in 4% formaldehyde freshly prepared from paraformaldehyde in phosphate buffer at pH 7.2 overnight. Non-AMD drusen was isolated from the perimacular area of the eyes while AMD drusen was isolated from the macular area. The isolated Bruch's membrane/choroid with drusen and retinas were then dehydrated through a series of ethanol solutions and embedded in paraffin using an automated tissue processor (Leica Microsystems TP1020, Benneck Burn, IL). Seven- to eight-micrometer sections were cut on a Leica RM2125 microtome (Leica Microsystems) and sections were collected on Superfrost/Plus Slides (Fisher Scientific, Pittsburg, PA). Sections were stretched on the slides on water and adhered to the slides by room temperature incubation overnight followed by 2 h incubation in an HI1210 slide warmer at 60 °C (Fisher Scientific). Prior to labeling, paraffin was removed through two consecutive xylene incubations for 10 min. Next the tissues were gradually re-hydrated by sequential incubation on ethanol 100%, 90%, 70%, 50% and 30% for 5 min each and processed for peroxidase-DAB labeling as previously described (Bonilha et al., 2006). After rehydration to PBS, sections were subjected to heat-mediated antigen retrieval by pressure cooking in 10 mM citric acid buffer, pH 6.0. Sections were probed with previously described rabbit antibodies to SgI in 5% BSA, PBS and 0.3% Triton-X100 overnight at 4 °C (Bjartell et al., 1996; Malm et al., 1996). The controls omitted the antibodies. Sections were washed, incubated with secondary antibody conjugated to biotin for 1 h at RT, washed, and incubated with avidin in PBS for 30 min, then developed with DAB for 2 min. The sections were examined with a Zeiss Axiophot light microscope and the images were digitized using a Hamamatsu CCD camera.

For cryosectioning, eye pieces of retina-RPE-choroid tissue were fixed as described above, quenched with 50 mM $NH_4Cl$ made in PBS for 1 h at 4 °C, infused successively with 15% and 30% sucrose made in the same buffer and with Tissue-Tek "4583" (Miles Inc., Elkhart, IN). Ten- to twelve-micrometer cryosections were cut on a cryostat HM 505E (Microm, Walldorf, Germany) equipped with a CryoJane Tape-Transfer system (Instrumedics, Inc., Hackensack, NJ, USA). For labeling, sections were blocked in PBS supplemented with 0.3 mM $CaCl_2$ + 1 mM $MgCl_2$ + 1% BSA (PBS/CM/BSA) for 30 min, and incubated with the antibodies to SgI. Cell nuclei were labeled with TO-PRO®-3 iodide (Molecular Probes). Secondary antibody (goat anti-rabbit IgG; 1:1000) was labeled with Alexa Fluor 488 (green). Sections were analyzed using a Leica laser scanning confocal microscope (TCS-SP2, Leica, Exton, PA). A series of 1 μm *xy* (*en face*) sections were collected. Each individual *xy* image of the retinas stained represents a three-dimensional projection of the entire cryosection (sum of all images in the stack). Microscopic panels were composed using Adobe Photoshop 5.5 (Adobe, San Jose, CA).

## 3. Results

### 3.1. Immunolocalization of SgI reduced in the retinas of AMD donors

To dissect the molecular localization of SgI in the neural retina of AMD donors, eyes were processed for cryosectioning (Fig. 1A–C) and paraffin embedding (Fig. 1D, E) followed by

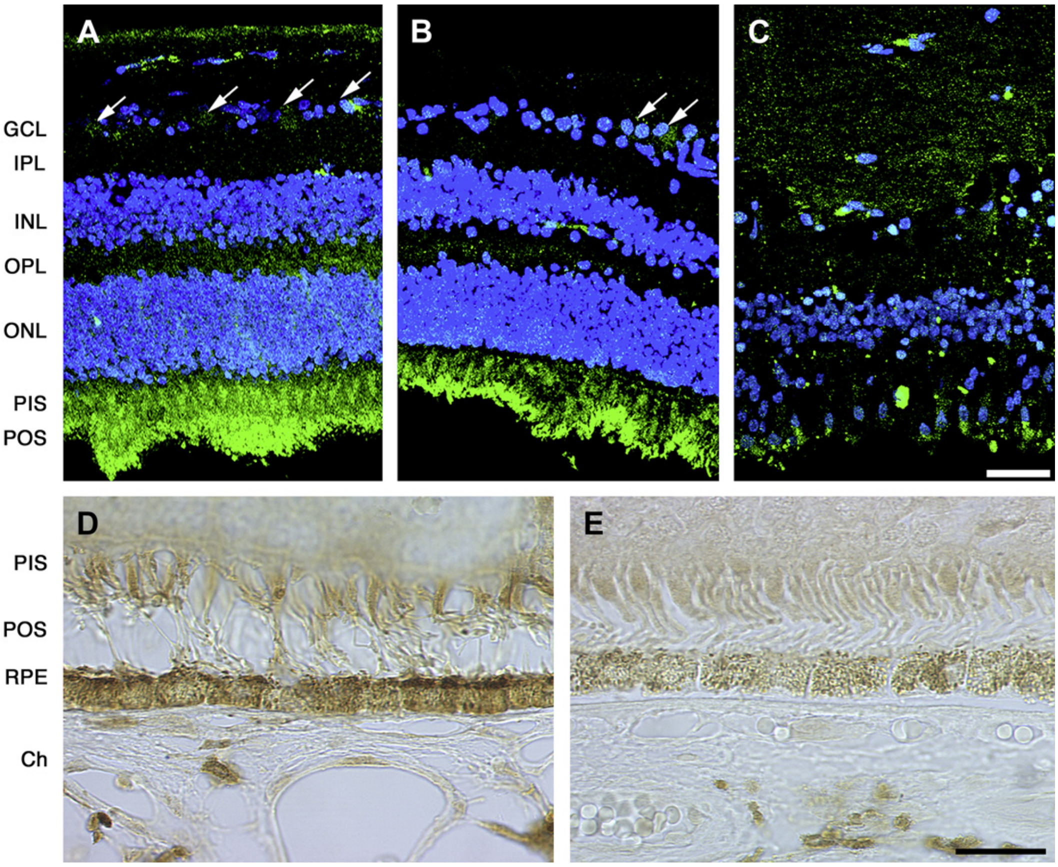

Fig. 1. SgI localization is low in the retinas of AMD donors. SgI staining is significantly reduced in all layers of the AMD retina when compared to the non-AMD eyes. Specifically, reduced labeling was observed in the photoreceptors and RPE cells. Five control and 8 AMD donors were analyzed. Human cryosections of human donors previously diagnosed with AMD (B, C, E,) and non-AMD eyes (A, D) were probed with SgI antibody in 5% BSA, PBS and 0.3% Triton-X100 overnight at 4 °C. Sections were washed, incubated with fluorophore-conjugated (A–C) or peroxidase-conjugated (D, E) secondary antibody. The controls (not shown) were omitted the antibodies and did not display any labeling. Non-AMD control retinas displayed SgI in the choroid, RPE, photoreceptor cells, cells in the inner nuclear layer, and ganglion cell layer, while in the AMD retinas SgI was mostly confined to the photoreceptor cells (B). Ch, choroid; RPE, retinal pigment epithelium; PIS, photoreceptor inner segments; POS, photoreceptor outer segments; ONL, outer nuclear layer; OPL, outer plexiform layer; INL, inner nuclear layer; IPL, inner plexiform layer; GCL, ganglion cell layer. Arrows, ganglion cells; bars: (A–C), 40 μm; (D, E), 200 μm.

immunohistochemistry. The distribution of SgI was analyzed both in the retinal perimacular area of non-AMD human donors (Fig. 1A, D) and in the retinas of human donors previously diagnosed with AMD (Fig. 1B, C, E). Analysis of the AMD eye sections showed that SgI immunoreactivity is significantly reduced in all layers of the retina when compared to the non-AMD eye sections. Specifically, reduced labeling was still observed in the ganglion cells and photoreceptors inner and outer segments of the AMD eyes (Fig. 1B, C). The SgI labeling was almost completely abolished from end-stage AMD retinas with fibrovascular scar (Fig. 1C). Due to the high autofluorescence levels in the RPE/choroid layer these cells were analyzed by DAB reaction (Fig. 1D and E). A significant decrease in the SgI labeling of the RPE from AMD retinas (Fig. 1E) was observed when compared to the non-AMD control RPE (Fig. 1D).

### *3.2. Immunolocalization of SgI is decreased in the drusen of AMD donors*

It is accepted that the pathogenesis of AMD involves changes of the RPE/Bruch's membrane and underlying choriocapillaris. To further understand the molecular localization of SgI we analyzed the immunoreactivity of SgI in the Bruch's membrane/choroid of AMD samples. Comparison of the AMD samples (Fig. 2F) showed that SgI staining is significantly reduced in the drusen from the AMD donor when compared to the non-AMD eyes (Fig. 2B). Control sections (Fig. 2A and E) had the antibodies omitted. Drusen and Bruch's membrane are characterized by autofluorescence when observed in an epifluorescence microscope, in the FITC channel. This property was used to confirm drusen presence in Bruch's membrane as shown in Fig. 2 (C, D, G, H).

### *3.3. SgI expression is decreased in the retina lysates of AMD donors*

The differences in levels of expression of Sgs within the AMD and non-AMD retinas were addressed by Western analysis. Whole retina lysates were harvested, resolved in an SDS-PAGE and transferred to a membrane and reacted with SgI antibody (Fig. 3). Western blot using anti-SgI antibody revealed greater immunoreactivity in non-AMD (Fig. 3B, lanes 1–4) than in AMD retinas (Fig. 3B, lanes 5–8). After partial transfer to PVDF membranes the gels were stained with Gelcode blue to serve as a reference for the load homogeneity of the samples (Fig. 3A). Immunoblots of retina lysates obtained from AMD donor eyes demonstrated a significant decrease in SgI levels. Quantitation of these blots showed that SgI immunoreactivity was downregulated 3.7-fold lower in AMD samples when compared with non-AMD samples. These differences were statistically significant ($p < 0.0056$) (Fig. 3C).

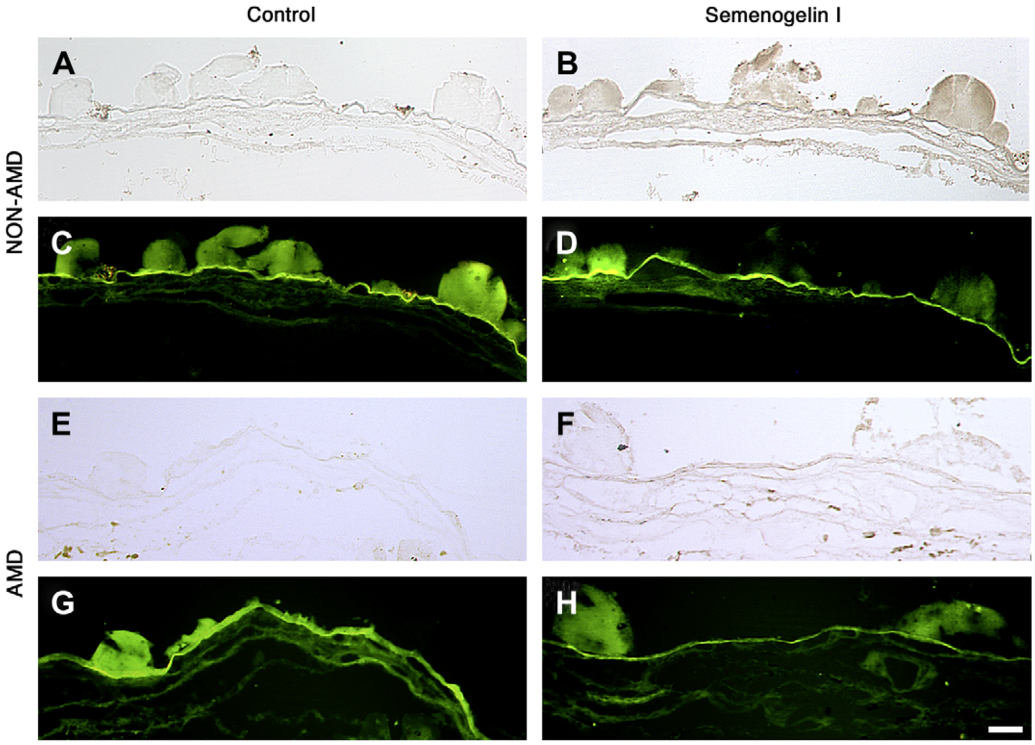

Fig. 2. SgI localization is low in the drusen of AMD donors. SgI staining is significantly reduced in the drusen from the AMD donors. Eight-micrometer paraffin sections of isolated Bruch's membrane and choroid from a human donor previously diagnosed with AMD (E–H) and non-AMD eyes (A–D) were probed with SgI antibody in 5% BSA, PBS and 0.3% Triton-X100 overnight at 4 °C. Sections were washed, incubated with secondary antibody, conjugated to biotin for 1 h at RT, washed, and incubated with avidin in PBS for 30 min, then developed with DAB for 2 min. The controls (A, C, E, G) were omitted the antibodies and did not display any labeling. The sections were examined in bright field (A, B, E, F) or FITC channel (C, D, G, H). Observation of the samples in the FITC channel revealed the autofluorescence of the Bruch's membrane and drusen. Five control and 8 AMD donors were analyzed. Bar, 200 μm.

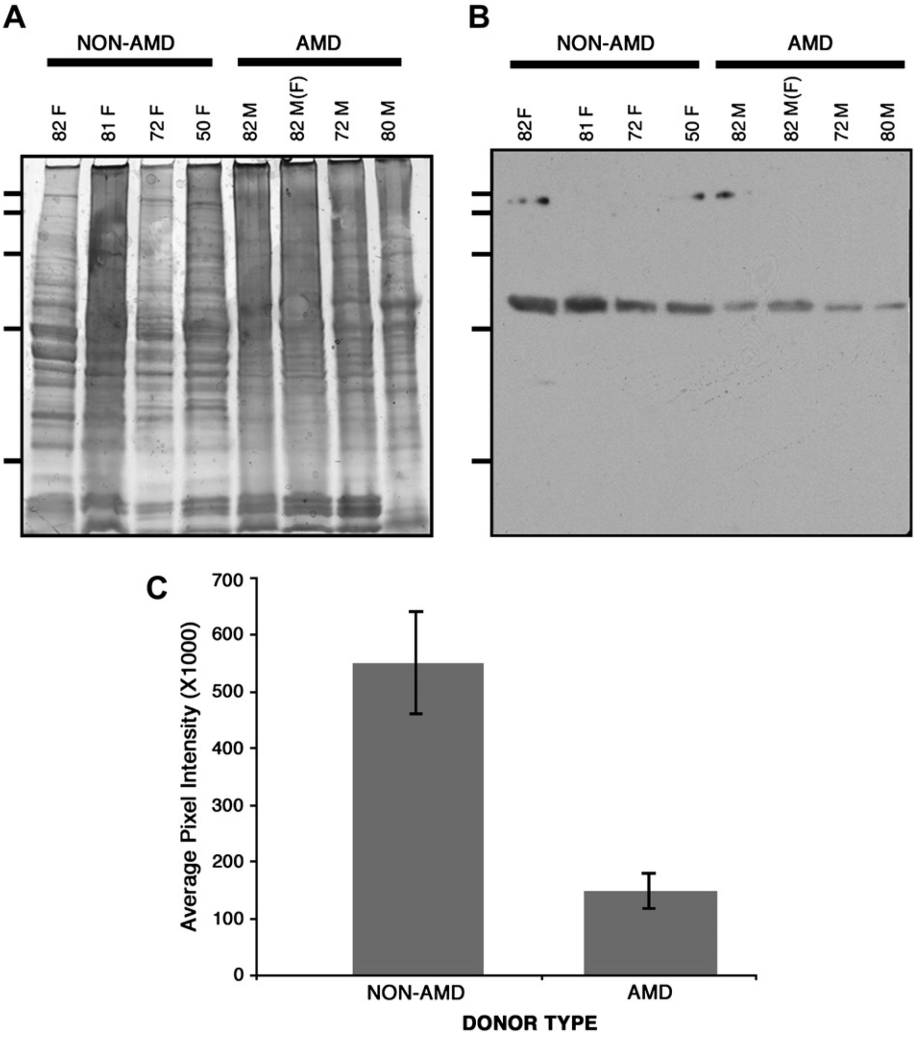

Fig. 3. SgI expression is low in the retinas of AMD donors. Retinas from several human donors (9 control and 9 AMD donors) previously diagnosed with AMD and non-AMD samples were harvested, lysed in RIPA buffer (150 mM NaCl, 25 mM Tris, pH 7.4, 2 mM EDTA, 1% Triton X-100, 1% deoxycholate, 0.1% SDS) supplemented with 1 mM PMSF, protease and phosphatase cocktail inhibitors (SIGMA). Forty micrograms of protein of each sample was separated on a 10–20% SDS gel, transferred to PVDF membranes and probed with antibodies specific to SgI followed by ECF detection of immunoreactivity (B). The gels were stained with Gelcode blue after partial transfer to PVDF membranes to serve as a reference for the load homogeneity of the samples (A). The age and gender of the donors are indicated on top of each lane; all donors were caucasians. Membranes were exposed to film, and films were scanned. In (C), a rectangular area was drawn around the most intense band signal and used as a template to measure the signal intensity in each band using the volume analysis report macro from Quantity One 4.2.3. Plotted signals represent mean pixel intensity for AMD and non-AMD samples ± error bars. SgI immunoreactivity was approximate 3.7-fold lower in AMD samples compared with non-AMD samples ($p < 0.0056$ by Student's *t*-test). (F) in sample 82M denotes the fovea of that donor.

### *3.4. SgI is decreased in RPE lysates from AMD donors*

The differences in levels of expression of Sgs within the AMD and non-AMD RPE were addressed by Western analysis. RPE lysates were harvested, resolved in an SDS-PAGE and transferred to a membrane and reacted with SgI antibody (Fig. 4). Western blot using anti-SgI antibody revealed greater immunoreactivity in non-AMD (Fig. 4B) than in AMD retinas (Fig. 4D). Immunoblots of RPE lysates obtained from AMD donor eyes demonstrated a significant decrease in SgI levels. Quantitation of these blots showed that SgI immunoreactivity was downregulated 5.6-fold lower in AMD samples compared with non-AMD samples (Fig. 4E). These differences were statistically significant ($p < 0.0001$).

It is important to notice that both the Western blot analysis and the immunohistochemistry analysis indicated higher levels of immunoreactivity present in non-AMD than in the AMD tissues.

## 4. Discussion

For many years, Sg was believed to be present only in the male genital tract and to originate exclusively from seminal vesicles (Robert and Gagnon, 1996). However, with time and the development of more sensitive methods, the presence of SgI and SgII transcripts was demonstrated in several tissues throughout the human body as well as in several malignant tissues and cell lines (Hienonen et al., 2005; Lundwall et al.,

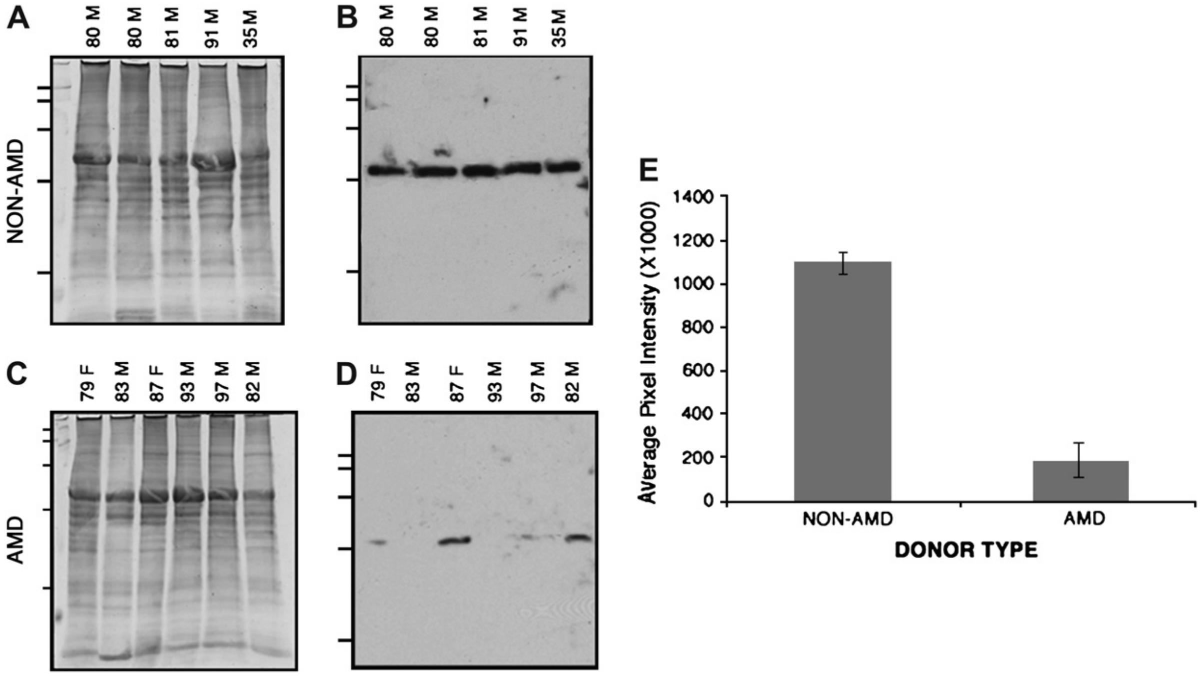

Fig. 4. SgI is significantly lower in RPE lysates from AMD donors. RPE lysates from several human donors (9 control and 9 AMD donors) previously diagnosed with AMD and non-AMD samples were harvested, lysed in RIPA buffer (150 mM NaCl, 25 mM Tris, pH 7.4, 2 mM EDTA, 1% Triton X-100, 1% deoxycholate, 0.1% SDS) supplemented with 1 mM PMSF, protease and phosphatase cocktail inhibitors (SIGMA). Forty micrograms of protein of each sample was separated on a 10–20% SDS gel, transferred to PVDF membranes and probed with antibodies specific to SgI followed by ECF detection of immunoreactivity (B, D). The gels were stained with Gelcode blue after partial transfer to PVDF membranes to serve as a reference for the load homogeneity of the samples (A, C). The age and gender of the donors are indicated on top of each lane; all donors were caucasians. Membranes were exposed to film, and films were scanned. In (E), a rectangular area was drawn around the most intense band signal and used as a template to measure the signal intensity in each band using the volume analysis report macro from Quantity One 4.2.3. Plotted signals represent mean pixel intensity for AMD and non-AMD samples ± error bars. SgI immunoreactivity was approximate 5.6-fold lower in AMD samples compared with non-AMD samples ($p < 0.0001$ by Student's *t*-test).

2002; Rodrigues et al., 2001; Zhang et al., 2003). Recently, we have shown the presence of both SgI and SgII in human retina and RPE lysates. Moreover, the Sgs distribution in the human eye tissues was associated with the choroid, RPE, photoreceptor cells, cells in the inner nuclear layer, and ganglion cell layer. In the photoreceptor cells, Sgs were observed in the inner and outer segments of both cones and rods and in the IPM (Bonilha et al., 2006). In the present study, we confirmed the presence of SgI in the retina of both non-AMD and AMD eyes. However, a significant decrease in the labeling of SgI was observed throughout the retina in the ganglion cell layer, cells in the inner nuclear layer, the photoreceptors, RPE and choroid of the AMD donor eyes. It was recently reported that both SgI and II display high $Zn^{2+}$-binding capacity (Jonsson et al., 2005), suggesting that Sgs might function as important regulators of extracellular $Zn^{2+}$ homeostasis. Our data suggest a possible function related to the ability of photoreceptors and RPE cells to sequester $Zn^{2+}$ for protection against disease progression in AMD. Another possibility could be that the Sgs function as extracellular storage reservoirs of $Zn^{2+}$, wherefrom it could be easily and rapidly mobilized for various purposes. Low Sg levels in AMD, whether due to increased catabolism or decreased synthesis, could then perhaps be compensated for by increasing the daily intake of $Zn^{2+}$.

Zinc is the second most abundant trace element in the human body and the most abundant in the eye where it plays a key role in the metabolism of the retina (Karcioglu, 1982). A randomized, placebo-controlled two years clinical trial showed that zinc supplementation reduced the risk of AMD development (Newsome et al., 1988). This early report was supported by the Age-Related Eye Disease Study (AREDS) clinical trial that found that long-term (~6 years) intake of zinc, alone or with antioxidants, significantly decreased the progression of AMD and reduced the rate of moderate vision loss in individuals (Age-Related Eye Disease Study Research Group, 2001; Clemons et al., 2005; Schmidt-Erfurth, 2005) suggesting that zinc deficiency is a suspected risk for AMD. The cellular targets in AMD are the RPE and macular photoreceptors (Penfold et al., 2001). Photoreceptors and RPE specifically were shown to be affected in $Zn^{2+}$ deficiency assays (Leure-duPree and McClain, 1982; Miceli et al., 1999). Moreover, studies on human eyes showed a correlation between low cytoplasmic $Zn^{2+}$ concentrations in RPE cells and signs of AMD (Newsome et al., 1994). Our observations showed that SgI is significantly reduced but still observed in AMD photoreceptors and RPE cells. Further studies are necessary to understand if Sgs expression is correlated to the $Zn^{2+}$ level in AMD retinas.

The formation of lipid and protein rich sub-RPE deposits, found both in the periphery and macula, has been suggested to be a risk factor in AMD. In the present study, we failed to detect SgI in drusen from AMD donors using our SgI antibody. However, SgI was recently identified in senile seminal vesicle amyloid, a common gender-specific localized form of fibril-related pathology found in older men (Linke et al., 2005). This same study has shown that SgI rendered amyloidogenic as a consequence of aging is only detected by a new SgI-reactive antibody but not by several SgI common antibodies. Amyloid β has been identified in AMD drusen (Anderson et al., 2004; Yoshida et al., 2005). A consequence of the low Sgs levels could be that $Zn^{2+}$ binds to other extracellular proteins such as beta-amyloid, complement factor H, serum albumin and crystallins, known to bind $Zn^{2+}$ (Lengyel et al., 2007). This new interaction might lead to the accumulation of $Zn^{2+}$ in sub-RPE deposits. Future studies will address if age-related amyloid SgI is present in AMD drusen and its role in AMD pathology.

In conclusion, we report here a significant decrease in SgI content in the retina, RPE and Bruch's membrane/choroid of AMD donors.

## Acknowledgements

Supported by NIH grants EY017153, EY014240, a Research Center grant from the Foundation Fighting Blindness, a Challenge Grant from Research to Prevent Blindness, and an NEI infrastructure grant (EY015638).

## References

Age-Related Eye Disease Study Research Group, 2001. A randomized, placebo-controlled, clinical trial of high-dose supplementation with vitamins C and E, beta carotene, and zinc for age-related macular degeneration and vision loss: AREDS Report No. 8. Arch. Ophthalmol. 119, 1417–1436.

Anderson, D.H., Talaga, K.C., Rivest, A.J., Barron, E., Hageman, G.S., Johnson, L.V., 2004. Characterization of β amyloid assemblies in drusen: the deposits associated with aging and age-related macular degeneration. Exp. Eye Res. 78, 243–256.

Bando, H., Shadrach, K.G., Rayborn, M.E., Crabb, J.W., Hollyfield, J.G., 2007. Clathrin and adaptin accumulation in drusen, Bruch's membrane and choroid in AMD and non-AMD donor eyes. Exp. Eye Res. 84, 135–142.

Bjartell, A., Malm, J., Moller, C., Gunnarsson, M., Lundwell, A., Lilja, H., 1996. Distribution and tissue expression of semenogelin I and II in man as demonstrated by in situ hybridization and immunocytochemistry. J Androl. 17, 17–26.

Bonilha, V.L., Rayborn, M.E., Shadrach, K.G., Lundwall, A., Malm, J., Bhattacharya, S.K., Crabb, J.W., 2006. Characterization of semenogelin proteins in the human retina. Exp. Eye Res. 83, 120–127.

Clemons, T.E., Milton, R.C., Klein, R., Seddon, J.M., Ferris 3rd, F.L., 2005. Risk factors for the incidence of Advanced Age-Related Macular Degeneration in the Age-Related Eye Disease Study (AREDS) AREDS report no. 19. Ophthalmology 112, 533–539.

Hienonen, T., Sammalkorpi, H., Enholm, S., Alhopuro, P., Barber, T.D., Lehtonen, R., Nupponen, N.N., Lehtonen, H., Salovaara, R., Mecklin, J.P., Jarvinen, H., Koistinen, R., Arango, D., Launonen, V., Vogelstein, B., Karhu, A., Aaltonen, L.A., 2005. Mutations in two short noncoding mononucleotide repeats in most microsatellite-unstable colorectal cancers. Cancer Res. 65, 4607–4613.

Jonsson, M., Linse, S., Frohm, B., Lundwall, A., Malm, J., 2005. Semenogelins I and II bind zinc and regulate the activity of prostate-specific antigen. Biochem. J. 387, 447–453.

Karcioglu, Z.A., 1982. Zinc in the eye. Surv. Ophthalmol. 27, 114–122.

de Lamirande, E., 2007. Semenogelin, the main protein of semen coagulum, regulates sperm function. Semin. Thromb. Hemost. 33, 60–68.

de Lamirande, E., Yoshida, K., Yoshiike, T.M., Iwamoto, T., Gagnon, C., 2001. Semenogelin, the main protein of semen coagulum, inhibits human sperm capacitation by interfering with the superoxide anion generated during this process. J. Androl. 22, 672–679.

Lengyel, I., Flinn, J.M., Peto, T., Linkous, D.H., Cano, K., Bird, A.C., Lanzirotti, A., Frederickson, C.J., van Kuijk, F.J.G.M., 2007. High concentration of zinc in sub-retinal pigment epithelial deposits. Exp. Eye Res. 84, 772–780.

Leure-duPree, A.E., McClain, C.J., 1982. The effect of severe zinc deficiency on the morphology of the rat retinal pigment epithelium. Invest. Ophthalmol. Vis. Sci. 23, 425–434.

Lilja, H., Abrahamsson, P.A., Lundwall, A., 1989. Semenogelin, the predominant protein in human semen. Primary structure and identification of closely related proteins in the male accessory sex glands and on the spermatozoa. J. Biol. Chem. 264, 1894–1900.

Lilja, H., Laurell, C.B., 1985. The predominant protein in human seminal coagulate. Scand. J. Clin. Lab. Invest. 45, 635–641.

Lilja, H., Lundwall, A., 1992. Molecular cloning of epididymal and seminal vesicular transcripts encoding a semenogelin-related protein. Proc. Natl. Acad. Sci. U.S.A. 89, 4559–4563.

Linke, R.P., Joswig, R., Murphy, C.L., Wang, S., Zhou, H., Gross, U., Rocken, C., Westermark, P., Weiss, D.T., Solomon, A., 2005. Senile seminal vesicle amyloid is derived from semenogelin I. J. Lab. Clin. Med. 145, 187–193.

Lundwall, A., Bjartell, A., Olsson, A.Y., Malm, J., 2002. Semenogelin I and II, the predominant human seminal plasma proteins, are also expressed in non-genital tissues. Mol. Hum. Reprod. 8, 805–810.

Malm, J., Hellman, J., Magnusson, H., Laurell, C.B., Lilja, H., 1996. Isolation and characterization of the major gel proteins in human semen, semenogelin I and semenogelin II. Eur. J. Biochem. 238, 48–53.

Miceli, M.V., Tate Jr., D.J., Alcock, N.W., Newsome, D.A., 1999. Zinc deficiency and oxidative stress in the retina of pigmented rats. Invest. Ophthalmol. Vis. Sci. 40, 1238–1244.

Nakata, K., Crabb, J.W., Hollyfield, J.G., 2005. Crystallin distribution in Bruch's membrane-choroid complex from AMD and age-matched donor eyes. Exp. Eye Res. 80, 821–826.

Newsome, D.A., Swartz, M., Leone, N.C., Elston, R.C., Miller, E., 1988. Oral zinc in macular degeneration. Arch. Ophthalmol. 106, 192–198.

Newsome, D.A., Tate Jr., D.J., Alcock, N.W., Oliver, P.D., 1994. Zinc content of human retinal pigment epithelium (RPE) declines with age. Invest. Ophthalmol. Vis. Sci. 35 (Suppl), 1768.

Penfold, P.L., Madigan, M.C., Gillies, M.C., Provis, J.M., 2001. Immunological and aetiological aspects of macular degeneration. Prog. Retin. Eye Res. 20, 385–414.

Robert, M., Gagnon, C., 1996. Purification and characterization of the active precursor of a human sperm motility inhibitor secreted by the seminal vesicles: identity with semenogelin. Biol. Reprod. 55, 813–821.

Rodrigues, R.G., Panizo-Santos, A., Cashel, J.A., Krutzsch, H.C., Merino, M.J., Roberts, D.D., 2001. Semenogelins are ectopically expressed in small cell lung carcinoma. Clin. Cancer Res. 7, 854–860.

Schmidt-Erfurth, U., 2005. Nutrition and retina. Dev. Ophthalmol. 38, 120–147.

Yoshida, T., Ohno-Matsui, K., Ichinose, S., Sato, T., Iwata, N., Saido, T.C., Hisatomi, T., Mochizuki, M., Morita, I., 2005. The potential role of amyloid β in the pathogenesis of age-related macular degeneration. J. Clin. Invest. 115, 2793–2800.

Zhang, Y., Wang, Z., Liu, H., Giles, F.J., Lim, S.H., 2003. Pattern of gene expression and immune responses to Semenogelin 1 in chronic hematologic malignancies. J Immunother. 26, 461–467.

THE JOURNAL OF BIOLOGICAL CHEMISTRY Vol. 280, No. 7, Issue of February 18, pp. 6080–6084, 2005
*Printed in U.S.A.*

# Proteomics Reveal Cochlin Deposits Associated with Glaucomatous Trabecular Meshwork*Ⓢ

Received for publication, September 30, 2004, and in revised form, November 23, 2004
Published, JBC Papers in Press, December 3, 2004, DOI 10.1074/jbc.M411233200

**Sanjoy K. Bhattacharya‡§, Edward J. Rockwood‡, Scott D. Smith‡, Vera L. Bonilha‡, John S. Crabb‡, Rachel W. Kuchtey‡, Nahid G. Robertson¶, Neal S. Peachey‡‖, Cynthia C. Morton¶, and John W. Crabb‡****

*From the ‡Cole Eye Institute and **Lerner Research Institute, Cleveland Clinic Foundation, Cleveland, Ohio 44195, ¶Brigham and Women's Hospital, Harvard Medical School, Boston, Massachusetts 02115, and ‖Louis Stokes Veterans Affairs Medical Center, Cleveland, Ohio 44106*

**The etiology of primary open angle glaucoma, a leading cause of age-related blindness, remains poorly defined, although elevated intraocular pressure (IOP) contributes to the disease progression. To better understand the mechanisms causing elevated IOP from aqueous humor circulation, we pursued proteomic analyses of trabecular meshwork (TM) from glaucoma and age-matched control donors. These analyses demonstrated that Cochlin, a protein associated with deafness disorder *DFNA9*, is present in glaucomatous but absent in normal TM. Cochlin was also detected in TM from the glaucomatous DBA/2J mouse preceding elevated IOP but found to be absent in three other mouse lines that do not develop elevated IOP. Histochemical analyses revealed co-deposits of Cochlin and mucopolysaccharide in human TM around Schlemm's canal, similar to that observed in the cochlea in *DFNA9* deafness. Purified Cochlin was found to aggregate after sheer stress and to induce the aggregation of TM cells *in vitro*. Age-dependent *in vivo* increases in Cochlin were observed in glaucomatous TM, concomitant with a decrease in type II collagen, suggesting that Cochlin may disrupt the TM architecture and render components like collagen more susceptible to degradation and collapse. Overall, these observations suggest that Cochlin contributes to elevated IOP in primary open angle glaucoma through altered interactions within the TM extracellular matrix, resulting in cell aggregation, mucopolysaccharide deposition, and significant obstruction of the aqueous humor circulation.**

---

Glaucoma encompasses a group of blinding diseases classified generally as primary, for which there is no known etiology, or as secondary, in which a previous illness or injury is contributory. Primary open angle glaucoma (POAG)[1] is the most common form of the disease, affecting 3 million Americans and over 70 million people worldwide (1). Vision loss in most but not all glaucoma cases is related to an increase in intraocular pressure (IOP) with subsequent damage to the optic nerve. The molecular basis of the pathology is understood poorly, but the risk for POAG clearly increases with age, and ethnicity plays a role (*e.g.* blacks exhibit a higher incidence of POAG than whites and at an earlier age of onset). Although specific genes have been implicated in glaucoma pathology, including for example, *TIGR* and its gene product of unknown function, myocilin, genetic studies to date remain inconclusive regarding glaucoma disease mechanisms (2).

Elevated IOP typically develops into glaucoma as a result of impeded aqueous humor outflow (3). Aqueous humor is actively produced by the ciliary epithelium in the posterior chamber of the eye and circulates through the pupil to the anterior chamber where it drains through the trabecular meshwork (TM) into Schlemm's canal and the episcleral veins (4). Resistance to outflow occurs commonly in the TM, which has a complex extracellular matrix (ECM) composed of collagen beams lined with endothelium-like cells (5, 6). The mechanisms of resistance are not known; however, the pseudoendothelial cells in the TM produce a mucopolysaccharide (MPS) (7) that appears to function in attracting macrophages for phagocytic self-cleaning of the TM (8). A loss of control of MPS levels in the TM appears to disrupt the self-cleaning process and can result in large changes in IOP (9). In other sensory systems, MPS deposits in the cochlea have been associated with the late onset and progressive auditory and vestibular disorder *DFNA9*, which involves increased intracranial pressure (10, 11). Drugs for treating POAG slow the disease progression by reducing aqueous production or by increasing aqueous outflow but do not provide a cure. Trabeculectomy is the most common treatment of last resort for POAG and involves the surgical removal of a small amount of TM tissue and redirection of the aqueous flow through the conjunctiva to the episcleral vessels. To better understand the molecular mechanisms involved in glaucoma and specifically in the blockage of aqueous outflow, we initiated a classical proteomics study to compare the protein composition of glaucomatous TM obtained by trabeculectomy with that of normal TM. Here we present evidence that Cochlin, a protein associated with the auditory disorder *DFNA9*, is absent in

---

* This work was supported by the National Glaucoma Research Program of American Health Assistance Foundation (to S. K. B.), National Institutes of Health Grants DC03402 (to C. C. M.) and EY6603, EY14239, and EY015638 (to J. W. C.), a Merit Award from the Department of Veterans Affairs (to N. S. P.), a Research Center Grant from The Foundation Fighting Blindness (to J. W. C.), and funds from the Cleveland Clinic Foundation (to J. W. C.). The costs of publication of this article were defrayed in part by the payment of page charges. This article must therefore be hereby marked "*advertisement*" in accordance with 18 U.S.C. Section 1734 solely to indicate this fact.

Ⓢ The on-line version of this article (available at http://www.jbc.org) contains supplemental Table I and Figs. 1 and 2.

§ To whom correspondence should be addressed: Cole Eye Institute (i31), Cleveland Clinic Foundation, Cleveland, OH 44195. Tel.: 216-445-0676; Fax: 216-445-3670; E-mail: bhattas@ccf.org.

[1] The abbreviations used are: POAG, primary open angle glaucoma; IOP, intraocular pressure; TM, trabecular meshwork; ECM, extracellular matrix; MPS, mucopolysaccharide; LC, liquid chromatography; MS/MS, tandem mass spectrometry; TRITC, tetramethylrhodamine isothiocyanate; HA, hemagglutinin; FCH, factor C homology; VWFA, von Willebrand factor A; EST, expressed sequence tag; PBS, phosphate-buffered saline.

normal TM but increases with age in glaucomatous TM in association with MPS deposits.

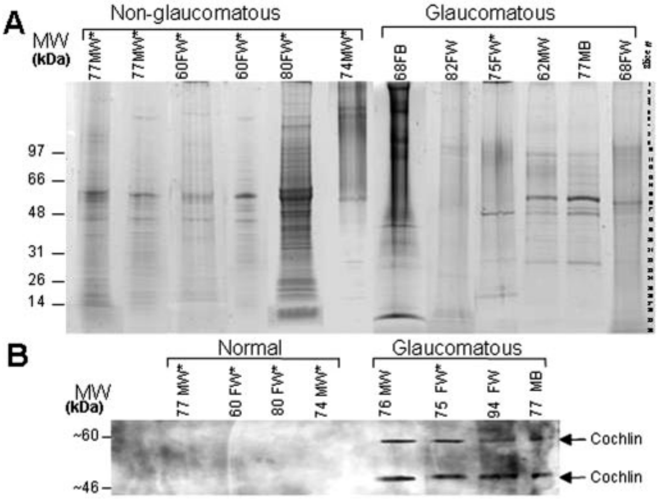

FIG. 1. **SDS-PAGE and Cochlin Western analysis.** *A*, SDS-PAGE is shown of human TM protein (~10 $\mu$g/lane) from POAG (*Glaucomatous*) and normal (*Non-glaucomatous*) donors (Coomassie Blue staining). Gel slices were excised as indicated by slice number, and proteins were identified by LC MS/MS (see supplemental Table I). *B*, representative Western analyses are shown with polyclonal chicken anti-Cochlin of protein extracts from human TM demonstrating the presence of ~60- and ~46-kDa Cochlin isoforms (*arrows*) in glaucomatous tissues. Donor age, gender, and race are indicated in *A* and *B* (*M*, male; *F*, female; *W*, Caucasian; *B*, black). *, cadaver tissue; all other tissues are from trabeculectomy.

## EXPERIMENTAL PROCEDURES

*Tissue Procurement*—Human eyes from 35 normal donors and 5 POAG donors, all between 40 and 85 years of age, were used in this study, and were obtained through the Cleveland Eye Bank. Eyes were enucleated within 12 h of death and stored at −80 °C until TM tissue was isolated by dissection. Normal control eyes were from donors with no visual field defects, no evidence of glaucoma, and without central nervous system abnormalities. Fixed human TM tissues used for immunohistochemistry were obtained from the Eye Donor Program of the Foundation Fighting Blindness (Owings Mills, MD). Glaucomatous eyes and tissues were from clinically documented POAG donors. Glaucomatous TM tissues (~1–2 mm$^3$) were obtained by trabeculectomy from 30 POAG patients in the Cole Eye Institute, Cleveland Clinic Foundation, with institutional review board approval. Human tissue obtained by trabeculectomy consisted predominantly of TM, but possible contamination with small amounts of surrounding tissue (*e.g.* sclera) cannot be excluded. TM cells for cell culture were isolated from the rim tissue associated with corneas used for transplantation at the Cole Eye Institute and were obtained from healthy human eyes within 3 h of death and stored until use in Optisol-GS medium (Chiron Vision, Clairmont, CA).

Adult mice from inbred strains DBA/2J, BALBc/ByJ, CD1, and C57BL/6J were obtained from The Jackson Laboratory (Bar Harbor, ME) and bred in the Cole Eye Institute animal facility. TM samples were obtained surgically following sacrifice with carbon dioxide using animal procedures approved by the Institutional Animal Care and Use Committee of the Cleveland Clinic Foundation.

*Protein Analyses*—TM tissue from cadaver and trabeculectomy samples was extracted by homogenization in 100 mM Tris-Cl buffer, pH 7.8, containing 5 mM dithiothreitol, 1 mM $SnCl_2$, 50 mM $NaHPO_4$, 1 mM diethylenetriaminepentaacetic acid, 100 mM butylated hydroxy toluene, and 0.5% SDS. Insoluble material was removed by centrifugation ($8000 \times g$ for 5 min), and soluble protein was quantified by the Bradford assay (12), yielding ~15–20 $\mu$g of total soluble protein/trabeculectomy tissue sample (~1–2 mm$^3$). Protein extracts were subjected to SDS-PAGE on 4–15% gradient gels (Bio-Rad), and the gels were used either for mass spectrometric proteomic analyses or for Western analyses (13). For protein identifications, gel slices were excised and digested *in situ* with trypsin, and peptides were analyzed by liquid chromatography electrospray tandem mass spectrometry using a CapLC system and a quadrupole time-of-flight mass spectrometer (QTOF2, Waters Corp., Milford, MA). Protein identifications from MS/MS data utilized the ProteinLynx$^{TM}$ Global Server (Waters Corp.) and Mascot (Matrix Science) search engines and the Swiss Protein and NCBI protein sequence data bases (13, 14). Western analysis on a polyvinylidene difluoride membrane utilized established protocols (13) and chicken polyclonal antibody against human Cochlin (at ~5 $\mu$g/ml) (15), mouse monoclonal anti-collagen II, and anti-glyceraldehyde-3-phosphate dehydrogenase (Chemicon International, Temecula, CA). For quantitative Western analyses, anti-mouse secondary antibody linked to 700 nm IR dye and anti-chicken secondary antibody coupled to 800 nm IR dye were used with analyses on an Odyssey infrared imaging system according to the manufacturer's instructions (Li-Cor Biosciences, Lincoln, NE).

*Histochemical Analyses*—Immunohistochemical analyses to localize Cochlin in ocular tissue were performed with cadaver eyes enucleated within 8 h of death and fixed immediately with calcium acetate-buffered 4% *para*-formaldehyde. Paraffin-embedded tissue was blocked and sectioned (12 $\mu$m) in 5% BlokHen (Aves Labs, Inc., Tigard, OR) in phosphate-buffered saline, then incubated overnight with 10 ng of anti-Cochlin antibody (15) at 4 °C and subsequently with 10 ng of rhodamine-conjugated secondary antibody (Jackson ImmunoResearch Laboratories, Inc., West Grove, PA) for 1 h at room temperature. Sections were sealed with Vectashield and analyzed with a Nikon EFD-3 fluorescence microscope attached to a charge-coupled device camera. Movat's pentachrome staining for MPS was performed on multiple sections from each donor tissue according to a published protocol (16). Ten donor tissues each for control and glaucomatous TM were examined, with alternate sections used for Movat's staining and immunohistochemistry. To ensure identical processing and uniform exposure, control and glaucomatous sections were examined side by side on the same slide. For confocal immunohistochemistry, 12-$\mu$m paraffin-embedded sections were labeled with antibodies specific to Cochlin and with a secondary antibody coupled to TRITC (red) and then analyzed using a Leica laser scanning confocal microscope (TCS-SP2, Leica, Exton, PA). A series of 1-$\mu$m thick *x-y* (*en face*) images were collected and added to obtain an image representing a three-dimensional projection of the entire 12-$\mu$m section. Confocal microscopic panels were composed using Adobe Photoshop 5.5.

*Aggregation Assays*—TM cells, from rim tissue associated with healthy corneas used for transplantation, were isolated for *in vitro* assays by dissection and extracellular matrix digestion (17). TM primary cell cultures were established in Dulbecco's modified Eagle's medium containing 10% bovine serum, 50 units/ml penicillin G sodium, and 50 $\mu$g/ml streptomycin sulfate (Invitrogen). For the aggregation assay, approximately 3000 cells were seeded in 4-well plates (35-mm wells, BD Biosciences) and grown for 5–7 days at 37 °C in humidified air containing 5% $CO_2$. The cells were washed with PBS, the PBS was aspirated, and then the cells were treated with 5 $\mu$g of either purified recombinant Cochlin or purified recombinant Notch produced in COS-7 cells or with an equal volume of medium from empty vector-transfected COS-7 cells after HA-affinity fractionation. To evaluate whether antibody could neutralize the observed cell aggregation, Cochlin (5 $\mu$g) was preincubated for 30 min with either 20 $\mu$g of polyclonal chicken anti-Cochlin or nonspecific chicken IgG (Immun System, Uppsala, Sweden), and then the mixture was used to treat the primary TM cells in an identical manner. After 2 min, Dulbecco's modified Eagle's medium with 10% bovine serum was added, and cells were further incubated for 24–36 h as above. Cells were examined with an inverted microscope (model IM 35, Zeiss) and photographed using the Pix Cell II microscope system (Arcturus, Mountain View, CA) equipped with an Olympus camera, an Hitachi digital converter/Sony visual screen, and a Dell Oph Plex GX 110 computer. Recombinant Cochlin and recombinant Notch-1 were produced in COS-7 cells with 3-HA and 4-HA epitope tags, respectively, using the pcDNA 3.0 vector and SuperFect transfection reagent (Qiagen, Valencia, CA) (18, 19). The proteins were affinity-purified from the media of transiently transfected COS-7 cells using rabbit anti-HA antibody (Y-11, Santa Cruz Biotechnology, Inc., Santa Cruz, CA) coupled to protein A-agarose beads with dimethyl pimelimidate. Purified recombinant Cochlin was subjected to sheer stress by passing the protein (5 $\mu$g) through a Hamilton syringe (50 $\mu$l) five times in 50 mM Tris-Cl, pH 7.5, 125 mM NaCl, and 0.1% genapol and then was analyzed by non-reducing SDS-PAGE immunoblotting.

## RESULTS

*Cochlin Is Uniquely Associated with Glaucomatous TM*—Protein extracts from six POAG and six normal TM tissues were subjected to SDS-PAGE, the gel slices were excised (Fig. 1*A*), and the proteins were identified using well established

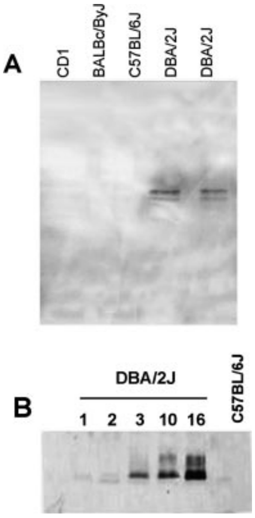

FIG. 2. **Cochlin expression in DBA/2J mice.** Protein (~10 $\mu g$) extracted from mouse TM was subjected to Western analysis with anti-Cochlin antibody. *A*, Cochlin expression in TM from C57BL/6J, CD1, BALBc/ByJ, and DBA/2J mice (all 10 weeks old) is shown with chemiluminescence detection. *B*, Cochlin expression is shown in TM from DBA/2J mice (1–16 weeks old) and a 16-week-old C57BL/6J control mouse detected using 800 nm IR dye-coupled anti-chicken secondary IgG.

mass spectrometric and bioinformatic methods. Overall, 368 proteins were identified, of which 52 were detected only in glaucomatous TM but with variable frequency (see supplemental Table I). Cochlin, a protein of unknown function, was the component identified most frequently in glaucomatous TM. Indeed, Cochlin was detected by mass spectrometry in 5 of the 6 POAG samples (see supplemental Table I) and by immunoblotting analyses in 20 of 20 glaucomatous TM samples but not in the 20 normal control TM samples, irrespective of cadaver or trabeculectomy tissue source (Fig. 1*B*). Based on these findings from human TM, we probed Cochlin expression in an established animal model of glaucoma, the DBA/2J mouse. This mouse line exhibits increased IOP at 6–8 months of age, with progressive damage to the optic nerve and progressive hearing loss (20). Western analyses of TM extracts from 10-week-old DBA/2J mice and from age-matched C57BL/6J, CD1, or BALBc/ByJ control mice, which do not develop increased IOP, revealed Cochlin expression only in TM from the DBA/2J mice (Fig. 2*A*). Western analysis of DBA/2J mouse TM over the first 16 weeks of postnatal development detected Cochlin expression at 1–2 weeks of age and demonstrated progressively increased expression at 3, 10, and 16 weeks of age (Fig. 2*B*).

*Cochlin Co-localizes with Mucopolysaccharide in Glaucomatous TM Deposits*—Sheath-derived plaques and microfibrillar deposits have been reported previously (21, 22) in the TM of POAG donor eyes. To probe the possible association of Cochlin with TM deposits, we pursued histochemical localization of Cochlin in the anterior segment of the human eye by staining alternate tissue sections with anti-Cochlin antibody or hematoxylin-eosin (Fig. 3*A*). Immunohistochemical analyses of 10 glaucomatous and 10 normal donor eyes confirmed the presence of Cochlin in glaucomatous but not normal TM (Fig. 3, *B–D*). Additional lower magnification and confocal microscopic images supporting the unique presence of Cochlin in glaucomatous TM deposits are shown in supplemental Figs. 1 and 2, respectively. Cochlin was localized within glaucomatous TM to variably sized deposits extending 80–150 $\mu m$ along the length of Schlemm's canal (Fig. 3, *C* and *D*). Movat's pentachrome staining revealed the presence of acidophilic MPS or glycosaminoglycan in the core of the Cochlin deposits (Fig. 3*F*) but not in control eyes (Fig. 3*E*). Cochlin and MPS co-localized throughout the inner portion of the glaucomatous deposits, around Schlemm's canal, and in pseudoendothelial cells, but MPS staining was lacking around the periphery of the deposits. The dense, highly branched microfibrillar plaques in the cochlea that have been reported (18) in *DFNA9* also contain both Cochlin and MPS or glycosaminoglycans.

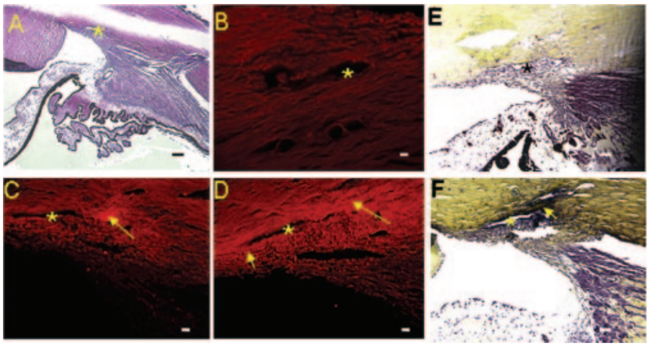

FIG. 3. **Histochemical localization of Cochlin in human TM.** *A*, an anterior segment section stained with hematoxylin-eosin is shown. *B–D*, representative immunohistochemical analysis is shown with chicken polyclonal anti-Cochlin. *B*, normal TM from a 75-year-old Caucasian female donor; *C* and *D*, glaucomatous TM sections approximately 60 $\mu m$ apart, obtained from a 77-year-old Caucasian female donor. Rhodamine-conjugated secondary antibody (anti-chicken) was used for immunofluorescence detection. *Arrows*, Cochlin deposits (*C* and *D*) that are ~80–150 $\mu m$; *, Schlemm's canal. *D*, *small* and *large arrows* show spotty and large deposits, respectively. *E* and *F*, light microscopy of Movat's pentachrome-stained tissue is shown. *E*, normal TM from a 75-year-old Caucasian female; *F*, glaucomatous TM from a 77-year-old Caucasian female. *Arrow*, MPS deposit around Schlemm's canal. *Bars* = 100 $\mu m$ (*A*, *E*, and *F*) and 40 $\mu m$ (*B–D*).

*Cochlin Causes in Vitro Aggregation of TM Cells*—The Cochlin protein structure contains an amino-terminal factor C homology (FCH) domain, two von Willebrand factor A-like (VWFA) domains, and two potential *N*-linked glycosylation sites. The FCH domain is named after the horseshoe crab coagulation factor, which becomes activated on binding lipopolysaccharides, initiating a host defense coagulation cascade. The FCH domain exists with unknown function in several other proteins. VWFA domains exist in a number of ECM and immune system components, interact with collagen proteins such as GpIb$\alpha$ and integrin $\alpha_{IIb}\beta_3$, and have been implicated in adherence to and aggregation of platelets and macrophages. To explore a possible role for Cochlin in ocular cell adhesion, we performed aggregation assays using human primary TM cells in culture and purified human recombinant Cochlin (Fig. 4). Aggregation of the TM cells was observed with the addition of exogenous Cochlin to the culture (Fig. 4*A*) but not with control protein Notch or with the empty recombinant vector-transfected medium (Fig. 4, *B* and *C*). Preincubating recombinant Cochlin with anti-Cochlin chicken antibody prior to adding it to the primary TM cell prevented cell aggregation, whereas preincubation with control chicken IgG did not (data not shown). Notably, the aggregation of purified recombinant Cochlin following sheer stress was also observed by non-reducing SDS-PAGE Western analysis, suggesting that disulfide bond formation may be involved in the aggregation mechanism (Fig. 4*F*). These *in vitro* observations are consistent with an extracellular role for Cochlin involving interactions with ECM components such as collagen.

*Age-dependent Changes in the Cochlin and Collagen Content of Glaucomatous TM*—To probe the molecular role of Cochlin in glaucomatous TM and a possible connection with ECM instability, expression levels of Cochlin and type II collagen were compared by quantitative Western analyses of glaucomatous and normal TM from donors of ages 40–85 years (Fig. 5). An

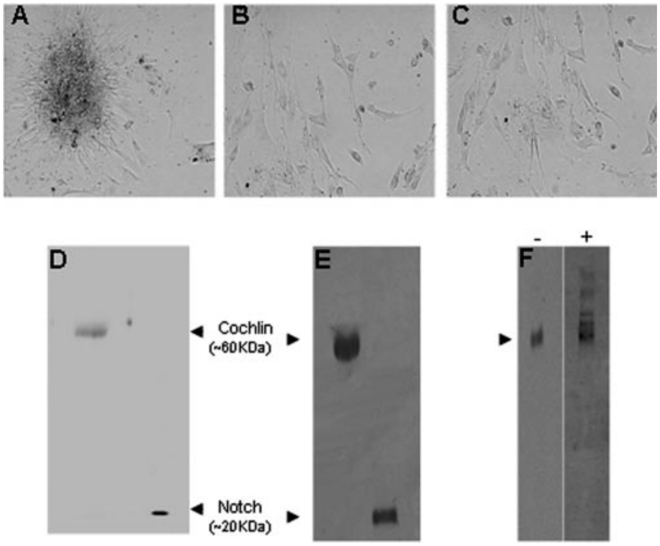

FIG. 4. **Aggregation of TM cells by Cochlin.** Primary TM cell cultures were established and treated as described under "Experimental Procedures" with: *A*, purified recombinant Cochlin (5 $\mu$g in 10 $\mu$l of PBS); *B*, purified recombinant Notch (5 $\mu$g in 10 $\mu$l of PBS); *C*, medium (10 $\mu$l) from mock empty vector-transfected COS-7 cells; *D*, Coomassie Blue-stained SDS-PAGE of purified recombinant Cochlin and Notch; *E*, Western analysis of purified recombinant Cochlin (~2 $\mu$g) and recombinant Notch (~1 $\mu$g) using polyclonal rabbit anti HA-antibody, and *F*, Western analysis after non-reducing 10% SDS-PAGE of purified recombinant Cochlin using anti-Cochlin antibody before (−) and after (+) sheer stress, revealing stress-induced higher mass aggregates (*arrowhead*).

age-dependent increase in Cochlin content was detected in glaucomatous TM, with a concomitant decrease in type II collagen. No significant change with age was apparent in the type II collagen content of normal TM. These results suggest that the increased presence of Cochlin may contribute to the alteration of ECM interactions in glaucomatous TM, perhaps resulting in the collapse or degradation of the collagen-containing microfibrils in TM beams.

## DISCUSSION

Classical proteomic methods initially detected Cochlin in the TM of glaucomatous but not normal human donors, irrespective of whether the tissue source was a cadaver or a fresh surgical specimen. Subsequently, Cochlin was found to be uniquely associated with glaucomatous human TM by Western and immunohistochemical analyses of additional POAG and normal TM donors. Western analyses also demonstrated the presence of Cochlin in TM from the DBA/2J glaucomatous mouse but not from three other mouse strains that do not develop elevated IOP. Proteomic analyses identified many other proteins in human TM (see supplemental Table I), including myocilin; however, the significance of proteins detected only in glaucomatous TM remains to be determined. A recent expressed sequence tag (EST) analysis (23) reported 1888 possibly expressed genes in normal human TM, including 198 of the 368 proteins (53%) identified in the present study. Other investigators (24) have demonstrated that protein and mRNA abundance levels in tissues are not directly proportional, and the lack of detection by LC MS/MS does not necessarily mean the absence of protein expression. Accordingly, comparisons of supplemental Table I data with the recent EST study results must be interpreted with caution. Our proteomic analyses were performed on individual, clinically documented TM samples, whereas the EST analysis was performed on mRNA pooled from 28 normal TM donors. The lack of rigorous quantitation further complicates the comparison of protein expression levels, which is exemplified by the EST detection of 28 clones of myocilin in normal donor TM in contrast to mass spectrometric detection of myocilin in 3 of 6 POAG TM analyzed but in none of 6 normal TM analyzed. Of relevance to the present study, two clones of Cochlin were observed in the EST analysis of pooled mRNA (23), implying a possible low level gene expression in normal TM. We have detected the *COCH* transcript in both normal and glaucomatous TM by reverse transcription PCR.[2] Nevertheless, our Western analysis reproducibly failed to detect the protein in non-glaucomatous tissues regardless of the amount of TM analyzed, strongly suggesting that Cochlin was absent or in very low abundance in normal TM.

Cochlin is the product of the *COCH* gene, and its FCH domain is mutated in patients with the autosomal dominant nonsyndromic auditory and vestibular disorder *DFNA9* (25, 26). *COCH* mutations have also been implicated in Ménière's disease (with features of hearing loss and vertigo) (27) and in presbyacusis (age-related hearing loss) (28). These disorders are late onset and progressive in nature and parallel the clinical manifestations of POAG. Cochlin comprises the major non-collagen component of the ECM of the inner ear (29) but is also expressed in very low levels in the cerebellum and eye (25, 30). Localization of Cochlin within the eye has not been reported previously. The protein structure is highly conserved, with human Cochlin exhibiting 94 and 79% amino acid sequence identity, respectively, with the mouse and chicken proteins. Cochlin is a secreted protein with three glycosylated isoforms detectable in human cochlea, with apparent masses of ~40, ~46, and ~60 kDa (15, 18, 31). Two Cochlin isoforms (~46 and ~60 kDa) were detected in glaucomatous TM; however, the antibody we used recognizes only the higher molecular weight isoforms (18). Misfolded Cochlin has been implicated in the formation of cochlear deposits in *DFNA9*; interestingly, the ~40- and ~46-kDa isoforms contain VWFA-like domains but lack the amino-terminal FCH domain, which contains the disease-associated mutations (18). It has been suggested (25, 30) that Cochlin plays a structural role in the architecture of the cochlea by binding to components of the ECM. In patients with *DFNA9*, there is a marked decrease in cellularity and an accumulation of eosinophilic deposits that obstruct the cochlear and vestibular nerve channels (16, 25, 32). In patients with POAG, Cochlin expression in the TM increases with age, along with acidophilic Cochlin deposits around Schlemm's canal, which are formed apparently by interactions with MPS and other ECM components.

Cochlin VWFA-like domains may contribute significantly to deposit formation in TM because hydrodynamic forces induce von Willebrand factor aggregation in suspension and may influence cell adhesion rates in the circulation (33). Although both wild type and mutant Cochlin expressed in COS-7 cells are processed and secreted normally, without apparent aggregation (18, 34), we found that sheer stress could induce the *in vitro* aggregation of purified recombinant Cochlin, possibly through disulfide bond formation. ECM interactions appear likely to underlie the formation of Cochlin deposits in glaucoma; however, hydrodynamic forces may exacerbate the process.

Cochlin may remain in the ECM of glaucomatous TM for a prolonged period and interact through its VWFA-like domains with fibrillar collagens. Altered interactions between fibrillar collagens and other ECM components have been suggested to trigger collagen degradation (35). Even simple dissociation between collagens and the surrounding ECM proteins may result in collagen degradation (36). Perturbations in collagenous

---

[2] S. K. Bhattacharya and J. W. Crabb, unpublished data.

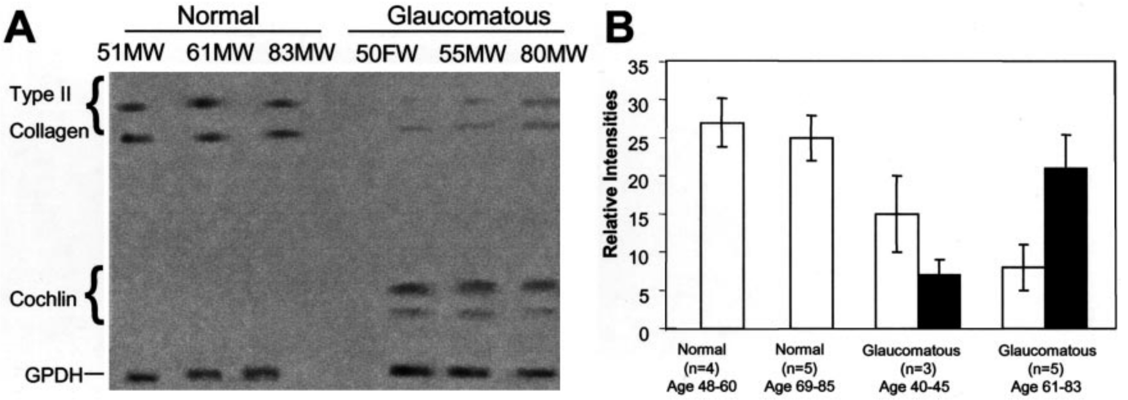

FIG. 5. **Cochlin increases and type II collagen decreases in glaucomatous TM.** *A*, representative quantitative Western analyses of normal and glaucomatous TM protein extracts (5 $\mu$g each) are shown for Cochlin, type II collagen, and glyceraldehyde-3-phosphate dehydrogenase (*GPDH*) using IR dye-coupled secondary antibodies detected with an Odyssey infrared imaging system. Donor age, race, and gender are indicated (*M*, male; *F*, female; *W*, Caucasian). *B*, quantitative summary of multiple Western analyses as in *A* with normalization to glyceraldehyde-3-phosphate dehydrogenase staining intensity. *Open bars*, type II collagen; *filled bars*, Cochlin; *error bars*, ±S.D. for the indicated number of samples analyzed.

fibrillar assembly caused by changes in collagen levels are known to result in a loss of tissue-specific morphology (36). Normally absent in healthy TM, Cochlin in combination with MPS may disrupt collagenous fibrillar assembly and contribute to collagen degradation in glaucomatous TM. The age-dependent increase in Cochlin and decrease in type II collagen that we observed in glaucomatous TM are consistent with an altered ECM. Although decreased collagen biosynthesis cannot be ruled out, the increased Cochlin may help to dissociate collagen from other TM proteins, rendering the ECM more susceptible to proteolytic degradation, collapse, and debris deposition. The large Cochlin deposits observed in glaucomatous TM could obstruct aqueous outflow across a wide region and thus have the potential to increase IOP.

Does Cochlin cause increased IOP or does increased IOP up-regulate Cochlin expression and deposition? Purified Cochlin exogenously added to TM primary cells resulted in the aggregation of the cells. Although the physiological relevance of this observation remains to be established, it is possible that Cochlin overexpression is associated with cell aggregation and MPS deposition, resulting in increased resistance and significant obstruction of the aqueous outflow. It is noteworthy that Cochlin is detectable in the DBA/2J mouse TM shortly after birth, and therefore, its expression precedes the earliest signs of elevated IOP at 6–8 months of age (20). Overall, the evidence presented here suggests that Cochlin may be involved in the intermediate events in glaucoma that lead to increased IOP. In any event, the presence of Cochlin-MPS deposits in TM from POAG patients opens new therapeutic avenues for treatment, for example, by targeted strategies for decreasing Cochlin expression or for increasing its degradation.

*Acknowledgments*—We thank Professors Ted Acott, M. Rosario Hernandez, Claude Burgoyne, and David Dueker for valuable discussions and comments on the manuscript, Marg Esser for technical assistance, Professor Joe Hollyfield for valuable discussions and for previously fixed histological samples, and Drs. Roger Langston, David Meisler, Bennie Jeng, and Victor Perez for control tissues.

## REFERENCES

1. Quigley, H. A. (1996) *Br. J. Ophthalmol.* **80,** 389–393
2. Cohen, C. S., and Allingham, R. R. (2004) *Curr. Opin. Ophthalmol.* **15,** 75–79
3. Tomarev, S. I. (2001) *Nat. Med.* **7,** 294–295
4. Morrison, J. C., and Acott, T. S. (2003) in *Glaucoma Science and Practice* (Morrison, J. C., and Pollack, I. P., eds) pp. 34–41, Thieme Medical Publishers Inc., NY
5. Lutjen-Drecoll, E. (1999) *Prog. Retin. Eye Res.* **18,** 91–119
6. Lutjen-Drecoll, E. (2000) *J. Glaucoma* **9,** 417–418
7. McMenamin, P. G., and Steptoe, R. J. (1991) *J. Anat.* **178,** 65–77
8. Sherwood, M. E., and Richardson, T. M. (1988) *Exp. Eye Res.* **46,** 881–895
9. Nickla, D. L., Wildsoet, C. F., and Troilo, D. (2002) *Investig. Ophthalmol. Vis. Sci.* **43,** 2519–2528
10. Bitner-Glindzicz, M. (2002) *Br. Med. Bull.* **63,** 73–94
11. Bom, S. J., Kunst, H. P., Huygen, P. L., Cremers, F. P., and Cremers, C. W. (1999) *Br. J. Audiol.* **33,** 335–348
12. Bradford, M. M. (1976) *Anal. Biochem.* **72,** 248–254
13. Crabb, J. W., Miyagi, M., Gu, X., Shadrach, K., West, K. A., Sakaguchi, H., Kamei, M., Hasan, A., Yan, L., Rayborn, M. E., Salomon, R. G., and Hollyfield, J. G. (2002) *Proc. Natl. Acad. Sci. U. S. A.* **99,** 14682–14687
14. West, K. A., Yan, L., Shadrach, K., Sun, J., Hasan, A., Miyagi, M., Crabb, J. S., Hollyfield, J. G., Marmorstein, A. D., and Crabb, J. W. (2003) *Mol. Cell. Proteomics* **2,** 37–49
15. Robertson, N. G., Resendes, B. L., Lin, J. S., Lee, C., Aster, J. C., Adams, J. C., and Morton, C. C. (2001) *Hum. Mol. Genet.* **10,** 2493–2500
16. Khetarpal, U. (2000) *Laryngoscope* **110,** 1379–1384
17. Stamer, W. D., Roberts, B. C., Howell, D. N., and Epstein, D. L. (1998) *Investig. Ophthalmol. Vis. Sci.* **39,** 1804–1812
18. Robertson, N. G., Hamaker, S. A., Patriub, V., Aster, J. C., and Morton, C. C. (2003) *J. Med. Genet.* **40,** 479–486
19. Nam, Y., Aster, J. C., and Blacklow, S. C. (2002) *Curr. Opin. Chem. Biol.* **6,** 501–509
20. Chang, B., Smith, R. S., Hawes, N. L., Anderson, M. G., Zabaleta, A., Savinova, O., Roderick, T. H., Heckenlively, J. R., Davisson, M. T., and John, S. W. (1999) *Nat. Genet.* **21,** 405–409
21. Ueda, J., Wentz-Hunter, K., and Yue, B. Y. (2002) *Investig. Ophthalmol. Vis. Sci.* **43,** 1068–1076
22. Lutjen-Drecoll, E., Shimizu, T., Rohrbach, M., and Rohen, J. W. (1986) *Exp. Eye Res.* **42,** 457–465
23. Tomarev, S. I., Wistow, G., Raymond, V., Dubois, S., and Malyukova, I. (2003) *Investig. Ophthalmol. Vis. Sci.* **44,** 2588–2596
24. Gygi, S. P., Rochon, Y., Franza, B. R., and Aebersold, R. (1999) *Mol. Cell. Biol.* **19,** 1720–1730
25. Robertson, N. G., Lu, L., Heller, S., Merchant, S. N., Eavey, R. D., McKenna, M., Nadol, J. B., Jr., Miyamoto, R. T., Linthicum, F. H., Jr., Lubianca Neto, J. F., Hudspeth, A. J., Seidman, C. E., Morton, C. C., and Seidman, J. G. (1998) *Nat. Genet.* **20,** 299–303
26. Kamarinos, M., McGill, J., Lynch, M., and Dahl, H. (2001) *Hum. Mutat.* **17,** 351
27. Fransen, E., Verstreken, M., Verhagen, W. I., Wuyts, F. L., Huygen, P. L., D'Haese, P., Robertson, N. G., Morton, C. C., McGuirt, W. T., Smith, R. J., Declau, F., Van de Heyning, P. H., and Van Camp, G. (1999) *Hum. Mol. Genet.* **8,** 1425–1429
28. de Kok, Y. J., Bom, S. J., Brunt, T. M., Kemperman, M. H., van Beusekom, E., van der Velde-Visser, S. D., Robertson, N. G., Morton, C. C., Huygen, P. L., Verhagen, W. I., Brunner, H. G., Cremers, C. W., and Cremers, F. P. (1999) *Hum. Mol. Genet.* **8,** 361–366
29. Ikezono, T., Omori, A., Ichinose, S., Pawankar, R., Watanabe, A., and Yagi, T. (2001) *Biochim. Biophys. Acta* **1535,** 258–265
30. Robertson, N. G., Skvorak, A. B., Yin, Y., Weremowicz, S., Johnson, K. R., Kovatch, K. A., Battey, J. F., Bieber, F. R., and Morton, C. C. (1997) *Genomics* **46,** 345–354
31. Ikezono, T., Shindo, S., Li, L., Omori, A., Ichinose, S., Watanabe, A., Kobayashi, T., Pawankar, R., and Yagi, T. (2004) *Biochem. Biophys. Res. Commun.* **314,** 440–446
32. Merchant, S. N., Linthicum, F. H., and Nadol, J. B., Jr. (2000) *Adv. Otorhinolaryngol.* **56,** 212–217
33. Shankaran, H., Alexandridis, P., and Neelamegham, S. (2003) *Blood* **101,** 2637–2645
34. Grabski, R., Szul, T., Sasaki, T., Timpl, R., Mayne, R., Hicks, B., and Sztul, E. (2003) *Hum. Genet.* **113,** 406–416
35. Pareti, F. I., Niiya, K., McPherson, J. M., and Ruggeri, Z. M. (1987) *J. Biol. Chem.* **262,** 13835–13841
36. Marchant, J. K., Hahn, R. A., Linsenmayer, T. F., and Birk, D. E. (1996) *J. Cell Biol.* **135,** 1415–1426

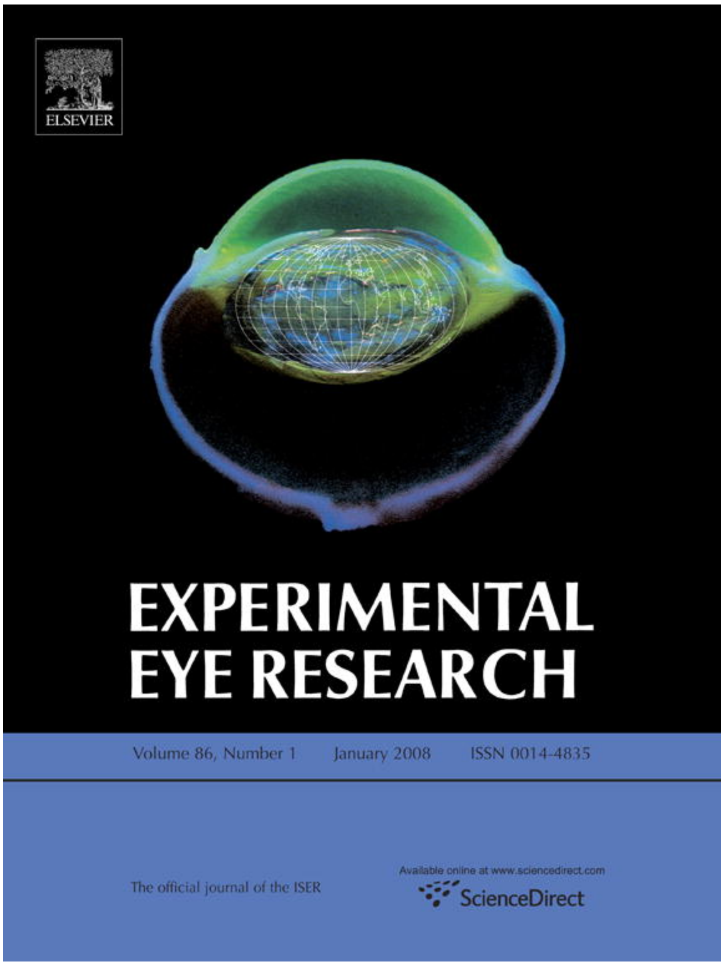
ELSEVIER
EXPERIMENTAL
EYE RESEARCH
Volume 86, Number 1 January 2008 ISSN 0014-4835
The official journal of the ISER
Available online at www.sciencedirect.com
ScienceDirect

Ophthalmic Genetics, 26:69–76, 2005

ISSN: 1381-6810 (print) / 1744-5094 (online)
DOI: 10.1080/13816810590968041

Taylor & Francis
Taylor & Francis Group

RESEARCH REPORT

# Abnormal Distribution of Red/Green Cone Opsins in a Patient with an Autosomal Dominant Cone Dystrophy

**Vera L. Bonilha and Joe G. Hollyfield**
*The Cole Eye Institute, The Cleveland Clinic Foundation, Cleveland, OH, USA*

**Sandeep Grover and Gerald A. Fishman**
*Department of Ophthalmology and Visual Sciences, University of Illinois, Chicago, IL, USA*

***Purpose:*** **To define the distribution of the red/green and blue opsins in cones from donor eyes from an affected member of a clinically well-characterized family with an autosomal dominant form of cone dystrophy.** ***Methods:*** **Tissue was fixed and processed for immunohistochemistry. Cryosections were studied by indirect immunofluorescence, using well-characterized antibodies to cone cytoplasm, rhodopsin, and cone opsins. The cone-associated matrix was also labeled with the lectin PNA. The affected donor eyes were compared to a postmortem matched normal eye.** ***Results:*** **Electroretinogram (ERG) testing three years prior to the affected member's death showed normal rod function, while the cone b-wave amplitude was reduced 40% below the lower limit of normal. Fundus exam showed only isolated drusen within the macula. Either a normal-appearing or only nonspecific macular findings were noted in the other affected family members who were examined. Immunofluorescence studies showed that blue cone opsin was restricted to the outer segments of blue cones in the affected retina. Red/green opsins were distributed along the entire plasma membrane of these cone types, from the tip of the outer segment to the synaptic base. Cone-associated matrix displayed a heterogeneous distribution. These patterns were observed both in the macula and in the periphery of the affected retina. Cone pedicles appeared larger than normal. In contrast, rhodopsin staining appeared normal.** ***Conclusions:*** **The immunocytochemical data obtained suggest that the clinical manifestation of this dystrophy is associated with an abnormal distribution of cone red/green opsins. Additionally, changes in the cone pedicles could have contributed to the abnormal cone ERG in this patient.**

**Keywords** Autosomal dominant cone dystrophy; cone opsins; clinical findings; immunohistochemistry

## INTRODUCTION

There are two types of photoreceptor cells in the human eye, namely rods and cones. These two cell types perform different functions. Rods primarily mediate vision at low light levels, while the cone photoreceptors mediate vision under standard light conditions. Vertebrate retinal cones play a major role in both visual acuity and color perception. Several investigational methods have shown that the L (red) and M (green) cone pathways subserve high visual acuity as well as color vision through the midget ganglion cell pathway.[1,2] On the other hand, the S (blue) cone pathway is characterized by having its own bistratified ganglion cell type and a separate channel.[2,3] The molecular genetics of color vision has turned out to be extremely complex due, at least in part, to the fact that the red and the green opsin genes are adjacent to one another and that they are 98% identical.[4]

Progressive cone dystrophies are characterized by bilateral visual loss, color vision abnormalities, central scotomas, and electroretinogram (ERG) recordings that show a predominant loss in cone function.[5–9] Funduscopic examination may show either minimal and nonspecific pigmentary changes within the fovea, an easily discernible atrophic bull's-eye-appearing macular lesion, or more diffuse pigmentary degenerative changes involving both the macula and retinal peripheral areas.[8] Variable degrees of nystagmus and photoaversion may also be present. Cone dystrophies can show autosomal dominant, autosomal recessive, or X-linked recessive inheritance. There is clinical as well as genetic heterogeneity.[5–9] Various phenotypes are well

---

Accepted 24 January 2005.

Address correspondence to Vera L. Bonilha, Ph.D., Cole Eye Institute, Cleveland Clinic Foundation, 9500 Euclid Avenue, i31, Cleveland, OH 44195, USA. E-mail: bonilhav@ccf.org

characterized both clinically and psychophysically and several causative genes have been identified.[10,11] Many of these encode proteins involved in the cone phototransduction pathway. To gain further understanding of specific alterations of cone photoreceptors, immunocytochemistry studies with the eyes of a member from a family with an autosomal dominant form of cone dystrophy are discussed.

## METHODS

### Patient Information

The donor was an affected 85-year-old man who died from bladder and prostate cancer. He was an affected member (member IV-1, Fig. 1) of a family with an autosomal dominant form of cone dystrophy with incomplete penetrance. His eyes were obtained through the National Retinitis Pigmentosa Foundation Donor Program (donation number #686). The patient and several other affected members in the family were clinically evaluated. The donor had had an ocular exam three years prior to his death. Goldmann visual field and full-field ERG were also obtained at that time. Other selected members of the family underwent an evaluation by Goldmann visual field, full-field ERG, and either focal or multifocal ERG testing.

The clinical evaluation of the affected members was carried out at the University of Illinois with the approval of the Institutional Review Board (IRB) at the University of Illinois Medical Center. The immunocytochemistry analysis was performed in the Cleveland Clinic Foundation and is exempt of IRB approval.

### Histopathology

The donor's globes were fixed 14.5 h postmortem in a mixture of 4% paraformaldehyde and 0.5% glutaraldehyde made in 0.1 M phosphate buffer (pH 7.3). After a month in this fixative, the globes were transferred and stored in 2% paraformaldehyde prepared in the same buffer. As a control, the eyes from a 68-year-old female were fixed 14.5 h postmortem in 2% paraformaldehyde made in the same buffer. The tissues were infused successively with 10% and 20% sucrose in PBS, and embedded in Tissue-Tek '4583' (Miles Inc., Elkhart, IN, USA). Twelve $\mu$m cryosections were cut on a cryostat HM 505E (Microm, Walldorf, Germany) equipped with a CryoJane Tape-Transfer system (Instrumedics, Inc., Hackensack, NJ, USA).

Sections were processed for immunofluorescence as previously described.[12] Cryosections of both the matched control and affected donor tissues were labeled with the following antibodies: rabbit polyclonal antibody p4924A to blue cone opsin (1:10, from the late Dr. C. Lerea), rabbit polyclonal antibody p108B to red/green cone opsins (1:50, from the late Dr. C. Lerea), rabbit polyclonal antibody UW-16 to red/green cone opsins (1:200, from Dr. J. Saari, University of Washington, Seattle, WA, USA), monoclonal antibody B630N to rhodopsin (1:50, from Dr. P. Hargrave, University of Florida, Gainesville, FL, USA), and the

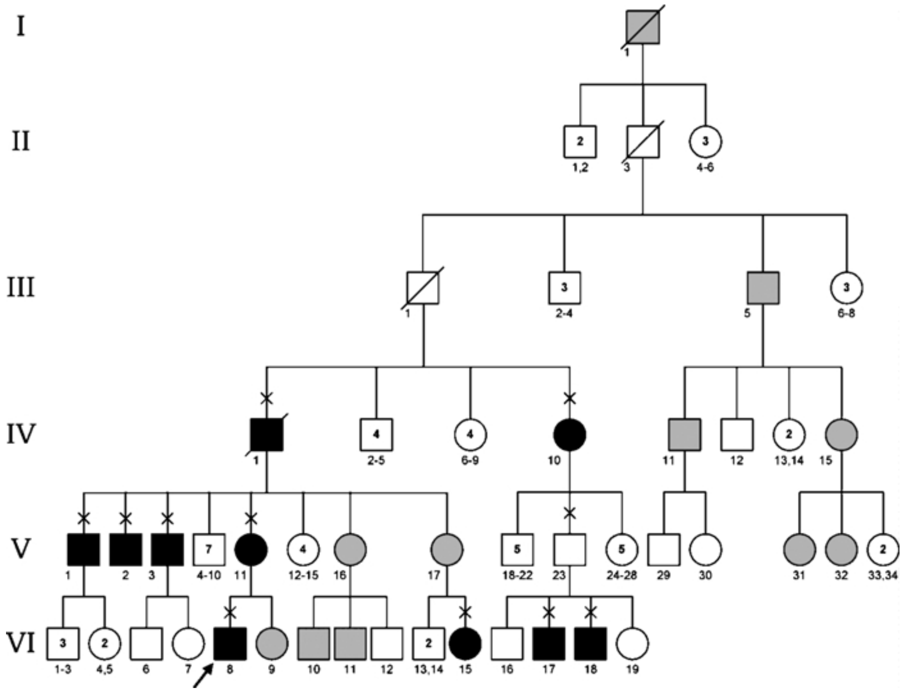

FIG. 1. Pedigree of the family with autosomal dominant cone dystrophy with incomplete penetrance showing affected (solid symbols) and unaffected (open symbols) family members. The symbol x indicates patients examined personally; hatched symbols, patients who are affected by history but not personally examined; arrow, proband; single oblique line, deceased. The postmortem analysis in this study was done on member IV-1.

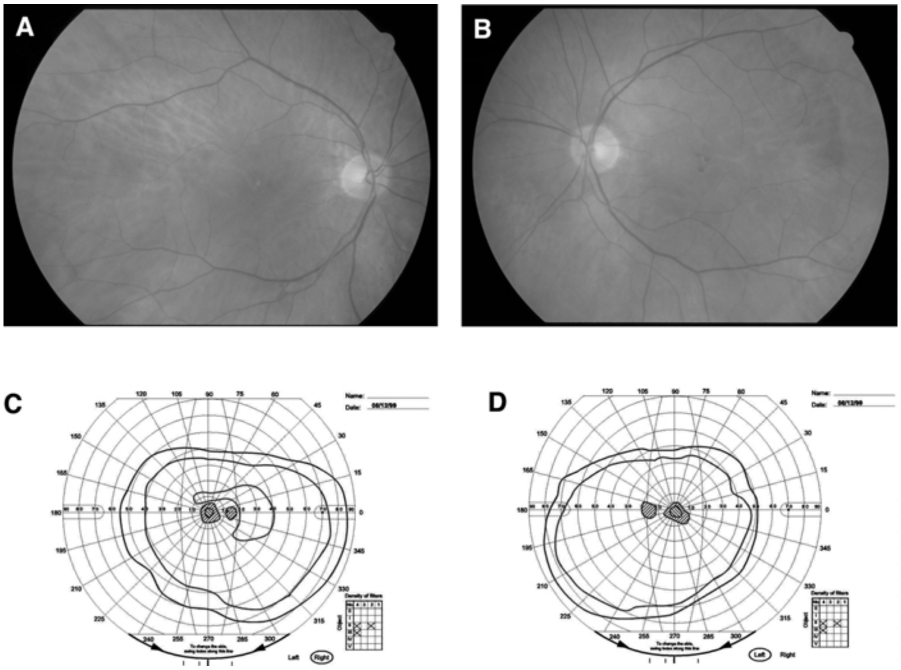

FIG. 2. Fundus photograph of both the right (A) and left (B) eyes of family member IV-1 showing a normal-appearing optic disc, retinal vessels, and macula with isolated drusen in the foveal region. Goldmann visual field of the right (C) and left (D) eyes of the same family member showing central scotomas to targets III4e and II4e with normal-appearing peripheral isopters. Right eye (OD) shows an additional central scotoma to target II2e.

monoclonal antibody 7G6 to cone cytoplasm (1:100, from Dr. P. MacLeish, Morehouse School of Medicine, Atlanta, GA, USA). Cone-associated matrix was labeled with PNA-FITC (1:100, Vector, Burlingame, CA, USA) and cell nuclei were labeled with TO-PRO® -3 iodide (1 $\mu$g/ml, Molecular Probes, Eugene, OR, USA). Secondary antibodies (goat anti-mouse or anti-rabbit IgG; 1:1000) were labeled with Alexa Fluor 488 (green) and Alexa Fluor 594 (red; Molecular Probes). Sections were analyzed using a Leica laser scanning confocal microscope (LSCM) (TCS-SP2, Leica, Exton, PA, USA). A series of 1 $\mu$m *xy* (en face) sections were collected. Each individual *xy* image of the retinas stained represents a three-dimensional projection of the entire cryosection (sum of all images in the stack). Microscopic panels were composed using AdobePhotoshop 5.5 (Adobe, San Jose, CA, USA).

## RESULTS

### Clinical Findings

Figure 1 shows the pedigree of the family affected with an autosomal dominant form of cone dystrophy with incomplete penetrance. The donor (member IV-1), at age 85 years, was last examined three years before his death. At age 82 years, the patient complained of problems with central vision, but had no history of difficulty with peripheral or night vision. His best-corrected visual acuity was 20/200 in the right eye with a $-0.75$ D sph $+1.25$ D cyl at 90° and 20/200 in the left eye with a $-0.50$ D sph $+1.00$ cyl at 90°. Except for mild cataracts in both eyes, the anterior segment exam was normal. Fundus examination showed normal-looking optic disc, retinal vessels, and peripheral retina in both eyes. The fovea in each eye showed punctate drusen (Fig. 2A,B). Goldmann visual field (Fig. 2C,D) showed small central scotomas to targets III4e and II4e in both eyes and an additional central scotoma to target II2e in the right eye (Fig. 2C). The peripheral isopters were within normal limits. A full-field ERG recording obtained from the patient showed normal rod function and mildly subnormal cone function (Fig. 3).

Nine other affected family members were also examined (see Figure 1). The ages at the most recent visit ranged from 20 to 76 years. All the affected members initially noted problems with their central vision in the first ($n = 7$) or second ($n = 2$) decade of life. Five out of nine patients complained of photoaversion. None of them had any problems with peripheral or night vision. Best-corrected visual acuity in the better-seeing eye ranged from 20/50 to 20/70. Whereas all the affected members showed normal-looking optic discs, retinal vessels, and peripheral retina, only two out of nine had an entirely normal-appearing fovea. The foveal changes included a blunted foveal reflex ($n = 4$) or mild pigment mottling within the fovea ($n = 3$). Seven out of eight patients, on whom Goldmann visual field testing was performed, showed a relative central scotoma. Four out of seven patients on whom a full-field ERG was obtained showed normal cone and rod responses, two additional patients showed a normal rod response and reduced cone b-wave responses, and one patient had

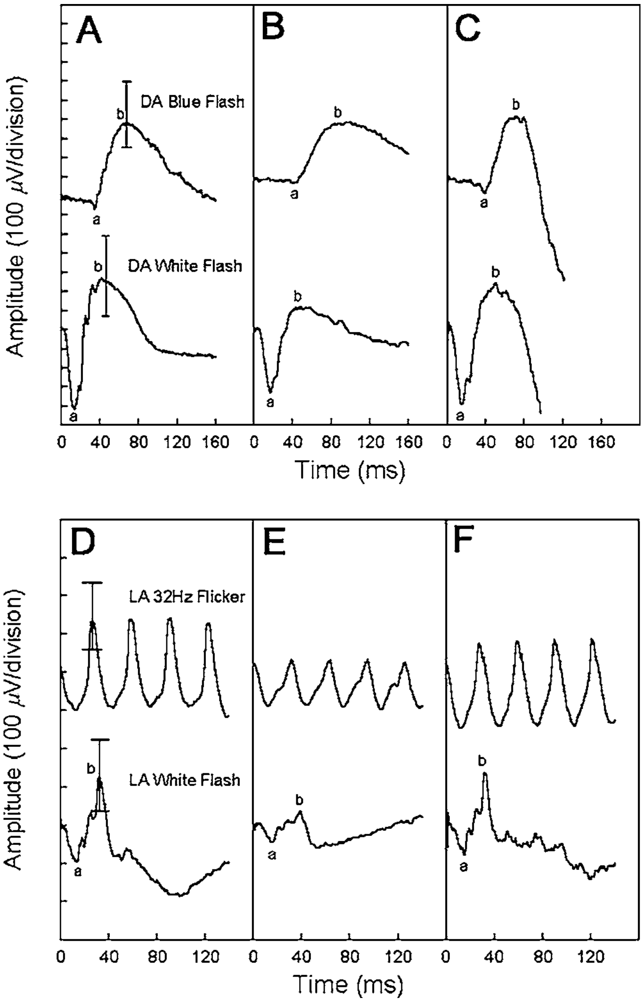

FIG. 3. Full-field, dark (A-C)- and light (D-F)-adapted electroretinograms (ERG) from the right eye of family member IV-1 (B and E). Normal dark-adapted b-wave amplitudes are observed compared to a visually normal subject (A). Also shown are the ERG from the right eye of one of his affected sons (family member V-2) with normal dark-adapted b-wave amplitudes (C). The light-adapted ERG shows reduced b-wave amplitudes in family member IV-6 (E), but normal amplitudes (F) from the right eye of his affected son (family member V-2) compared to a visually normal subject (D).

both rod and cone b-wave responses that were slightly reduced. In the two patients on whom full-field ERG data were not obtained, a multifocal ERG was obtained which showed reduced cone responses selectively in the central rings. Of the four members who had normal cone and rod responses on full-field ERG, a focal ERG was obtained in two and both were abnormal.

### Histological Pathology

To understand some of the molecular changes associated with the autosomal dominant cone dystrophy (ADCD) phenotype in this family, both eyes of one of the family members (IV-1, Fig. 1) were processed for cryosectioning and immunofluorescence. The distribution of the red/green cone opsins was analyzed both in the retinal periphery and in the macular region of the ADCD-affected member (Fig. 4D-F) and a matched control eye (Fig. 4A-C). Cryosections of each donor eye were labeled with both a cone cytoplasmic marker (Fig. 4B, E) and with an antibody specific to red/green opsins (Fig. 4A, D). A striking abnormal distribution of the red/green opsins throughout the entire cone cell body was observed in all the ADCD-affected eyes (Fig. 4D-F) when compared to the matched control eye (Fig. 4A-C). This unique distribution was observed in all reactive cones present in the macula (Fig. 4) and the periphery (data not shown) of all the sections that were labeled and observed from the affected eye. The same unrestricted distribution of the red/green opsin was observed with a different red/green opsin antibody (data not shown). Cell nuclei, labeled with TO-PRO-3, did not display any significant difference to the matched control. The retinal pigment epithelium (RPE) and choroid also did not display any significant difference between both samples.

In addition, abnormally enlarged cone pedicles were observed in affected retina (Fig. 4H) when the entire cone cell body was labeled with a cone cytoplasm antibody and compared to the matched control eye (Fig. 4G). Again, these observations were apparent in both the macula and periphery (data not shown) of the affected eye.

In contrast, the blue cone opsin of the affected ADCD eye (Fig. 5D) displayed restricted distribution to the cone outer segments when compared to the matched control eye (Fig. 5A). Results are shown in the macula, but were also observed in the periphery.

The rod outer segments were visualized through labeling with rhodopsin antibodies. There was no detectable difference between the rhodopsin labeling of the ADCD-affected eye (Fig. 6E) and the control matched eye (Fig. 6B). Furthermore, the cone interphotoreceptor matrix (IPM) was also labeled in these eyes. Again, the cone-associated matrix of the ADCD-affected eye sections (Fig. 6D) was disorganized and heterogeneous when compared to the cone IPM from the control postmortem-matched eye (Fig. 6A). These findings were observed both in the macula (Fig. 6D) and retinal periphery (data not shown).

## DISCUSSION

The diagnosis of cone dystrophy in this family was made on the basis of decreased central visual acuity in all ten affected members (8 out of 10 noted this symptom in their first decade of life and the remaining 2 in the second decade). Additionally, relative central scotomas were observed in eight out of nine members who were tested by Goldmann perimetry. Also considered in the diagnosis were decreased cone responses on electrophysiological testing in eight out of ten affected members by either full-field (n = 4), focal (n = 2), or multifocal (n = 2) electroretinography. Progressive cone dystrophies show appreciable clinical

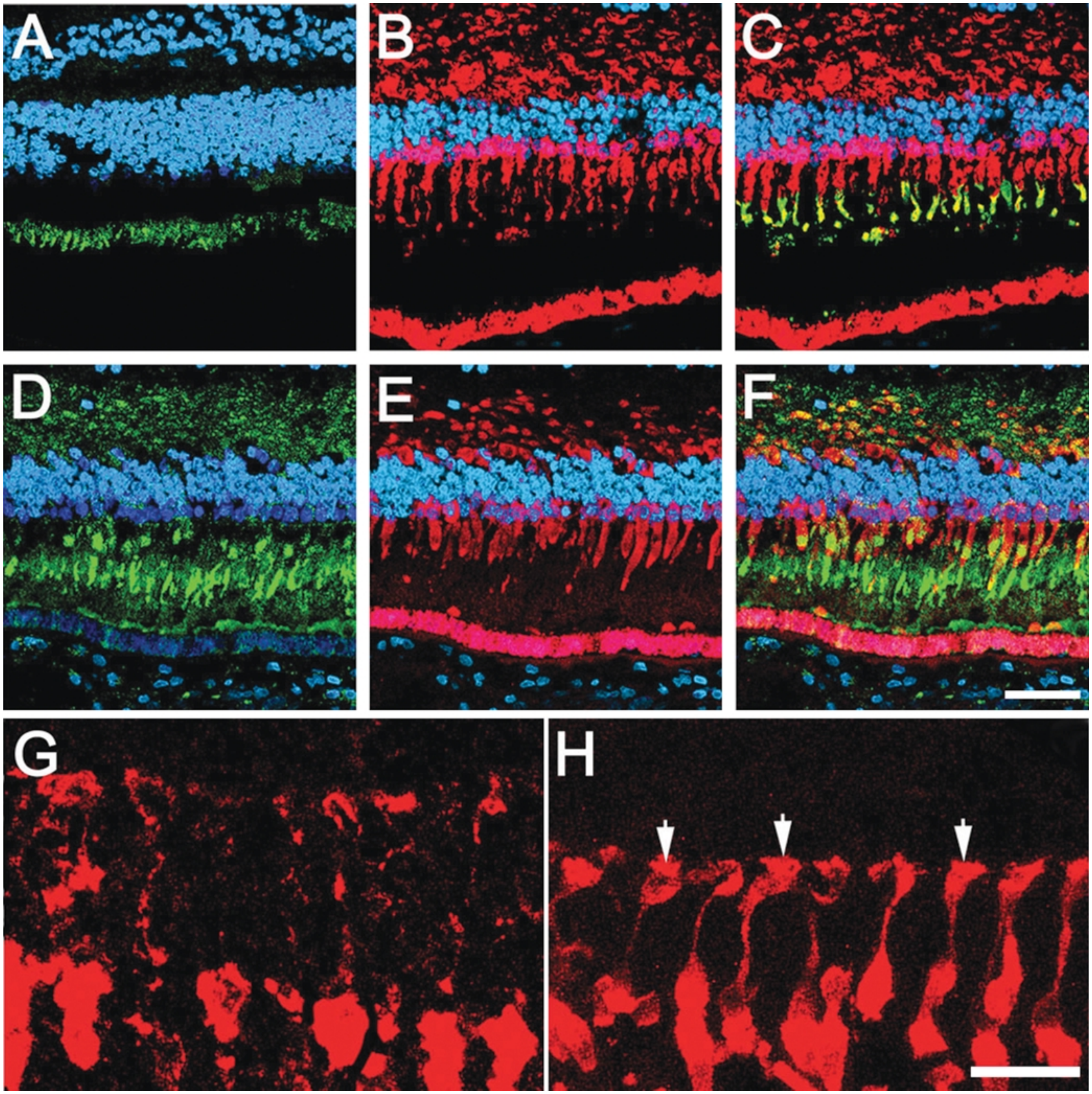

FIG. 4. Red/green cone opsins are distributed along the entire plasma membrane of this cone type in the ADCD patient's retina. Human cryosections of both the ADCD family member (D-F) and the matched control (A-C) were labeled with antibodies specific to red/green cone opsins (green) (A,D) and the cone cytoplasm marker 7G6 (red) (B, E, G, H). Cell nuclei were labeled with TO-PRO-3 (blue). A series of 1 $\mu$m *xy* (en face) sections were collected using an LSCM. Each individual *xy* image of the retinas stained represents a three-dimensional projection of the entire cryosection (sum of all images in the stack). The merged images are shown in C and F. Comparison of the samples showed that red/green cone opsins are distributed along the entire plasma membrane of these cone types, from the tip of the outer segments to the synaptic base in the ADCD eye, while they are restricted to the outer segments in the matched control eye. Higher magnifications showed that the cone pedicles of the affected retina (arrowheads) are markedly enlarged when compared to those in the normal retina. Bars: 40 $\mu$m and 20 $\mu$m (G and H).

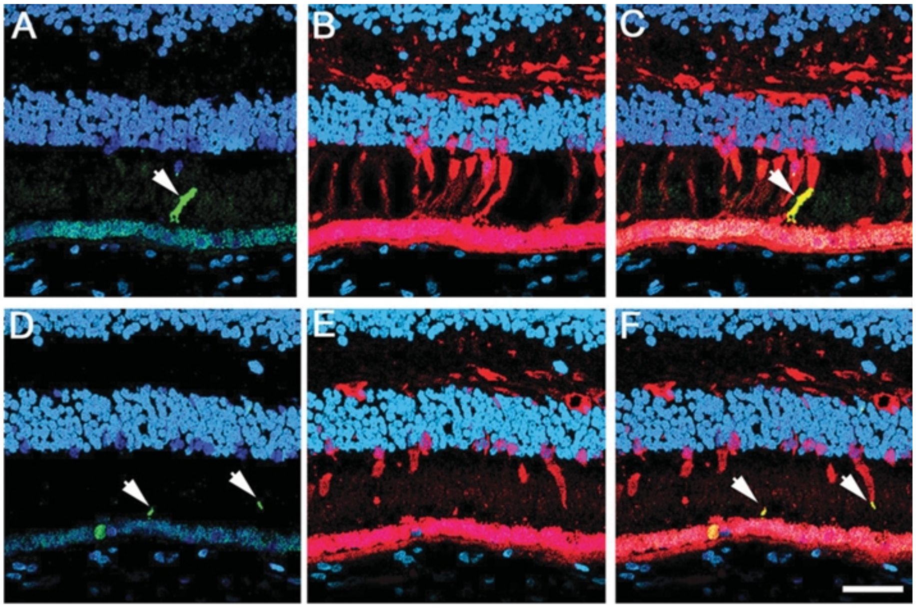

FIG. 5. Blue cone opsin is restricted to the outer segments of the cones in the affected retina. Human cryosections of both the ADCD family member (D-F) and the matched control (A-C) were labeled with antibodies specific to blue cone opsin (green) (A, D) and the cone cytoplasm marker 7G6 (red) (B, E). Cell nuclei were labeled with TO-PRO-3 (blue). The merged images are shown in C and F. Sections were analyzed using an LSCM. A series of 1 $\mu$m *xy* (en face) sections were collected. Each individual *xy* image of the retinas stained represents a three-dimensional projection of the entire cryosection (sum of all images in the stack). Comparison of the samples showed that blue cone opsin is restricted to the outer segments of the cones in both the normal and ADCD eyes (arrowheads). Bar: 40 $\mu$m.

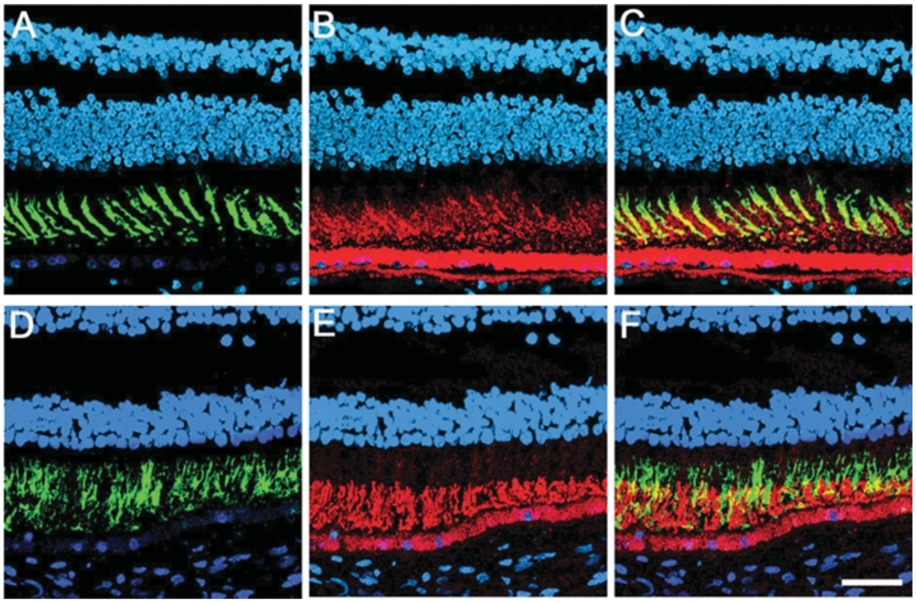

FIG. 6. Rod distribution is normal, but cone IPM is disorganized in the affected retina. Human cryosections of both the ADCD family member (D-F) and the matched control (A-C) were labeled with the cone IPM marker PNA (green) (A, D) and an antibody specific to rhodopsin (red) (B, E). Cell nuclei were labeled with TO-PRO-3 (blue). The merged images are shown in C and F. Sections were analyzed using an LSCM. A series of 1 $\mu$m *xy* (en face) sections were collected. Each individual *xy* image of the retinas stained represents a three-dimensional projection of the entire cryosection (sum of all images in the stack). Comparison of the samples showed that the cone IPM displayed a heterogeneous distribution in the affected eye sections. In contrast, rhodopsin staining was not different from the matched control eye. Bar: 40 $\mu$m.

as well as genetic heterogeneity, which likely results from diverse molecular mechanisms underlying the pathogenesis and the functional loss of central vision.[5–9] This study demonstrated substantial alterations in the distribution of red/green cone pigments compared to the distribution in normal control tissues. These changes included loss of opsin restriction to the cone outer segment, resulting in its distribution throughout the entire cone cell body. The pedicles of these red/green cones were enlarged.

A previous histological study that analyzed eyes from a patient with cone-rod dystrophy (CRD) detected shortening of photoreceptor outer segments in the central and far peripheral regions of the retina.[13] More recently, analysis of a case of CRD and a case of central areolar choroidal dystrophy detected similar pathologic changes in the outer segments of both cones and rods with abnormally enlarged pedicles and axons.[14] Our results did not detect any gross structural abnormalities associated with the photoreceptor cells. However, the presence of abnormal cone pedicles could possibly, at least in part, explain the slightly reduced cone ERG b-wave amplitude results recorded in our donor.

The outer segments of the cones contain visual pigments, which are excited by photons of absorbed light. Visual pigment consists of molecules composed of two distinct portions: a protein portion called opsin and a light-absorbing portion, which is the cis-retinal chromophore. Specific structural features of the opsin protein determine the wavelength sensitivity to light at the different regions of the visible spectrum. Our immunofluorescence studies were carried out with previously described antibodies specific to the red/green and the blue cone opsins.[15,16] Our labeling of the red/green opsins detected a large population of these cone types throughout the entire retina when compared to those with blue cone opsin. This result is in agreement with several reports demonstrating that the human retina is composed of roughly 90% red/green and 10% blue cones.[17–20]

In this specific case of cone dystrophy, the most striking cone abnormality was the presence of red/green opsins throughout the entire cone cell body instead of the usual restriction to the outer segment. A previous study of enhanced S-cone syndrome donor eyes reported the presence of abnormal distribution of both S (blue)- and L/M (red/green)-cone opsin along the entire plasma membranes of the cell, including their inner segments, cell bodies, axon, and pedicles.[16] Moreover, a patient with X-linked cone degeneration (a known 6.5-kilobase deletion in the red cone pigment gene) showed a significant diminution of the red and green cone population when compared with an age-matched control eye. Some remaining red and green cones without outer segments, however, did stain weakly with the antibody to red and green opsin in the inner segments.[21] Although the molecular mechanism of visual excitation in the cone is not as well understood as in the rod, it is generally thought to involve a cone-specific G protein (cone transducin) that couples the cone visual pigment to a cGMP phosphodiesterase. The functional significance of the red/green opsin delocalization is not known, but it could result in a major loss of sensitivity which, in turn, could lead to sufficient cone degeneration to cause the scotomas detected in our affected patients. Furthermore, it is known that in primates, all cone types display opsin labeling through out the entire cone cell body when they are first expressed in the fetal period becoming restricted to the outer segments later in their development.[22] It is not known whether the red/green opsins failed to become restricted to the outer segment in development or whether the normal distribution was lost during the progression of the disease.

In conclusion, we report the clinical findings and abnormal distribution of the red/green cone opsins throughout the entire cone cell body and the enlargement of the cone pedicles from a member of a family with an autosomal dominant form of cone dystrophy. These results are important to our understanding of one of likely several molecular mechanisms underlying various types of cone dystrophy.

## ACKNOWLEDGEMENTS

The authors thank Dr. Peter MacLeish (Morehouse School of Medicine, Atlanta, GA, USA) for providing the antibody to cone cytoplasmic marker (7G6), Dr. Paul Hargrave (University of Florida, Gainesville, FL, USA) for providing the antibody to rhodopsin (B630N), and Dr. John C. Saari (University of Washington, Seattle, WA, USA) for providing the antibody to red/green cone opsins (UW-16). The anti-blue (p4924A) and red/green (p108B) cone opsin antibodies were prepared by the late Dr. Connie Lerea. This work was supported by The Foundation Fighting Blindness, Owings Mills, MD (JGH), The Grant Healthcare Foundation (GAF), and National Institute of Health (NEI) grant EY 015638 (JGH).

This work was presented at the Association for Research in Vision and Ophthalmology Annual Meeting, May 2004, and at the XIth International Symposium on Retinal Degeneration Meeting, August 2004.

## REFERENCES

1. Jacobs GH. Primate photopigments and primate color vision. *Proc Natl Acad Sci USA.* 1996;93:577-581.
2. Dacey DM. Primate retina: cell types, circuits and color opponency. *Prog Retin Eye Res.* 1999;18:737-763.
3. Dacey DM, Lee BB. The ‘blue-on’ opponent pathway in primate retina originates from a distinct bistratified ganglion cell type. *Nature.* 1994;367:731-735.
4. ►Neitz M, Neitz J. Molecular genetics of color vision and color vision defects. *Arch Ophthalmol.* 2000;118:691-700.
5. Krill AE, Deutman AF, Fishman M. The cone degenerations. *Doc Ophthalmol.* 1973;35:1-80.
6. Kellner U, Kleine-Hartlage P, Foerster MH. Cone dystrophies: clinical and electrophysiological findings. *Ger J Ophthalmol.* 1992;1:105-109.
7. Moore AT, Evans K. Molecular genetics of central retinal dystrophies. *Aust NZ J Ophthalmol.* 1996;24:189-198.

8. Szlyk JP, Fishman GA, Alexander KR, Peachey NS, Derlacki DJ. Clinical subtypes of cone-rod dystrophy. *Arch Ophthalmol.* 1993;111:781-788.
9. Yagasaki K, Jacobson SG. Cone-rod dystrophy. Phenotypic diversity by retinal function testing. *Arch Ophthalmol*. 1989;107:701-708.
10. Koenekoop RK. The gene for Stargardt disease, ABCA4, is a major retinal gene: a mini-review. *Ophthalmic Genet.* 2003;24:75-80.
11. Palczewski K, Sokal I, Baehr W. Guanylate cyclase-activating proteins: structure, function, and diversity. *Biochem Biophys Res Commun.* 2004;322:1123-1130.
12. Bonilha VL, Finnemann SC, Rodriguez-Boulan E. Ezrin promotes morphogenesis of apical microvilli and basal infoldings in retinal pigment epithelium. *J Cell Biol.* 1999;147:1533-1548.
13. Rabb MF, Tso MO, Fishman GA. Cone-rod dystrophy. A clinical and histopathologic report. *Ophthalmology.* 1986;93:1443-1451.
14. Gregory-Evans K, Fariss RN, Possin DE, Gregory-Evans CY, Milam AH. Abnormal cone synapses in human cone-rod dystrophy. *Ophthalmology.* 1998;105:2306-2312.
15. Lerea CL, Bunt-Milam AH, Hurley JB. Alpha transducin is present in blue-, green-, and red-sensitive cone photoreceptors in the human retina. *Neuron.* 1989;3:367-376.
16. Milam AH, Rose L, Cideciyan AV, Barakat MR, Tang WX, Gupta N, Aleman TS, Wright AF, Stone EM, Sheffield VC, Jacobson SG. The nuclear receptor NR2E3 plays a role in human retinal photoreceptor differentiation and degeneration. *Proc Natl Acad Sci USA*. 2002;99:473-478. Epub 2002 Jan 2002.
17. Curcio CA, Allen KA, Sloan KR, Lerea CL, Hurley JB, Klock IB, Milam AH. Distribution and morphology of human cone photoreceptors stained with anti-blue opsin. *J Comp Neurol.* 1991;312:610-624.
18. Roorda A, Williams DR. The arrangement of the three cone classes in the living human eye. *Nature.* 1999;397:520-522.
19. Takada Y, Ohhashi T, Suzuki M, Kitahara K, Kobayashi M. Immunohistochemical detection of retinal cones in monkey retina: light and electron microscopic study. *Jpn J Ophthalmol.* 2000;44:503-510.
20. Roorda A, Metha AB, Lennie P, Williams DR. Packing arrangement of the three cone classes in primate retina. *Vision Res.* 2001;41:1291-1306.
21. To KW, Adamian M, Jakobiec FA, Berson EL. Histopathologic and immunohistochemical study of an autopsy eye with X-linked cone degeneration. *Arch Ophthalmol.* 1998;116:100-103.
22. Xiao M, Hendrickson A. Spatial and temporal expression of short, long/medium, or both opsins in human fetal cones. *J Comp Neurol.* 2000;425:545-559.